Technische Universität München
Institut für Energietechnik

Lehrstuhl für Thermodynamik

Boundary Layer Flashback in Premixed Combustion Systems

Vera Hoferichter

Vollständiger Abdruck der von der Fakultät für Maschinenwesen der Technischen Universität München zur Erlangung des akademischen Grades eines

DOKTOR – INGENIEURS

genehmigten Dissertation.

Vorsitzender:
    Prof. dr.ir. Daniel J. Rixen
Prüfer der Dissertation:
    Prof. Dr.-Ing. Thomas Sattelmayer
    Prof. Dr. rer. nat. Friedrich Dinkelacker

Die Dissertation wurde am 14.11.2016 bei der Technischen Universität München eingereicht und durch die Fakultät für Maschinenwesen am 30.03.2017 angenommen.

Acknowledgments

This work was conducted during my time at Lehrstuhl für Thermodynamik, Technische Universität München. It is part of the BIGCCS Centre, performed under the Norwegian research program "Centres for Environment-friendly Energy Research" (FME). I highly acknowledge the financial support and the contributions of the following BIGCCS partners: ConocoPhilips, Gassco, Shell, Statoil, TOTAL, GDF SUEZ and the Research Council of Norway (193816/S60).

I would like to thank my supervisor, Professor Thomas Sattelmayer for giving me the opportunity to experience the friendly and pleasant atmosphere at his institute. I appreciated his confidence in me and my work and the resulting freedom to shape the goals of my project according to my ideas and preferences. At the same time, he provided the necessary support and advice during challenging periods of my Ph.D..

Apart from that, I am very thankful for the numerous opportunities to attend international conferences and for the regular meetings with the BIGCCS partners in Norway which effectively stimulated the personal and scientific exchange. I am grateful for the chance to getting to know and to collaborate with Yoshikazu Matsumura from Mitsubishi Hitachi Power Systems, Japan, and for the opportunity to visit the University of California Combustion Laboratory (UCICL). In this context, I also would like to thank Vincent McDonell for allowing me to work in his group and for the warm welcome in Irvine. I thank Alireza Kalantari and Elliot Sullivan-Lewis for the fruitful and friendly cooperation during our joint experimental work. Special thanks to Hannah Bower for her friendship and for making my stay in Irvine very enjoyable.

I also would like to thank Professor Dinkelacker from Leibniz Universität Hannover for being the second examiner in my committee as well as Professor

Rixen for taking over the examination presidency.

Furthermore, I would like to thank all current and former colleagues at Lehrstuhl für Thermodynamik for the good collaboration, the mutual assistance and the delightful time. Special thanks to Denise Ahrens and Michael Kolb for letting me be part of their Ph.D. projects during my Diploma thesis and for convincing me to stay for my Ph.D.. More special thanks to Christoph Hirsch for the many fruitful discussions on the details of flame flashback, to my predecessor Georg Baumgartner for the smooth transfer of our project and test rig, and to Frederik Berger, Aaron Endres, Georg Fink, Peter Katzy and Nicolai Stadlmaier for reviewing this thesis. Since this work has been produced with the help and commitment of many students, I would like to thank all of them for their contributions, especially Payam Mohammadzadeh Keleshtery, who has assisted me in the experimental work and in the data analysis over a long period of time.

My greatest thanks to my family, especially my parents, who have supported and encouraged me in all decisions and at all times. Finally, I would like to thank Thomas for his meticulous formal correction of this thesis and all my publications, as well as for his support and understanding.

München, May 2017

Vera Hoferichter

Kurzfassung

Flammenrückschlag in die Vormischzone ist seit der Verwendung vorgemischter Verbrennungssysteme eine Herausforderung in der Entwicklung von Gasturbinenbrennern. Bei der Verwendung hochreaktiver Brennstoffe stellt vor allem Flammenückschlag in den Bereichen niedriger Strömungsgeschwindigkeiten in der Grenzschicht der Brennerwand ein Hauptproblem dar. Treten Verbrennungsinstabilitäten auf, kann Wandrückschlag durch die induzierten Geschwindigkeitsschwankungen am Brenneraustritt ausgelöst werden.

Im experimentellen Teil dieser Arbeit wird der Effekt von Geschwindigkeitsschwankungen auf das Wandrückschlagsverhalten turbulenter Wasserstoff-Luft-Flammen in Bezug auf Schwankungsamplitude und -frequenz untersucht. Es kann zwischen zwei Rückschlagsformen unterschieden werden: Bei niedrigen Anregungsamplituden schlägt die Flamme zurück, wenn die minimale Strömungsgeschwindigkeit während des Oszillationszyklus die Rückschlagsgrenze nicht eingeschlossener Flammen ohne akustische Anregung unterschreitet. Hohe Geschwindigkeitsamplituden führen zu periodischem Stromaufwandern der Flamme in den Brennerkanal hinein. Rückschlag findet statt, wenn die maximale Geschwindigkeit im Oszillationszyklus unter die Rückschlagsgrenze im Kanal eingeschlossener, nicht angeregter Flammen fällt. Da folglich die beiden Grenzfälle der eingeschlossenen und nicht eingeschlossenen Flammen in der Auslegung von Gasturbinenbrennern von großem Interesse sind, werden im theoretischen Teil dieser Arbeit quantitative, semi-analytische Vorhersagemodelle entwickelt und validiert. Grundlage dafür sind qualitative Beschreibungen der Rückschlagsmechanismen, die in vorangegangenen Studien erarbeitet wurden.

Abstract

Flame flashback into the premixing section is a challenge in the design of gas turbine burners since the beginning of the application of premixed combustion systems. For highly reactive fuels, especially flame flashback inside the low velocity region of the burner wall is a major issue. In the presence of combustion instabilities, boundary layer flashback can be triggered by induced velocity oscillations at the burner exit.

In the experimental part of this work, the effect of velocity oscillations on the boundary layer flashback characteristics of turbulent hydrogen-air flames is investigated depending on oscillation amplitude and frequency. Two flashback regimes can be distinguished: For low oscillation amplitudes, the flashback limits in terms of minimum flow velocities in the oscillation cycle correspond to the well-established flashback limits of unconfined flames. At high oscillation amplitudes, the flame periodically enters the burner duct. Flashback occurs if the maximum flow velocity in the oscillation cycle falls below the flashback limit of flames confined in ducts. As the two limiting cases of confined and unconfined flames are of special interest in the design of gas turbine burners, quantitative semi-analytic prediction models are developed and validated in the theoretical part of this work based on qualitative descriptions of the flashback processes introduced in previous studies.

Contents

Nomenclature

Latin Symbols

A	Area	[m^2]
B	Model parameter of logarithmic law of the wall	[–]
c	Reynolds averaged reaction progress variable	[–]
c_1	Temperature dependence power law exponent for $S_{\mathrm{l},0}$	[–]
c_2	Pressure dependence power law exponent for $S_{\mathrm{l},0}$	[–]
c_3	Exponent of turbulent burning velocity correlation	[–]
c_p	Specific heat capacity	[J/(kg K)]
C	Speed of Sound	[m/s]
C_B	Blending factor for effective Lewis number calculation	[–]
C_IL	Ratio of inner layer thickness to boundary layer thickness	[–]
C_p	Pressure coefficient	[–]
C_S	Parameter of turbulent burning velocity correlation	[–]
C_κ	Model constant for laminar flame stretch rate	[–]
C_Λ	Ratio of turbulent macroscale to burner height	[–]
d_h	Hydraulic diameter	[m]
D	Molecular diffusion coefficient	[m^2/s]
e	Euler’s number	[–]
E	Global activation energy	[J/mol]
f	Acoustic excitation frequency	[Hz]
G_1	Factor of flame generated turbulence (FGT) correlation	[–]
G_2	Exponent of FGT correlation	[–]
G_3	Temperature exponent of FGT correlation	[–]
G_4	Pressure exponent of FGT correlation	[–]
h	Channel height/pipe diameter	[m]

i	Marker for spatial directions	[–]
j	Enumerator	[–]
k	Turbulent kinetic energy	[J/kg]
K	Von Kármánn constant	[–]
l	Length scale	[m]
L	Flame wrinkling length	[m]
L_{M}	Markstein length	[m]
$\dot{m}$	Mass flow rate	[kg/s]
n	Order of natural frequency	[–]
N	Number of samples	[–]
p	Pressure	[Pa]
$\dot{q}$	Heat flux	[W/m^2]
$\dot{Q}$	Heat release	[W]
r	Radial coordinate of circular duct flow	[m]
R	Universal gas constant	[J/(mol K)]
s	Parameter of efficiency function in ITNFS model	[–]
S	Burning velocity	[m/s]
t	Time	[s]
T	Temperature	[K]
u	Velocity component in x-direction	[m/s]
u_τ	Shear stress velocity	[m/s]
U	Free stream/burner center line velocity	[m/s]
v	Velocity	[m/s]
V	Flame speed	[m/s]
x	Coordinate in flow direction	[m]
X	Molar fraction	[–]
y	Coordinate perpendicular to burner wall	[m]
Y	Mass fraction	[–]

Greek Symbols

α	Flame angle	[°]
β	Parameter for Markstein length calculation	[–]

γ_1, γ_2	Parameters for Markstein length calculation	[–]
Γ_K	Efficiency funcion in ITNFS model	[–]
δ	Thickness	[m]
ϵ	Dissipation rate of turbulent kinetic energy	[J/(kg s)]
ζ	Pressure loss coefficient	[–]
η	Kolmogorov scale	[m]
κ	Flame stretch rate	[1/s]
λ	Thermal conductivity	[W/(m K)]
Λ	Turbulent macroscale	[m]
ν	Kinematic viscosity	[m^2/s]
ρ	Density	[$\mathrm{kg/m}^3$]
σ	Expansion ratio	[–]
τ	Shear stress	[Pa]
ϕ	Equivalence ratio	[–]
χ	Normalized flame position	[–]
Ω	Normalized acoustic velocity oscillation amplitude	[–]

Superscripts

*	Electronically excited state
$\overline{}$	Value averaged over channel height/pipe diameter
$'$	Fluctuating value
$^+$	Value in wall units
$\vec{}$	Vector
$\tilde{}$	Locally preheated value
$\hat{}$	Oscillation amplitude

Subscripts

ad	Adiabatic
b	Burned
B	Burner

c	Correlation
BL	Boundary layer
D	Deficient
e	Experiment
E	Excess
f	Fuel
F	Flame
FF	Free flame
IL	Inner layer
l	Laminar
norm	Normalized value
mix	Mixture of fuel and oxidizer
PM	Value obtained from prediction model
q	Quenching
ref	Reference
R	Reactants
s	Stretched
st	Stoichiometric
t	Turbulent
u	Unburned
w	Wall
0	Unstretched

Dimensionless Numbers

Da	Damköhler number
Ka	Karlovitz number
Le	Lewis number
Ma	Markstein number
Pe	Péclet number
Re	Reynolds number
Tu	Turbulence intensity
Ze	Zeldovich number

Acronyms

BLF	Boundary Layer Flashback
CCS	Carbon Capture and Storage
CCGT	Combined Cycle Gas Turbines
CIVB	Combustion Induced Vortex Breakdown
CTA	Constant Temperature Anemometry
DNS	Direct Numerical Simulation
FA	Flame Arrestor
FGT	Flame Generated Turbulence
HSC	High Speed Camera
IED	Industrial Emissions Directive
ISO	International Organization for Standardization
ITNFS	Intermittent Net Flame Stretch
LES	Large Eddy Simulation
PIV	Particle Image Velocimetry
PLIF	Planar Laser Induced Fluorescence
RC	Reference Case
TC	Thermocouple
UV	Ultraviolet

Mathematical Operators

d	Derivative
Δ	Difference
∂	Partial derivative
$\lvert\,\rvert$	Absolute value

List of Figures

List of Tables

1 Introduction

Power generation based on renewable resources is subject to characteristic high fluctuations in power output. Consequently, a balancing technology is required to ensure a reliable power supply. Due to short start up times, high turn-down ratios and high efficiency, gas turbines are suitable to perform this task. In combination with a steam turbine in Combined Cycle Gas Turbine (CCGT) plants, modern gas turbines operated on natural gas achieve an efficiency of 60 % [1].

To protect our environment, emissions from gas turbines are strictly regulated. In Europe, regulations for combustion plants with a total rated thermal input ≥ 50 MW are defined in Chap. III and Annex V of the Industrial Emissions Directive 2010/75/EU (IED) [2] which replaced Directive 2001/80/EC [3] on January 1, 2016. Emission levels for gas turbines including CCGT are given for carbon monoxide (CO) and nitrous oxides (NO_x). CO emissions are limited to $100\,mg/m^3$ (≈ 80 ppmv) and NO_x emissions to $50\,mg/m^3$ (≈ 40 ppmv). [1] These limits are high compared to international regulations. The US Environmental Protection Agency, for example, limits NO_x emissions of natural gas-fired gas turbines (250 MW thermal input) to 15 ppmv [4]. Consequently, the technology development in gas turbines is mainly driven by US regulations.

In order to comply with the emission limitations, modern gas turbine combustors are operated in lean premixed mode. Fuel and air are mixed upstream of the combustion chamber to control the equivalence ratio distribution in the combustion zone. The flame temperature can be reduced by excess air which significantly lowers NO_x emissions.

---

[1] For single cycle gas turbines with an efficiency > 35 % at ISO base load conditions, the NO_x emission limit is set to $50 \times \text{efficiency}/35\,mg/m^3$. These emission limits only apply to operation above 70 % load and not for gas turbines for emergency use with less than 500 operating hours per year. To compare emissions with the limitations, they have to be calculated at standard conditions of 273.15 K and 1.013 bar and are normalized to an oxygen content of 15 %.

Apart from the pollutants carbon monoxide and nitrous oxides, the greenhouse gas carbon dioxide (CO_2) got into the focus of public debate as it is responsible for global warming. Consequently, also CO_2 emissions from gas turbine combustion should be limited. As CO_2 is a final product of the combustion of fossil fuels, it cannot be reduced by modifications in the combustion process. A possibility to avoid CO_2 emissions from gas turbines is the combustion of alternative, carbon-free fuels such as hydrogen.

Hydrogen can be obtained in different ways. In the context of renewable resources, hydrogen generated from electrolysis is considered a means to store excessive electrical energy. Regarding fossil fuels, hydrogen-rich fuels with hydrogen contents up to 100 % are obtained from pre-combustion Carbon Capture and Storage (CCS) technologies, where the fuel's carbon content is removed by gasification or partial oxidation prior to combustion and stored underground as carbon dioxide [5, 6].

Burning hydrogen instead of natural gas in gas turbines implies certain challenges. Especially in the context of premixed combustion, safety and stability issues are more distinct due to the high reactivity and burning velocity of hydrogen-rich fuels. Mixing of fuel and oxidizer upstream of the combustion chamber always bears the risk of flame propagation into the premixing section. This phenomenon is called flame flashback. Since the flame usually cannot be washed out of the premixing section once it has entered, flashback requires engine shutdown. Even structural damage might be caused as the premixing section is not designed for the high temperatures associated with the flame. Whereas flashback safety is commonly achieved for premixed combustion of natural gas, highly reactive fuels like hydrogen still pose a considerable challenge.

Lean premixed flames are prone to thermoacoustic instabilities. If there is a constructive interference of heat release and pressure fluctuations, small fluctuations can amplify into large amplitude limit cycle oscillations. This induces velocity oscillations at the burner exit. Since the flame stabilization is sensitive to the velocity distribution in this region, thermoacoustic instabilities might affect the burner's flashback characteristics.

1.1 State of the Art

As flame flashback and thermoacoustic instabilities constrain the stable and safe operation of gas turbines, these issues have been widely investigated [7, 8]. The following sections provide an overview on these fields.

1.1.1 Flame Flashback in Technical Applications

Flame flashback into the premixing section has been an issue since the beginning of the development of premixed combustion systems. From the resulting numerous studies, four basic flashback mechanisms can be distinguished [7, 9, 10]:

1. **Turbulent flame propagation in the core flow:** If the flow velocity at some point in the burner cross section falls below the turbulent burning velocity of the fuel-oxidizer mixture, the flame is able to propagate upstream on the streamline of the velocity deficit. This means that a uniform velocity profile without strong wakes can be seen as a simple design rule for gas turbine burners to prevent flashback in the core flow [7]. As this goal is typically achieved in modern gas turbine burners, this mechanism is a minor issue in regular gas turbine operation.
2. **Flashback in the boundary layer (BLF):** Boundary layers at the burner walls represent low velocity regions which are probable locations of flame flashback. Flashback directly at the wall is only prevented by quenching of the combustion reactions due to heat losses to the wall (cf. Sec. 2.3.4). Hence, there is a high risk of boundary layer flashback for fuels with low quenching distances. For such highly reactive fuels like hydrogen, boundary layer flashback is one of the most critical flashback mechanisms in gas turbine combustion.
3. **Flashback due to combustion instabilities:** As combustion instabilities generate velocity oscillations at the burner exit, velocity deficits are periodically induced. As stated by Lieuwen et al. [7] the pulsation levels at which these deficits reach a critical magnitude for flashback to occur in

the core flow are higher than pulsation levels which can be tolerated for structural reasons in regular gas turbine operation. However, for highly reactive fuels, which are prone to flashback in the boundary layer, even small velocity oscillations at the burner exit might have a significant influence on flashback limits.

4. **Vortex breakdown driven flame propagation in the core of swirling flows (CIVB):** In typical swirl-stabilized burners the flame is stabilized in a recirculation zone downstream of a sudden area increase from the swirl generator and the straight or conical mixing duct to the combustion chamber. If the interaction of swirling flow and flame leads to an upstream propagation of the recirculation zone, flashback conditions are reached and the flame propagates upstream on the burner axis [11, 12]. Burmberger and Sattelmayer [13] showed that CIVB can be avoided by a suitable aerodynamic design of the swirling flow.

As this work concentrates on boundary layer flashback, the first and the fourth flashback mechanisms will not be discussed further. However, the interaction of BLF with combustion instabilities is of major interest. It will be analyzed how velocity oscillations of different amplitudes and frequencies at the burner exit influence boundary layer flashback limits in non-swirling jet flames. Before the goals and structure of this work are further introduced, a short overview on BLF as well as on combustion instabilities is given in the following sections.

1.1.2 Boundary Layer Flashback

The investigation of boundary layer flashback began in 1943 with the studies of laminar natural gas-air flames in different-sized tube burners by Lewis and von Elbe [14]. They introduced the widely known critical gradient concept which is described in detail in [9]. Two years later, von Elbe and Mentser [15] published a follow up study on laminar hydrogen-air flames. In 1949, the same group introduced theoretical background regarding flame stabilization and quenching [16] as well as a study on laminar methane-air flames [17]. In the same year, Putnam and Jensen [18] rewrote the critical gradient concept of

Lewis and von Elbe in terms of dimensionless parameters. Wohl [19] extended the flashback research to laminar butane-air flames in 1953.

Turbulent flames have first been investigated with respect to boundary layer flashback by Bollinger and Edse [20] in 1956 and Khitrin et al. [21] in 1965. A first attempt to analyze the effect of pressure was made by Fine [22] in 1958. It has to be noted that he investigated laminar and turbulent propane- and hydrogen-oxidizer mixtures at reduced pressures. This means that his results cannot be transferred to high pressure conditions relevant for gas turbines.

Since these early flashback studies, numerous investigations are reported in literature regarding the effect of fuel composition [23], flame confinement and tip temperature [9, 23–25] and pressure [26–28]. It was found that flame confinement substantially increases the risk of boundary layer flashback. For flames confined inside the burner duct Eichler [9] measured flow velocities at flashback which were about two times higher than the well-established flashback limits of unconfined turbulent jet flames stabilized downstream of the burner exit. Together with Baumgartner's work [10] and numerical studies [29–33] the reason for this discrepancy in flashback limits can be assigned to differences in the physics of the flashback process. The state of knowledge on the flashback mechanisms in such unconfined and confined flames is introduced in Sec. 1.1.2.1 and 1.1.2.2.

1.1.2.1 Unconfined Flames

Baumgartner et al. [10, 34] studied the physical process of boundary layer flashback in unconfined turbulent flames by means of high-speed microscopic Particle Image Velocimetry (PIV) and Planar Laser Induced Fluorescence (PLIF). They identified the flashback mechanism illustrated in Fig. 1.1. Starting from a stable flame (1), flashback is initiated by the formation of a distortion in the turbulent flame front at $\Delta x_{\mathrm{FB}} \approx 3\,\mathrm{mm}$ downstream of the burner exit (2). This initial distortion forms the leading flame tip which propagates upstream at a wall distance of $y_{\mathrm{FB}} \approx 1\,\mathrm{mm}$ (3). During the upstream propagation the adverse pressure gradient induced by the flame becomes aligned with the main flow direction inside the burner duct. This leads to deflection and re-

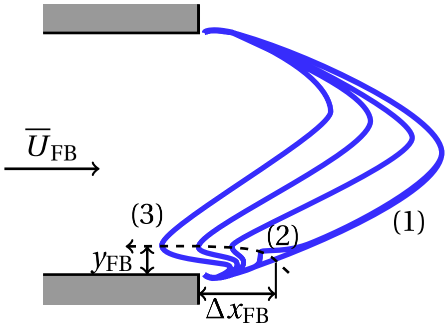

Figure 1.1: Flashback process of unconfined turbulent flame (adapted from [34, 35]). (1): stable flame, (2): formation of initial distortion, (3): upstream flame propagation.

tardation of the incoming flow which accelerates the flame's upstream propagation. If the flame has entered a sufficient distance into the burner duct, the burner walls prevent flow deflection. This causes increased retardation and eventually leads to the formation of a backflow region upstream of the flame tip as observed in boundary layer flashback of confined flames [36].

1.1.2.2 Confined Flames

Boundary layer flashback of confined flames was investigated by means of high speed OH* chemiluminescence and microscopic Particle Image Velocimetry (PIV) by Eichler et al. [9, 24, 36]. Numerical studies were conducted by Gruber et al. [30, 31] using Direct Numerical Simulation (DNS) and by Lietz et al. [32] using Large Eddy Simulation (LES). The obtained knowledge on the mechanism of boundary layer separation in confined flames is summarized in Fig. 1.2. In the vicinity of the flame tip, the initially undisturbed turbulent velocity profile (1) is distorted (2) due to a pressure rise induced upstream of the flame. If the pressure rise exceeds a critical value, the boundary layer separates (3) and a backflow region forms (light grey region). In this backflow region, the flame propagates upstream at the flame speed V_{FB}. According to [9] the absolute value of V_{FB} is higher than the mixture's burning velocity since the negative flow velocity in the backflow region accelerates the upstream propagation. The observed formation of the backflow region can be used to estimate flashback limits by evaluating the pressure rise upstream of the flame tip re-

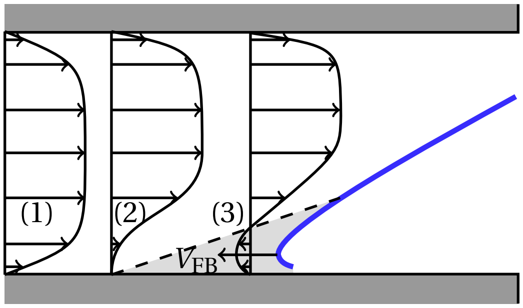

Figure 1.2: Mechanism of boundary layer flashback of confined turbulent flame (adapted from [9]). (1): undisturbed turbulent velocity profile, (2): velocity profile at the onset of boundary layer separation, (3): separated boundary layer.

quired to cause boundary layer separation (cf. Chap. 5).

1.1.2.3 Influence of Acoustic Velocity Oscillations on Flame Flashback

Apart from the details of the confined and unconfined flashback mechanisms, especially the effect of acoustic velocity oscillations on flame flashback is of interest in this work. A numerical study on that topic was conducted by Thibaut and Candel [37]. They simulated a backward-facing step according to the experiments of Keller et al. [38] with fluctuations of the inlet velocity at a frequency of $f = 500\,\mathrm{Hz}$ and a normalized amplitude up to 110 %. They observed a periodic upstream propagation of the flame in the near wall region.

Besides this numeric work, several experimental studies are reported in literature. Davu et al. [39] used acoustic excitation of their tube burner at 300, 500 and 700 Hz and analyzed the effect on the flashback limits of different hydrocarbon and hydrogen fuel blends. They observed a shift of flashback limits to leaner conditions for the hydrocarbon fuel blends. For hydrogen fuel blends, however, the effect of the added hydrogen was much higher than the effect of the acoustic oscillations. For that reason, they judged the excitation effect to be negligible. Follow-up studies by Subramanya and Choudhuri [40] and Dam et al. [41] came to the same conclusion. However, those studies were focused on the effect of fuel composition and did not concentrate on the influence of acoustic excitation.

In another experimental study Sabel'nikov et al. [42] analyzed low-frequency instabilities of highly turbulent methane-air flames in a model lean-premixed stepped combustor. They observed a periodic upstream propagation of the flame at a frequency of $f = 66\,\text{Hz}$ but no complete flashback into the burner duct. The observations of Eichler et al. [24] indicate that this might be different if hydrogen is used as fuel, because the flame could easily propagate in the wall boundary layer after entering the burner duct.

Since the influence of velocity oscillations on the flashback limits of highly reactive fuels remains an open question, the experimental study conducted in this work concentrates on this topic. It will be investigated whether thermoacoustic instabilities can trigger the transition from a stable unconfined to a confined flame due to the induced velocity oscillations at the burner exit.

1.1.3 Thermoacoustic Instabilities in Gas Turbines

Thermoacoustic instabilities result from a constructive feedback between flame and combustion chamber. Combustion driven pressure oscillations can cause the following problems [43]: Constraining of the operating envelope and power output, serious damage of hot section components and vibration induced fretting. The fact that the heat release

$$\dot{Q} = \dot{Q}(t) \tag{1.1}$$

of premixed flames is not constant but fluctuates in time is the driving force for themoacoustic oscillations. Reasons can be equivalence ratio fluctuations due to oscillations in the fuel or air supply, coherent flow structures or turbulence [7, 44]. Fluctuations in the heat release are directly linked to temperature and density oscillations which act as an acoustic source. The feedback mechanism of thermoacoustic instabilities is visualized in Fig. 1.3. Parts of the generated acoustic waves exit the combustor or are damped. However, due to the high Mach numbers, the turbine inlet acoustically acts as an almost closed end and reflects a significant share of the acoustic waves. The resulting acoustic field depends on the acoustic characteristics of the combustion chamber

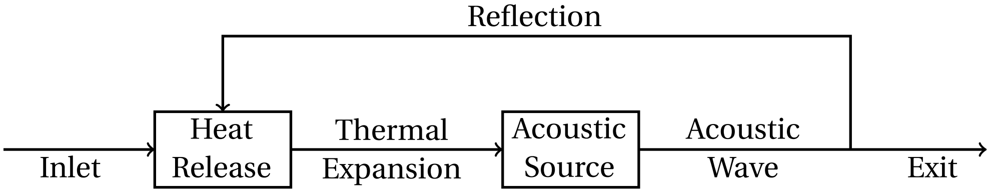

Figure 1.3: Feedback mechanism of thermoacoustic instabilities (adapted from [45]).

and interacts with the flame. If the interference of heat release fluctuations $\dot{Q}'$ and pressure fluctuations p' is constructive, i.e. if the phase shift is smaller than 90°, pressure oscillations can amplify. This precondition is formulated mathematically in the Rayleigh criterion [46]

$$\oint p' \dot{Q}' \, \mathrm{d}t > 0 \, . \tag{1.2}$$

In gas turbines, the constructive interference of pressure and heat release fluctuations can lead to high amplitude limit cycle oscillations which are critical for operation and hardware. Lieuwen and Yang [43] propose three categories of thermoacoustic instabilities depending on the oscillation frequency:

1. **Low frequency dynamics** ($f \leq 50$ Hz), referred to as “breathing” modes, “bulk” modes or “Helmholtz” modes.
2. **Intermediate frequency dynamics** (50 Hz $< f <$ 1000 Hz) due to longitudinal modes of the gas turbine combustor.
3. **High frequency dynamics** ($f \geq 1000$ Hz) due to transverse modes of the gas turbine combustor.

In this work, the effect of intermediate frequency dynamics on boundary layer flashback propensity will be analyzed. In typical industrial gas turbine combustors, the first natural frequency lies between 50 and 300 Hz [43]. Common pressure oscillations in this frequency range are about one percent of the static pressure inside the combustor. However, the corresponding normalized velocity oscillations can be significantly higher [43]. Velocity oscillations affect the flame stabilization at the burner exit and might pose a trigger for flame flashback.

1.2 Goals and Structure of this Work

The goals of this work can be divided into two categories: First, the influence of acoustic velocity oscillations at the burner exit on the flashback characteristics of unconfined turbulent hydrogen-air flames is analyzed experimentally. The experimental results show that in the investigated frequency range the flashback limits with acoustic excitation can be attributed to the two limiting cases of unexcited confined and unconfined flames. For that reason, the second goal of this work is to develop analytic prediction models for the flashback limits of these cases. The prediction models are based on the physical process of flashback of unconfined and confined flames introduced in Sec. 1.1.2.1 and 1.1.2.2.

This work is structured as follows: In Chap. 2 basic principles of laminar flow, turbulent flow and premixed combustion are introduced. This theoretical background is required to understand the prediction models at the end of this work. Chapter 3 describes the setup and the measurement techniques applied in the experimental study. Subsequently, the experimental results are discussed in Chap. 4. The development of predictive models in terms of flashback limits is split into two chapters: Chapter 5 discusses the model development and validation for turbulent hydrogen-air flames confined in ducts. A sensitivity analysis is included to identify the dominant influencing parameters. Unconfined flames are analyzed in Chap. 6. After treating laminar boundary layer flashback in hydrogen- and methane-air flames, the prediction model for turbulent hydrogen-air flames is introduced and validated. As for the confined case, a sensitivity analysis is included to assess main sources for prediction inaccuracies. Afterwards, a short discussion on the effect of different degrees of burner exit cooling is added to show the capability of the developed model to reproduce experimentally observed discrepancies in flashback limits. This work ends with a summary and concluding remarks in Chap. 7.

2 Basic Principles

In this chapter, basic principles of laminar flow, turbulent flow and premixed combustion are reviewed. First, laminar duct flow as well as turbulent boundary layers, fully developed turbulent duct flow and turbulent mixing layers are discussed. Finally, properties of unstretched laminar flames, flame stretch and turbulent flames are introduced. The detailed discussion of these parameters is required to understand the prediction models developed in Chap. 5 and 6.

2.1 Laminar Flow

Laminar flows are characterized by parallel fluid layers without any lateral mixing. A fluid flow is laminar if the Reynolds number

$$\mathrm{Re} = \frac{U\,l}{\nu}, \tag{2.1}$$

describing the ratio of momentum to viscous forces, is below a critical value for laminar-turbulent transition. Velocity U and length scale l used to calculate the Reynolds number are characteristic for each flow configuration. The motion of viscous fluid flow is described by the Navier-Stokes equations. Several analytic solutions of these equations exist for simple flow configurations such as Couette flows and Poiseuille flows [47]. Whereas Couette flows describe steady flows between one fixed and one moving object, Poiseuille flows are driven by pressure gradients as for example in channel or pipe flows. After a certain entrance length, the velocity profile of such flows is independent of the spatial coordinate in flow direction. The resulting velocity profile $u(r)$ of the fully developed laminar pipe flow can be described with the Hagen-Poiseuille solution of the Navier-Stokes equations:

$$u(r) = U\left(1 - \left(\frac{r}{h/2}\right)^2\right). \tag{2.2}$$

The radial coordinate r divided by the pipe radius $h/2$ can be replaced by the wall normal coordinate y using the coordinate transform

$$\frac{r}{h/2} = 2\frac{y}{h} - 1\,. \tag{2.3}$$

From integration of Eq. (2.2) over the pipe area, the bulk flow velocity $\overline{U} = 0.5\,U$ is obtained. Inserting this into Eq. (2.2) together with Eq. (2.3) leads to the velocity profile

$$u(y) = 2\,\overline{U}\left(1 - \left(2\frac{y}{h} - 1\right)^2\right) \tag{2.4}$$

which will be used in Sec. 6.1 to predict boundary layer flashback limits in laminar tube burner flames.

2.2 Turbulent Flow

If the flow Reynolds number exceeds a critical value, inertial forces dominate viscous forces and turbulence is generated. In technical applications turbulent flows are highly relevant as they are beneficial in many technical devices. For example, turbulence enhances entrainment in mixing processes or increases the resistance against separation of boundary layers. Those advantages are always at the cost of higher friction losses. For a detailed review on turbulent flows the reader is referred to the work of Pope [48], White [47] and Schlichting and Gersten [49].

In order to describe turbulent flow, the velocity $\vec{v}(\vec{x},t)$ is commonly divided into a mean flow velocity $\vec{v}(\vec{x})$ and a fluctuating component $\vec{v}\,'(\vec{x},t)$:

$$\vec{v}(\vec{x},t) = \vec{v}(\vec{x}) + \vec{v}\,'(\vec{x},t)\,. \tag{2.5}$$

This method is known as Reynolds decomposition. The mean flow field

$$\vec{v}(\vec{x}) = \frac{1}{\Delta t}\int_{t_1}^{t_2} \vec{v}(\vec{x},t)\mathrm{d}t \tag{2.6}$$

can be obtained from integration of $\vec{v}(\vec{x},t)$ over a sufficient time period $\Delta t = t_2 - t_1$. If discrete velocities are available for example from Particle Image Velocimetry (PIV), the integral can be replaced by averaging of N instantaneous velocity fields:

$$\vec{v}(\vec{x}) = \frac{1}{N}\sum_{j=1}^{N} \vec{v}(\vec{x}, t_j)\,. \tag{2.7}$$

The instantaneous turbulent velocity fluctuations

$$\vec{v}'(\vec{x}, t) = \vec{v}(\vec{x}, t) - \vec{v}(\vec{x}) \tag{2.8}$$

are obtained by subtracting the mean velocity $\vec{v}(\vec{x})$ from the instantaneous velocity $\vec{v}(\vec{x}, t)$ at each time t. The time-averaged turbulent velocity fluctuations in spatial direction x_i can be calculated as follows:

$$v'_i(x_i) = \frac{1}{N}\sum_{\mathrm{j=1}}^{N} \sqrt{v'_i(x_i, t_j)^2}\,. \tag{2.9}$$

The local turbulence intensity

$$\mathrm{Tu}_i = \frac{v'_i(x_i)}{v_i(x_i)} \tag{2.10}$$

is defined by the ratio of time-averaged velocity fluctuation $v'_i(x_i)$ and mean velocity $v_i(x_i)$. As in the present study the velocity u in x-direction is the most relevant component, usually the turbulence intensity $\mathrm{Tu}_x = u'(x)/u(x)$ will be analyzed.

In order to assess the kinetic energy contained in turbulent eddies, the turbulent kinetic energy k in Einstein notation

$$k = \frac{1}{2} v'_i(x_i)^2 \tag{2.11}$$

is introduced. Assuming isotropic turbulence Eq. (2.11) simplifies to

$$k = \frac{3}{2} u'(x)^2\,. \tag{2.12}$$

Turbulence is composed of different sized eddies ranging from the largest eddies characterized by the turbulent macroscale Λ down to the smallest eddies described by the Kolmogorov scale η. Turbulent kinetic energy is produced at the macroscale Λ defined by the flow configuration and is transferred to smaller scales until it is dissipated at the Kolmogorov scale. The idea of this energy cascade was first introduced in 1922 by Richardson [50] in the context of weather prediction. His idea was refined and quantified by Kolmogorov [51]. Kolmogorov defined the scale of the smallest eddies

$$\eta = \left(\frac{\nu^3}{\epsilon}\right)^{\frac{1}{4}} \tag{2.13}$$

based on kinematic viscosity ν and dissipation rate ϵ. Based on Kolmogorov's second similarity hypothesis and the assumption of isotropic turbulence, the dissipation rate

$$\epsilon = \frac{u'(x)^3}{\Lambda} \tag{2.14}$$

can be expressed by means of macroscopic turbulent properties. In the following sections, the characteristics of those macroscopic turbulent properties are introduced for different canonical turbulent flows relevant for the modeling of boundary layer flashback.

2.2.1 Boundary Layer

If fluid flows interact with solid, motionless walls, for example a flat plate, the fluid particles directly at the wall are decelerated to stagnation due to friction. This no-slip boundary condition leads to the development of boundary layers. The velocity profile of boundary layers can be described by $u(x, y)$ where y denotes the wall normal coordinate. A boundary layer can be characterized by the Reynolds number

$$\mathrm{Re}(x) = \frac{Ux}{\nu} \tag{2.15}$$

based on free stream velocity U and boundary layer length x. The boundary layer thickness $\delta(x)$ can be defined as the wall normal distance where the velocity $u(x, y)$ has reached 99 % of the free stream velocity U. $\delta(x)$ increases with the boundary layer length x. For flows with low Reynolds numbers, due to low free stream velocities or small boundary layer lengths, boundary layers are laminar. At a critical Reynolds number turbulent boundary layers evolve from laminar-turbulent transition and the velocity profile becomes time dependent. Using Eq. (2.5), the velocity profile of turbulent boundary layers can be expressed as

$$u(x, y, t) = u(x, y) + u'(x, y, t)\,. \tag{2.16}$$

The mean velocity profile $u(x, y)$ of turbulent boundary layers can be divided into inner $(y/\delta < 0.1)$ and outer layer $(y/\delta \geq 0.1)$ [48]. In the inner layer, the mean velocity $u(x, y)$ is commonly expressed in terms of dimensionless wall units:

$$y^+ = \frac{u_\tau(x)\, y}{\nu}, \quad u^+(y^+) = \frac{u(x, y)}{u_\tau(x)}. \tag{2.17}$$

The shear stress velocity $u_\tau = \sqrt{\tau_\mathrm{w}/\rho}$ depends on wall shear stress τ_w and fluid density ρ. By means of the normalized wall distance y^+ the normalized velocity profile u^+ can be divided into different regions [48]:

- **Viscous sublayer** $(y^+ < 5)$: Viscus shear stress plays a major role in defining the velocity profile.
- **Buffer layer** $(5 < y^+ < 30)$: Transition region from viscous sublayer to logarithmic region.
- **Logarithmic region** $(y^+ > 30, y/\delta < 0.3)$: The normalized velocity profile can be described by a logarithmic law of the wall.

In the viscous sublayer, also called laminar region, the normalized velocity is equal to the normalized wall distance:

$$u^+ = y^+. \tag{2.18}$$

The logarithmic region is defined as the normalized wall distance where the logarithmic law of the wall

$$u^+ = \frac{1}{K} \ln y^+ + B \tag{2.19}$$

with the von Kármánn constant $K = 0.41$ and a model parameter B is valid. Different values for B are found in literature. Here, $B = 5.0$ is applied as suggested by White [47]. In order to describe the velocity field of the complete inner region of a turbulent boundary layer, Spalding [52] proposed the empirical function

$$y^+ = u^+ + 0.1108\left(\mathrm{e}^{0.4\,u^+} - 1 - 0.4\,u^+ - \frac{\left(0.4\,u^+\right)^2}{2} - \frac{\left(0.4\,u^+\right)^3}{6} - \frac{\left(0.4\,u^+\right)^4}{24}\right) \tag{2.20}$$

which he fitted to experimental data. This velocity profile can be disturbed by adverse pressure gradients which may cause boundary layer separation as described in the following section.

2.2.2 Boundary Layer Separation

If boundary layers are exposed to adverse pressure gradients, the wall velocity gradient is reduced until boundary layer separation occurs and a backflow region forms. The prediction of the onset of boundary layer separation is of high interest in technical applications as for example in airfoil or compressor blade circulation. In 1958, Stratford [53] published a semi-empirical criterion

$$C_\mathrm{p}(x)\left(x\frac{\mathrm{d}C_\mathrm{p}(x)}{\mathrm{d}x}\right)^{\frac{1}{2}} = 0.39\left(10^{-6}\mathrm{Re}(x)\right)^{0.1} \tag{2.21}$$

to predict the separation location x for a given pressure distribution $C_\mathrm{p}(x)$ and a Reynolds number $\mathrm{Re}(x)$ based on the free stream velocity U. His criterion was developed for $\mathrm{d}^2p/\mathrm{d}x^2 \geq 0$ and $C_\mathrm{p} \geq 4/7$. For $\mathrm{d}^2p/\mathrm{d}x^2 < 0$, the model constant 0.39 should be replaced by 0.35. Stratford's criterion relates the pressure coefficient

$$C_\mathrm{p}(x) = \frac{p(x) - p(x=0)}{\frac{1}{2}\rho U^2} \tag{2.22}$$

of a given pressure distribution $p(x)$ to the Reynolds number $\mathrm{Re}(x) = U\,x/\nu$ at the position of separation. The applicability of the criterion was confirmed by Cebeci et al. [54]. Stratford states that the pressure rise at separation predicted with his method is likely to be up to 10 % too low leading to a conservative design.

Other methods to predict boundary layer separation based on pressure coefficient or a boundary layer shape factor are reported in literature and summarized by Cebeci et al. [54] and Baumgartner [10]. Due to its ease of use, Stratford's criterion will be used in Chap. 5 to predict boundary layer separation induced by a flame confined inside a burner duct.

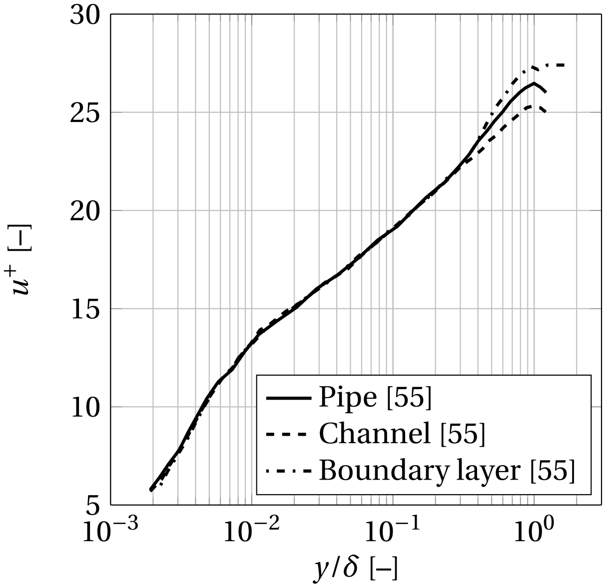

Figure 2.1: Comparison of normalized mean velocity profiles of pipe, channel and boundary layer flow (adapted from [55]).

2.2.3 Channel and Pipe Flow

In a fluid flow through a duct, boundary layers develop from the entrance until they converge in the duct center after a certain hydrodynamic entrance length. At this point, the dependence of the velocity profiles on axial position x disappears and the duct flow is called “fully developed”. The hydrodynamic entrance length depends on the hydraulic duct diameter d_h which is defined as the ratio of four times the cross-sectional area to the duct’s circumference. As throughout this work turbulent duct flow will be approximated as fully developed, the characteristics of velocity profiles and velocity fluctuation profiles will be discussed in this section. Monty et al. [55] compared those profiles of turbulent pipe, channel and boundary layer flows at similar friction Reynolds numbers $\mathrm{Re}_\tau = \delta u_\tau / \nu$. In their definition, δ is either the pipe radius, the channel half height or the boundary layer thickness. The comparison of normalized mean velocity profiles $u^+(y/\delta)$ is presented in Fig. 2.1. Monty et al. [55] found that the normalized mean velocities collapse to one curve in the inner region up to $y/\delta = 0.15$. A distinct deviation is observed starting at the upper limit of the logarithmic region at $y/\delta = 0.3$. This shows that the empiri-

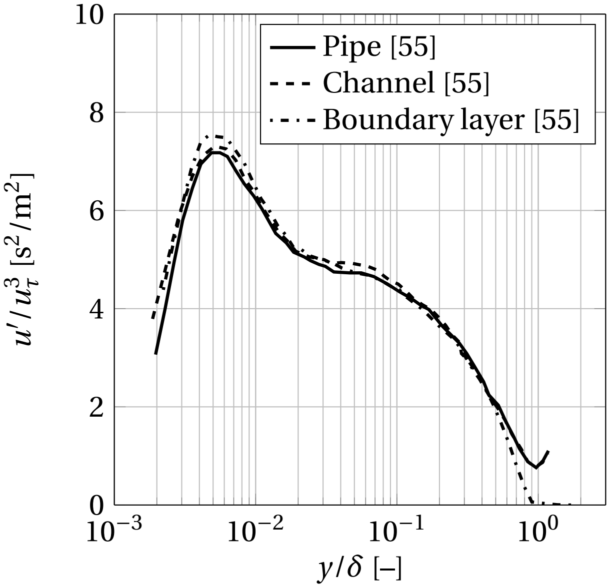

Figure 2.2: Comparison of averaged turbulent velocity fluctuation profiles of pipe, channel and boundary layer flow (adapted from [55]).

cal function introduced by Spalding to describe the normalized mean velocity in the inner region presented in Eq. (2.20) can also be applied to pipe and channel flow although it was developed for boundary layers.

Figure 2.2 compares the turbulent velocity fluctuations u'/u_τ^3 of pipe, channel and boundary layer flow corresponding to the normalized mean velocity profiles from Fig. 2.1 [55]. A maximum in turbulent velocity fluctuation is observed close to the wall around $y/\delta = 0.005$. According to Monty et al. [55], the three profiles are in agreement up to $y/\delta \approx 0.5$. They state that the variations around the maximum lie within the error of the applied Constant Temperature Anemometry (CTA) and should not be assigned to differences in flow configuration. Above $y/\delta = 0.5$, pipe and channel flow still show high similarities whereas deviations are observed compared to the turbulent boundary layer. It can be concluded that at similar friction Reynolds numbers the profiles of turbulent velocity fluctuations are very similar for pipe and channel flow.

In order to analyze the effect of flow Reynolds number on turbulent velocity fluctuations, Fig. 2.3 depicts experimental data by Laufer [56] and Wei and Willmarth [57] ranging from Re = 2970 to Re = 30800. The Reynolds numbers

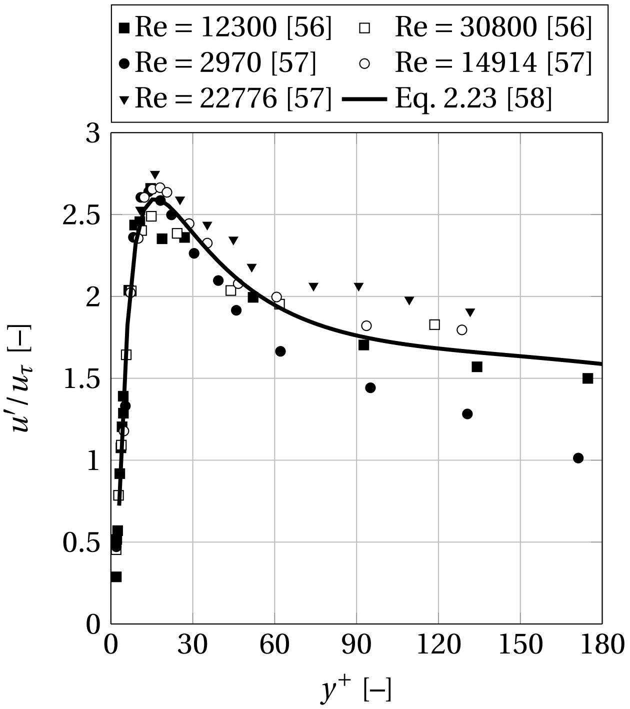

Figure 2.3: Normalized turbulent velocity fluctuations in the near wall region of turbulent channel flow at different Reynolds numbers [58].

are based on the channel half height $h/2$ and the channel center line velocity U. Close to the wall the data collapse to one curve and can be represented by the following fit [58] which is included in Fig. 2.3 as a black line:

$$\frac{u'}{u_\tau} = a_0 + a_1 \ln\left(y^+\right) + a_2 \ln\left(y^+\right)^2 + a_3 \ln\left(y^+\right)^3 + a_4 \ln\left(y^+\right)^4 + a_5 \ln\left(y^+\right)^5 . \quad (2.23)$$

The parameters are $a_0 = 2.661$, $a_1 = -7.211$, $a_2 = 7.600$, $a_3 = -2.900$, $a_4 = 0.472$ and $a_5 = -0.028$. The maximum in turbulent velocity fluctuation $u'/u_\tau = 2.6$ seen in Fig. 2.2 is located at $y^+ = 16.4$. Due to the observations of Monty et al. [55], this fit can be applied to calculate the turbulent velocity fluctuations close to the wall for channel as well as pipe flow. According to [59], the corresponding turbulent macroscale Λ can be approximated for fully developed internal flows by

$$\Lambda = 0.07\, d_\mathrm{h} \quad (2.24)$$

depending on the hydraulic diameter d_h of the flow configuration.

Apart from the local turbulence distribution close to the wall, the turbulent velocity fluctuations averaged over the channel height $\overline{u'}$ will be a flow property of interest in this work. According to [59], they can be described for fully developed duct flows as a function of the Reynolds number based on bulk flow velocity $\overline{U}$ and hydraulic diameter d_h:

$$\frac{\overline{u'}}{\overline{U}} = 0.16 \left(\frac{d_\mathrm{h} \overline{U}}{\nu} \right)^{-1/8} . \tag{2.25}$$

In Chapter 5 and 6, relations to calculate bulk flow velocities from near wall velocities or shear stress velocities for channel and pipe flow are required. For turbulent channel flow, White [47] suggests a relation based on the logarithmic law of the wall (cf. Eq. (2.19))

$$\frac{\overline{U}}{u_\tau} = \frac{1}{K} \ln\left(\frac{h\, u_\tau}{\nu} \right) + B - \frac{1}{K} \tag{2.26}$$

with the von Kármánn constant $K = 0.41$ and the model parameter $B = 5.0$. For turbulent pipe flow, Schlichting and Gersten [49] present

$$u_\tau^2 = \frac{\tau_\mathrm{w}}{\rho} = 0.03955\, \overline{U}^{7/4} \nu^{1/4} h^{-1/4} \tag{2.27}$$

derived from the resistance concept of Blasius. With these two relations the shear stress velocity u_τ can be linked to the bulk flow velocity $\overline{U}$. Pope [48] introduces the expression

$$U \approx \overline{U} + 2.4\, u_\tau \tag{2.28}$$

to relate channel center line velocity U to averaged flow velocity $\overline{U}$ and shear stress velocity u_τ. It is assumed that Eq. (2.28) can be used in pipe flow as well although this introduces some error due to the differences in mean velocity profile (cf. Fig. 2.1).

2.2.4 Mixing Layer

If a fully developed turbulent flow exits a channel or pipe into a stationary environment, a plane or round turbulent free jet evolves. The velocity profiles of free jets become self-similar in the far field at some distance downstream

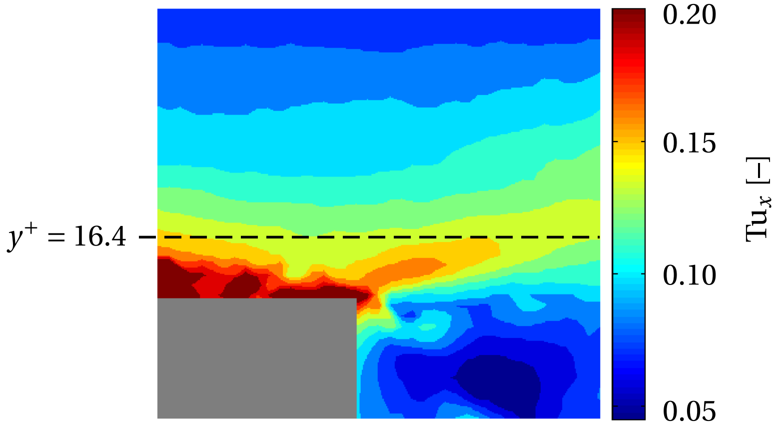

Figure 2.4: Turbulence intensity in the exit region of a channel burner at the presence of a stable hydrogen-air flame at $\phi = 0.5$ (adapted from [10]). The grey area marks the burner edge.

of the duct exit ($x/h = 30$ for round jets and $x/h = 40$ for plane jets [48]). As in this study the region close to the duct exit is of interest, the near field of free jets will be discussed in this section. At the duct exit, turbulent mixing layers start to form in the shear layers at the duct circumference. The mean velocity and turbulent velocity fluctuation fields have been widely studied in literature (e.g. [60–62]) identifying a strong influence of initial conditions on flow development [62].

In this study, the velocity field downstream of a duct exit will be of interest in combination with a premixed flame stabilized in the turbulent mixing layer. Compared to isothermal flow, the present flow field is strongly affected by the combustion-induced thermal expansion. For that reason, isothermal descriptions of mixing layers cannot be applied in this case. The interaction of a premixed flame and a turbulent mixing layer was analyzed with high resolution PIV and CH-PLIF by Foley et al. [63]. They found that a shear layer stabilized flame is exposed to significant flame stretch levels. The distribution of turbulent velocity fluctuations u' in terms of turbulence intensities Tu_x was analyzed by Baumgartner [10] in microscopic PIV of a mixing layer with a stable hydrogen-air flame at an equivalence ratio of $\phi = 0.5$ and ambient conditions. The turbulence intensity field is shown in Figure 2.4. Inside the burner duct, typical high turbulence intensities of around 20 % are observed close to the burner wall. This corresponds to normalized turbulent velocity fluctuations of $u'/u_\tau = 2.6$ as discussed in Section 2.2.3. Downstream of the burner exit the maximum turbulence intensity decreases. For the modeling of the flashback process of turbulent unconfined flames in Chap. 6, the turbulent velocity fluctuations at the location of flashback initiation are of interest. It is assumed that this location coincides with the intersection of the streamline of maximum turbulence at $y^+ = 16.4$ with the flame front. From Baumgartner's data (see also [34]), a turbulence intensity of 13 % corresponding to $u'/u_\tau = 1.5$ is estimated at this location. This value will be required in Chap. 6 to describe the turbulent burning velocity at the point of flashback initiation.

As the length scale of turbulent structures downstream of the burner exit are limited by the duct height or diameter, the corresponding turbulent macroscale is estimated by

$$\Lambda = C_\Lambda \, h \,. \tag{2.29}$$

Considering symmetrically evolving structures at the burner exit, the model constant C_Λ is set to 0.5 in this work. Turbulence intensity and turbulent macroscale will be required in Chap. 6 to define the influence of turbulence on burning velocity at flashback conditions.

2.3 Premixed Combustion

Premixed combustion is defined as chemical reaction of fuel and oxidizer if mixed far upstream of the flame. In contrast to non-premixed flames, the equivalence ratio

$$\phi = \frac{\dot{m}_{\mathrm{Fuel}} / \dot{m}_{\mathrm{Air}}}{(\dot{m}_{\mathrm{Fuel}} / \dot{m}_{\mathrm{Air}})_{\mathrm{st}}} \tag{2.30}$$

can be adjusted from lean ($\phi < 1$) over stoichiometric ($\phi = 1$) to rich conditions ($\phi > 1$). Flame properties, such as adiabatic flame temperature T_{ad}, burning velocity S, flame thickness δ_{F} and the flame's susceptibility to stretch, change with equivalence ratio. These properties are important to describe flame flashback and are introduced in the following sections starting with a review on unstretched laminar flames. The flame properties are discussed for atmospheric pressure representing the experimental conditions of this work compared to gas turbine conditions at $p = 20\,\mathrm{bar}$.

2.3.1 Unstretched Laminar Flames

If an undisturbed planar flame stabilizes in laminar flow, it can be described as unstretched and one-dimensional. Figure 2.5 shows the structure of such a premixed laminar flame. If the flame is stationary, the flow velocity of the reactants u_u equals the unstretched laminar burning velocity $S_{\mathrm{l},0}$. Due to heat conduction from the reaction zone, the temperature rises in the preheat zone from the unburned temperature T_u up to a critical temperature at which the reaction rate strongly increases. This inner layer temperature marks the boundary between preheat zone and reaction zone, also called inner layer (IL), where the mass fraction of reactants drops from its initial value $Y_\mathrm{R} = 1$ to $Y_\mathrm{R} = 0$. The gradient of Y_R leads to mass diffusion of reactants into the reaction zone. If the system is adiabatic, the product temperature T_b downstream of the reaction zone equals the adiabatic flame temperature T_ad. From mass conservation, the product velocity u_b referred to a fixed reference system can be determined from the expansion ratio

$$\sigma = \frac{\rho_\mathrm{u}}{\rho_\mathrm{b}} \tag{2.31}$$

and the unstretched laminar burning velocity:

$$u_\mathrm{b} = \sigma\, S_{\mathrm{l},0}\,. \tag{2.32}$$

The laminar flame thickness δ_F describes the thickness of preheat and reaction zone. The thickness of the reaction zone is much smaller than that of the preheat zone and can be described by

$$\delta_\mathrm{IL} = C_\mathrm{IL}\delta_\mathrm{F}\,, \tag{2.33}$$

where the ratio C_IL is typically around 0.1 [64].

Adiabatic flame temperature, unstretched laminar burning velocity and laminar flame thickness are characteristic for each fuel-oxidizer mixture. Since they have a high influence on the flashback process, several methods to define these parameters are compared with each other in the following sections.

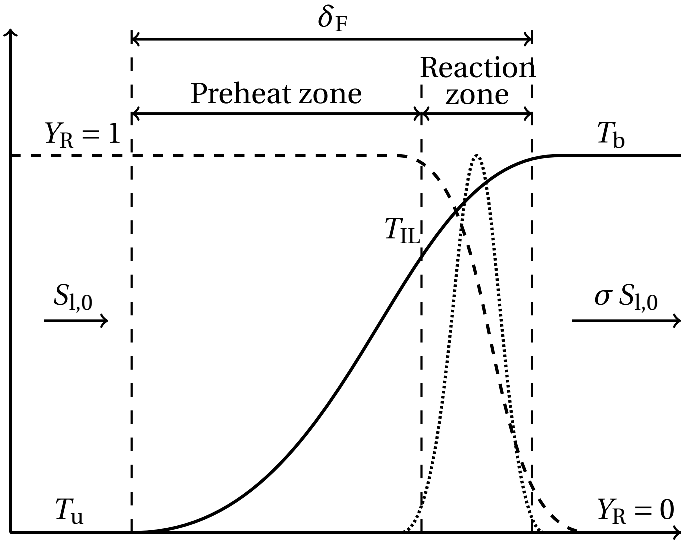

Figure 2.5: Structure of an unstretched one-dimensional premixed laminar flame (adapted from [65]). Solid line: temperature T, dashed line: mass fraction of reactants Y_R, dotted line: reaction rate.

2.3.1.1 Adiabatic Flame Temperature

The adiabatic flame temperature is defined as the temperature of the combustion products if there is no heat exchange with the surroundings. It can be derived from an enthalpy balance between products and reactants taking the reaction enthalpy into account. The adiabatic flame temperature depends on the reactants temperature T_u, called preheating temperature, and on the pressure p. As the pressure dependence is weak, Peters [66] suggests to approximate the adiabatic flame temperature

$$T_{ad} = a_1 T_u + a_2 + a_3\phi + a_4\phi^2 + a_5\phi^3 \tag{2.34}$$

as a function of preheating temperature T_u, equivalence ratio ϕ and the fuel-dependent coefficients a_1–a_5. In this approximation, a linear dependence on preheating temperature and a third order polynomial dependence on equivalence ratio is assumed. Alternatively, the adiabatic flame temperature can be computed with the chemical kinetics software *Cantera 2.2* [67] in chemical equilibrium calculations at constant pressure and enthalpy. Both methods are compared in the following for hydrogen-air and methane-air mixtures.

Table 2.1: Coefficients of adiabatic flame temperature correlation by Peters [66] (Eq. (2.34)) for hydrogen-air and methane-air mixtures.

Coefficient	H_2	CH_4	Unit
a_1	0.522	0.627	–
a_2	673.8	1270.15	K
a_3	807.9	−2449	K
a_4	2515.6	6776	K
a_5	−1765.9	−3556	K

Hydrogen-Air Mixtures: The adiabatic flame temperature of hydrogen-air mixtures is depicted in Fig. 2.6(a) for atmospheric pressure (p = 1 bar) and different preheating temperatures varying from ambient (T_u = 293 K) to gas turbine conditions (T_u = 673 K). The different preheating temperatures are marked with different symbols. The filled symbols originate from a *Cantera 2.2* [67] computation with the reaction mechanism of Ó Conaire et al. [68] which is designed for hydrogen combustion and was validated for T_u = 298–2700 K and p = 0.05–85 bar. The mechanism consists of nineteen elementary reactions of eleven species. Furthermore, results from Eq. (2.34) are included as solid, dashed and dotted lines. The correlation parameters are given in Tab. 2.1. Figure 2.6(a) shows that the adiabatic flame temperature increases with equivalence ratio due to a corresponding increase in fuel bound energy up to a maximum around $\phi = 1.1$. For richer conditions the adiabatic flame temperature decreases as combustion becomes incomplete. At lean conditions and ambient temperature the results from the correlation by Peters [66] match the computed temperatures with growing deviations for rich conditions. At higher preheating temperatures, these deviations increase and a growing underestimation of T_ad is observed in the lean region compared to the kinetics simulation.

The influence of pressure on adiabatic flame temperature is depicted in Fig. 2.6(b). As the correlation by Peters [66] neglects this influence, only *Cantera 2.2* [67] results with the reaction mechanism of Ó Conaire et al. [68] are presented at atmospheric (p = 1 bar, filled symbols) and gas turbine pressure (p = 20 bar, empty symbols). At lean conditions the pressure influence on adi-

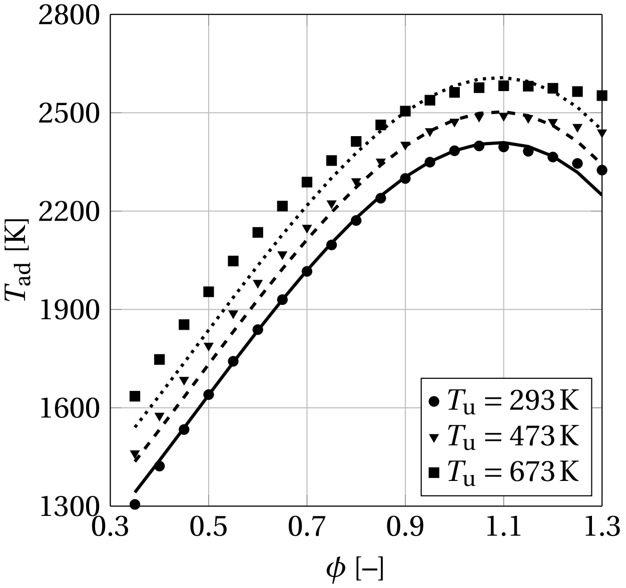

(a) Effect of T_u (p = 1 bar). Symbols: Ó Conaire et al. [68], lines: Eq. (2.34) [66].

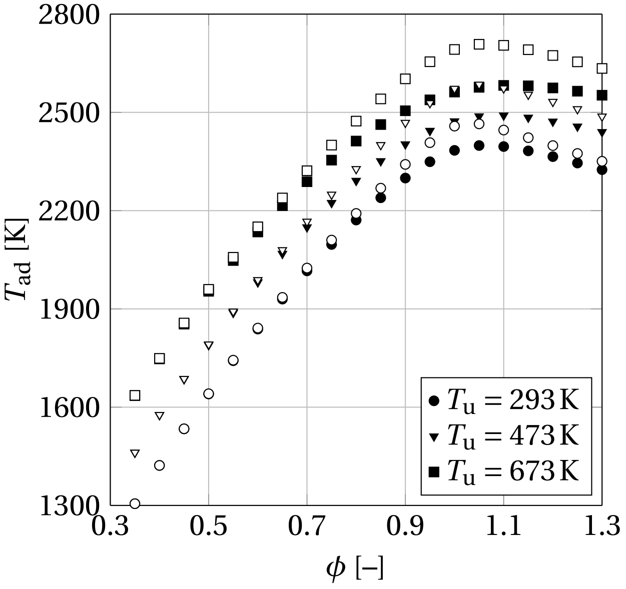

(b) Effect of p computed with Ó Conaire et al. [68]: Filled symbols: $p = 1$ bar, empty symbols: $p = 20$ bar.

Figure 2.6: Preheating temperature and pressure effect on the adiabatic flame temperature of hydrogen-air mixtures.

abatic flame temperature is negligibly small. Around stoichiometry, however, the adiabatic flame temperature increases with pressure due to enhanced recombination of intermediate species to final products. This shifts the maximum of T_{ad} to $\phi = 1$ and leads to a maximum increase in adiabatic flame temperature of 2.8 % at $T_{\mathrm{u}} = 293\,\mathrm{K}$, 3.9 % at $T_{\mathrm{u}} = 473\,\mathrm{K}$ and 5.1 % at $T_{\mathrm{u}} = 673\,\mathrm{K}$. Due to this non-negligible pressure effect, the *Cantera 2.2* [67] results will be used for the adiabatic flame temperature of hydrogen-air mixtures in this work rather than the correlation by Peters [66].

Methane-Air Mixtures: Figure 2.7(a) and 2.7(b) show similar trends for methane-air mixtures as observed for hydrogen-air flames in the previous section. In general, the adiabatic flame temperatures are lower. For methane-air mixtures the detailed reaction mechanism GRI-Mech 3.0 [69] is chosen for the *Cantera 2.2* [67] calculations. This mechanism consists of 325 elementary reactions of 53 species. In Fig. 2.7(a) the ambient pressure data are compared to the correlation by Peters in Eq. (2.34) with the coefficients given in Tab. 2.1. At ambient temperature, simulation and correlation are in good agreement between $\phi = 0.5$ and $\phi = 1.2$. In contrast to hydrogen-air mixtures, the adiabatic flame temperatures from the equilibrium calculations are well reproduced by the correlation at lean preheated conditions. However, they are overestimated around stoichiometry and underestimated at rich conditions.

The influence of pressure is depicted in Fig. 2.7(b) based on *Cantera 2.2* [67] calculations with GRI-Mech 3.0 [69]. The observed increase of maximum adiabatic flame temperature at stoichiometry amounts 2.3 % at $T_{\mathrm{u}} = 293\,\mathrm{K}$, 3.0 % at $T_{\mathrm{u}} = 473\,\mathrm{K}$ and 3.9 % at $T_{\mathrm{u}} = 673\,\mathrm{K}$. Especially at high preheating temperatures it is lower than for hydrogen-air mixtures.

2.3.1.2 Unstretched Laminar Burning Velocity

One-dimensional free flame calculations in *Cantera 2.2* [67] are one method to obtain the unstretched laminar burning velocity $S_{\mathrm{l},0}$. The laminar burning velocity is equal to the resulting inlet flow velocity of the final solution. Alternatively, Peters [66] suggests the following correlation including temperature

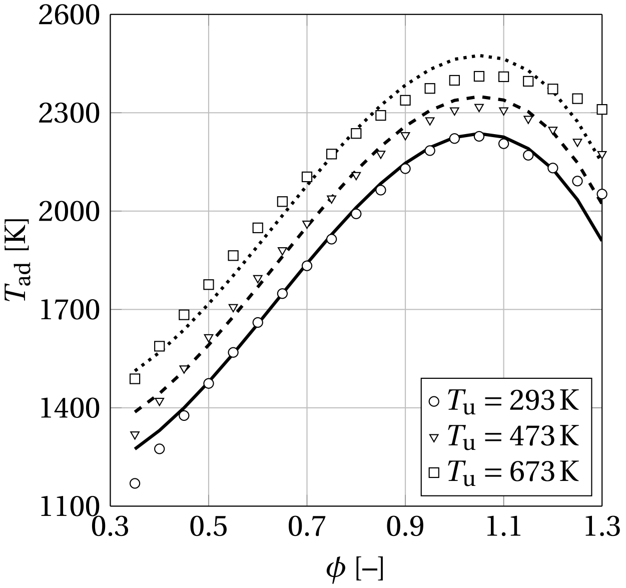

(a) Effect of T_{u} ($p = 1\,\mathrm{bar}$). Symbols: GRI-Mech 3.0 [69], lines: Eq. (2.34) [66].

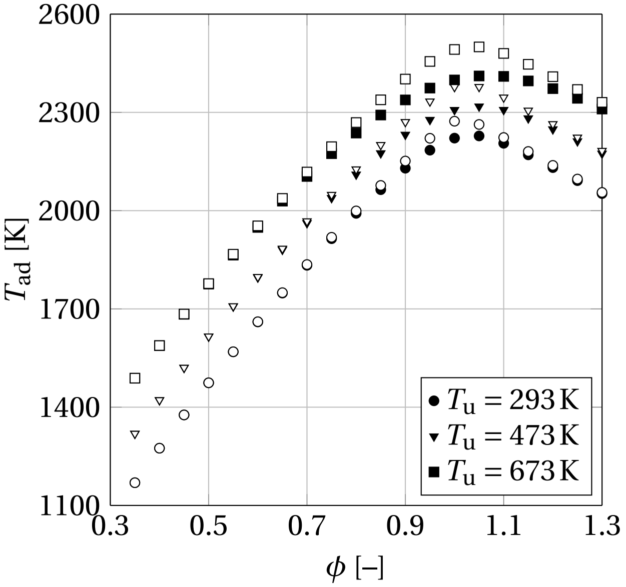

(b) Effect of p computed with GRI-Mech 3.0 [69]: Filled symbols: $p = 1\,\mathrm{bar}$, empty symbols: $p = 20\,\mathrm{bar}$.

Figure 2.7: Preheating temperature and pressure effect on the adiabatic flame temperature of methane-air mixtures.

and pressure dependencies based on the work of Göttgens et al. [70]:

$$S_{\mathrm{l},0} = b_1 Y_{\mathrm{f}}^{b_2} \mathrm{e}^{-\frac{b_3}{T_{\mathrm{IL}}}} \frac{T_{\mathrm{u}}}{T_{\mathrm{IL}}} \left(\frac{T_{\mathrm{ad}} - T_{\mathrm{IL}}}{T_{\mathrm{ad}} - T_{\mathrm{u}}} \right)^{b_4} . \tag{2.35}$$

Assuming that the inner layer temperature T_{IL} does not depend on equivalence ratio, it can be calculated from

$$p = b_5 \mathrm{e}^{-\frac{b_6}{T_{\mathrm{IL}}}} . \tag{2.36}$$

The coefficients b_1–b_6 are fuel dependent. The adiabatic flame temperature can be obtained from Eq. (2.34) or from equilibrium kinetics computations.

If the unstretched laminar burning velocity at a reference temperature T_{ref} and a reference pressure p_{ref} is known, a third method to determine $S_{\mathrm{l},0}$ can be applied:

$$S_{\mathrm{l},0} = S_{\mathrm{l},0}(T_{\mathrm{ref}}, p_{\mathrm{ref}}) \left(\frac{T}{T_{\mathrm{ref}}} \right)^{c_1} \left(\frac{p}{p_{\mathrm{ref}}} \right)^{c_2} . \tag{2.37}$$

This method was introduced by Metghalchi and Keck [71, 72] for propane-air mixtures and was applied by Dahoe [73] to hydrogen-air flames. The power law exponents c_1 and c_2 depend on fuel and equivalence ratio. The presented methods to determine $S_{\mathrm{l},0}$ will be discussed for hydrogen- and methane-air mixtures in the following paragraphs.

Hydrogen-Air Mixtures: Measured unstretched laminar burning velocities of hydrogen-air mixtures at $T_{\mathrm{u}} = 293\,\mathrm{K}$ and $p = 1\,\mathrm{bar}$ presented by Konnov [74] are summarized in Fig. 2.8. The figure also includes a fourth order polynomial fit

$$S_{\mathrm{l},0}[\mathrm{m/s}] = 2.1600\phi^4 - 9.1537\phi^3 + 12.4930\phi^2 - 3.7952\phi + 0.3972 . \tag{2.38}$$

It will be used throughout this work to represent experimentally determined unstretched laminar burning velocities of hydrogen-air mixtures at ambient conditions. Figure 2.8 shows that $S_{\mathrm{l},0}$ increases with equivalence ratio. In contrast to the adiabatic flame temperature, the maximum is not found around $\phi = 1.1$ but around $\phi = 1.5$ [73] which is beyond the equivalence ratio range of interest in this work.

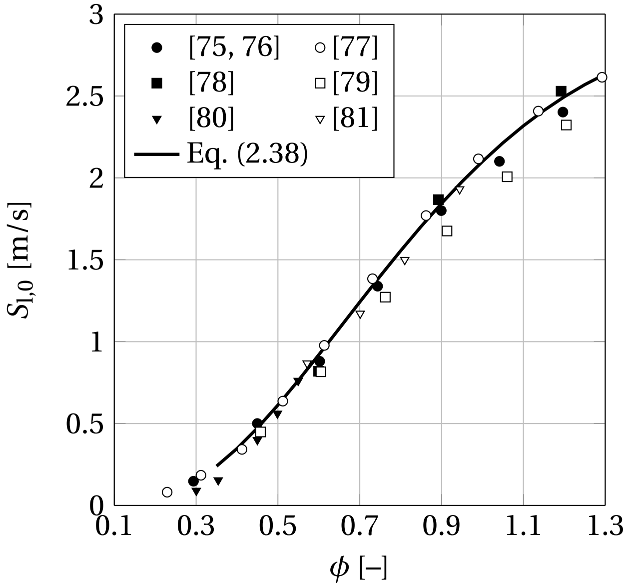

Figure 2.8: Measured unstretched laminar burning velocity $S_{l,0}$ of hyrogen-air mixtures at ambient conditions compared to Eq. (2.38).

Table 2.2: Coefficients of unstretched laminar burning velocity correlation by Peters and Göttgens et al. [66, 70] (Eq. (2.35)) for hydrogen-air and methane-air mixtures.

Coefficient	H_2	CH_4	Unit
b_1	12928.8	0.22176	m/s
b_2	1.08721	0.565	–
b_3	2057.56	−6444.27	K
b_4	3.535	2.516	–
b_5	30044.1	3.1557×10^8	bar
b_6	10200.8	23873	K

Figure 2.9 compares the unstretched laminar burning velocity at ambient conditions computed with *Cantera 2.2* [67], the correlation by Peters and Göttgens et al. [66, 70] in Eq. (2.35) and the experimental data fit from Eq. (2.38). The filled symbols represent the *Cantera 2.2* [67] data computed with the reaction mechanism of Ó Conaire et al. [68]. The results from Eq. (2.35) are shown as a dashed line. The coefficients are given in Tab. 2.2. Compared to the experimental data shown as black line, the simulations underestimate $S_{l,0}$ at

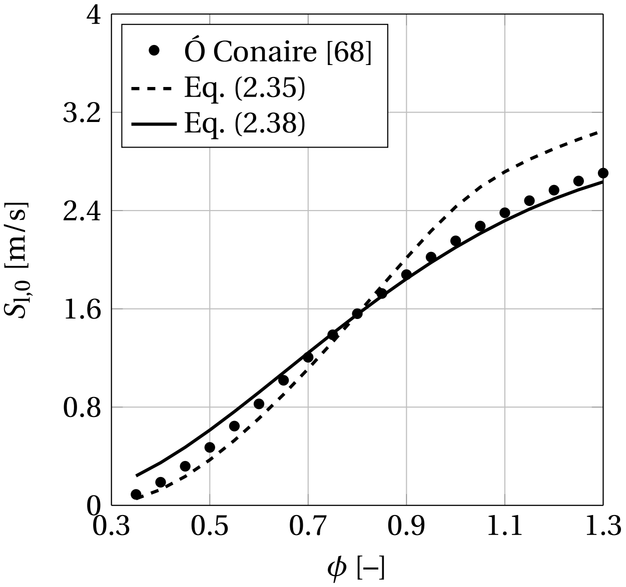

Figure 2.9: Computed unstretched laminar burning velocity $S_{l,0}$ of hyrogen-air mixtures at ambient conditions compared to Eq. (2.38).

lean conditions and overestimate it around stoichiometry. The presented results from the correlation by Peters and Göttgens et al. [66, 70] are similar to the *Cantera 2.2* [67] data in the lean region but strongly overestimate the unstretched laminar burning velocity around stoichiometry.

In the following, the influence of preheating temperature will be analyzed. Apart from *Cantera 2.2* [67] computations and the correlation by Peters and Göttgens et al. [66, 70], the power law method presented in Eq. (2.37) can be used for this purpose. Different methods to determine the power law exponent c_1 are depicted in Fig. 2.10. Gelfand [82] derives values between $c_1 = 1.6$ around stoichiometry and $c_1 = 2.5$ at $\phi = 0.35$ from computations of spherical flame propagation. Alternatively, the power law exponent can be extracted from one-dimensional free flame (FF) computations at 293 K and 473 K as described in [58]. If only the temperature dependence in Eq. (2.37) is considered, the temperature power law exponent is obtained from:

$$c_1 = \frac{\ln\left(\frac{S_{l,0,\mathrm{FF}}(473\,\mathrm{K})}{S_{l,0,\mathrm{FF}}(293\,\mathrm{K})}\right)}{\ln\left(\frac{473\,\mathrm{K}}{293\,\mathrm{K}}\right)}\,. \tag{2.39}$$

The exponents obtained with the reaction mechanism of Ó Conaire et al. [68]

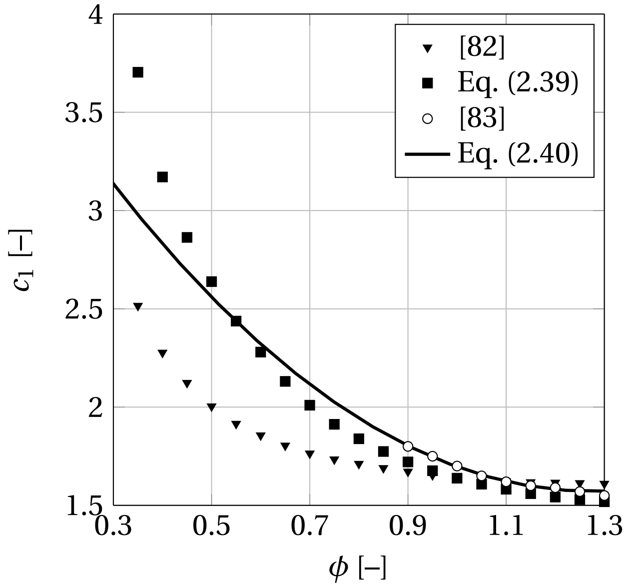

Figure 2.10: Power law exponent c_1 for hydrogen-air mixtures.

are presented in Fig. 2.10 and range from $c_1 = 1.6$ at $\phi = 1$ to $c_1 = 3.6$ at $\phi = 0.35$. A third method to determine c_1 is based on experimentally determined unstretched laminar burning velocities by Heimel [83] and is introduced in [35]. The power law exponents extracted from Heimel's data are included in Fig. 2.10 as empty circles. They cover the range from $\phi = 0.9$ to $\phi = 1.3$. To extend the data to lean conditions a quadratic fit

$$c_1 = 1.6429\phi^2 - 4.1907\phi + 4.2441 \tag{2.40}$$

is used for extrapolation. It has to be noted that such extrapolation holds a considerable uncertainty. The obtained power law exponents range from $c_1 = 1.7$ at $\phi = 1$ to $c_1 = 3.0$ at $\phi = 0.35$.

Figure 2.10 shows that all three presented methods deliver similar exponents c_1 around stoichiometry. However, at lean conditions large deviations are observed leading to high uncertainties in the definition of $S_{l,0}$ at preheated conditions.

Figure 2.11 compares the unstretched laminar burning velocities at preheated conditions computed in laminar free flames with those obtained from the correlation by Peters and Göttgens et al. [66, 70] in Eq. (2.35). Filled symbols represent data at $T_u = 473\,\text{K}$ and empty symbols data at $T_u = 673\,\text{K}$. As expected

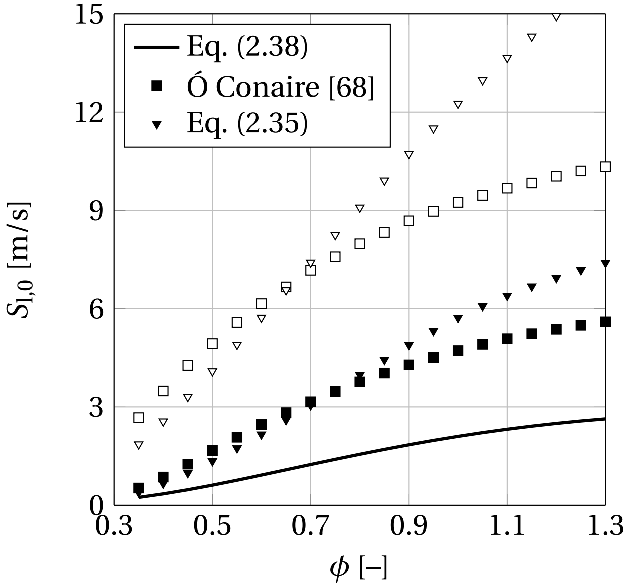

Figure 2.11: Unstretched laminar burning velocity at different preheating temperatures for hydrogen-air mixtures. Filled symbols: T_u = 473 K, empty symbols: T_u = 673 K.

from the ambient temperature case presented in Fig. 2.9, the correlation by Peters and Göttgens widely overestimates the unstretched laminar burning velocity around stoichiometry. Therefore, it does not seem suitable to represent $S_{l,0}$ for hydrogen-air mixtures in this work. For that reason, the free flame method is preferred in this work to define $S_{l,0}$ at preheated conditions.

In order to obtain a correlation-based representation of $S_{l,0}$, free flame simulations at different preheating temperatures are performed and used to generate third order polynomials of the form

$$S_{l,0}(T_u) = b_7 T_u^3 + b_8 T_u^2 + b_9 T_u + b_{10}\,. \tag{2.41}$$

The coefficients b_7–b_{10} depend on equivalence ratio and are presented in Tab. C.1 for atmospheric pressure. An example polynomial for $\phi = 1$ is shown in Fig. 2.12. The unstretched laminar burning velocity at ambient temperature is calculated from Eq. (2.38) to include the available experimental data. Equation (2.41) in combination with the coefficients presented in App. C will be used throughout this work to calculate $S_{l,0}$. It should be kept in mind that at low burning velocities, i.e. low equivalence ratios, and preheated conditions

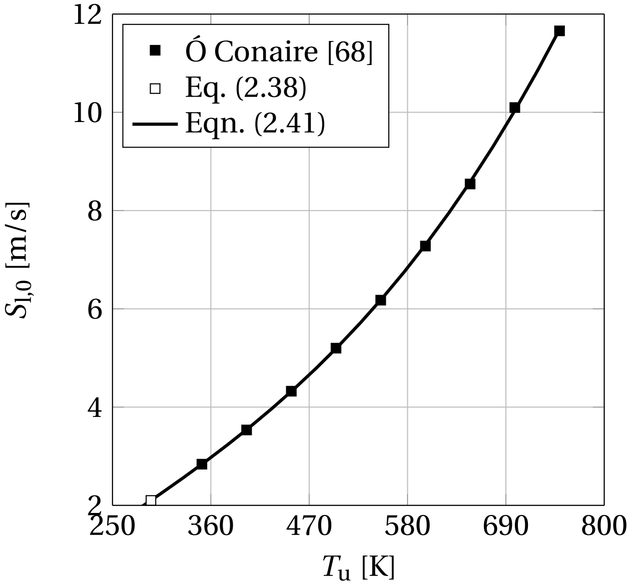

Figure 2.12: Effect of preheating temperature on unstretched laminar burning velocity at atmospheric pressure ($\phi = 1$).

$S_{l,0}$ might be underestimated (cf. Fig. 2.9).

Similar to the dependence on temperature, little experimental data is available to determine the influence of pressure on unstretched laminar burning velocity. Dahoe [73] introduces the power law exponent $c_2 = 0.194$ (Eq. (2.37)) based on the work of Iijima and Takeno [84] for a pressure range of $p = 0.5$–$5.5\,\mathrm{bar}$ and the equivalence ratio $\phi = 1$. This exponent reflects an increase of $S_{l,0}$ with pressure. Konnov [74] presents experimental data at ambient temperature by Aung et al. [76] for four different equivalence ratios ranging from $\phi = 0.75$ to $\phi = 3$. The data in the lean and stoichiometric region are shown in Fig. 2.13 in comparison to one-dimensional free flame computations with the reaction mechanism of Ó Conaire et al. [68]. Around stoichiometry an initial increase of $S_{l,0}$ with pressure is observed up to atmospheric pressure. Beyond that, the unstretched laminar burning velocity decreases contradicting the observations of Iijima and Takeno [84]. With decreasing equivalence ratio, the maximum unstretched laminar burning velocity is shifted to lower pressures. Comparing ambient temperature free flame simulations at $p = 1\,\mathrm{bar}$

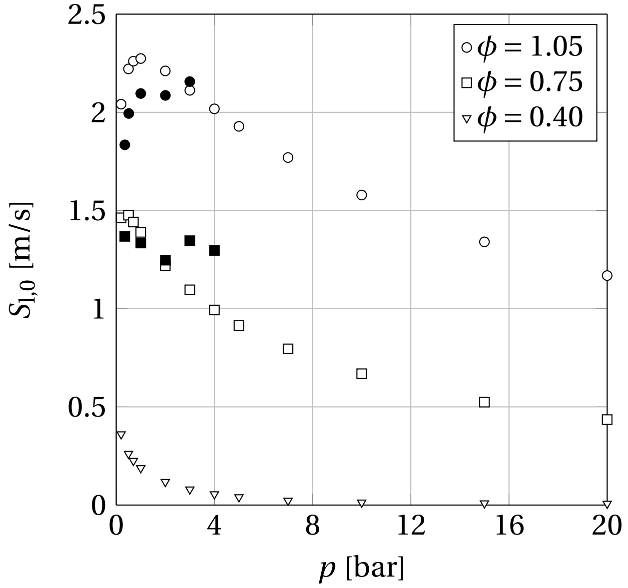

Figure 2.13: Pressure influence on $S_{l,0}$ of hydrogen-air mixtures $T_u = 293\,\text{K}$. Filled symbols: experimental data [74], empty symbols: one-dimensional free flame (Ó Conaire et al. [68]).

and $p = 20\,\text{bar}$, the power law exponent for Eq. (2.37) can be defined by

$$c_2 = \frac{\ln\left(\frac{S_{l,0,\mathrm{FF}}(20\,\mathrm{bar})}{S_{l,0,\mathrm{FF}}(1\,\mathrm{bar})}\right)}{\ln\left(\frac{20\,\mathrm{bar}}{1\,\mathrm{bar}}\right)}. \tag{2.42}$$

The resulting power law exponents are depicted in Fig. 2.14. In contrast to the value presented by Dahoe [73], c_2 is negative for equivalence ratios up to $\phi = 1.3$. The absolute value decreases with increasing equivalence ratio indicating a reduced influence of pressure. However, it has to be noted that as shown in Fig. 2.15 the power law exponents are not suitable to represent the pressure influence over the whole displayed pressure range.

Alternatively, the unstretched laminar burning velocity at elevated pressure can be computed with the correlation of Peters and Göttgens et al. [66, 70] in Eq. (2.35). In Fig. 2.16, the result is compared to one-dimensional free flame simulations with the reaction mechanism of Ó Conaire et al. [68] at $p = 20\,\text{bar}$ and different preheating temperatures. At lean conditions, both methods show similar results whereas around stoichiometry the correlation of Peters and Göttgens et al. [66, 70] underestimates $S_{l,0}$ compared to the free

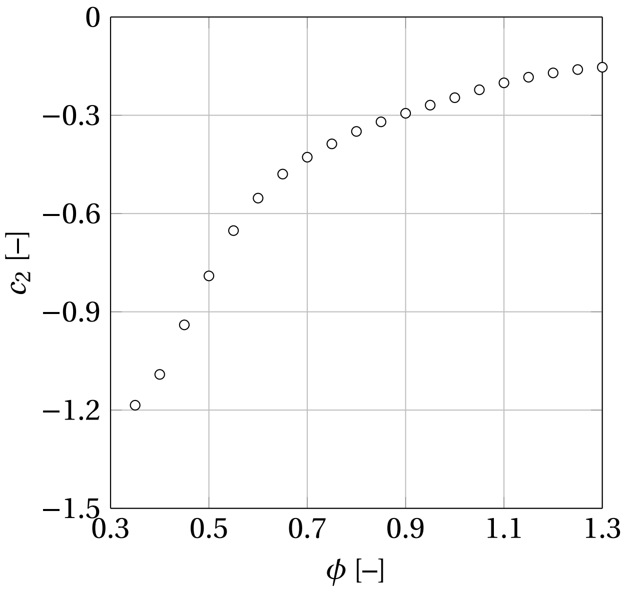

Figure 2.14: Power law exponents c_2 for hydrogen-air mixtures obtained from free flame simulations at ambient temperature (Ó Conaire et al. [68], Eq. (2.42)).

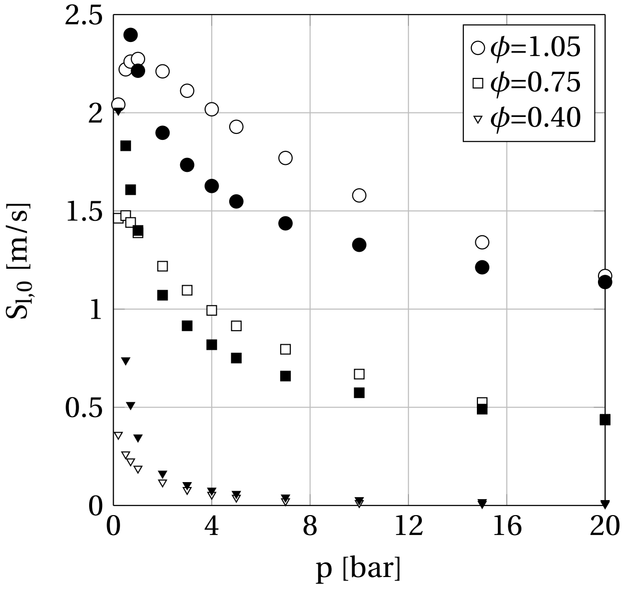

Figure 2.15: Pressure influence on $S_{l,0}$ of hydrogen-air mixtures at ambient temperature. Filled symbols: power law (Eq. (2.37)) with exponents from Eq. (2.42) ($S_{l,0}(T_{ref}, p_{ref})$ from Eq. (2.38)), empty symbols: free flame simulation (Ó Conaire et al. [68]).

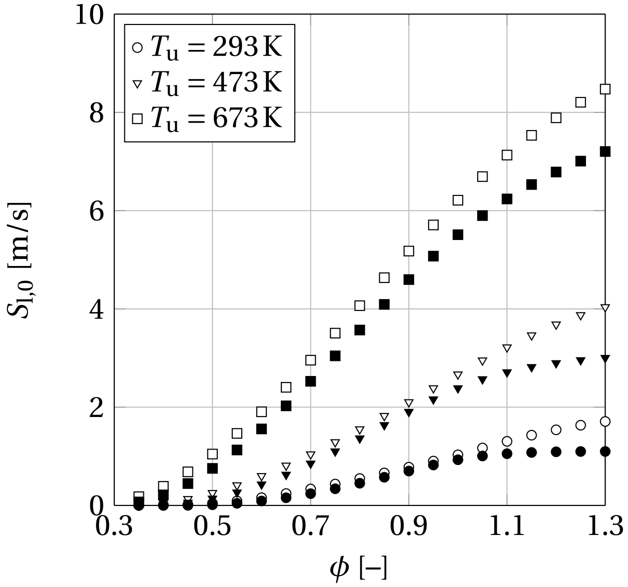

Figure 2.16: $S_{l,0}$ of hydrogen-air mixtures at $p = 20\,bar$ and different preheating. Filled symbols: Eq. (2.35) [66, 70], empty symbols: free flame simulation (Ó Conaire et al. [68]).

flame simulation. Compared to the values in Fig. 2.11 it can be observed that the unstretched laminar burning velocity is strongly reduced by pressure at lean conditions and only slightly reduced around stoichiometry as indicated by the computed power law exponents in Fig. 2.14.

Due to the lack of experimental data, the values computed from one-dimensional free flame simulations with the reaction mechanism of Ó Conaire et al. [68] presented as empty symbols in Fig. 2.16 will be used in this work to represent the unstretched laminar burning velocity at elevated pressure and different preheating temperatures. Similar to the atmospheric pressure case, third order polynomials in the form of Eq. (2.41) are extracted for 3, 5, 7 and 20 bar resulting in the coefficients presented in App. C.

Methane-Air Mixtures: Experimental data of several authors for the unstretched laminar burning velocity of methane-air mixtures at ambient temperature and pressure were summarized by Chen [85]. They are shown in Fig. 2.17 compared to the results of one-dimensional free flame simulations

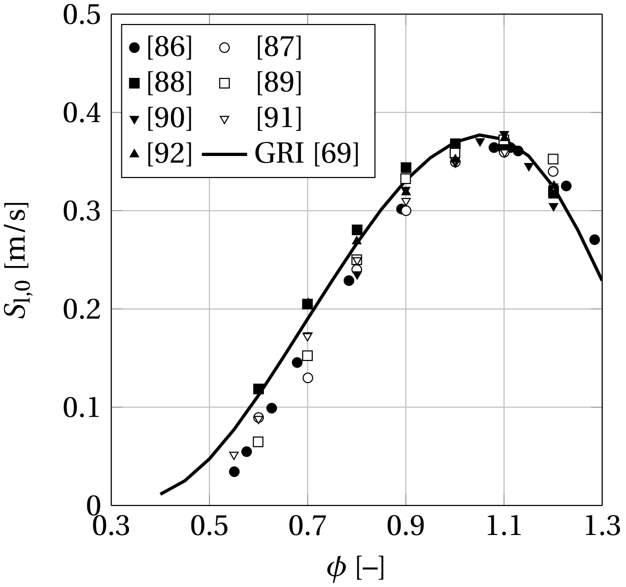

Figure 2.17: Measured unstretched laminar burning velocity $S_{l,0}$ of methane-air mixtures at ambient conditions compared to laminar free flame computation with GRI-Mech 3.0 [69].

with the reaction mechanism GRI-Mech 3.0 [69]. As for hydrogen-air mixtures, the unstretched laminar burning velocity increases with equivalence ratio until a maximum is reached at slightly rich conditions. For methane-air mixtures this maximum is located close to stoichiometry around $\phi = 1.05$. In general, $S_{l,0}$ is lower compared to hydrogen-air mixtures (approximately by a factor of 10 at the maximum). Fig. 2.17 shows that the reaction mechanism GRI-Mech 3.0 [69] well represents the experimental data over a broad equivalence ratio range. Only slight deviations are observed around $\phi = 0.5$. For that reason, it is assumed that GRI-Mech 3.0 [69] can also be applied to investigate the effect of preheating temperature and pressure on $S_{l,0}$.

Fig. 2.18 shows the unstretched laminar burning velocity of methane-air mixtures for different preheating temperatures at 1 bar and 20 bar computed with GRI-Mech 3.0 [69] in comparison to the correlation of Peters and Göttgens et al. [66, 70] in Eq. (2.35). The required parameters for Eq. (2.35) can be found in Tab. 2.2. The adiabatic flame temperature is taken from chemical equilibrium calculations presented in Fig. 2.7(b). For methane-air mixtures, preheating leads to an increase of $S_{l,0}$ whereas increasing pressure leads to a $S_{l,0}$ re-

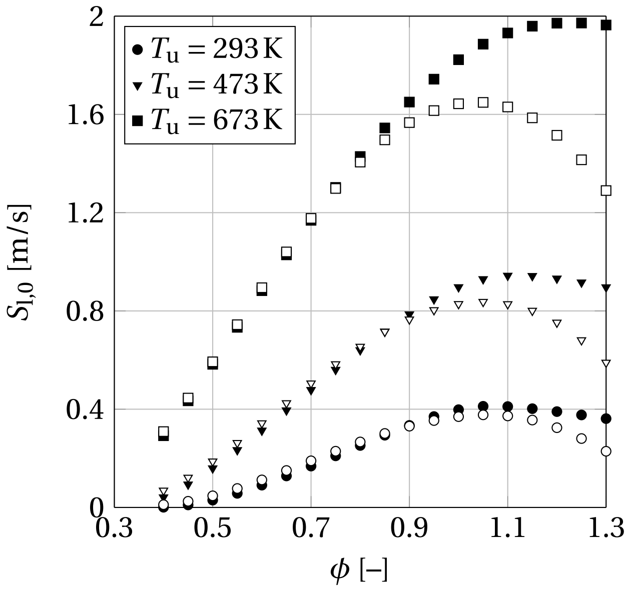

(a) $p = 1\,\text{bar}$

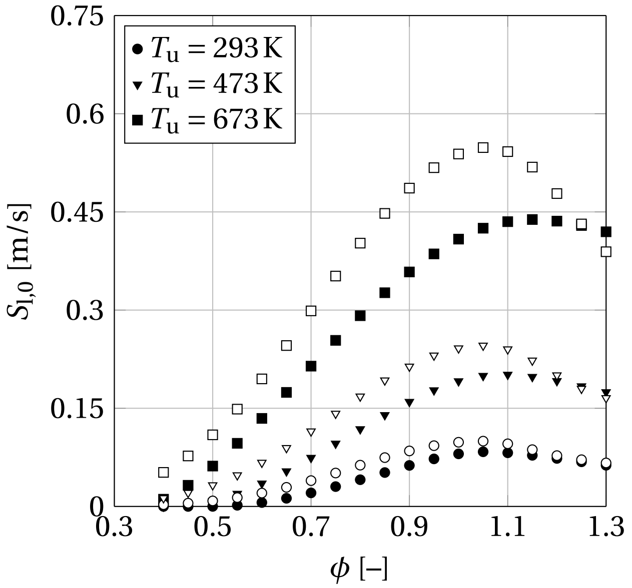

(b) $p = 20\,\text{bar}$

Figure 2.18: $S_{l,0}$ for methane-air mixtures at different preheating temperatures. Empty symbols: laminar free flame (*Cantera 2.2* [67], GRI-Mech 3.0 [69]), filled symbols: correlation of Peters and Göttgens et al. [66, 70] (Eq. (2.35)). T_{ad} is taken from Fig. 2.7(b).

duction. The correlation of Peters and Göttgens et al. [66, 70] fits the laminar free flame results at lean conditions and ambient pressure. High deviations are observed in the rich region and at elevated pressure. As Rozenchan et al. [89] compared $S_{l,0}$ obtained from GRI-Mech 3.0 [69] with experimental data and found good agreement up to $p = 20\,\mathrm{bar}$, the one-dimensional free flame results will be used to represent $S_{l,0}$ of methane-air mixtures in this work.

In order to obtain a correlation-based representation of $S_{l,0}$ at different pressures for varying preheating temperature similar to the hydrogen-air mixture case, third order polynomials in the form of Eq. (2.41) are extracted for 1 and 20 bar. The resulting coefficients are presented in Tab. C.6 and C.7.

2.3.1.3 Laminar Flame Thickness

As indicated in Fig. 2.5, the laminar flame thickness δ_F consists of preheat and reaction zone. Based on the simplification of a linear temperature increase, the laminar flame thickness

$$\delta_\mathrm{F} = \frac{T_\mathrm{b} - T_\mathrm{u}}{\max\left(\frac{\mathrm{d}T}{\mathrm{d}x}\right)} \tag{2.43}$$

can be defined [93] and calculated from the temperature profile of a one-dimensional laminar free flame.

Different alternative expressions for δ_F are found in literature and typically depend on thermal conductivity λ, density ρ, specific heat capacity c_p and unstretched laminar burning velocity $S_{l,0}$. It has to be noted that these expressions assume a Lewis number $\mathrm{Le} = 1$. Turns [93] proposes the relation

$$\delta_\mathrm{F} = \frac{2\lambda_\mathrm{u}}{\rho_\mathrm{u} c_\mathrm{p,u} S_{l,0}} \tag{2.44}$$

based on unburned mixture properties. A similar expression is given by Ciccarelli and Dorofeev [65]

$$\delta_\mathrm{F} = \frac{\lambda_\mathrm{b}}{\rho_\mathrm{b} c_\mathrm{p,b} S_{l,0} \sigma} \tag{2.45}$$

depending on burned mixture properties and the expansion ratio σ. Peters [94] suggests to evaluate thermal conductivity λ and specific heat capacity

c_p at the inner layer temperature T_IL:

$$\delta_\mathrm{F} = \frac{\lambda_\mathrm{IL}}{\rho_\mathrm{u} c_\mathrm{p,IL} S_\mathrm{l,0}} \,. \tag{2.46}$$

He suggests that an estimate of the mixture properties at T_IL can be obtained from averaging the unburned mixture properties at T_u and the product properties at T_b.

Apart from these three definitions of laminar flame thickness Ciccarelli and Dorofeev [65] mention

$$\delta_\mathrm{F} = \frac{\nu_\mathrm{u}}{S_\mathrm{l,0}} \tag{2.47}$$

based on the unburned kinematic viscosity. In the following sections the five definitions will be compared for hydrogen-air and methane-air mixtures.

Hydrogen-Air Mixtures: Figure 2.19 shows a comparison of the laminar flame thickness of hydrogen-air mixtures at ambient temperature and pressure computed with the five introduced methods. The unstretched laminar burning velocity is obtained from Eq. (2.41) and the coefficients presented in Tab. C.1. In general, the laminar flame thickness decreases with equivalence ratio. It can be seen that the three methods based on thermal diffusivity deliver similar results whereas the values from the fifth method based on kinematic viscosity are smaller. The temperature based method shows the highest laminar flame thicknesses. This might be caused by the Le = 1 assumption in the other four methods. However, as the method proposed by Turns [93] in Eq. (2.44) is used in literature to derive calculation models for different combustion properties, it will be used in this work in the context of these models (cf. Sec. 2.3.2). Furthermore, it is used in the following compared to the temperature based method in Eq. (2.43) to study how the laminar flame thickness is affected by temperature and pressure.

Figure 2.20 shows the laminar flame thickness at different preheating temperatures at 1 bar and 20 bar calculated from Eq. (2.43) and (2.44). At atmospheric pressure the temperature based method in Eq. (2.43) suggests an increase of laminar flame thickness with preheating over a wide equivalence ratio range.

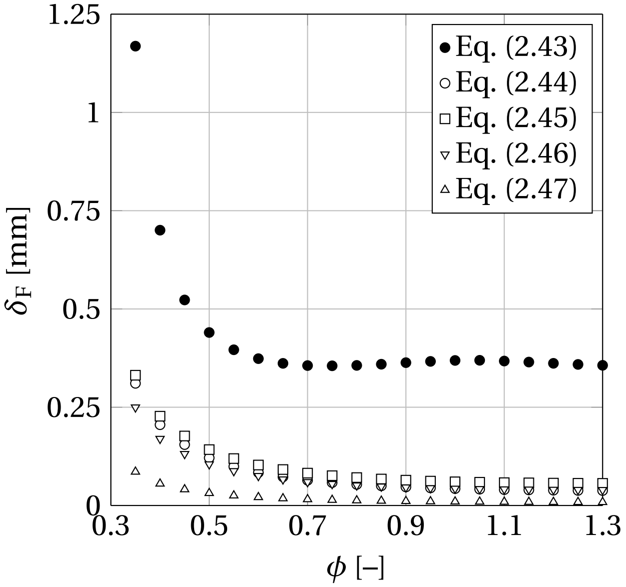

Figure 2.19: Laminar flame thickness of hydrogen-air mixtures at ambient temperature and pressure computed from five different approaches presented in Eq. (2.43)–(2.47).

Only below $\phi = 0.5$ a reduction in δ_F is observed. Whereas the flame thickness remains approximately constant at high preheating it significantly increases at ambient temperature. The small variation of laminar flame thickness with equivalence ratio at $T_u = 673\,K$ is also reproduced by the diffusivity based method of Turns [93]. But, as already seen in Fig. 2.19, the general level of flame thicknesses is much lower. The same trend is found at $p = 20\,bar$. The flame thickness around stoichiometry of $\delta_F \approx 0.003\,mm$ is lower compared to ambient pressure but strongly increases at leaner conditions due to lower unstretched laminar burning velocities. In all cases, the diffusivity based method of Turns [93] (Eq. (2.44)) underestimates the laminar flame thickness compared to the temperature based approach. This has to be kept in mind when it is applied in models to calculate flame stretch and Markstein length.

Methane-Air Mixtures: The laminar flame thicknesses of methane-air mixtures computed with the five methods presented in Eq. (2.43)–(2.47) are shown in Fig. 2.21. The unstretched laminar burning velocity is computed from Eq. (2.41) and the coefficients presented in C.2. The dependence of flame

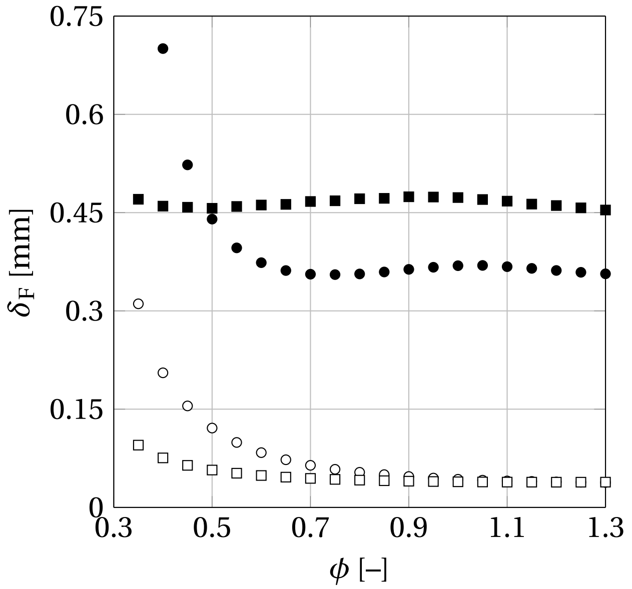

(a) $p = 1\,\mathrm{bar}$

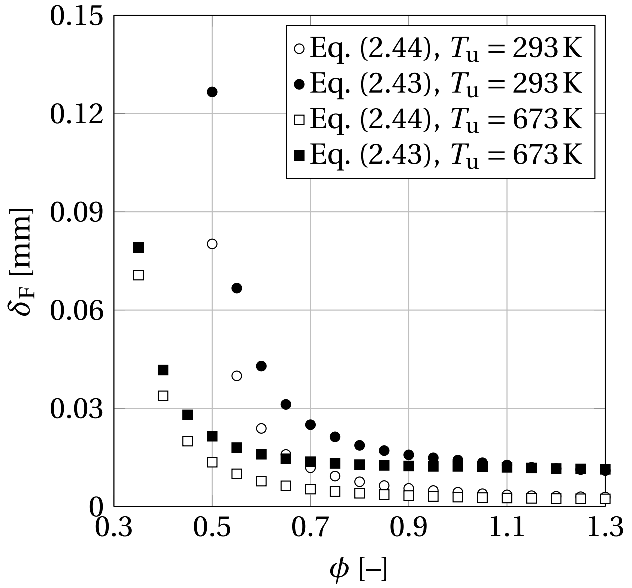

(b) $p = 20\,\mathrm{bar}$

Figure 2.20: Laminar flame thickness of hydrogen-air mixtures at different preheating temperatures and pressures computed from Eq. (2.43) and (2.44). Legend in (b) applies to both plots.

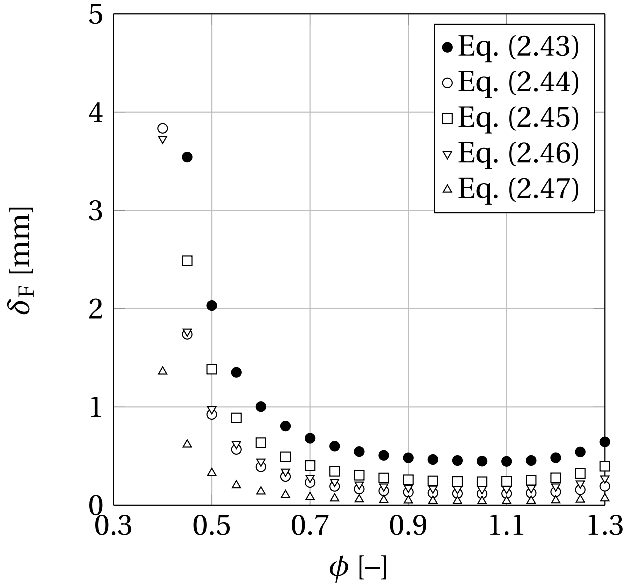

Figure 2.21: Laminar flame thickness of methane-air mixtures at ambient temperature and pressure computed from five different approaches presented in Eq. (2.43)–(2.47).

thickness on equivalence ratio is similar to hydrogen-air mixtures although δ_F is generally higher due to lower unstretched laminar burning velocities. It can be seen that the temperature based method in Eq. (2.43) better fits the other four methods compared to the hydrogen-air mixture case. This is reasonable as methane-air mixtures better fulfill the Le = 1 assumption. As for hydrogen-air mixtures, the method based on kinematic viscosity delivers the lowest results. The approach proposed by Turns [93] (Eq. (2.44)) lies in between the other two thermal diffusivity based methods. In accordance with the previous paragraph it will be applied in this work to represent laminar flame thicknesses of methane-air mixtures.

The effect of preheating and pressure on laminar flame thickness of methane-air mixtures is presented in Fig. 2.22 based on Eq. (2.44). As for hydrogen-air mixtures, preheating especially affects the laminar flame thickness below $\phi = 0.6$ whereas no significant effect is observed around stoichiometry. At atmospheric pressure the laminar flame thickness varies between $\delta_F = 0.1\,\text{mm}$ and $\delta_F = 3.8\,\text{mm}$. Increasing pressure reduces the laminar flame thickness leading to values ranging from $\delta_F = 0.02\,\text{mm}$ to $\delta_F = 0.8\,\text{mm}$.

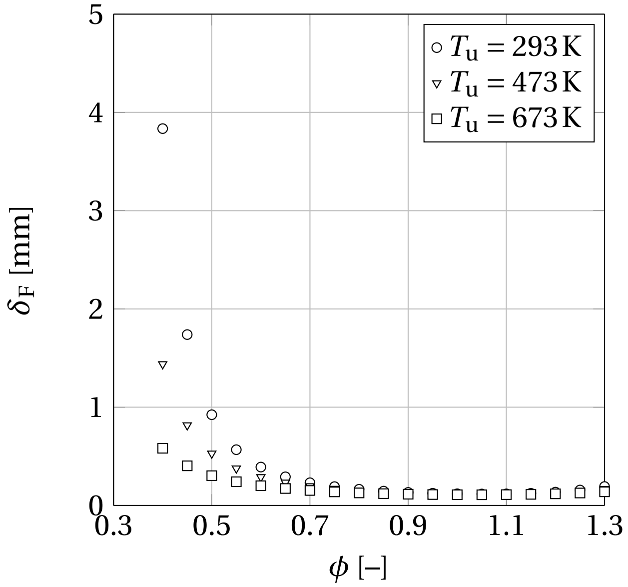

(a) $p = 1\,bar$

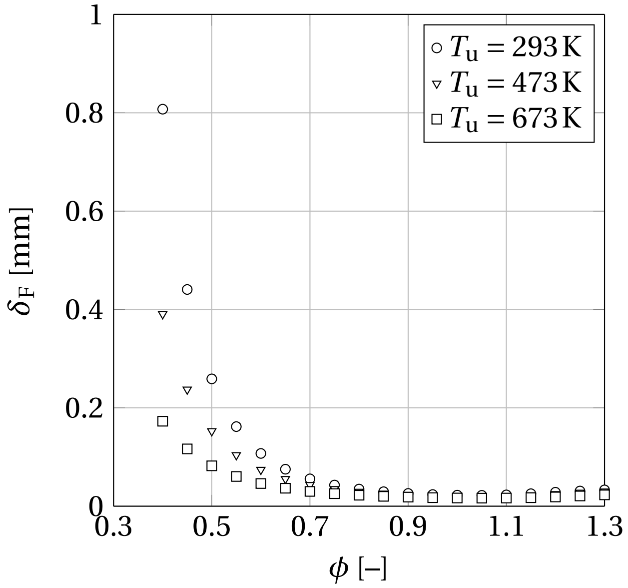

(b) $p = 20\,bar$

Figure 2.22: Laminar flame thickness of methane-air mixtures at different preheating temperatures and pressures computed from Eq. (2.44).

2.3.2 Flame Stretch

Flame stretch is defined as the normalized temporal change of flame surface area and can be quantified with the flame stretch rate κ. How a certain fuel-oxidizer mixture reacts to flame stretch can be described by the Markstein length L_M. Based on the work of Markstein [95] in 1964, the influence of flame stretch is accounted for by defining a stretched laminar burning velocity

$$S_\mathrm{l,s} = S_\mathrm{l,0} - L_\mathrm{M}\kappa \tag{2.48}$$

with a linear dependence on L_M and κ. This relation is only valid in the linear region of flame stretch were the Karlovitz number $\mathrm{Ka} = \kappa\delta_\mathrm{F}/S_\mathrm{l,0}$ is smaller than one [96]. This criterion is fulfilled for most operating conditions investigated in this work. The validity limit of Eq. (2.48) is exceeded only for lean hydrogen-air mixtures around $\phi = 0.33$ at low preheating temperatures (293 K) or high pressure (20 bar).

Positive Markstein lengths lead to a reducing effect of flame stretch on laminar burning velocity whereas flame stretch increases burning velocities of mixtures with negative Markstein lengths. The two parameters flame stretch rate and Markstein length are introduced in the following sections.

2.3.2.1 Flame Stretch Rate

As flame stretch is defined as normalized temporal change of flame surface area, the flame stretch rate can be described by the following derivative [97]:

$$\kappa = \frac{1}{A_\mathrm{F}}\frac{\mathrm{d}A_\mathrm{F}}{\mathrm{d}t}. \tag{2.49}$$

Flame stretch is caused by two reasons: flow non-uniformity (strain) and flame front curvature [96]. Hence, the flame stretch rate can be divided into two components:

$$\kappa = \kappa_\mathrm{strain} + \kappa_\mathrm{curv}. \tag{2.50}$$

As introduced by Chong et al. [98], the strain rate κ_strain consists of contributions from the mean flow κ_mean and from turbulence κ_turb. Chong et al. [98]

suggest to use the mean flow divergence for the mean flow contribution

$$\kappa_{\mathrm{mean}} = \frac{2}{3}\frac{\partial u_{\mathrm{i}}}{\partial x_{\mathrm{i}}}. \tag{2.51}$$

As incompressible fully developed duct flows or the near field of turbulent free jets are considered in this work, the divergence of the flow and, thus, the mean flow contribution are negligibly small.

The turbulence contribution to strain rate can be described by the Intermittent Turbulent Net Flame Stretch (ITNFS) model by Meneveau and Poinsot [99]:

$$\kappa_{\mathrm{turb}} = \Gamma_{\mathrm{K}}\frac{\epsilon}{k}. \tag{2.52}$$

This model includes the efficiency function Γ_{K}, the turbulence dissipation rate $\epsilon = u'^3/\Lambda$ and the turbulent kinetic energy $k = 3/2\,u'^2$. Turbulent dissipation rate and turbulent kinetic energy can be described by the turbulent velocity fluctuations u' and the turbulent macroscale Λ as introduced in Eq. (2.14) and (2.12). Inserting both into Eq. (2.52), the turbulence contribution can be rewritten as

$$\kappa_{\mathrm{turb}} = \frac{2}{3}\Gamma_{\mathrm{K}}\frac{u'}{\Lambda}. \tag{2.53}$$

Following [59], the turbulent macroscale Λ in turbulent duct flows can be set to 7 % of the hydraulic diameter. Downstream of the burner exit the turbulent macroscale is described by the burner duct height h as stated in Eq. (2.29). Meneveau and Poinsot [99] introduce the efficiency function

$$\log_{10}(\Gamma_{\mathrm{K}}) = -\frac{1}{s+0.4}\mathrm{e}^{-(s+0.4)} + \left(1-\mathrm{e}^{-(s+0.4)}\right)\left(\frac{2}{3}\left(1-\frac{1}{2}\mathrm{e}^{\left(-(u'/S_{\mathrm{l},0})^{1/3}\right)}\right)s - 0.11\right) \tag{2.54}$$

based on turbulent velocity fluctuations u', unstretched laminar burning velocity $S_{\mathrm{l},0}$ and

$$s = \log_{10}\left(\frac{\Lambda}{\delta_{\mathrm{F}}}\right) \tag{2.55}$$

depending on turbulent macroscale Λ and laminar flame thickness δ_{F}. The effects of u' and Λ on Γ_{K} are illustrated in Fig. 2.23 and 2.24. The efficiency function increases with u' up to a limit $\Gamma_{\mathrm{K}}(u' \to \infty)$ depending on preheating temperature and pressure. $\Gamma_{\mathrm{K}}(u' \to \infty)$ for hydrogen-air and methane-air

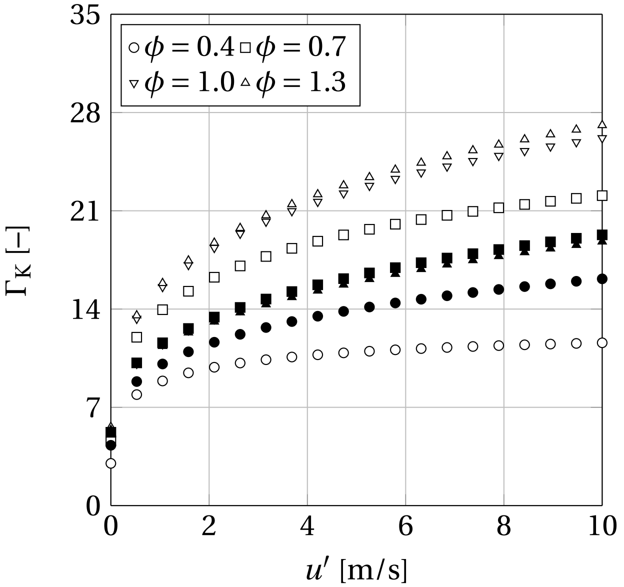

(a) $p = 1\,\text{bar}$, empty symbols: $T_u = 293\,\text{K}$, filled symbols: $T_u = 673\,\text{K}$

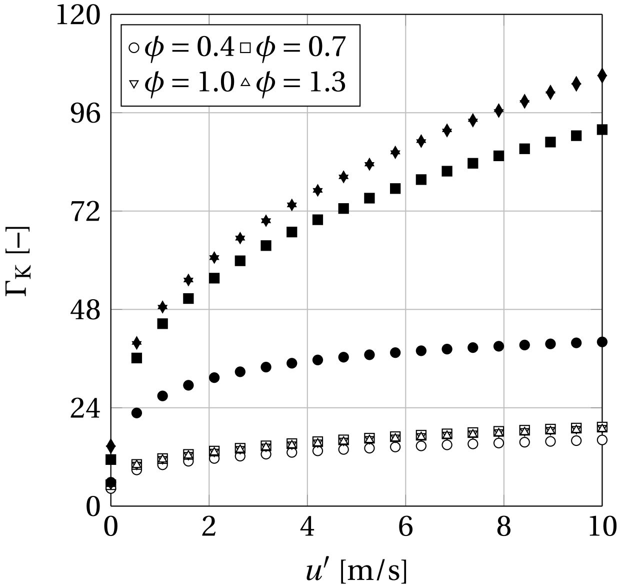

(b) $T_u = 673\,\text{K}$, empty symbols: $p = 1\,\text{bar}$, filled symbols: $p = 20\,\text{bar}$

Figure 2.23: Effect of turbulent velocity fluctuations u' on ITNFS model efficiency function Γ_K for hydrogen-air mixtures ($\Lambda = 0.02\,\text{m}$).

Table 2.3: Limits of ITNFS model efficiency function Γ_K for $u' \to \infty$ and stoichiometric hydrogen-air and methane-air mixtures ($\Lambda = 0.02\,\mathrm{m}$).

Fuel	p [bar]	T_u [K]	s [–]	$\Gamma_K(u' \to \infty)$ [–]
H_2	1	293	2.6676	37.6353
H_2	1	473	2.6579	37.0237
H_2	1	673	2.6647	37.4515
H_2	20	293	3.6590	192.6906
H_2	20	473	3.7240	213.9707
H_2	20	673	3.8376	256.8216
CH_4	1	293	2.2255	17.6454
CH_4	1	473	2.2221	17.5412
CH_4	1	673	2.2626	18.8207
CH_4	20	293	2.9501	60.4123
CH_4	20	473	2.9881	64.3481
CH_4	20	673	3.0791	74.8111

mixtures is summarized in Tab. 2.3. At ambient pressure preheating of the unburned mixture does not significantly change $\Gamma_K(u' \to \infty)$. However, the influence of preheating increases with pressure leading to higher turbulence induced stretch rates κ_{turb} at constant u'/Λ.

The influence of turbulent macroscale on Γ_K is shown in Fig. 2.24 for hydrogen-air mixtures at different preheating temperatures and pressures. The turbulent macroscale is normalized with a burner duct diameter of $h = 20\,\mathrm{mm}$. At all investigated conditions Γ_K increases with Λ. In contrast to the dependence on u', Γ_K tends to infinity for $\Lambda \to \infty$. For the range of $\Lambda/h < 1$, applied in this study, still a distinct influence of Λ on Γ_K and on κ_{turb} is observed.

For the contribution of turbulence induced flame curvature to stretch rate Veynante et al. [100] propose a model based on the unstretched laminar burning velocity $S_{l,0}$, the Reynolds averaged reaction progress variable c and the flame wrinkling length L:

$$\kappa_{\mathrm{curv}} \approx S_{l,0} \frac{0.5 - c}{L} \tag{2.56}$$

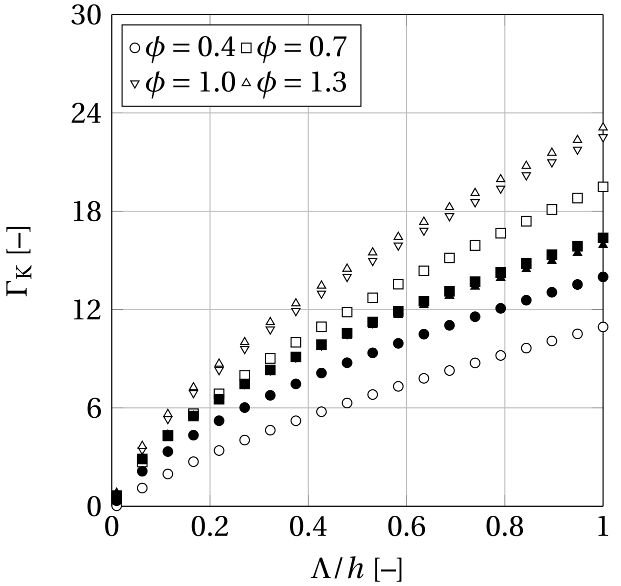

(a) $p = 1\,\text{bar}$, empty symbols: $T_u = 293\,\text{K}$, filled symbols: $T_u = 673\,\text{K}$

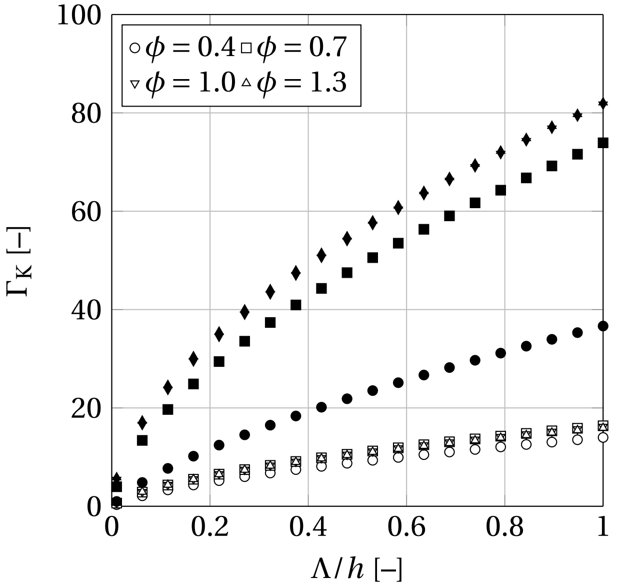

(b) $T_u = 673\,\text{K}$, empty symbols: $p = 1\,\text{bar}$, filled symbols: $p = 20\,\text{bar}$

Figure 2.24: Effect of turbulent macroscale Λ on ITNFS model efficiency function Γ_K for hydrogen-air mixtures and a $h = 20\,\text{mm}$ burner ($u' = 5\,\text{m/s}$).

with the flame wrinkling length

$$L = \Lambda \frac{S_{\mathrm{l},0}}{u'} \tag{2.57}$$

introduced by Bray [101]. In this model, the maximum flame stretch rate is obtained at the beginning ($c = 0$) and at the end ($c = 1$) of the reaction leading to the maximum absolute value of

$$\kappa_{\mathrm{curv}} = \frac{1}{2}\frac{u'}{\Lambda}\,. \tag{2.58}$$

Based on the simplifications introduced in Eq. (2.58) and (2.53) the total flame stretch rate results in:

$$\kappa = \frac{2}{3}\Gamma_{\mathrm{K}}\frac{u'}{\Lambda} + \frac{1}{2}\frac{u'}{\Lambda}\,. \tag{2.59}$$

The total stretch rate mainly depends on the turbulent velocity fluctuations u' and the turbulent macroscale Λ. Considering the magnitude of Γ_{K}, the strain contribution is the dominant component of the total stretch rate in the investigated configuration.

2.3.2.2 Markstein Length

The Markstein length L_{M} is a characteristic of fuel-oxidizer mixtures. It defines how the flame properties respond to flame stretch. The Markstein length can be determined in radially outwards propagating spherical flame experiments as for example described by Chen for methane-air mixtures [85] and by Sun et al. for hydrogen-air and propane-air flames [102]. Apart from that, Markstein lengths can be derived from conservation equations as introduced by Matalon and Matkowsky [103] and Chen and Ju [85, 104].

Based on the work of Matalon and Matkowsky [103], Bechtold and Matalon [105] suggest the following relation:

$$L_{\mathrm{M}} = \delta_{\mathrm{F}}\left(\beta - (\sigma - 1)\,\frac{\gamma_1}{\sigma}\right). \tag{2.60}$$

The Markstein length is calculated from the laminar flame thickness (Eq. (2.44)), the expansion ratio $\sigma = \rho_{\mathrm{u}}/\rho_{\mathrm{b}}$ and a parameter

$$\beta = \gamma_1 + \frac{1}{2}\mathrm{Ze}\,(\mathrm{Le} - 1)\,\gamma_2 \tag{2.61}$$

depending on Lewis number Le, Zeldovich number Ze and the parameters γ_1 and γ_2. Assuming a linear dependence of thermal conductivity on temperature, Bechtold and Matalon [105] suggest:

$$\gamma_1 = \sigma \, , \gamma_2 = 1 \, . \tag{2.62}$$

An effective Lewis number of the specific fuel-oxidizer mixture has to be defined depending on equivalence ratio. Bechtold and Matalon [105] introduce a weighted average between the Lewis numbers of the deficient (D) and the excess (E) species:

$$\mathrm{Le} = 1 + \frac{\mathrm{Le_E} - 1 + C_\mathrm{B}\,(\mathrm{Le_D} - 1)}{1 + C_\mathrm{B}} \tag{2.63}$$

with the blending factor

$$\begin{aligned} C_\mathrm{B} &= 1 + \mathrm{Ze}\left(\frac{1}{\phi} - 1\right) \ \forall \ \phi \leq 1 \, , \\ C_\mathrm{B} &= 1 + \mathrm{Ze}\left(\phi - 1\right) \ \forall \ \phi > 1 \end{aligned} \tag{2.64}$$

depending on Zeldovich number and equivalence ratio. The Zeldovich number

$$\mathrm{Ze} = \frac{E\,(T_\mathrm{ad} - T_\mathrm{u})}{R\,T_\mathrm{ad}^2} \tag{2.65}$$

depends on adiabatic flame temperature T_ad, unburned gas temperature T_u, universal gas constant $R = 8.314\,\mathrm{J/(mol\,K)}$ and global activation energy E.

According to Sun et al. [102], the global activation energy can be defined as

$$E = -2R \frac{\partial \ln(\rho_\mathrm{u} S_{\mathrm{l},0})}{\partial (1/T_\mathrm{b})} \, . \tag{2.66}$$

For an assumed adiabatic system, the product temperature T_b can be set to the adiabatic flame temperature T_ad. A variation of adiabatic flame temperature is achieved by varying the amount of nitrogen dilution $X_{\mathrm{N_2}}$ in the reactants from $X_{\mathrm{N_2},1} = X_{\mathrm{N_2,air}} - \Delta X_{\mathrm{N_2}}$ to $X_{\mathrm{N_2},2} = X_{\mathrm{N_2,air}} + \Delta X_{\mathrm{N_2}}$. It is assumed that the partial derivative can be replaced by

$$E = -2R \frac{\ln(\rho_\mathrm{u}(X_{\mathrm{N_2},1}) S_{\mathrm{l},0}(X_{\mathrm{N_2},1})) - \ln(\rho_\mathrm{u}(X_{\mathrm{N_2},2}) S_{\mathrm{l},0}(X_{\mathrm{N_2},2}))}{1/T_\mathrm{ad}(X_{\mathrm{N_2},1}) - 1/T_\mathrm{ad}(X_{\mathrm{N_2},2})} \, . \tag{2.67}$$

The required mixture parameters can be calculated with *Cantera 2.2* [67] and the reaction mechanism of Ó Conaire et al. [68] for hydrogen-air and GRI-Mech 3.0 [69] for methane-air mixtures.

An alternative definition of Markstein length is introduced by Chen and Ju [85, 104]:

$$L_\mathrm{M} = \delta_\mathrm{F} \left(\frac{1}{\mathrm{Le}} - \frac{\mathrm{Ze}}{2} \left(\frac{1}{\mathrm{Le}} - 1 \right) \right) . \tag{2.68}$$

Lewis number Le and Zeldovich number Ze can be obtained from Eq. (2.63) and (2.65), respectively.

Normalizing L_M by the flame thickness leads to the dimensionless Markstein number

$$\mathrm{Ma} = \frac{L_\mathrm{M}}{\delta_\mathrm{F}} . \tag{2.69}$$

The two presented approaches to define Markstein length L_M and Markstein number Ma are compared in the following sections for hydrogen-air and methane-air mixtures.

Hydrogen-Air Mixtures: In order to calculate the Markstein length of hydrogen-air mixtures from Eq. (2.60) and (2.68), Lewis number and Zeldovich number have to be defined based on Eq. (2.63) and (2.65). In this work, the asymptotic Lewis numbers of hydrogen and oxygen are set to $\mathrm{Le}_{\mathrm{H}_2} = 0.33$ and $\mathrm{Le}_{\mathrm{O}_2} = 2.32$ as proposed by Sun et al. [102]. These asymptotic values are held constant for various preheating temperatures and pressures as they are only weakly dependent on these parameters. The blending factor C_B as defined in Eq. (2.64) depends on Zeldovich number Ze and therefore on the overall activation energy E. For the overall activation energy different values are reported in literature: Bechtold and Matalon [105] propose $E = 20\,\mathrm{kcal/mol}$ whereas Mitani and Williams [106] suggest $E = 40\,\mathrm{kcal/mol}$. A more detailed study on global activation energy depending on equivalence ratio and pressure is presented by Sun et al. [102].

The global activation energies of Sun et al. [102] are shown in Fig. 2.25 for two different pressures compared to results from the calculation approach presented in Eq. (2.67). At lean conditions, the global activation energy decreases

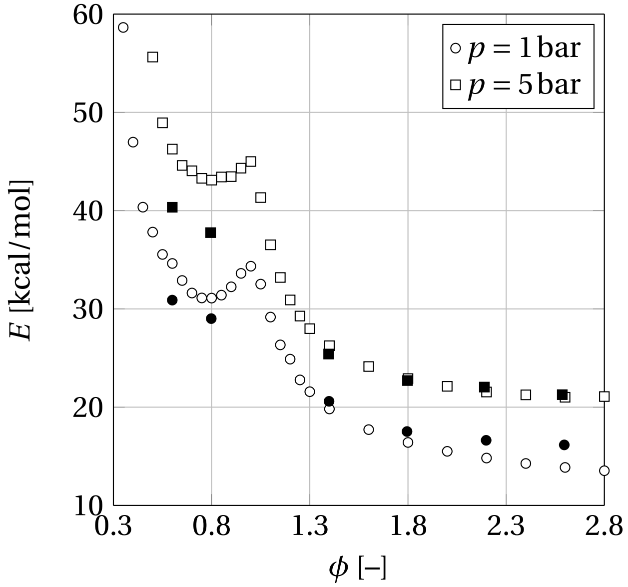

Figure 2.25: Global activation energy of hydrogen-air mixtures. Filled symbols mark data presented by Sun et al. [102], empty symbols mark results from Eq. (2.67).

with equivalence ratio. In the calculated data a local maximum at stoichiometry is observed which is not found in the results of Sun et al. [102]. However, this region was not fully resolved by Sun et al. [102] as they focused on rich conditions.[1] It is unclear if the observed maximum represents a physical effect. At rich conditions, the calculated activation energies match the data of Sun et al. [102] at both pressure levels.

Based on Eq. (2.67) the preheating temperature and pressure dependence of E is illustrated in Fig. 2.26. At lean conditions preheating reduces the global activation energy whereas negligible influence is found at rich conditions. At $p = 20\,\text{bar}$ and $\phi < 0.5$ a drop of global activation energy is observed. This drop might be a numerical artifact caused by the low unstretched laminar burning velocities at these conditions since it does not seem reasonable that the activation energy drops approaching the flammability limit.

As the pressure influence is much higher compared to the influence of equiv-

---

[1] In an e-mail conversation with Law and Liang it was assured that the method used by Sun et al. [102] delivers a similar maximum if the region around stoichiometry is resolved.

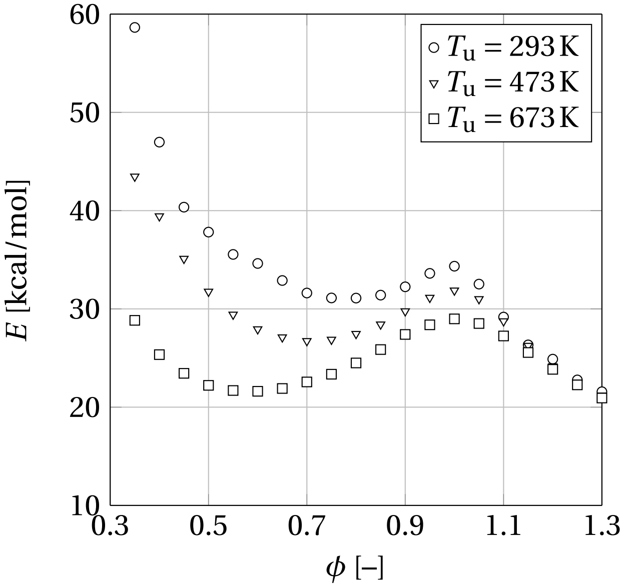

(a) $p = 1\,\text{bar}$

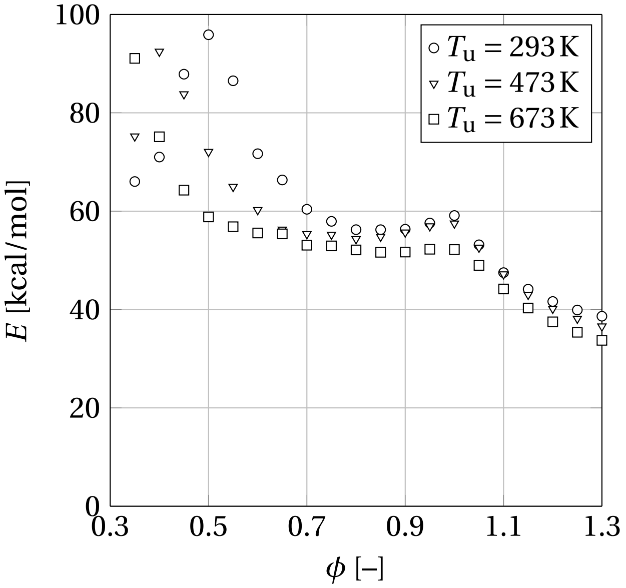

(b) $p = 20\,\text{bar}$

Figure 2.26: Global activation energy of hydrogen-air mixtures at different preheating temperatures and pressures calculated with Eq. (2.67).

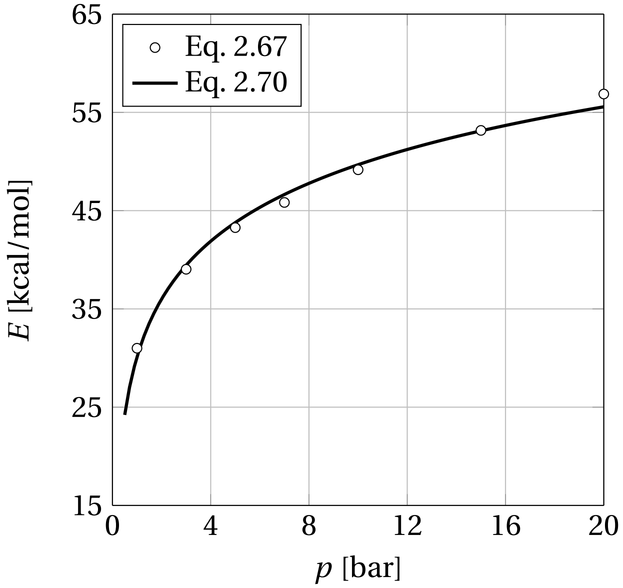

Figure 2.27: Pressure dependence of global activation energy of hydrogen-air mixtures. Values are calculated at $\phi = 0.8$ and $T_\mathrm{u} = 293\,\mathrm{K}$.

alence ratio and preheating temperature, E will be set to a constant value depending on pressure only. As reference point $\phi = 0.8$ is chosen leading to $E \approx 30\,\mathrm{kcal/mol}$ at atmospheric pressure. The dependence on pressure is illustrated in Fig. 2.27. E can be represented with the logarithmic fit

$$E\,[\mathrm{kcal/mol}] = 8.4986\,\ln(p\,[\mathrm{bar}]) + 30.1050\,. \tag{2.70}$$

From the global activation energies presented in Fig. 2.27 the corresponding Zeldovich numbers can be calculated based on Eq. (2.65) for different preheating temperatures and pressures as shown in Fig. 2.28. The adiabatic flame temperatures are computed with *Cantera 2.2* [67] and the reaction mechanism of Ó Conaire et al. [68] as described in Sec. 2.3.1.1. Generally, the Zeldovich number of hydrogen-air mixtures decreases with equivalence ratio and preheating temperature because of higher adiabatic flame temperatures. Increasing pressure leads to higher global activation energies and to higher values of the Zeldovich number.

The presented Zeldovich numbers are used to compute the mixture Lewis numbers from Eq. (2.63) and (2.64). Results are shown in Fig. 2.29. With in-

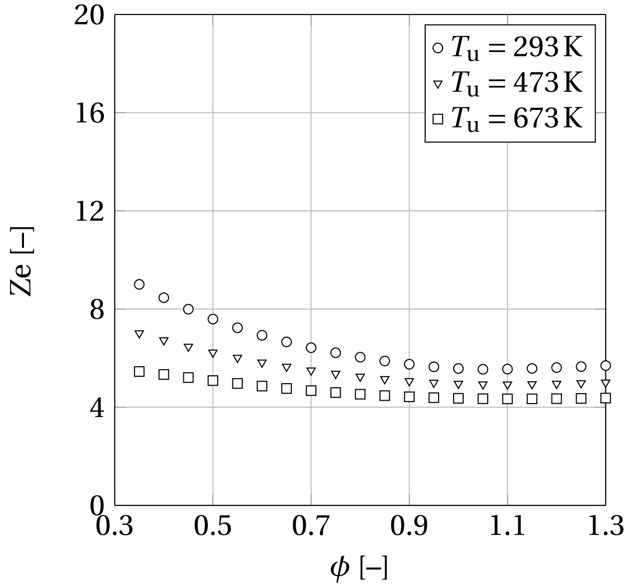

(a) $p = 1\,bar$

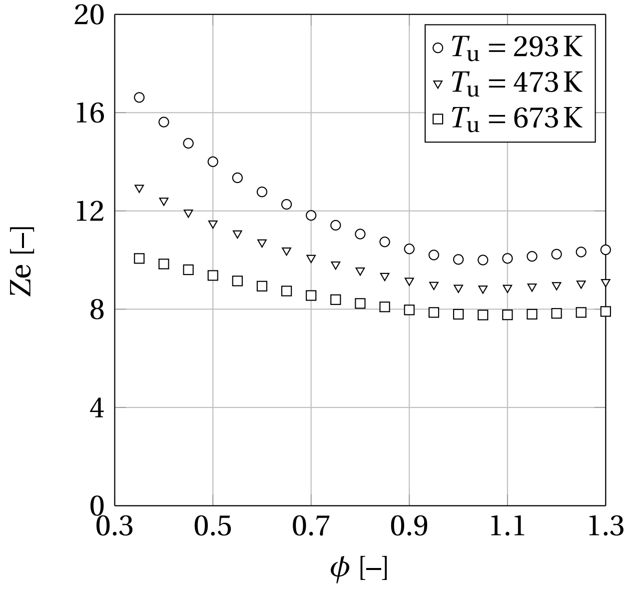

(b) $p = 20\,bar$

Figure 2.28: Zeldovich number of hydrogen-air mixtures at different preheating temperatures.

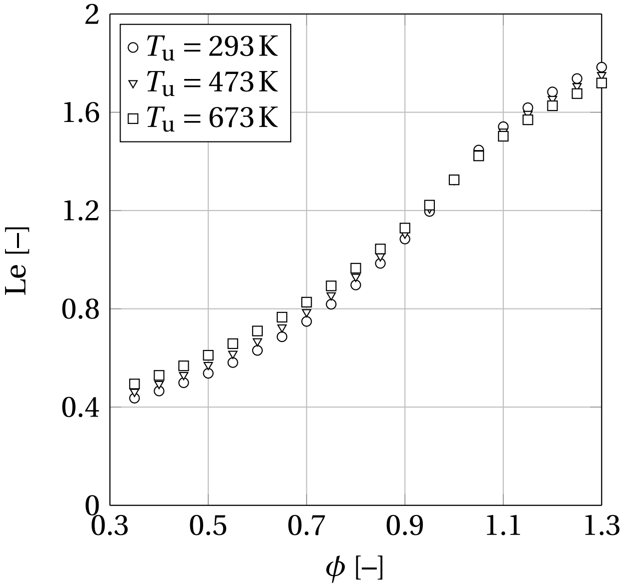

(a) $p = 1\,\text{bar}$

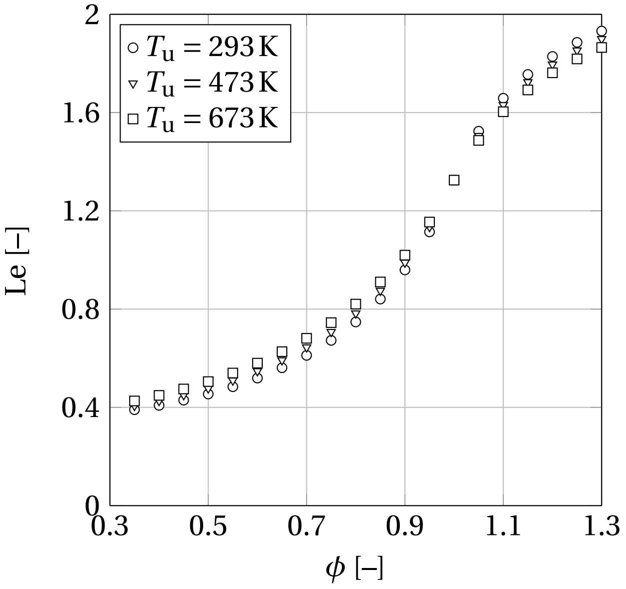

(b) $p = 20\,\text{bar}$

Figure 2.29: Lewis number of hydrogen-air mixtures at different preheating temperatures.

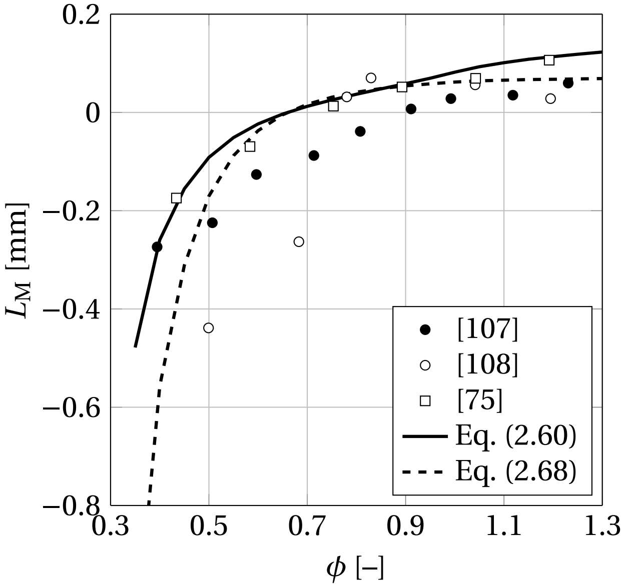

Figure 2.30: Markstein length of hydrogen-air mixtures at $T_u = 293\,\text{K}$ and $p = 1\,\text{bar}$. Symbols mark experimental data, lines represent calculated values.

creasing equivalence ratio, the mixture Lewis number increases from Le ≈ 0.4 at $\phi = 0.35$ to Le > 1 at near stoichiometric and rich conditions. At atmospheric pressure, Le = 1 is reached at $\phi \approx 0.85$. At high pressure, this point is shifted to higher equivalence ratios of $\phi \approx 0.90$ and the slope of the Lewis number curve changes.

Before the corresponding Markstein lengths and numbers are computed from the presented Lewis numbers, the two Markstein length models of Bechtold and Matalon [105] and Chen and Ju [85, 104] in Eq. (2.60) and (2.68) are compared to experimental data at ambient temperature and pressure (Fig. 2.30). The Markstein length is negative at lean conditions and increases with equivalence ratio up to a cross-over to positive values. In the calculated data this cross-over is reached at $\phi \approx 0.70$. The Markstein length data show that the burning velocity of hydrogen-air mixtures is increased by flame stretch at lean conditions and is reduced around stoichiometry. Considering the scatter in the experimental data the calculated Markstein lengths are in acceptable agreement with literature. The method presented by Chen and Ju [85, 104] (Eq. (2.68)) results in lower Markstein lengths at lean and rich conditions compared to the method of Bechtold and Matalon [105]. Due to the low Markstein lengths at lean conditions obtained from Eq. (2.68) and the better agreement of Eq. (2.60) with the experimental data of Aung et al. [75], the method of Bechtold and Matalon [105] is chosen in this work to calculate Markstein numbers and Markstein lengths.

Figures 2.31 and 2.32 show the Markstein numbers and Markstein lengths computed with the method of Bechtold and Matalon [105] at different preheating temperatures and pressures. Preheating reduces the absolute value of Ma and L_{M} at lean and rich conditions. Around stoichiometry it remains almost unchanged. Preheating shifts the cross-over from negative to positive Markstein lengths towards leaner conditions. Increasing pressure leads to higher absolute values of Ma which is in agreement with the observations of Peters [66]. The Markstein lengths presented in Fig. 2.32 are used in Sec. 2.3.2.3 to analyze the effect of flame stretch on laminar burning velocity.

Methane-Air Mixtures: As a starting point to calculate the Markstein lengths of methane-air mixtures, the global activation energy is computed from Eq. (2.67) and the reaction mechanism GRI-Mech 3.0 [69]. The result is depicted in Fig. 2.33 in comparison to the global activation energy at $T_{\mathrm{u}} = 293\,\mathrm{K}$ and $\phi = 1$ presented by Egolfopoulos and Law [109]. Similar to the hydrogen-air mixtures, the global activation energy decreases at atmospheric pressure with equivalence ratio until it starts to increase up to a local maximum at stoichiometry. At rich conditions, E increases again as the unstretched laminar burning velocity decreases. Similar to the hydrogen-air case preheating decreases the global activation energy at lean and rich conditions and has negligible effect around stoichiometry. At high pressures, the dependence of E on equivalence ratio changes. The global activation energy is low at lean conditions and increases with equivalence ratio up to its maximum at stoichiometry. As before, it is not certain if this reflects the physical behavior of the activation energy or if it is an error induced by the applied calculation method.

In analogy to the hydrogen-air mixture case, the dependence of the global activation energy on preheating temperature and equivalence ratio will be neglected in this work. The computed value of $E \approx 40\,\mathrm{kcal/mol}$ at $\phi = 0.8$ is

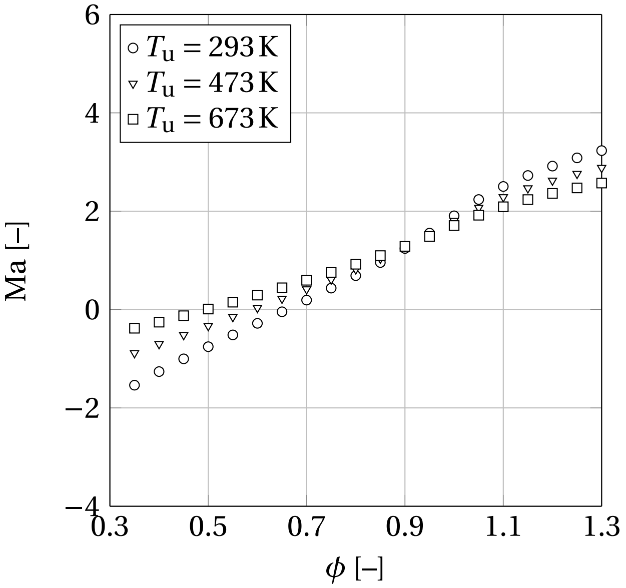

(a) $p = 1\,bar$

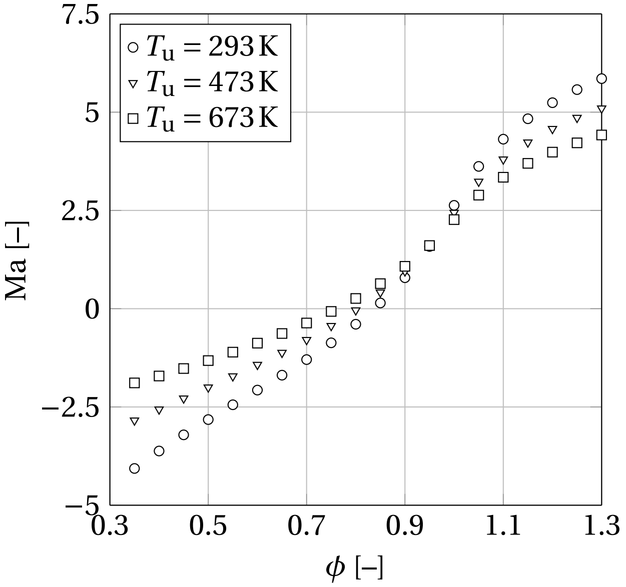

(b) $p = 20\,bar$

Figure 2.31: Markstein numbers of hydrogen-air mixtures at different preheating temperatures.

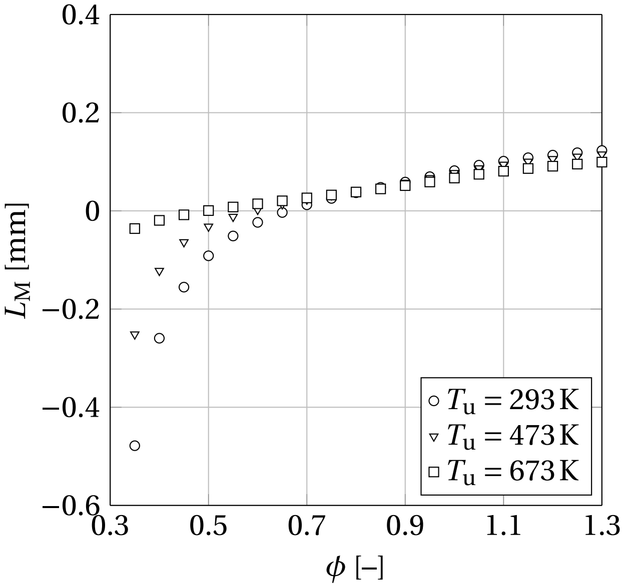

(a) $p = 1\,bar$

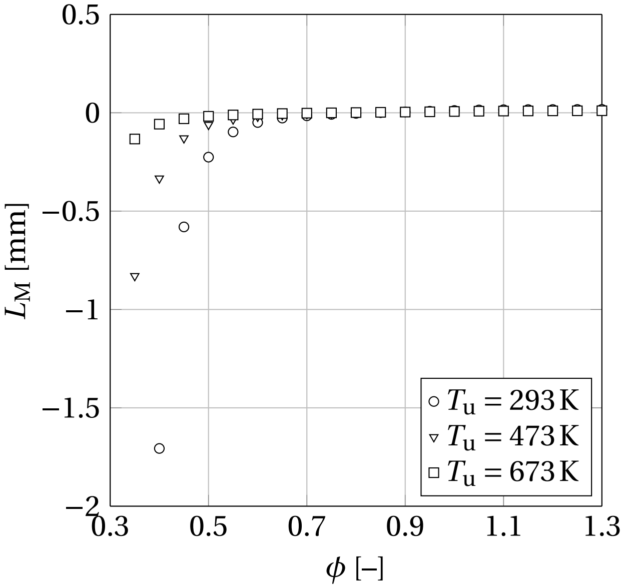

(b) $p = 20\,bar$

Figure 2.32: Markstein lengths of hydrogen-air mixtures at different preheating temperatures.

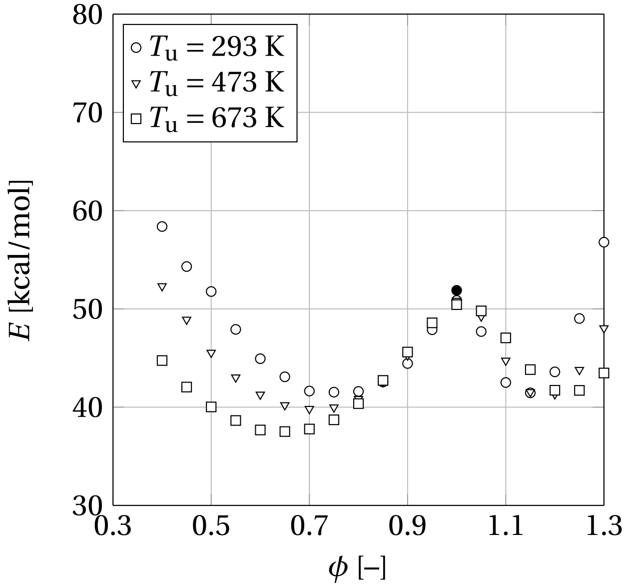

(a) $p = 1\,\text{bar}$

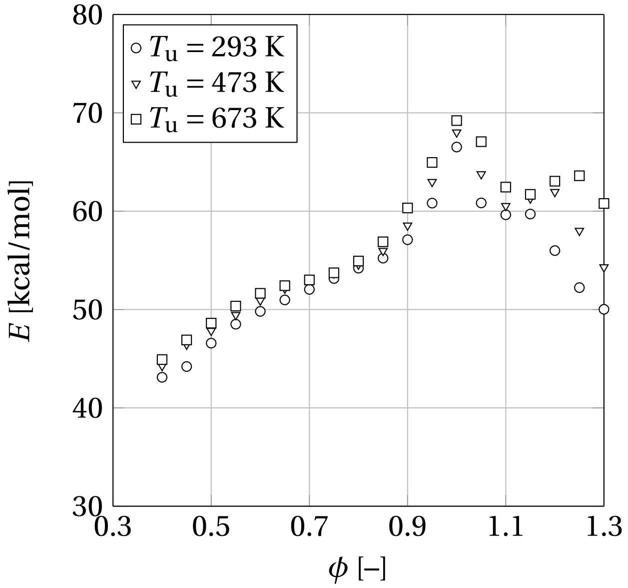

(b) $p = 20\,\text{bar}$

Figure 2.33: Global activation energy of methane-air mixtures at different preheating temperatures. The included filled symbol marks data at $T_u = 293\,\text{K}$ and $\phi = 1$ presented by Egolfopoulos and Law [109].

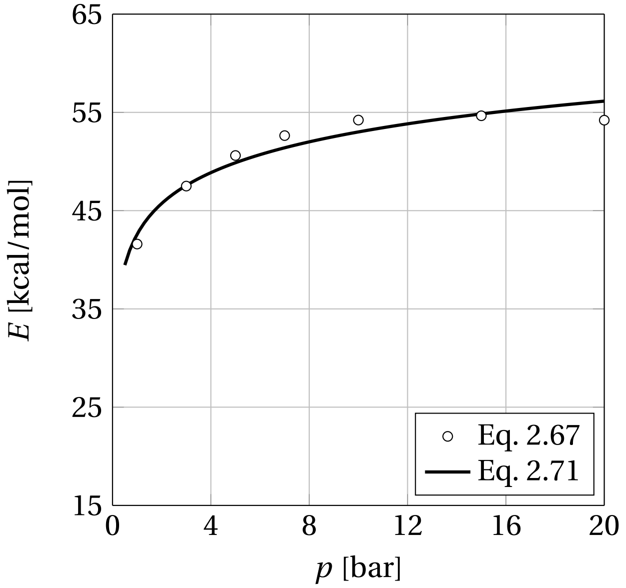

Figure 2.34: Pressure dependence of global activation energy of methane-air mixtures. Values are calculated at $\phi = 0.8$ and $T_u = 293\,K$.

chosen to represent the global activation energy at atmospheric pressure. The variation of E with pressure is depicted in Fig. 2.34. As in the previous paragraph, a logarithmic fit

$$E\,[\mathrm{kcal/mol}] = 4.5224\,\ln(p\,[\mathrm{bar}]) + 42.5960 \tag{2.71}$$

is used to compute the activation energy for varying pressures.

Figure 2.35 shows the Zeldovich numbers computed with Eq. (2.65) corresponding to the global activation energies from Eq. (2.71). The adiabatic flame temperatures are computed with *Cantera 2.2* [67] and the reaction mechanism GRI-Mech 3.0 [69] as described in Sec. 2.3.1.1. The dependence on equivalence ratio, preheating temperature and pressure is comparable to the hydrogen-air mixture case although the pressure influence is lower and the Zeldovich numbers at atmospheric pressure are higher.

In order to calculate the mixture Lewis number (Fig. 2.36), the limiting Lewis numbers of methane and oxygen for methane-air mixtures have to be defined. Due to the lack of literature data, they are set to $\mathrm{Le}_{\mathrm{CH_4}} = 0.75$ and $\mathrm{Le}_{\mathrm{O_2}} = 1.40$ to match the experimentally determined Markstein lengths presented in Fig. 2.37. At ambient temperature and pressure L_M is positive at rich

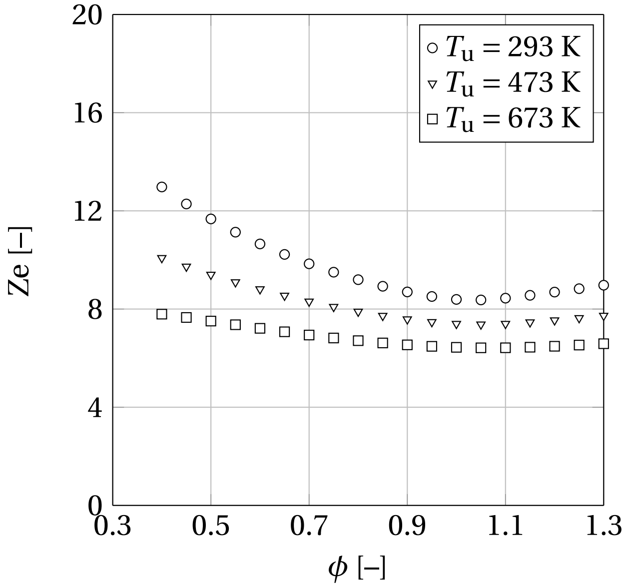

(a) $p = 1\,\text{bar}$

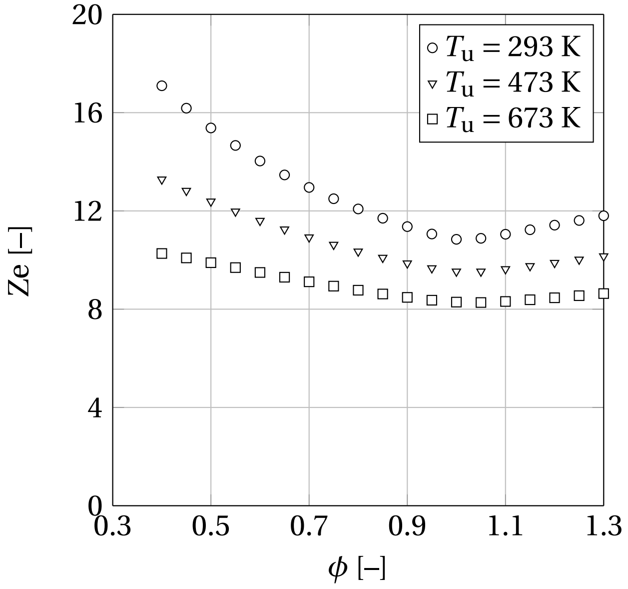

(b) $p = 20\,\text{bar}$

Figure 2.35: Zeldovich number of methane-air mixtures at different preheating temperatures.

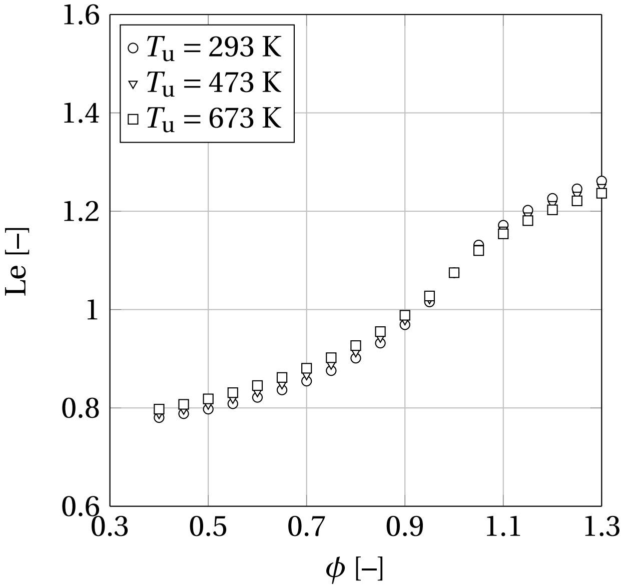

(a) $p = 1\,\text{bar}$

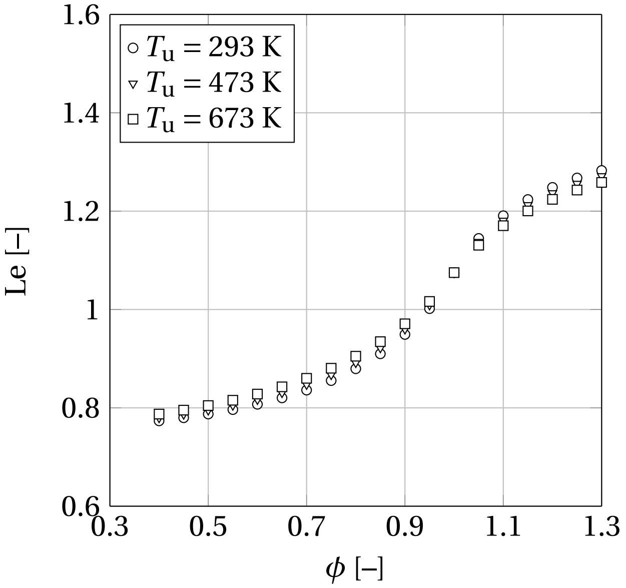

(b) $p = 20\,\text{bar}$

Figure 2.36: Lewis number of methane-air mixtures at different preheating temperatures.

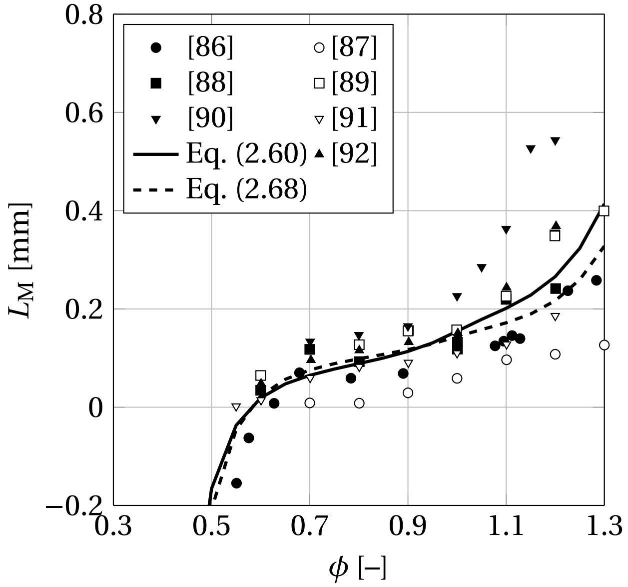

Figure 2.37: Markstein lengths of methane-air mixtures at T_u = 293 K and p = 1 bar. Symbols mark experimental data, lines represent calculated values.

conditions and decreases with decreasing equivalence ratio. At $\phi \approx 0.55$ the Markstein length suddenly drops to negative values as observed in the data of Taylor [86]. Chen [85] comprehensivly explains the large scatter in experimental data with different methods applied by different authors to extract L_M from outwards propagating flame experiments. Fig. 2.37 shows that the two approaches to compute L_M presented in Eq. (2.60) and (2.68) deliver similar results for methane-air mixtures. For consistency with the previous paragraph on hydrogen-air mixtures, Bechtold and Matalon's method [105] (Eq. (2.60)) is chosen to investigate the influence of preheating temperature and pressure.

Figures 2.38 and 2.39 show the resulting Markstein numbers and lengths. Similar to the hydrogen-air mixture case, Ma increases with equivalence ratio. However, its values are positive at most of the investigated equivalence ratios. Negative values are only obtained at lean conditions and low preheating. This means that the laminar burning velocity of methane-air mixtures is predominantly reduced by flame stretch. The effect of pressure on Ma is small.

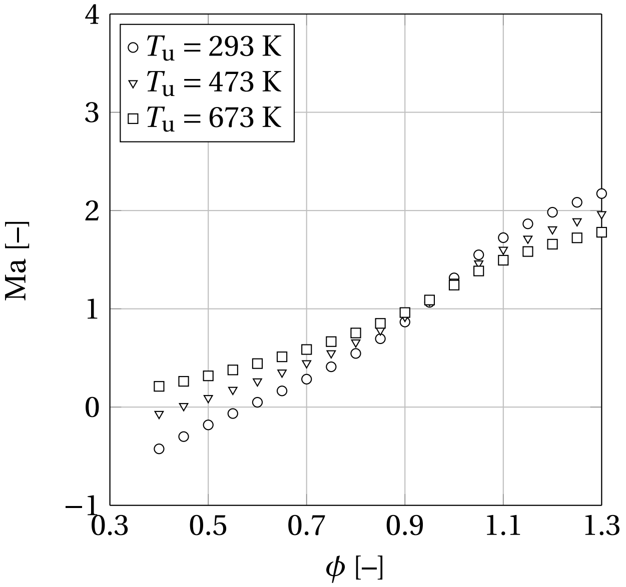

(a) $p = 1\,\text{bar}$

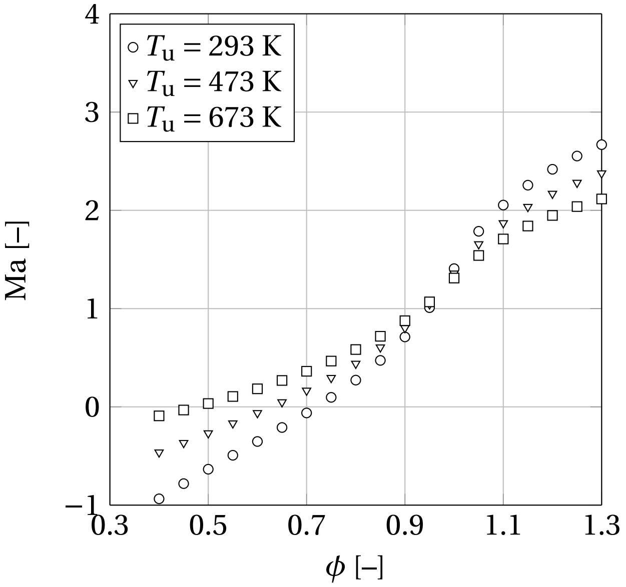

(b) $p = 20\,\text{bar}$

Figure 2.38: Markstein numbers of methane-air mixtures at different preheating temperatures.

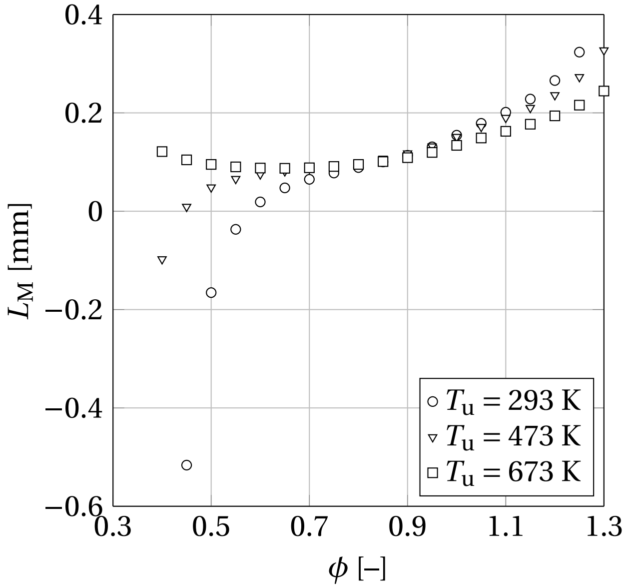

(a) $p = 1$ bar

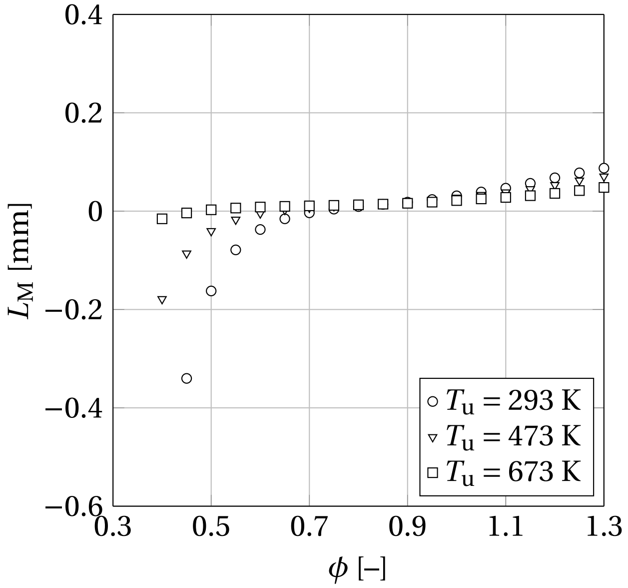

(b) $p = 20$ bar

Figure 2.39: Markstein lengths of methane-air mixtures at different preheating temperatures.

2.3.2.3 Stretched Laminar Burning Velocity

As introduced in the beginning of Sec. 2.3.2 in Eq. (2.48), the stretched laminar burning velocity $S_{\mathrm{l,s}}$ is obtained from the unstretched laminar burning velocity by subtracting the product of Markstein length (Eq. (2.60)) and flame stretch rate (Eq. (2.59)). The effect of flame stretch on the burning velocity of hydrogen-air and methane-air mixtures is illustrated in the following.

Hydrogen-Air Mixtures: Figure 2.40 illustrates the effect of flame stretch on the burning velocity of hydrogen-air mixtures at different preheating temperatures and pressures in a $h = 40\,\mathrm{mm}$ burner. The turbulent velocity fluctuations are held constant at $u' = 5\,\mathrm{m/s}$. As derived in Sec. 2.3.2.2, negative Markstein lengths lead to increasing burning velocities at lean conditions. Positive Markstein lengths cause a burning velocity reduction around stoichiometry and at rich conditions. At constant turbulent velocity fluctuations, the effect of flame stretch is reduced by preheating temperature and increased with pressure leading to a high increase in burning velocity at lean conditions. Although the unstretched burning velocities are lower at low equivalence ratios and 20 bar compared to atmospheric pressure, the corresponding stretched laminar burning velocities are in the same range or even higher. This is an important observation regarding the comparison and prediction of atmospheric and high pressure flashback limits presented in Chap. 6 and App. A.

Methane-Air Mixtures: The influence of flame stretch on laminar burning velocities of methane-air mixtures is shown in Fig. 2.41 for a $h = 40\,\mathrm{mm}$ burner. The turbulent velocity fluctuations are set to $u' = 0.5\,\mathrm{m/s}$ as the burning velocities are generally lower than for hydrogen-air mixtures. Higher turbulence would lead to flame quenching. As indicated in the previous section, flame stretch predominantly reduces the burning velocity of methane-air mixtures. This leads to a stabilizing effect regarding flame front instabilities and reduces the risk of flame flashback as will be discussed in Chap. 6 for laminar flames. The effect increases with equivalence ratio and pressure and decreases with preheating temperature.

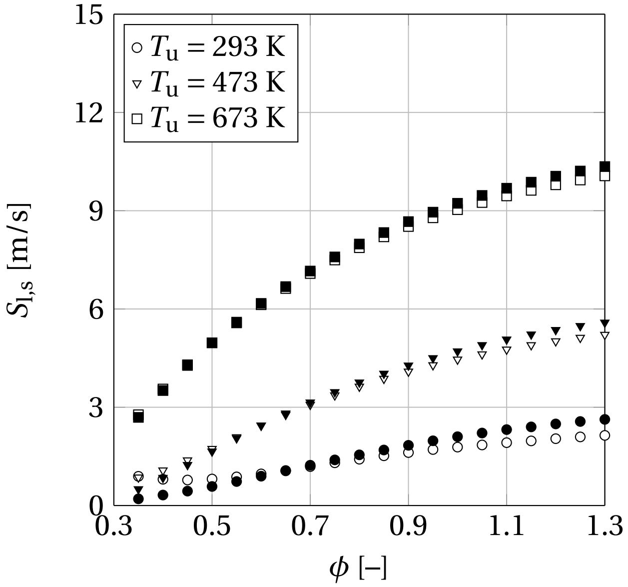

(a) $p = 1\,\text{bar}$

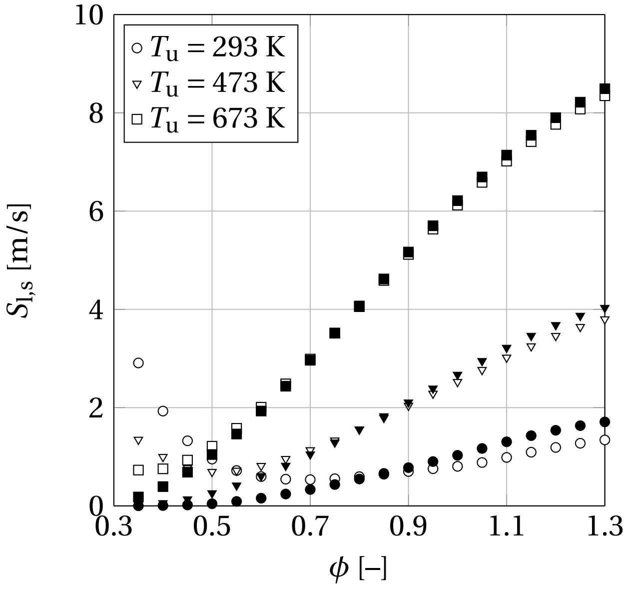

(b) $p = 20\,\text{bar}$

Figure 2.40: Stretched laminar burning velocity of hydrogen-air mixtures at different preheating temperatures (empty symbols) compared to unstretched laminar burning velocity (filled symbols). $u' = 5\,\text{m/s}$, $\Lambda = 0.02\,\text{m}$.

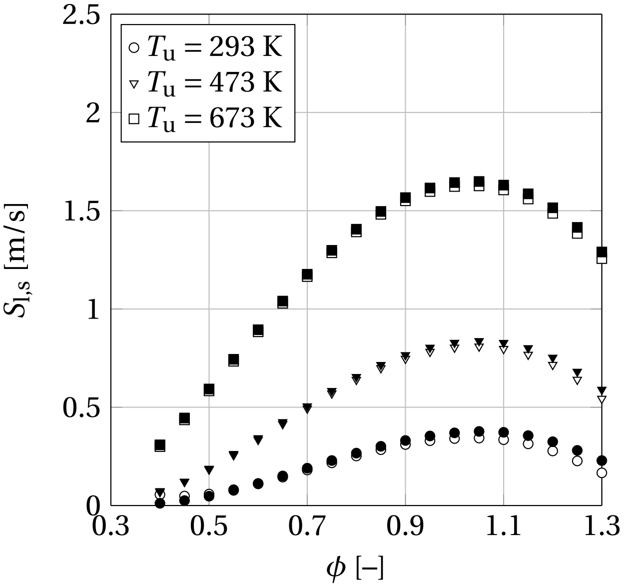

(a) $p = 1\,\mathrm{bar}$

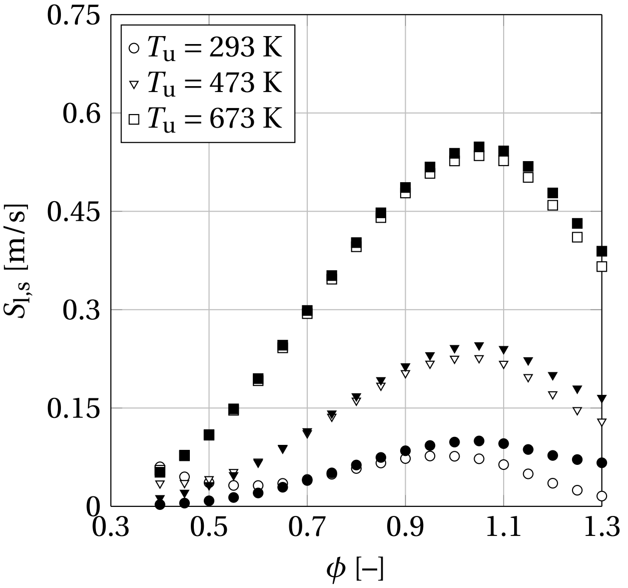

(b) $p = 20\,\mathrm{bar}$

Figure 2.41: Stretched laminar burning velocity of methane-air mixtures at different preheating temperatures (empty symbols) compared to unstretched laminar burning velocity (filled symbols). $u' = 0.5\,\mathrm{m/s}$, $\Lambda = 0.02\,\mathrm{m}$.

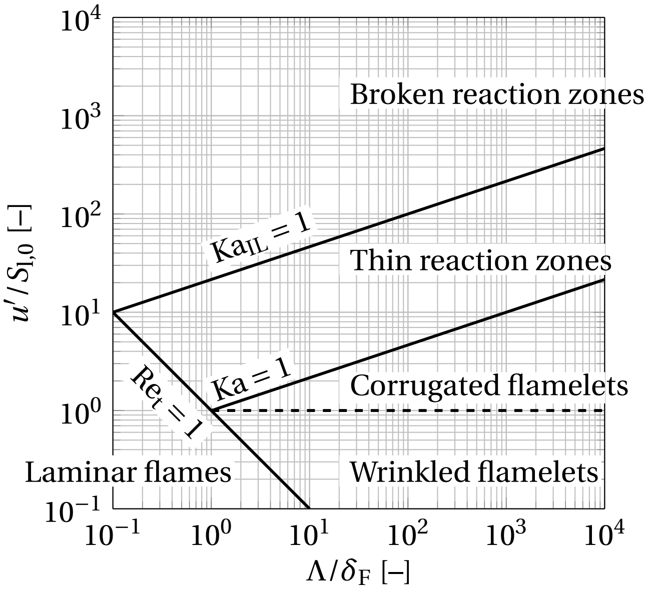

Figure 2.42: Flame regime diagram according to Peters [64].

2.3.3 Turbulent Flames

Turbulent flames can be divided into different flame regimes depending on velocity and length scale ratios as reviewed in the following section in brief. The influence of turbulence on burning velocity will be discussed in relation to the defined flame regimes.

2.3.3.1 Flame Regimes

The interaction between turbulence and combustion is an important factor to define the burning velocity. Depending on the structure of this interaction, i.e. velocity and length scale ratios, different flame regimes can be distinguished as proposed by Borghi [110] and Peters [64, 94, 111]. Figure 2.42 shows the flame regime diagram in terms of velocity ratio $u'/S_{l,0}$ over length scale ratio Λ/δ_F as introduced by Borghi [110] and extended by Peters [64]. Peters defines a turbulent Reynolds number

$$\mathrm{Re}_t = \frac{u'\Lambda}{S_{l,0}\delta_F} \tag{2.72}$$

based on turbulent velocity fluctuations u' and turbulent macro scale Λ assuming a laminar flame thickness of $\delta_\mathrm{F} = \nu / S_{\mathrm{l},0}$ (cf. Eq (2.47)). In the flame regime diagram $\mathrm{Re}_\mathrm{t} = 1$ separates laminar flames ($\mathrm{Re}_\mathrm{t} < 1$) from turbulent flames ($\mathrm{Re}_\mathrm{t} > 1$). As laminar flames have been discussed previously, this section will focus on the turbulent flame regimes with $\mathrm{Re}_\mathrm{t} > 1$.

In order to distinguish turbulent flame regimes, Peters [64] defines two Karlovitz numbers, Ka and Ka_IL. The turbulent Karlovitz number

$$\mathrm{Ka} = \frac{t_\mathrm{F}}{t_\eta} = \frac{\delta_\mathrm{F}^2}{\eta^2} \tag{2.73}$$

represents the ratio of chemical time scale $t_\mathrm{F} = \delta_\mathrm{F} / S_{\mathrm{l},0}$ to the Kolmogorov timescale of the smallest turbulent eddies $t_\eta = (\nu/\epsilon)^{1/2}$. With $\delta_\mathrm{F} = \nu / S_{\mathrm{l},0}$, Ka can be expressed by flame thickness δ_F and Kolmogorov length scale $\eta = (\nu^3/\epsilon)^{1/4}$ (cf. Eq. (2.13)). With $\epsilon = u'^3/\Lambda$ (cf. Eq (2.14)), the Karlovitz number can be rewritten in terms of $u'/S_{\mathrm{l},0}$ and $\Lambda/\delta_\mathrm{F}$:

$$\mathrm{Ka} = \left(\frac{u'}{S_{\mathrm{l},0}}\right)^{\frac{3}{2}} \left(\frac{\Lambda}{\delta_\mathrm{F}}\right)^{-\frac{1}{2}} . \tag{2.74}$$

In the flame regime diagram Ka = 1 separates the flamelet regime from the thin reaction zone regime.

The second Karlovitz number

$$\mathrm{Ka}_\mathrm{IL} = \frac{\delta_\mathrm{IL}^2}{\eta^2} \tag{2.75}$$

is based on the inner layer thickness δ_IL. With Eq. (2.33), it relates to Ka via

$$\mathrm{Ka}_\mathrm{IL} = C_\mathrm{IL}\mathrm{Ka} . \tag{2.76}$$

The line $\mathrm{Ka}_\mathrm{IL} = 1$ separates the thin reaction zone regime from the broken reaction zone regime.

In the wrinkled and corrugated flamelet regime the flame thickness δ_F is smaller than the Kolmogorov scale η. This means that the smallest turbulent eddies do not perturb the flame structure. Transport of reactants into the preheat and reaction zone is only based on molecular diffusion. The wrinkled

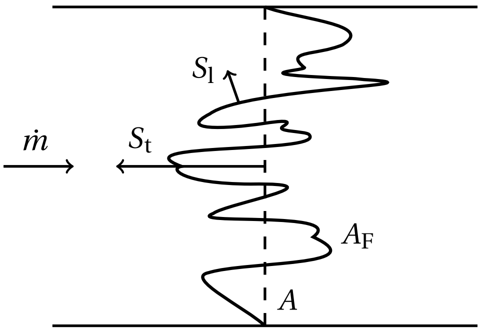

Figure 2.43: Schematic of a premixed turbulent flame in a duct (adapted from [94]).

flamelet regime represents flames with turbulent velocity fluctuations smaller than the laminar burning velocity ($u'/S_{l,0} < 1$).

The thin reaction zone regime is characterized by the idea that the smallest turbulent eddies can penetrate into the flame structure as $\eta < \delta_F$. However, with $\eta > \delta_{IL}$, the eddies are not able to enter the inner layer. The interaction of small eddies with the preheat zone increases scalar mixing and, therefore, the reaction rate and the turbulent burning velocity.

In the broken reaction zone regime turbulent eddies are small enough to penetrate the reaction zone. As cold reactants can be transported into the reaction zone, local quenching of the reaction can occur. This poses an upper limit to the increase of burning velocity due to turbulence.

2.3.3.2 Turbulent Burning Velocity

In literature, numerous concepts and correlations can be found to represent the influence of turbulence on burning velocity. An overview is for example given by Driscoll [112]. In 1940, Damköhler [113] was the first to develop a theoretical expression for the turbulent burning velocity S_t. For a comprehensive summary of Damköhler's approach the reader is referred to Peters [64, 94]. The basic principle of Damköhler's theory is presented in Fig. 2.43. Assuming a turbulent flame at a fixed position in a turbulent flow, the mass flow rate $\dot{m}$

is equal to the mass flow rate consumed by the turbulent flame:

$$\dot{m} = \rho_u S_l A_F = \rho_u S_t A . \tag{2.77}$$

The mass flow rate consumed by the flame can be expressed either with the turbulent burning velocity S_t and the flow's cross-sectional area A (dashed line) or the local laminar burning velocity S_l perpendicular to the flame front and the turbulent flame surface area A_F. Based on Eq. (2.77) the ratio of laminar and turbulent burning velocity

$$\frac{S_t}{S_l} = \frac{A_F}{A} \tag{2.78}$$

is defined by the ratio of flame surface area and flow cross-sectional area. Damköhler [113] identified two flame regimes, the large scale and the small scale turbulence regime which are comparable to the corrugated flamelet and the thin reaction zone regime introduced in the previous section. He developed expressions for the area ratio A_F/A for both cases.

In the large scale turbulence or corrugated flamelet regime, turbulent eddies do not penetrate the flame front. Consequently, the area increase due to combustion is proportional to the ratio of turbulent velocity fluctuations and laminar burning velocity:

$$\frac{A_F}{A} \propto \frac{u'}{S_l} . \tag{2.79}$$

This relation combined with Eq. (2.78) leads to

$$S_t \propto u' . \tag{2.80}$$

If the turbulent eddies are able to perturb the preheat zone in the small scale turbulence or thin reaction zone regime, diffusion of reactants into the preheat zone is increased and the molecular diffusion coefficient D has to be replaced by the turbulent value D_t. According to Damköhler [113], the turbulent burning velocity can be expressed by

$$S_t \propto \left(\frac{D_t}{t_F}\right)^{1/2} \tag{2.81}$$

analogous to

$$S_l \propto \left(\frac{D}{t_F}\right)^{1/2} , \tag{2.82}$$

where the laminar burning velocity is related to molecular diffusion into the preheat zone divided by the chemical timescale at which reactants are consumed by the combustion reaction. From Eq. (2.81) and (2.82) the proportionality

$$\frac{S_\mathrm{t}}{S_\mathrm{l}} \propto \left(\frac{D_\mathrm{t}}{D}\right)^{1/2} \tag{2.83}$$

is derived. With $D \propto S_\mathrm{l}\delta_\mathrm{F}$ and $D_\mathrm{t} \propto u'\Lambda$ the turbulent burning velocity can be related to turbulence properties and laminar flame characteristics:

$$\frac{S_\mathrm{t}}{S_\mathrm{l}} \propto \left(\frac{u'\Lambda}{S_\mathrm{l}\delta_\mathrm{F}}\right)^{1/2} . \tag{2.84}$$

A correlation related to Damköhler's approach has been widely used to represent experimental turbulent burning velocity data [94]:

$$\frac{S_\mathrm{t}}{S_\mathrm{l}} = 1 + C_\mathrm{S}\left(\frac{u'}{S_\mathrm{l}}\right)^{c_3} . \tag{2.85}$$

According to Damköhler [113] the model parameter C_S should depend on the length scale ratio $\Lambda/\delta_\mathrm{F}$ and the exponent c_3 should be set to 0.5. He used the unstretched value $S_{\mathrm{l},0}$ for the laminar burning velocity S_l.

As the conditions analyzed in this work typically lie around the boundary between corrugated flamelet and thin reaction zone regime, Eq. (2.85) will be used in Chap. 5 and 6 to compute turbulent burning velocities. In order to include the effect of flame stretch, the laminar burning velocity S_l will be set to the stretched value $S_{\mathrm{l,s}}$ introduced in Sec. 2.3.2.3.

2.3.4 Wall Quenching

If combustion takes place in the vicinity of a cold wall, the chemical reactions are influenced. A comprehensive summary of the interaction between flame and cold wall is given by Eichler [9], who divides the wall effects in three categories: Heat loss due to the temperature gradient between flame and wall, third body reactions with the wall as inert third body, and surface reactions at chemically non-inert walls. The first two mechanisms lead to lower flame temperatures and reaction rates. Close to the wall the reactions are fully quenched. The distance of full flame quenching is called quenching distance δ_{q} and is proportional to the flame thickness δ_{F}. A dimensionless Péclet number

$$\mathrm{Pe}_{\mathrm{q}} = \frac{\delta_{\mathrm{q}}}{\delta_{\mathrm{F}}} \tag{2.86}$$

can be defined. This parameter depends on the quenching configuration. Typically three generic quenching configurations are distinguished: Parallel plate or tube quenching, head-on quenching and sidewall quenching. For these configurations, quenching distances or Péclet numbers for different fuel-oxidizer mixtures can be found in literature. Boust et al. [114], Sotto et al. [115] and Bellenoue et al. [116] present experimentally determined head-on and sidewall quenching distances for methane-air mixtures at different pressures. At atmospheric pressure they obtain $\delta_{\mathrm{q}} = 0.7\,\mathrm{mm}$ at $\phi = 0.7$ and $\delta_{\mathrm{q}} = 0.3\,\mathrm{mm}$ at $\phi = 1.0$. Together with the laminar flame thickness $\delta_{\mathrm{F}} \approx 0.118\,\mathrm{mm}$ shown in Sec. 2.3.1.3, a quenching Péclet number of $\mathrm{Pe}_{\mathrm{q}} \approx 2.5$ is obtained at stoichiometry. As Pe_{q} has only a weak dependence on mixture composition, this value remains approximately constant for all equivalence ratios.

Experimental data for sidewall quenching distances of hydrogen-air mixtures are presented by Enomoto [117] at atmospheric pressure and $\phi = 0.6$. Unfortunately, his measurement accuracy only allowed a qualitative discussion. Gruber et al. [30] found a hydrogen-air mixture quenching Péclet number of $\mathrm{Pe}_{\mathrm{q}} = 1.4$ in their DNS study. They state that this value is in good agreement with the head-on quenching Péclet number of $\mathrm{Pe}_{\mathrm{q}} = 1.7$ given by Dabireau et al. [118].

Apart from the quenching distance, Gruber et al. [30] also investigated the behavior of the laminar burning velocity close to the burner wall. Their result is summarized in Fig. 2.44. Approaching the burner wall, the burning velocity is slowly reduced until a steep decrease starts at $y^+ = 9$. Between $y^+ = 9$ and the quenching distance at $y^+ \approx 3$ the burning velocity drops from 83 % to 52 % of the laminar burning velocity. As this phenomenon is observed very close to the laminar region of the turbulent boundary layer, it is assumed that it is similar for laminar boundary layers. The wall distance corresponding to $y^+ \approx 3$ can be seen as quenching distance. This means that, based on the observations of Gruber et al. [30], the wall distance at the beginning of the steep

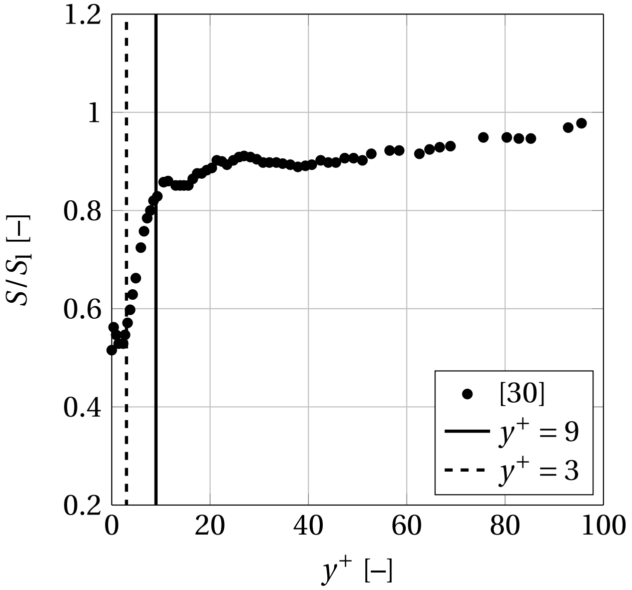

Figure 2.44: Burning velocity close to the burner wall (adapted from [30]).

burning velocity drop is estimated to $3\delta_\mathrm{q}$. In Sec. 6.1 it will be assumed that flashback in laminar boundary layers is initiated at this location as it is the position closest to the burner wall where burning velocities are still sufficiently high. It will be shown in Sec. 6.1 that this assumption satisfactorily reproduces laminar boundary layer flashback limits of hydrogen-air as well as methane-air flames.

3 Experiment

In this chapter, the experimental setup and the procedure of the flashback tests as well as the applied measurement techniques are introduced.

3.1 Experimental Setup

The experimental setup used in this work is very similar to those described by Eichler [9] and Baumgartner [10]. The laboratory infrastructure was designed by Eichler [9] who investigated boundary layer flashback of confined flames. In his setup a flame was stabilized inside a rectangular burner duct connected to a combustion chamber and an exhaust duct. The rectangular design was chosen to be able to apply laser diagnostics in the quasi two-dimensional center plane. A key feature of Eichler's burner design was the injection of pure air into the corners of the rectangular burner to prevent flashback inside the thick corner boundary layers. Building on Eichler's work, Baumgartner developed a burner configuration to analyze boundary layer flashback of unconfined flames. He removed the combustion chamber and designed a rectangular channel burner ($158 \times 17.5\,\mathrm{mm}^2$) with a hydraulic diameter of $d_\mathrm{h} = 31.5\,\mathrm{mm}$. Downstream of this burner, a triangular shaped flame was stabilized in the open environment. Details of Baumgartner's burner including pilot burners and ignitor can be found in [10]. The corner injection remained unchanged. Its details are described in [9].

In this work, Baumgartner's setup was modified in the following aspects: The optical accessibility through the three quartz glass windows (two side windows and one top window) was positioned closer to the burner exit to enhance the quality of OH* chemiluminescence imaging of the flashback process from the top view. Furthermore, the air cooling system of the burner exit region was

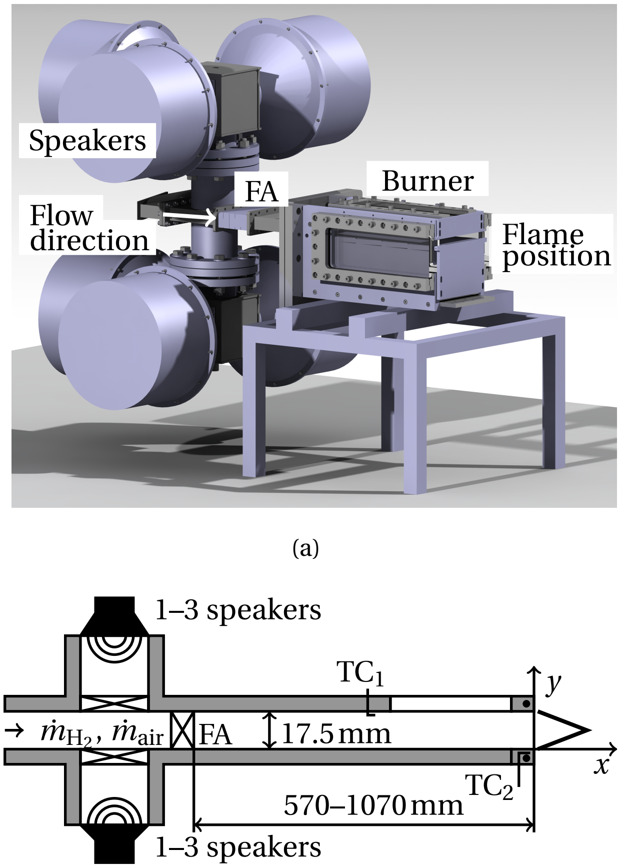

(a)

(b)

Figure 3.1: Flashback test rig with acoustic excitation unit [119].

replaced by a water cooling system to achieve lower burner rim temperatures, especially at high flame temperature conditions. Finally, an acoustic excitation unit was inserted upstream of a flow straightening device designed by Eichler [9]. Details of the acoustic design of the excitation unit can be found in B.2. The flow straightening device was replaced by one that additionally functions as flame arrestor to protect the acoustic excitation section from the upstream propagating flame.

Figure 3.1(a) shows the final experimental setup. Details of the main components of the test rig can be found in App. B.1. A simplified sketch is depicted in Fig. 3.1(b). A hydrogen-air mixture passes the acoustic excitation section with two to six symmetrically installed speakers before entering the burner duct through the flame arrestor (FA). Two pieces of relatively coarse metal foam prevent the formation of large scale vortices at the connection between the rectangular main flow channel and the two forcing tubes. In the flashback test different configurations are analyzed. For that purpose two different speaker types are connected to the test rig: Type 1 (T1) delivers high sound pressures between 50 and 220 Hz. Type 2 (T2) has a broader frequency range of high sound pressure of 50–1000 Hz. The flame arrestor consists of two fine wire meshes surrounding a metal foam with small pore sizes required to reliably stop the upstream flame propagation in hydrogen-air mixtures. The flame arrestor induces a significant pressure loss which limits the excitation amplitudes. In order to achieve sufficiently high velocity oscillation amplitudes at the burner exit, the speakers have to be operated at a natural frequency of the test rig's flow system. The natural frequencies can be varied by changing the length of the burner duct. Details of the acoustic design of the test rig are presented in App. B.2.

Sinusoidal acoustic velocity oscillations

$$\overline{U}'(t) = \widehat{\overline{U}} \sin(2\pi f t) \tag{3.1}$$

are investigated at different amplitudes $\widehat{\overline{U}}$ and frequencies f. The open flame configuration without combustion chamber is beneficial in this acoustic study as there is no coupling between acoustic excitation, flame and the acoustic modes of a combustion chamber. This means that the flow can be modulated at defined excitation frequencies and amplitudes. The excitation amplitude is varied in the flashback experiments by changing the speaker power.

In this work, different experiments are performed. First, flashback limits are measured without acoustic forcing in order to ensure that the acoustic excitation section does not influence the unexcited flashback limits. After that, flashback limits are determined for different excitation amplitudes and frequencies typical for intermediate frequency dynamics of gas turbine combustors. In all flashback tests, OH* chemiluminescence imaging is used to monitor the lateral position and the characteristics of the flashback process. After the flashback experiments, the excitation amplitude is determined with Constant Temperature Anemometry (CTA) in the non-reacting flow. Apart from that, Particle Image Velocimetry (PIV) of the stable flame at near flashback conditions without excitation is performed to generate validation data for the turbulence distribution and the flame angle required in the prediction model described in Sec. 6.2. The experimental procedure of the flashback tests and the different measurement techniques are introduced in the following sections.

3.2 Experimental Procedure

Each flashback experiment starts with the ignition procedure. Pure air flows through the test rig at a low mass flow rate of around 3 g/s. After the ignitor electrode at the lower pilot burner is switched on, the flow of pure hydrogen through the upper and lower pilot burner downstream of the burner exit is enabled. Diffusion flames stabilize at the pilot burners.

In order to ignite the main flame, the main air mass flow rate $\dot{m}_{\mathrm{air}}$ is increased and set to a value between 18 and 60 g/s which is held constant during the whole flashback test. The main hydrogen mass flow rate $\dot{m}_{\mathrm{H_2}}$ is then increased until a stable flame is established at $\phi = 0.33$. At this point, the pilot burners are switched off and the acoustic forcing is set to the desired frequency and amplitude. During the following flashback test, the fuel mass flow rate $\dot{m}_{\mathrm{H_2}}$ is slowly increased until flashback occurs. The corresponding equivalence ratio is defined as flashback limit for the total mass flow rate $\dot{m}_{\mathrm{mix,FB}} = \dot{m}_{\mathrm{air}} + \dot{m}_{\mathrm{H_2}}$ which can be transformed to the flashback limit $\overline{U}_{\mathrm{FB}}$.

Flashback is detected with the type K thermocouple TC_1 (cf. Fig. 3.1(b)) leading to automatic shutdown of the fuel supply and increase of the air mass flow rate to the maximum value of $\dot{m}_{\mathrm{air}} = 120$ g/s. The second thermocouple TC_2 monitors the burner exit temperature T_{B} to ensure that the water cooling system is operating properly.

3.3 Measurement Techniques

Apart from temperature measurements using thermocouples, Constant Temperature Anemometry, Particle Image Velocimetry and OH* chemilumines-

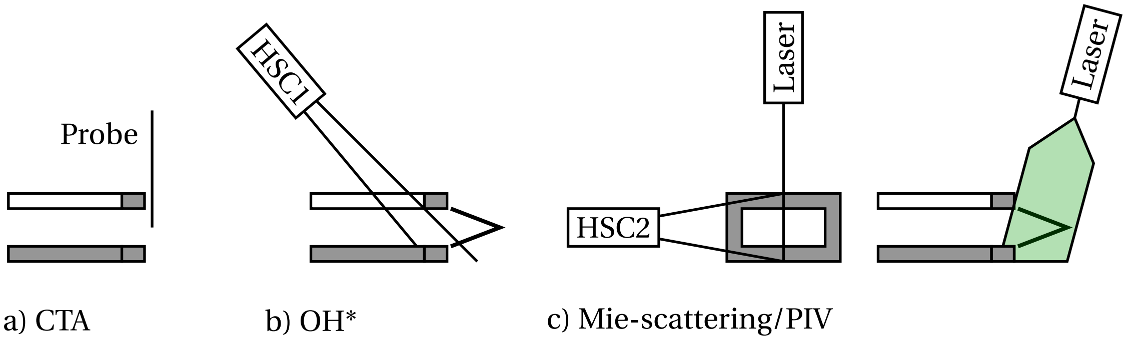

Figure 3.2: Measurement setups (adapted from [119] and [120]).

cence are applied in this work. These techniques are shortly introduced in the following sections. Figure 3.2 illustrates their integration into the test rig.

3.3.1 Constant Temperature Anemometry

Constant Temperature Anemometry (CTA) is an intrusive technique to measure flow velocity. For a detailed discussion of this technique the reader is referred to [121–123]. In this work, a hot wire probe made of a thin gold coated tungsten wire ($d = 0.005\,\mathrm{mm}$) is positioned at the burner exit. In order to measure the velocity component in x-direction, the wire is oriented perpendicular to the main flow. During the experiment the hot wire probe is connected to the Anemometer AN-1003 which applies a voltage to the wire. Due to its ohmic resistance the thin wire heats up. Since different flow velocities correspond to different degrees of convective cooling, the wire's temperature and resistance are changed. To keep temperature and resistance constant, the anemometer has to adjust the applied voltage. This control circuit usually consists of a Wheatstone bridge. In order to relate voltage and flow velocity, a probe calibration is required. Here, the probe is calibrated for velocities of 0–34 m/s by deriving a third order polynomial for the flow velocity depending on anemometer voltage. The measurement accuracy and the sensitivity of the CTA probe depend on the temperature difference between wire and fluid which is limited by the temperature stability of the wire material.

In this work, CTA is applied to determine the amplitude of the velocity oscillations at the burner exit. From the results, the natural frequencies of the flow system are identified. For that purpose, the hot wire probe is positioned at the center of the burner exit as indicated in Fig. 3.2. Before flashback tests are conducted, the velocity oscillation amplitudes at the burner exit are measured for frequencies of 50–1000 Hz. The result is the frequency dependent normalized velocity oscillation amplitude

$$\Omega(f) = \frac{\widehat{\overline{U}}(f)}{\overline{U}} . \tag{3.2}$$

The local maxima found in $\Omega(f)$ represent the natural frequencies of the test rig's flow system. They slightly vary with the time averaged bulk flow velocity $\overline{U}$. In order to define the frequencies for the flashback tests, the natural frequencies are evaluated at a representative air mass flow rate. These frequencies are then used as forcing frequencies for all operating conditions.

After the flashback experiments, CTA is used to determine the velocity oscillation amplitude Ω at the obtained flashback conditions. For that purpose, the speaker power is set to the same value as in the corresponding flashback test. As the CTA probe can only be inserted into the test rig if no flame is present, isothermal tests are conducted with pure air. The air mass flow rate

$$\dot{m}_{\text{air, CTA}} = \frac{\rho_{\text{air}}}{\rho_{\text{mix,FB}}} \dot{m}_{\text{mix,FB}} \tag{3.3}$$

is adapted such that the same bulk flow velocity $\overline{U}_{\text{FB}}$ as in the flashback tests is achieved. It is assumed that the obtained normalized velocity oscillations Ω are comparable to those in the flashback experiments as, due to the open flame configuration, the flame should not significantly influence the upstream flow [10].

3.3.2 OH* Chemiluminescence

Imaging of the chemiluminescence of the chemically excited hydroxyl radical OH* is a standard technique in combustion research to monitor combustion processes. A recent detailed study on flame radiation has been performed by Fiala [124] who gives a comprehensive summary of the basic principles of OH* chemiluminescence. For further background the reader is referred to [125].

If the intermediate species OH, which is formed in the flame front, is electronically excited to the radical OH* during the combustion reaction, it quickly returns to its electronic ground state under the emission of light at a characteristic wavelength band in the ultraviolet (UV) region. The maximum intensity is found at 306.4 nm [124]. This radiation is a marker for the flame position and can be detected with an image intensified camera equipped with a UV optics. In order to remove background noise, the UV optics is typically combined with an optical band pass filter for wavelengths around the maximum intensity.

In this study, a Photron Fastcam-ultima APX-I^2 high speed camera (HSC1) is operated at a repetition rate of 3 kHz and a resolution of 512 × 1024 pixels to capture the top view of the flashback process as indicated in Fig. 3.2. It is combined with a 105 mm UV optics and a 307 ± 5 nm band pass filter. The camera is inclined to monitor the lower burner wall edge through the upper quartz glass window. If flame flashback is initiated at the lower burner wall, the flashback process can be captured without interference of the flame flank at the upper burner wall. Two examples of captured OH* images at flashback are shown in Fig. 3.3. The solid white line marks the boundary between quartz glass and metal at the upper burner wall which limits the field of view. The dashed white line represents the edge of the lower burner wall. This means that during stable burner operation an OH* signal is detected only between these two white lines. At flashback, the flame starts to propagate upstream leading to an OH* signal to the left of the dashed white line. The obtained images are mainly used in this study to analyze the effect of different excitation amplitudes on the flashback process as discussed in Chap. 4.

Furthermore, flashback along the upper and lower wall can be distinguished with the help of the OH* images as shown in Fig. 3.3 and already discussed in [120]. Figures 3.3(a) and 3.3(b) depict typical upper and lower wall flashbacks at $\phi = 0.65$. The flame shape of the lower wall flashback is characterized by horizontally orientated structures as already observed experimentally by Eichler and Sattelmayer [36] and numerically by Gruber et al. [31]. During upper wall flashback the flame is recorded from its near wall side. The observed bulging structures can also be noticed in the DNS results of Gruber et al. [31].

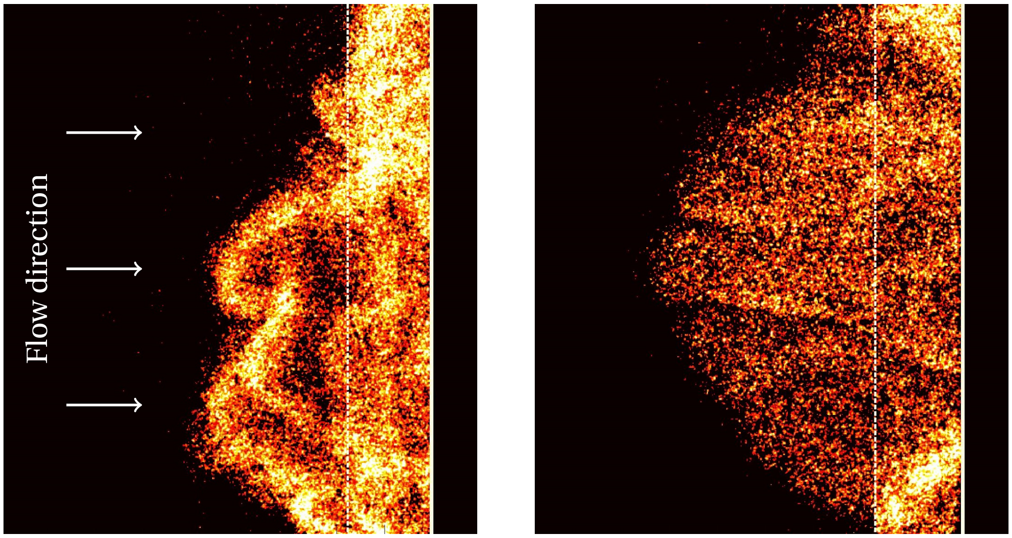

(a) Upper wall flashback (b) Lower wall flashback

Figure 3.3: Examples for OH* chemiluminescence images of upper and lower wall flashback. Solid white line: field of view limitation at upper burner wall, dashed white line: edge of lower burner wall.

3.3.3 Mie-scattering and Particle Image Velocimetry

Mie-scattering is an elastic scattering process on particles which are large compared to the wavelength of the scattered light. Elastic means that there is no permanent exchange of energy between light and particle. Consequently, the wavelength of the scattered light remains unchanged [126].

In combustion research, Mie-scattering on particles which are added to the fuel-oxidizer mixture can be used to visualize the position and shape of the flame front. As the gas density abruptly decreases at the flame front due to the combustion-induced gas expansion, the density of seeding particles in the post flame gases is reduced. This corresponds to a reduction of Mie-scattering intensity. Consequently, bright regions in Mie-scattering images represent unburned mixture whereas dark regions correspond to combustion products. The boundary between bright and dark regions can be detected and defined as flame front.

In this work, a pulsed Nd:YLF laser at 527 nm and a repetition rate of 3 kHz

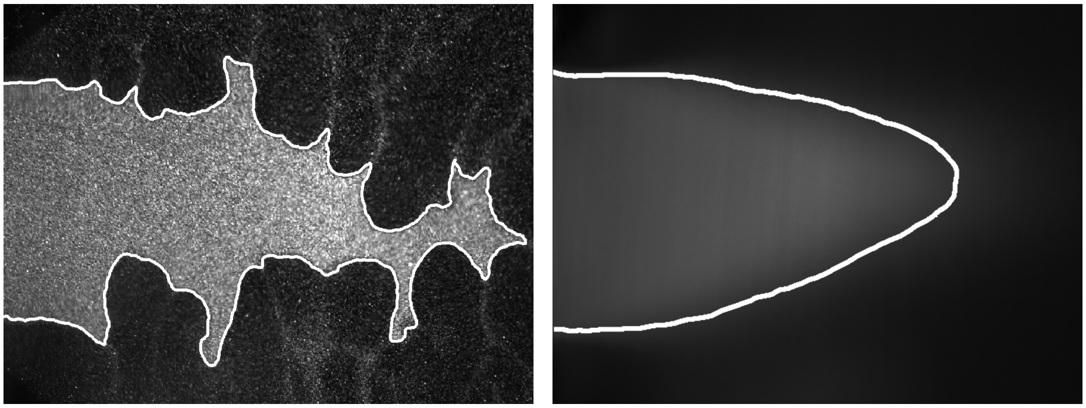
(a) Instantaneous
(b) Time-averaged

Figure 3.4: Examples for Mie-scattering images of a premixed hydrogen-air flame at $\phi = 0.71$. White line represents detected flame front.

is used to illuminate TiO_2 seeding particles in the burner center plane. The laser beam is extended to a light sheet as indicated in Fig. 3.2 using a convex spherical lens and a plano-concave cylindrical lens. The scattered light is captured with a Photron Fastcam SA5 high speed camera (HSC2) with a resolution of 1024 × 1024 pixels. A 527 ± 1 nm band pass filter is combined with a 180 mm optics to reduce background noise. An example for the obtained Mie-scattering images with detected flame front is presented in Fig. 3.4(a). The flame front is identified by edge detection in the binarized image and is included in Fig. 3.4(a) as a solid white line. If the captured instantaneous Mie-scattering images are averaged, the time-averaged flame shape is obtained (Fig. 3.4(b)). From the time-averaged flame front the averaged flame angle can be defined as introduced in [35]. The obtained flame angles are used for model validation in Sec. 6.2.5.

If two Mie-scattering images are captured with a short time difference Δt, the displacements of the particles Δx and Δy in x- and y-direction can be identified to calculate the particle velocity field. Under the assumption that the particles are small enough to perfectly follow the fluid flow, the particle velocity is equal to the fluid velocity and is determined via

$$\vec{v}(x,y,t) = \frac{1}{\Delta t}\begin{pmatrix} \Delta x(x,y,t) \\ \Delta y(x,y,t) \end{pmatrix}. \tag{3.4}$$

This method is called Particle Image Velocimetry (PIV) and is widely used to measure the velocity fields in liquid or gaseous fluid flows. For a detailed description of this method and the post processing algorithm the reader is referred to Merzkirch's Chap. 16 of [126]. In order to calculate the velocity field, the Mie-scattering image pairs are subdivided into small interrogation areas. At the position of each area one velocity value is determined. As the interrogation areas have a minimum size, some overlap can be designed to increase the resolution of the obtained velocity field. The averaged displacement of the particles is calculated using the autocorrelation of the gray values of all pixels forming the interrogation area.

Here, PIV measurements are performed with the same setup as in the Mie-scattering imaging. Each cavity of the pulsed two-cavity Nd:YLF laser is operated at 3 kHz. This means that the high speed camera (HSC2) has to be operated at 6 kHz to capture each laser pulse on a separate frame. A synchronization scheme for the camera and the two laser cavities is presented in [120]. A time difference $\Delta t = 20\,\mu$s between the laser pulses is chosen for the velocity range investigated in this work. The open-source tool PIVlab 1.4 [127, 128] is used for post processing. The spatial resolution is set to 0.5 mm in x- and y-direction. The computed velocity fields $\vec{v}(x, y, t)$ can be converted into time averaged velocity or turbulence intensity as described in Sec. 2.2. The turbulence intensity information is used for model validation in Sec. 6.2.5.

4 Influence of Acoustic Oscillations on Boundary Layer Flashback

In this chapter, the CTA results are used to determine the excitation configurations for the flashback experiments. Afterwards, the flashback limits of the current setup are compared to literature data to ensure that the acoustic forcing section does not influence the burner's stability. Finally, flashback limits are presented for different excitation amplitudes and frequencies in combination with OH* images of the flashback process. In the discussion of the influence of both parameters, two flashback regimes are identified.

4.1 Excitation Configurations

Figure 4.1 shows two examples for normalized velocity oscillation amplitude curves resulting from the CTA measurements. The two curves originate from the configuration with 2 and 6 installed speakers of type 2 (2T2, 6T2). At each frequency 190 excitation periods are averaged to obtain the oscillation amplitude. Maximum velocity oscillation amplitudes are found around 115 Hz for configuration 2T2 and around 135 Hz for configuration 6T2. It can be seen that installing and activating four additional speakers only slightly increases the achieved maximum oscillation amplitude but changes the natural frequency due to the change in geometry. Additional local maxima with sufficient oscillation amplitudes are observed at 330 Hz for 2T2 and 350 Hz for 6T2. Above 400 Hz, further local maxima are found, but the oscillation amplitude with speaker type 2 is not high enough to perform meaningful flashback tests. With speaker type 1 only the maximum at 135 Hz delivers sufficient velocity amplitudes to perform flashback experiments. By inserting an additional channel segment downstream of the flame arrestor, the natural frequency can be

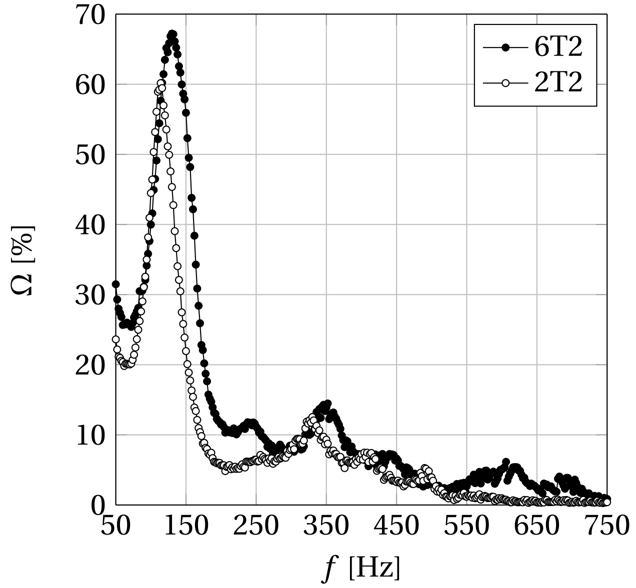

Figure 4.1: Normalized velocity oscillation amplitudes at the burner exit averaged over 190 excitation periods for varying excitation frequencies. 2T2 and 6T2 represent configurations with 2 and 6 speakers of type 2. [119]

changed from 135 to 120 Hz. The natural frequencies depend only slightly on flow velocity. Consequently, all flashback tests for one configuration can be performed at a constant excitation frequency.

The resulting configurations analyzed in the flashback experiments are summarized in Tab. 4.1. First, a reference case (RC) is studied to ensure that the speaker section and an inserted channel segment upstream of the burner do not influence the flashback limits. The obtained flashback data are compared to existing data in the following section. Apart from this reference case, eight different excitation configurations are investigated. The configuration names consist of the number of active speakers (2 or 6) followed by the speaker type (T1 or T2) and the excitation frequency in Hz. The eight configurations are analyzed in flashback tests at varying excitation amplitudes. The maximum analyzed excitation amplitude is $\Omega = 36\,\%$. Although, higher excitation amplitudes up to $A = 68\,\%$ can be achieved with the current design, no meaningful flashback limits can be determined because flashback always occurs in the channel corners due to limitations in the efficiency of the corner injection.

Table 4.1: Excitation configurations.

Configuration	Active/installed speakers	Speaker type	f [Hz]	Ω [%]
RC	0/6	T1	0	0
2T1-135	2/6	T1	135	0–9
6T1-135	6/6	T1	135	7–15
2T1-120	2/6	T1	120	0–9
6T1-120	6/6	T1	120	9–24
2T2-115	2/2	T2	115	0–28
2T2-330	2/2	T2	330	0–15
6T2-135	6/6	T2	135	28–36
6T2-350	6/6	T2	350	0–19

4.2 Flashback Limits Without Excitation

In order to ensure that the inserted excitation unit and the inserted channel segment do not influence the unexcited flashback limits, the measured flashback curve is compared to previous data as shown in Fig. 4.2. The previous data set obtained at the same test rig without the speaker section and additional channel segment was published in [120], where it was compared to flashback data from Kithrin et al. [21] and Baumgartner et al. [34]. It was found that the present configuration delivers flashback limits which are in line with literature data for channel as well as tube burners. Figure 4.2 shows that the addition of the excitation section does not change the burner's flashback limits. Therefore, the present setup can be used to study the effect of velocity oscillations on flashback resistance. The obtained flashback limits are presented in the following section.

4.3 Flashback Limits With Excitation

Figures 4.3–4.6 depict the flashback limits in terms of bulk flow velocity at flashback $\overline{U}_{\mathrm{FB}}$ for the eight excitation configurations introduced in Tab. 4.1. They are compared to the reference case (RC) representing the flashback limits without excitation. The data points are colored according to the normalized

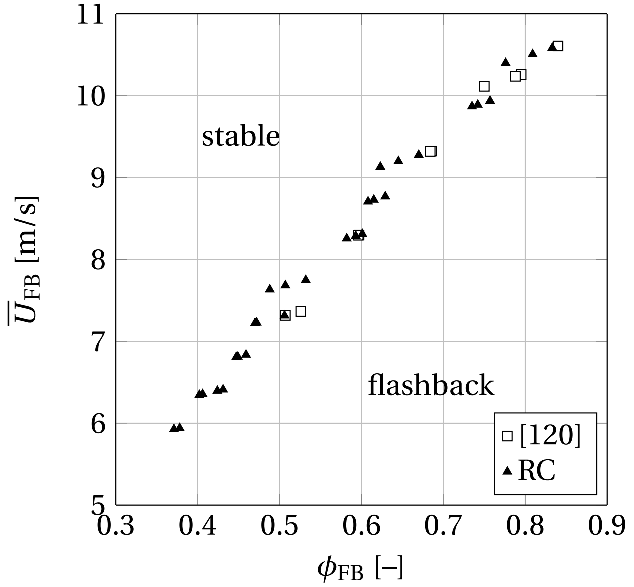

Figure 4.2: Flashback limits of hydrogen-air flames with the reference configurations RC compared to test rig data without speaker section [120].

acoustic velocity oscillation amplitude Ω. During a set of experiments, the air mass flow rate is held constant while the excitation amplitude is increased with the speaker power. This leads to linear data sets which correspond to one constant air mass flow rate and start at the flashback limit of the unexcited burner. With increasing excitation amplitude flashback is initiated at leaner conditions. This reduces the total mass flow rate and increases the mixture density. Both leads to a reduction of $\overline{U}_{\mathrm{FB}}$. For air mass flow rates which are above the flashback limits for all equivalence ratios, only high excitation amplitudes lead to flashback. For these cases, the data sets do not start at the curve of unexcited flashback limits (cf. Fig. 4.6).

Figure 4.3 shows the results for the 135 Hz configuration with two operated speakers of type 1 (2T1-135). Focusing on a constant equivalence ratio, acoustic velocity oscillations cause a significant shift of the flashback limits to higher velocities. At $\phi = 0.4$ the relative increase of $\overline{U}_{\mathrm{FB}}$ reaches up to 26 % for oscillation amplitudes of $\Omega = 5\,\%$ and up to 42 % for $\Omega = 9\,\%$. Increasing the equivalence ratio to $\phi = 0.55$ reduces $\Delta\overline{U}_{\mathrm{FB}}$ at $\Omega = 5\,\%$ to 20 %. At $\phi = 0.7$ an amplitude of $\Omega = 4\,\%$ leads to an increase in $\overline{U}_{\mathrm{FB}}$ of 9 %. The higher influence of velocity

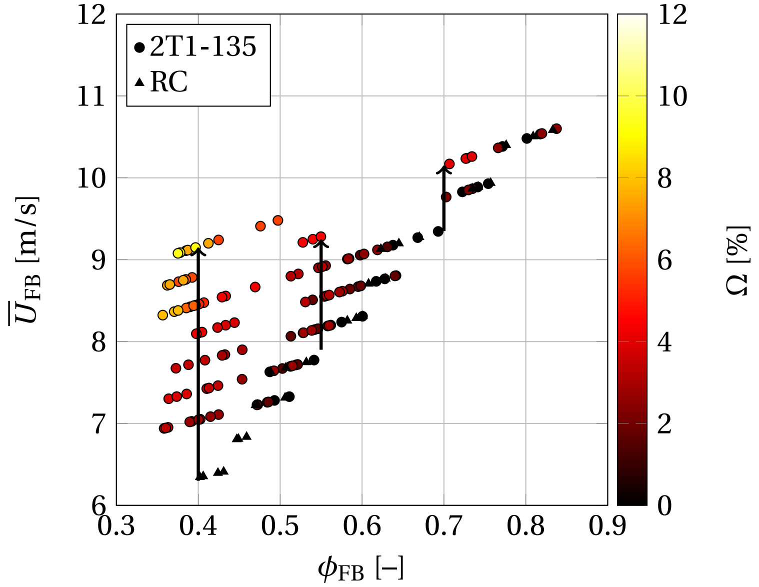

Figure 4.3: Flashback limits of configuration 2T1-135 for varying excitation amplitudes in comparison to reference case RC. [119]

oscillations at low equivalence ratios seems to be caused by the high influence of flame stretch at these conditions. If the acoustic oscillations increase the flame stretch rate, the high absolute values of Markstein length at low equivalence ratios lead to a strong increase of burning velocity. Consequently, the flame is more susceptible to flame flashback.

The flashback limits from configurations 2T1-120 and 2T2-115 presented in Fig. 4.4 indicate a behavior similar to 2T1-135 since the excitation frequencies are in the same range. The effect of higher frequencies is depicted in Fig. 4.5. Here, an excitation amplitude of $\Omega = 15\,\%$ is required at $\phi = 0.4$ to increase $\overline{U}_{FB}$ by about 11 %. At $\phi = 0.55$ a velocity amplitude of $\Omega = 12\,\%$ has the same effect on the flashback limit. The observation that lower oscillation amplitudes have a stronger effect on $\overline{U}_{FB}$ at 135 Hz compared to 350 Hz shows that the influence of velocity oscillations on the flashback limits decreases with frequency. This behavior will be analyzed in more detail in Sec. 4.3.1.

The flashback limits resulting from high excitation amplitudes are depicted in Fig. 4.6 based on configurations 6T1-135, 6T1-120 and 6T2-135. The flashback limits without excitation are shown for reference. For the configuration 6T1-

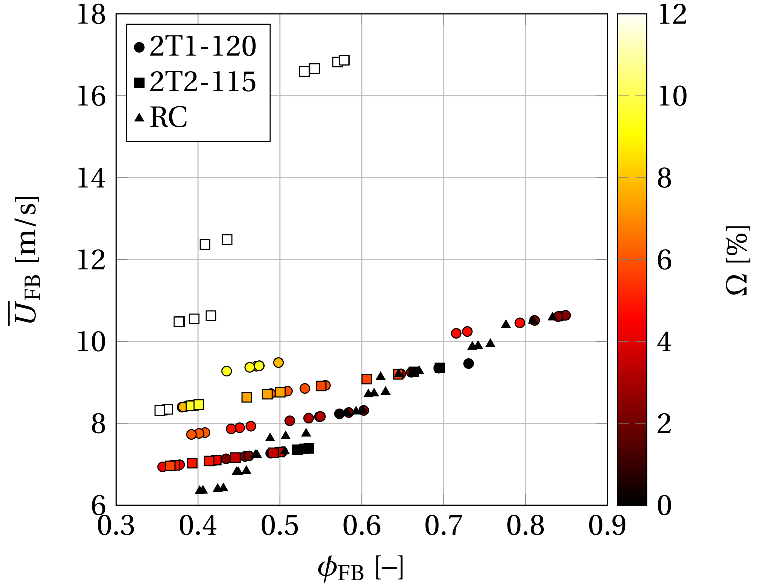

Figure 4.4: Flashback limits of configurations 2T1-120 and 2T2-115 for varying excitation amplitudes in comparison to reference case RC. [119]

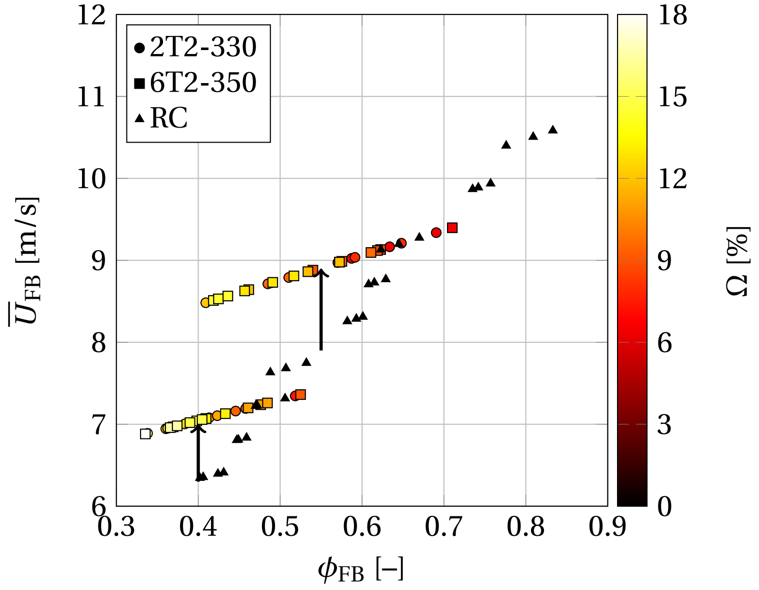

Figure 4.5: Flashback limits of configurations 2T2-330 and 6T2-350 for varying excitation amplitudes in comparison to reference case RC. [119]

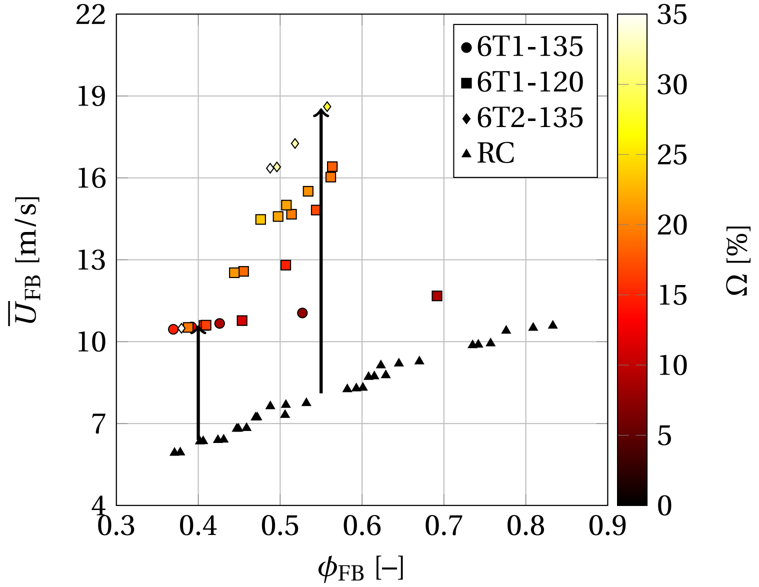

Figure 4.6: Flashback limits of configurations 6T1-135, 6T1-120 and 6T2-135 in comparison to reference case RC. [119]

135 at $\phi = 0.4$, an excitation amplitude of $\Omega = 15\,\%$ leads to an increase of 64 % in $\overline{U}_{\mathrm{FB}}$. At $\phi = 0.55$ an excitation amplitude of $\Omega = 19\,\%$ leads in 6T1-120 to a $\overline{U}_{\mathrm{FB}}$ increase of 100 %. At the same equivalence ratio, an amplitude of $\Omega = 30\,\%$ increases $\overline{U}_{\mathrm{FB}}$ about 130 % in configuration 6T2-135. This shows the serious effect of acoustic velocity oscillations on flashback resistance. Reasons for this distinct increase of velocity at flashback will be given in Sec. 4.3.2.

4.3.1 Influence of Excitation Frequency on Flashback Limits

Figure 4.7 shows the equivalence ratio at flashback depending on excitation amplitude for constant air mass flow rates and four different investigated frequencies. Figure 4.7(a) represents a low velocity case at $\dot{m}_{\mathrm{air}} = 20\,\mathrm{g/s}$ and Fig. 4.7(b) a high velocity case at $\dot{m}_{\mathrm{air}} = 24\,\mathrm{g/s}$. Both figures compare the influence of low frequencies around 120 Hz and intermediate frequencies around 350 Hz. Each depicted data set corresponds to one constant air mass flow rate in Fig. 4.4 and 4.5. In the low velocity case in Fig. 4.7(a) a distinct difference between the two frequency ranges is observed. For low frequencies, the equivalence ratio at flashback significantly decreases for excitation ampli-

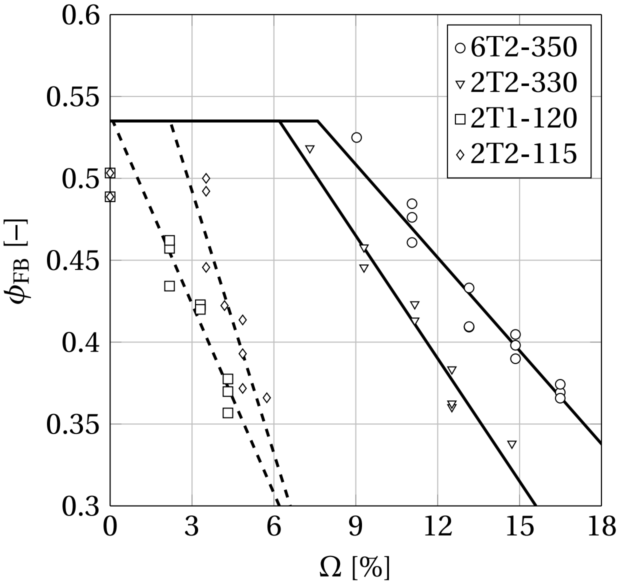

(a) Low velocity: $\dot{m}_{\text{air}} = 20\,\text{g/s}$

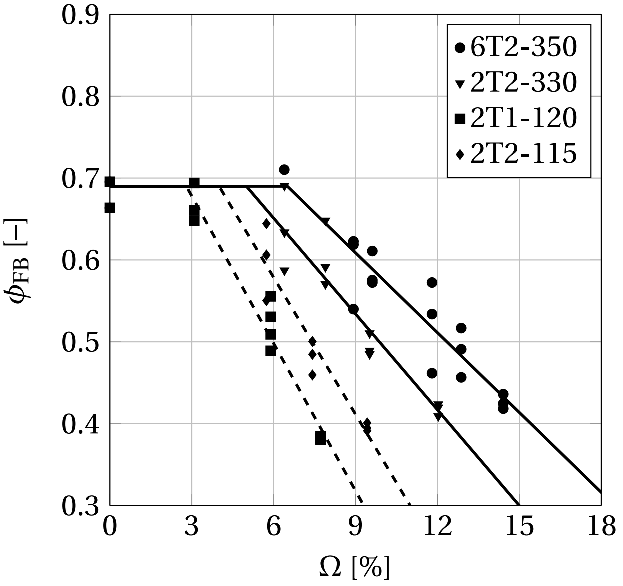

(b) High velocity: $\dot{m}_{\text{air}} = 24\,\text{g/s}$

Figure 4.7: Influence of excitation amplitude and frequency on flashback limits at constant air mass flow rates. Lines mark linear fits for low frequencies (dashed) and intermediate frequencies (solid). [119]

tudes above $\Omega = 2\,\%$. Small differences are observed between 115 and 120 Hz. At higher frequencies of 330 and 350 Hz, ϕ_{FB} remains approximately constant up to $\Omega = 7\,\%$. Higher excitation amplitudes are required to obtain the same reduction in equivalence ratio at flashback. For a reduction in ϕ_{FB} of 30 % an oscillation amplitude of $\Omega = 5\,\%$ is required at 115 and 120 Hz. The amplitude has to be increased to $\Omega = 14\,\%$ at 330 Hz and to $\Omega = 17\,\%$ at 350 Hz to achieve the same reduction in ϕ_{FB}.

The same trend is observed in the high velocity case depicted in Fig. 4.7(b). At low frequencies, ϕ_{FB} remains constant up to $\Omega \approx 3\,\%$. For frequencies around 350 Hz this limit is shifted to $\Omega \approx 6\,\%$. The amplitude to obtain a ϕ_{FB} reduction of 30 % is $\Omega = 7\,\%$ at 115 and 120 Hz. At 330 and 350 Hz, higher amplitudes of $\Omega = 10\,\%$ and $\Omega = 13\,\%$ are required.

4.3.2 Influence of Excitation Amplitude on Flashback Process

In the OH* images of the flashback process, a distinct difference between low and high excitation amplitudes was found. Figure 4.8 shows an OH* image sequence of a flashback at low excitation amplitude. The flashback process appears similar to an unexcited flashback test: A stable flame is located at the burner exit ($t = 0$ ms) and at some point a distortion in the flame front forms ($t = 2$ ms) and starts to continuously propagate upstream ($t = 2$–10 ms).

At high oscillation amplitudes, however, a different behavior is observed. The OH* image sequence in Fig. 4.9 is an example for the conducted flashback tests corresponding to the flashback limits in Fig. 4.6. The observed behavior was similar in all tests. The first image at $t = 0$ ms shows a stable flame. At $t = 2.33$ ms a flame tip has entered the burner duct but is washed out again. At $t = 28.67$ ms the flame tip which initiates flashback has formed. The subsequent image at $t = 32.67$ ms shows that this flame tip does not continuously propagate upstream but is pushed downstream again before it propagates further upstream. The fact that the time difference of 4 ms between the third and fourth image is approximately the time difference between minimum and maximum flow velocities in an excitation cycle at $f = 120$ Hz indicates that at low frequency the flame motion follows the acoustic excitation.

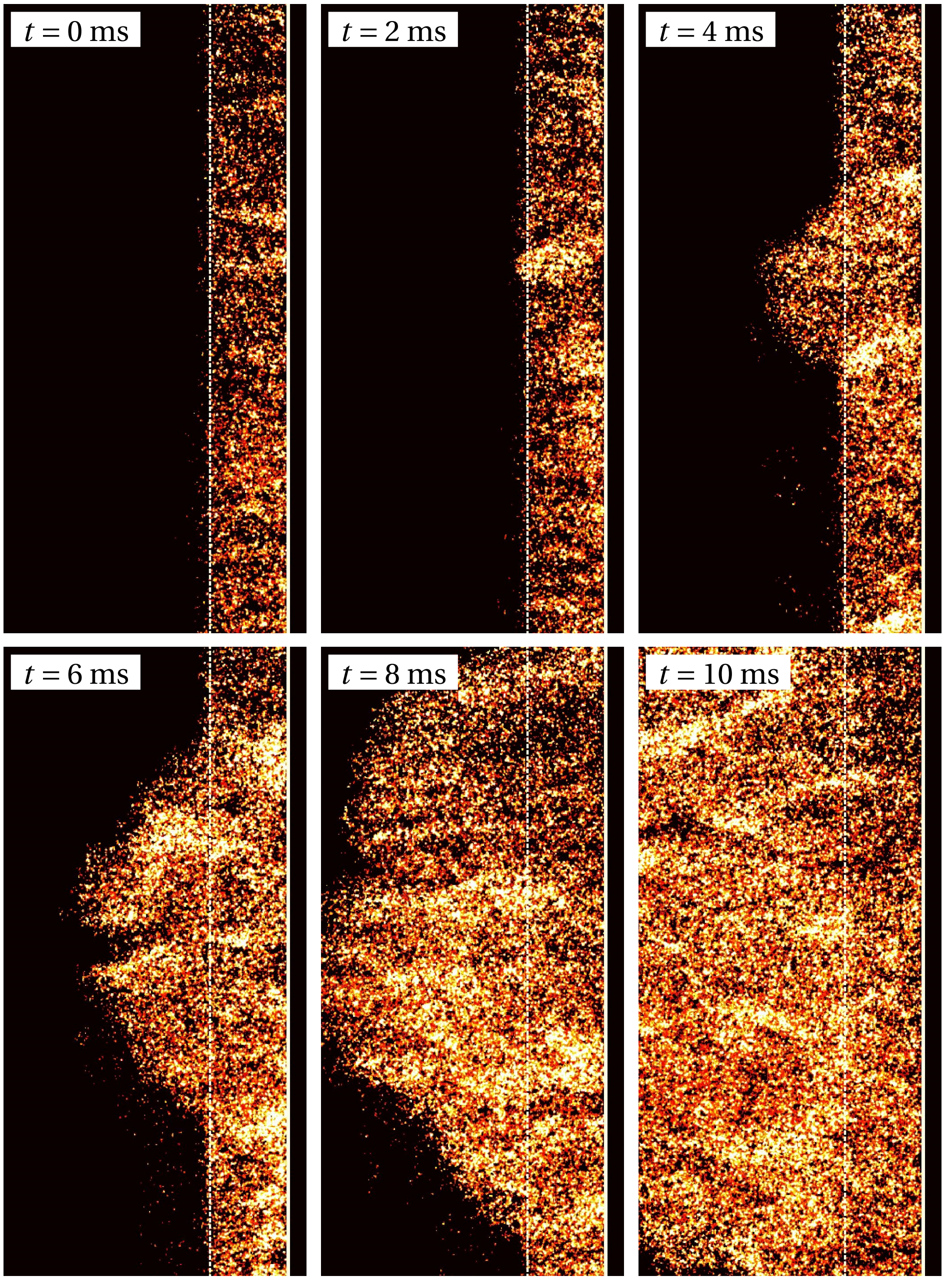

Figure 4.8: OH* images of low excitation amplitude flashback at $f = 115\,\mathrm{Hz}$, $\Omega = 7\,\%$, $\overline{U}_{\mathrm{FB}} = 8.8\,\mathrm{m/s}$ and $\phi_{\mathrm{FB}} = 0.50$. Flow direction from left to right.

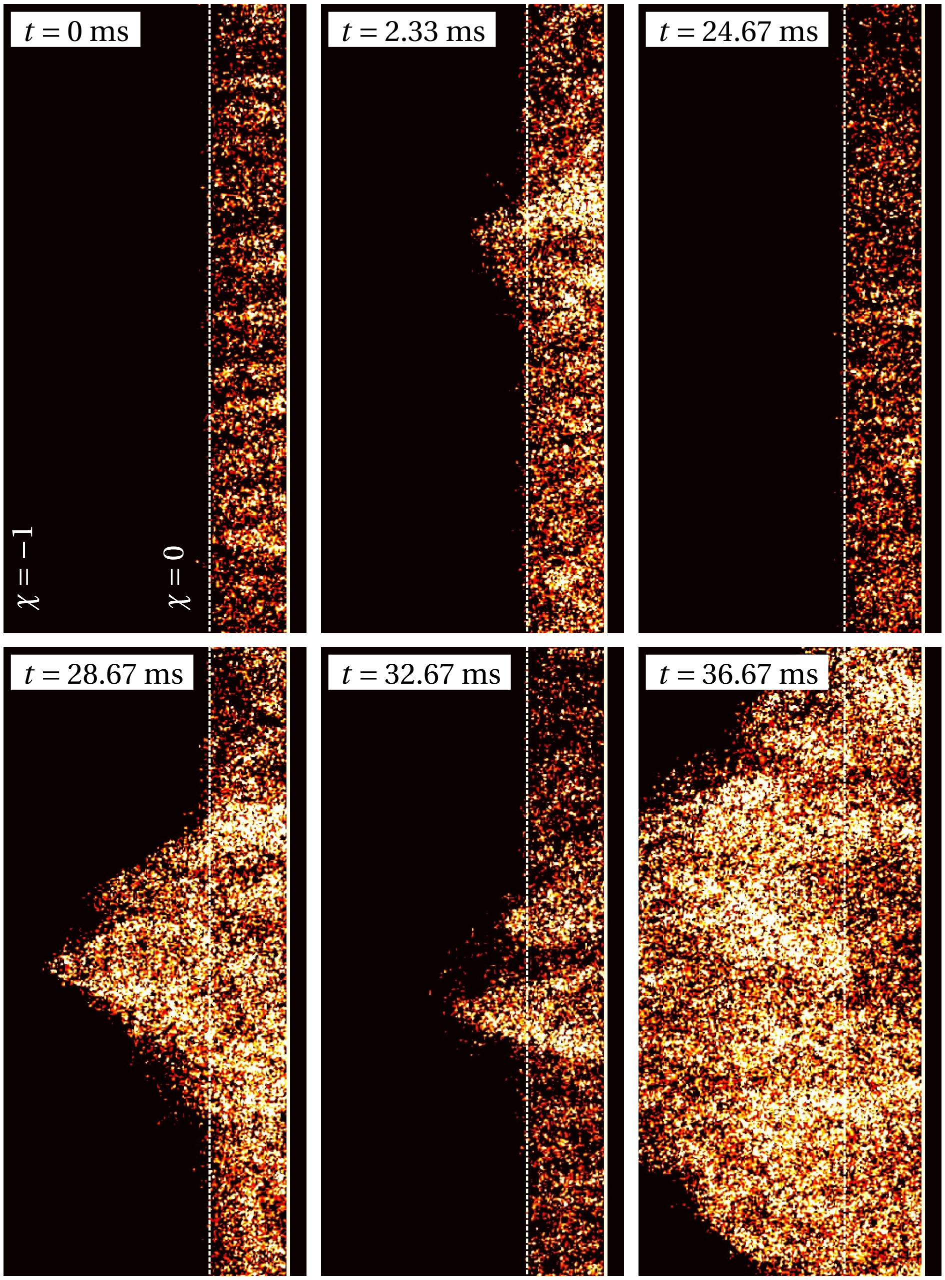

Figure 4.9: OH* images of high excitation amplitude flashback at $f = 120\,\mathrm{Hz}$, $\Omega = 23\,\%$, $\overline{U}_{\mathrm{FB}} = 14.5\,\mathrm{m/s}$ and $\phi_{\mathrm{FB}} = 0.48$. Flow direction from left to right. [119]

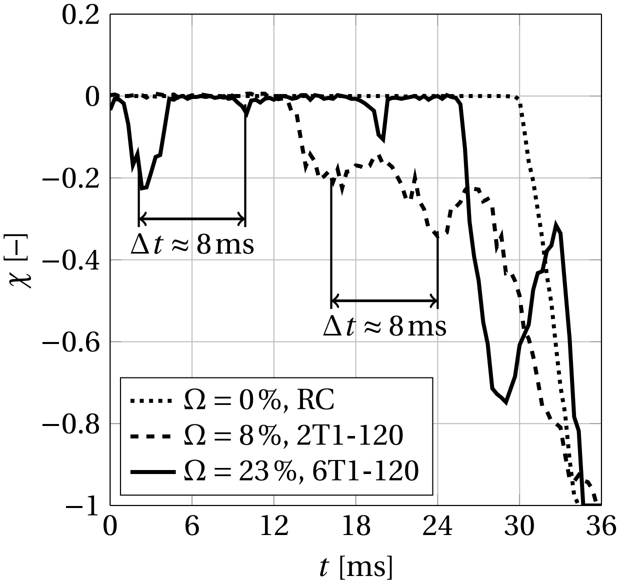

(a) Low frequencies (120 Hz)

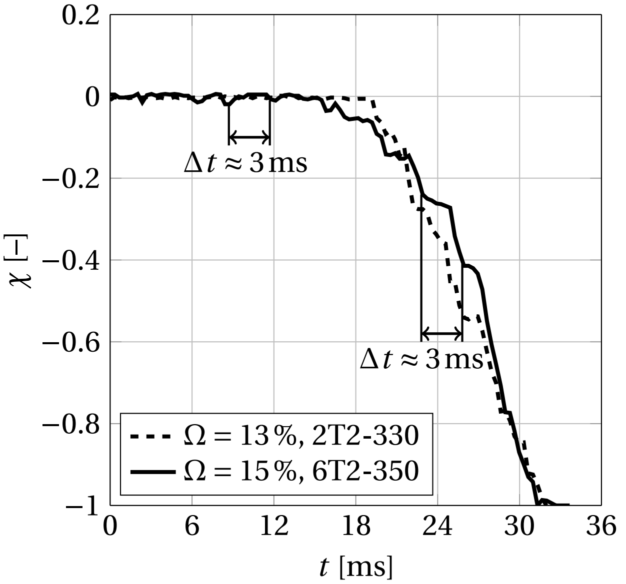

(b) Intermediate frequencies (330–350 Hz)

Figure 4.10: Flame tip trajectory during flashback for different excitation amplitudes. [119]

In order to support this statement, the normalized flame position χ of the high oscillation amplitude case is plotted in Fig. 4.10(a) in comparison to a lower oscillation amplitude case and an unexcited flashback. The definition of χ is illustrated in the first OH* image of Fig. 4.9. $\chi = 0$ represents the burner exit and $\chi = -1$ marks the upstream boundary of the field of view. The flame tip trajectory of the $\Omega = 0\,\%$ excitation case in Fig. 4.10(a) is characterized by a constant flame position at $\chi = 0$ until flashback is initiated at $t \approx 30\,\text{ms}$ and the flame starts to continuously propagate upstream.

If the excitation amplitude is increased to $\Omega = 8\,\%$, the flame position is as well constant at $\chi = 0$ until flashback is initiated at $t \approx 13\,\text{ms}$. In contrast to the unexcited case, the trajectory shows that the flame tip propagates upstream in an oscillating manner. A local maximum in upstream propagation (a local minimum in χ) is found at $t \approx 16\,\text{ms}$ where minimum flow velocities are present. After approximately $4\,\text{ms}$, at $t \approx 20\,\text{ms}$, the flame tip is forced downstream again due to a maximum in flow velocity. Half an excitation period later, at $t \approx 24\,\text{ms}$, the flame tip again reaches a local maximum in upstream position. This time it is located further upstream than in the previous excitation cycle. After another local minimum at $t \approx 28\,\text{ms}$ the flame starts to continuously propagate upstream without further oscillations. It seems that at this point, the flame tip has traveled far enough into the burner duct to influence the upstream flow field. In that case, the flashback process changes to the mechanism of confined flames where the pressure rise induced by the flame tip leads to boundary layer separation (cf. Sec. 1.1.2.2).

At further increased excitation amplitude of $\Omega = 23\,\%$ the flashback behavior has changed. Flashback starts at $t \approx 25\,\text{ms}$ and an oscillating upstream propagation of the flame tip is observed. Compared to the low excitation amplitude case, the amplitude of the oscillation in the flame tip trajectory is increased. Apart from that, a periodic upstream propagation of the flame tip is visible prior to flashback initiation at $t \approx 2.3\,\text{ms}$, $t \approx 10.6\,\text{ms}$ and $t \approx 19.0\,\text{ms}$. The time difference between the maxima in upstream position is equal to the duration of one excitation cycle $\Delta t = 1/f \approx 8\,\text{ms}$ indicating that the flame is able to enter the burner duct if minimum flow velocities are present.

Figure 4.10(b) shows the flame tip trajectory for the intermediate frequency excitation. Compared to Fig. 4.10(a), much smaller oscillations are observed during the upstream propagation as the flame has less time to follow the acoustic oscillations. However, the observed oscillations can still be attributed to faster upstream flame propagation during the low velocity part of the excitation cycle since the time difference between local maxima in upstream position is about $\Delta t = 1/f \approx 3\,\mathrm{ms}$.

4.3.3 Identification of Different Flashback Regimes

The different flashback behavior for low and high excitation amplitudes described in the previous section is analyzed in this section in terms of flashback limits. If a quasi steady state behavior of the flame is assumed, i.e. if the flame perfectly follows the modulation in flow velocity, flashback should be initiated when the minimum flow velocity in the excitation cycle falls below the flashback limit of unexcited unconfined flames. In order to verify this hypothesis, the flashback limits can be expressed in terms of minimum flow velocity at flashback

$$\overline{U}_{\mathrm{min,FB}} = \overline{U}_{\mathrm{FB}}(1-\Omega)\,. \tag{4.1}$$

The result is shown in Fig. 4.11 compared to the flashback limits of unexcited unconfined and confined flames. The figure includes all measured flashback limits presented in Fig. 4.3, 4.4 and 4.6. For low excitation amplitudes, the minimum flow velocities cluster around the flashback limits of the reference case without excitation. This confirms the hypothesis of a steady state behavior of the flame. However, a second branch of flashback limits is observed in Fig. 4.11 for high excitation amplitudes. This reflects the change in flashback mechanism described in the previous section. The fact that the flame is able to periodically enter the burner without initiating flashback shows that the minimum flow velocity in the high velocity oscillation amplitude cases is still higher than the flashback limit of unconfined flames. For that reason, the physical process of flashback has to change if flashback occurs at these conditions. As flame confinement significantly increases $\overline{U}_{\mathrm{FB}}$ (cf. Sec. 1.1.2), it seems likely that for high oscillation amplitudes a transition to the flashback mechanism of confined flames takes place. In that case, flashback should occur if, firstly, the flame tip has entered a sufficient distance into the burner duct to cause boundary layer separation and, secondly, if the separation is not destroyed during the high velocity part of the excitation cycle. Consequently, the

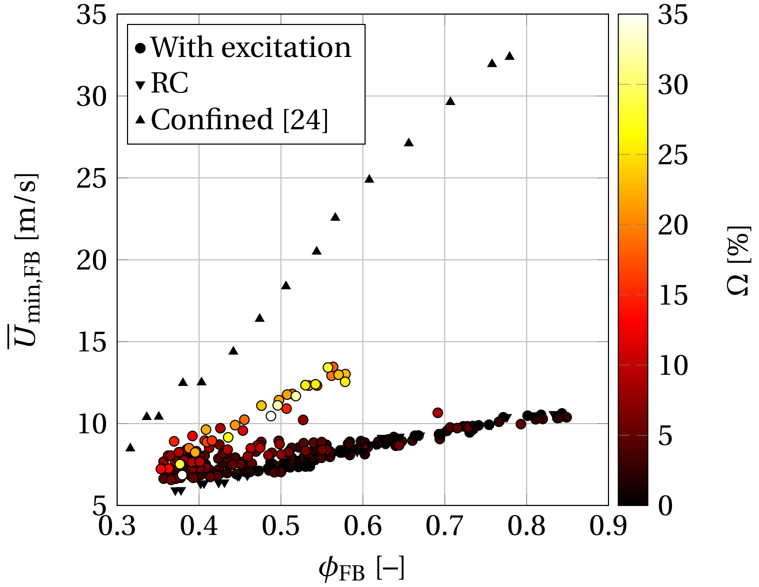

Figure 4.11: Flashback limits in terms of minimum flow velocities of the six low frequency excitation configurations in comparison to unconfined (RC) and confined [24] flashback data. [119]

maximum flow velocity

$$\overline{U}_{\mathrm{max,FB}} = \overline{U}_{\mathrm{FB}}(1+\Omega) \tag{4.2}$$

should be equal to the flashback limits of confined flames. The maximum flow velocities at the measured flashback conditions with low frequency excitation are depicted in Fig. 4.12. As assumed, the maximum flow velocities for high excitation amplitudes cluster around the flashback limits of confined flames. The transition between the two flashback regimes of low and high excitation amplitudes is observed at velocity oscillation amplitudes between 10 and 15 %.

In order to separate the two regimes more clearly, Fig. 4.13(a) shows the flashback limits of low excitation amplitudes in terms of $\overline{U}_{\mathrm{min,FB}}$ and those of high amplitudes in terms of $\overline{U}_{\mathrm{max,FB}}$. As threshold amplitude $\Omega_{\mathrm{lim}} = 14\,\%$ is chosen. This threshold to distinguish between the flashback regimes should not be seen as a fixed value. Rather the question if the acoustic velocity oscillations are high enough for the flame tip to periodically enter the burner duct can be seen as a criterion for the transition to confined flashback.

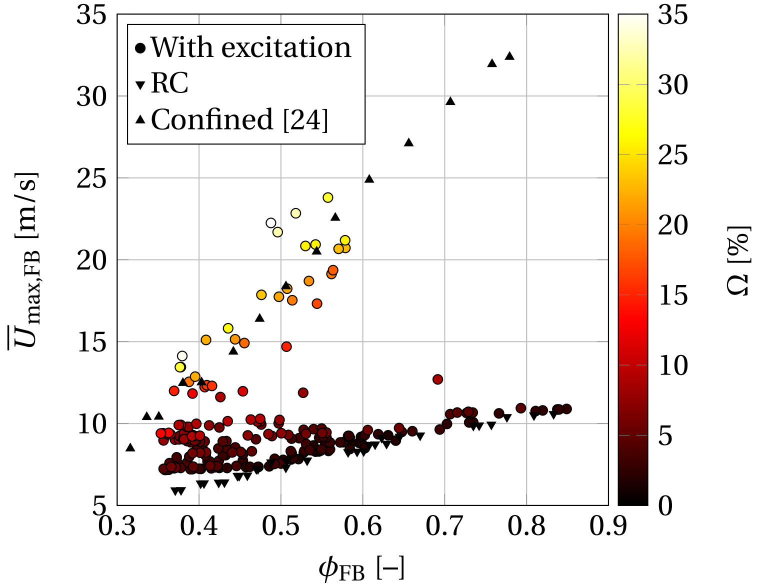

Figure 4.12: Flashback limits in terms of maximum flow velocities of the six low frequency excitation configurations in comparison to unconfined (RC) and confined [24] flashback data. [119]

Figure 4.13(a) shows that the differentiation into two flashback regimes works well for equivalence ratios above 0.45 and the investigated frequencies between 115 and 135 Hz. For leaner mixtures, the separation of the two regimes is not as distinct which is partly caused by the fact that the velocity difference between the flashback limits of confined and unconfined flames is small. Another reason might be the high influence of flame stretch in very lean hydrogen-air mixtures [35, 58]. Flame stretch and, therefore, burning velocity might be increased due to the acoustic velocity oscillations leading to a higher flashback risk.

Figure 4.13(b) shows the differentiation into two regimes for the intermediate frequencies between 330 and 350 Hz. In this frequency range, all flashback limits presented in Fig. 4.5 cluster around the flashback limits of unconfined flames (RC) if described in terms of minimum flow velocities at flashback. Since the maximum excitation amplitude is about 19 %, the threshold Ω_{lim} has definitely changed compared to the low frequency case. Unfortunately, Ω_{lim} cannot be determined for the intermediate frequencies since it is not possible to achieve higher oscillation amplitudes in this frequency range with the

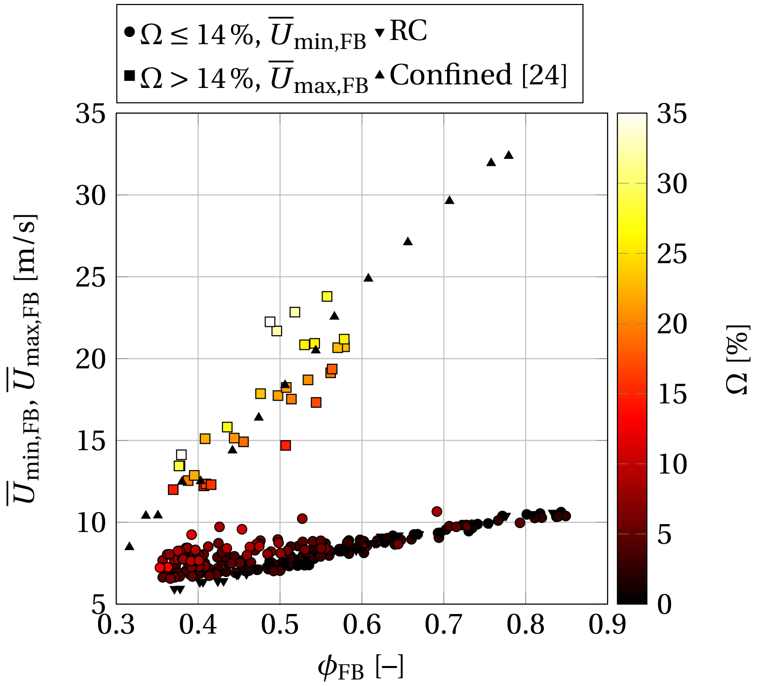

(a) Low frequencies (115–135 Hz)

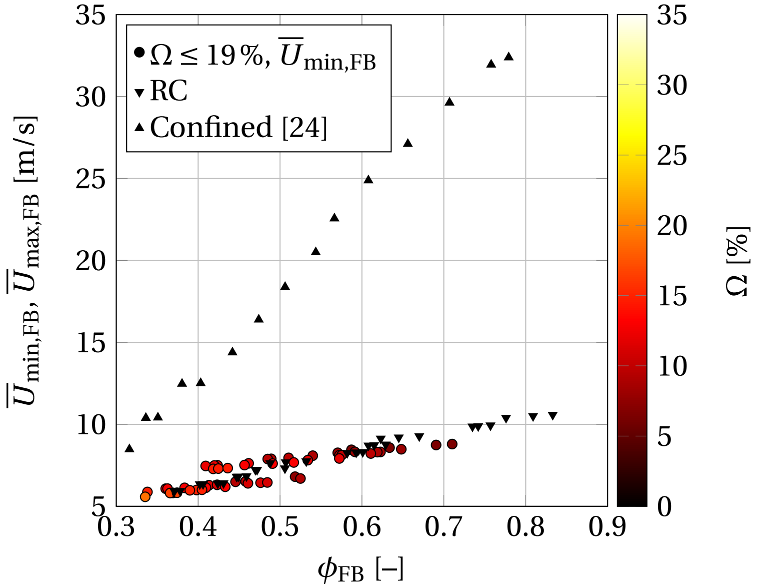

(b) Intermediate frequencies (330–350 Hz)

Figure 4.13: Flashback limits of all eight configurations in terms of minimum flow velocities for low excitation amplitudes and in terms of maximum flow velocities for high excitation amplitudes in comparison to unconfined (RC) and confined [24] flashback data. [119]

current setup. Still, the observed shift in Ω_{lim} is in line with the observation in Fig. 4.7 of a reduced influence of excitation at increasing frequencies. This seems understandable since the flame has less time to propagate upstream in the low velocity part of the excitation cycle. Consequently, higher excitation amplitudes are required for the flame to enter the burner duct and to reach confined conditions.

It can be concluded that the flashback limits of unconfined and confined flames pose limiting cases for the obtained flashback limits of acoustically excited flames. Hence, the flashback limits of unconfined flames can be used to estimate if certain operating conditions are critical in terms of BLF when compared to the minimum flow velocities in the excitation cycle. However, it also has to be ensured, that the maximum flow velocities do not fall below the flashback limits of confined flames. Due to the high importance of the two limiting cases in the design of gas turbine burners, prediction models for the flashback limits of confined and unconfined flames are developed in Chap. 5 and 6.

5 Prediction of Confined Flashback Limits

As introduced in Sec. 1.1.2.2, boundary layer flashback in confined flames is initiated by a backflow region upstream of the flame tip. Consequently, confined flashback limits can be predicted by estimating the operating conditions at which the pressure rise upstream of the flame tip is high enough to cause boundary layer separation. A semi-empirical criterion for boundary layer separation developed by Stratford [53] was introduced in Eq. (2.21). Based on this criterion a model to predict the flashback limits of confined flames is developed in the following sections.

5.1 Prediction Model

Figure 5.1 depicts the velocity and pressure conditions upstream of a premixed flame confined in a burner duct. This situation corresponds to the experiments conducted by Eichler [9]. The most upstream part of the flame, referred to as flame tip, is stabilized at the axial position x_F. The location $x = 0$ marks the point where the boundary layer starts to form. In this work, confined flames in fully developed turbulent duct flows will be analyzed. This means that x_F will be larger than the duct's hydrodynamic entrance length

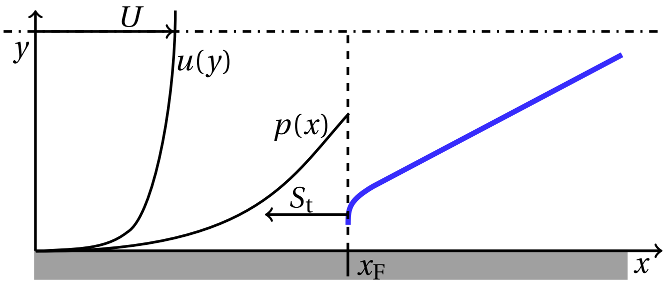

Figure 5.1: Premixed flame confined in burner duct [58].

(cf. Sec. 2.2.3). The flame (blue line) is stabilized in a typical turbulent duct flow profile $u(y)$ with the duct center line velocity U as shown in Fig. 5.1. The corresponding bulk flow velocity is denoted $\overline{U}$. The pressure $p(x)$ increases upstream of the flame tip due to the combustion induced pressure rise Δp over the flame front. In order to compute the pressure coefficient $C_\mathrm{p}(x)$ and its derivative required in Stratford's criterion for boundary layer separation (Eq. (2.21)), the pressure distribution $p(x)$ has to be defined. Based on the suggestions of Eichler [9] and Baumgartner [10], a quadratic pressure rise

$$p(x) = p(0) + \frac{\Delta p}{x_\mathrm{F}^2} x^2 \tag{5.1}$$

upstream of the flame tip from $p(0)$ to the maximum value $p(x_\mathrm{F}) = p(0) + \Delta p$ is assumed. From Eq. (5.1) and Eq. (2.22) the pressure coefficient

$$C_\mathrm{p}(x) = \frac{2\Delta p}{\rho_\mathrm{u} U^2} \frac{x^2}{x_\mathrm{F}^2} \tag{5.2}$$

is obtained, where the channel center line velocity U is inserted as free-stream velocity. Together with its derivative

$$\frac{\mathrm{d}C_\mathrm{p}(x)}{\mathrm{d}x} = \frac{4\Delta p}{\rho_\mathrm{u} U^2} \frac{x}{x_\mathrm{F}^2} \tag{5.3}$$

the pressure coefficient is inserted into Stratford's criterion in Eq. (2.21). As Stratford's criterion is applied to calculate the velocity $U = U_\mathrm{FB}$ at which boundary layer separation is induced at the flame tip, it is evaluated at $x = x_\mathrm{F}$:

$$\sqrt{2}\left(\frac{2\Delta p}{\rho_\mathrm{u} U_\mathrm{FB}^2}\right)^{3/2} = 0.39\left(10^{-6}\frac{U_\mathrm{FB} x_\mathrm{F}}{\nu_\mathrm{u}}\right)^a . \tag{5.4}$$

The original Stratford exponent for free boundary layers is $a = 0.1$. For fully developed flow, U_FB should not depend on the flame position x_F. For that reason, the exponent a is set to zero to remove the dependence on x_F. It was shown in [58] that this change in exponent has a negligible effect on the predicted flashback limits. For $a = 0$ Eq. (5.4) simplifies to

$$\sqrt{2}\left(\frac{2\Delta p}{\rho_\mathrm{u} U_\mathrm{FB}^2}\right)^{3/2} = 0.39 . \tag{5.5}$$

In this expression the velocity at flashback U_{FB} at a certain equivalence ratio only depends on the unburned gas density ρ_{u} and the pressure rise upstream of the flame tip Δp. In order to relate U_{FB} to the flashback limit $\overline{U}_{\mathrm{FB}}$, Eq. (2.28) is applied.

The pressure rise upstream of a turbulent premixed flame can be derived from mass conservation

$$\rho_{\mathrm{u}} u_{\mathrm{u}} = \rho_{\mathrm{b}} u_{\mathrm{b}} \tag{5.6}$$

and momentum conservation

$$\rho_{\mathrm{u}} u_{\mathrm{u}}^2 + p_{\mathrm{u}} = \rho_{\mathrm{b}} u_{\mathrm{b}}^2 + p_{\mathrm{b}} \tag{5.7}$$

leading to

$$\Delta p = p_{\mathrm{u}} - p_{\mathrm{b}} = \rho_{\mathrm{u}} u_{\mathrm{u}}^2 \left(\frac{\rho_{\mathrm{u}}}{\rho_{\mathrm{b}}} - 1 \right) . \tag{5.8}$$

If the flame tip position is fixed, the unburned gas velocity u_{u} is equal to the turbulent burning velocity S_{t} as indicated in Fig. 5.1. Inserting into Eq. (5.8) results in the final expression

$$\Delta p = \rho_{\mathrm{u}} S_{\mathrm{t}}^2 (\sigma - 1) . \tag{5.9}$$

This expression only requires the turbulent burning velocity S_{t} and the expansion ratio $\sigma = \rho_{\mathrm{u}}/\rho_{\mathrm{b}}$ as input parameters to define Δp. The expansion ratio σ for a certain equivalence ratio is obtained from equilibrium calculations in *Cantera 2.2* [67]. The turbulent burning velocity is defined by

$$S_{\mathrm{t}} = S_{\mathrm{l,s}} \left(1 + C_{\mathrm{S}} \left(\frac{u'(y_{\mathrm{FB}})}{S_{\mathrm{l,s}}} \right)^{0.5} \right) \tag{5.10}$$

based on Eq. (2.85) in combination with the stretched laminar burning velocity $S_{\mathrm{l,s}}$ to include flame stretch. The original Damköhler exponent of $c_3 = 0.5$ is applied here. In [58], the maximum pressure rise responsible for flashback initiation was found at the wall distance of maximum turbulent burning velocity. As the turbulent burning velocity mainly depends on turbulent velocity fluctuations u', y_{FB} is equal to the wall distance of maximum turbulent velocity fluctuations as long as this wall distance exceeds the quenching distance of the investigated fuel-oxidizer mixture. For hydrogen-air mixtures, Gruber et al. [31] observed a quenching distance in wall units of $y^+ \approx 3$ in their DNS. This distance is smaller than the wall distance of maximum turbulent velocity fluctuations at $y^+ = 16.4$ described in Sec. 2.2.3 for turbulent duct flow. However, it has to be noted that the DNS of Gruber et al. was performed at high temperatures of 750 K and not specifically at the flashback velocity $\overline{U}_{\mathrm{FB}}$ corresponding to these conditions. For that reason, it is uncertain if the quenching distance at flashback conditions is also smaller than $y^+ = 16.4$. However, assuming that this is the case, the maximum turbulent burning velocity is found at $y^+_{\mathrm{FB}} = 16.4$ [58]. At this wall distance the normalized turbulent velocity fluctuations $u'(y_{\mathrm{FB}})/u_\tau = 2.6$ can be calculated from the fit in Eq. (2.23). The shear stress velocity u_τ can be related to the flashback limit $\overline{U}_{\mathrm{FB}}$ using Eq. (2.26) for channel and Eq. (2.27) for tube burner flow.

Finally, the stretched laminar burning velocity $S_{\mathrm{l,s}}$ is required to close the prediction model for $\overline{U}_{\mathrm{FB}}$. It is obtained from Markstein's approach presented in Eq. (2.48) in combination with Bechtold and Matalon's description for the Markstein length L_{M} in Eq. (2.60) [105] and the derived expression for the flame stretch rate presented in Eq. (2.59) [99, 100]. The set of equations forming the prediction model for confined boundary layer flashback limits is summarized in the following section.

5.2 Summary of Equations

The model to predict boundary layer flashback limits of flames confined in ducts based on Stratford's criterion for boundary layer separation can be summarized in the following eight equations:

1) Eq. (5.5), (2.28) $$\sqrt{2}\left(\frac{2\Delta p}{\rho_{\mathrm{u}}(\overline{U}_{\mathrm{FB}} + 2.4\,u_\tau)^2}\right)^{3/2} = 0.39\,,$$

2) Eq. (5.9) $$\Delta p = \rho_{\mathrm{u}} S_{\mathrm{t}}^2\,(\sigma - 1)\,,$$

3) Eq. (5.10) $$S_{\mathrm{t}} = S_{\mathrm{l,s}}\left(1 + C_{\mathrm{S}}\left(\frac{u'(y_{\mathrm{FB}})}{S_{\mathrm{l,s}}}\right)^{0.5}\right),$$

4) Eq. (2.48) $$S_{\mathrm{l,s}} = S_{\mathrm{l,0}} - \kappa(y_{\mathrm{FB}})\,L_{\mathrm{M}}\,,$$

5) Eq. (2.59) $\kappa(y_{\mathrm{FB}}) = \frac{2}{3}\Gamma_{\mathrm{K}}(y_{\mathrm{FB}})\frac{u'(y_{\mathrm{FB}})}{\Lambda} + \frac{1}{2}\frac{u'(y_{\mathrm{FB}})}{\Lambda}$,

6) Eq. (2.54) $\log_{10}\left(\Gamma_{\mathrm{K}}(y_{\mathrm{FB}})\right) = -\frac{1}{s+0.4}\mathrm{e}^{-(s+0.4)} + \left(1-\mathrm{e}^{-(s+0.4)}\right)$
$\left(\frac{2}{3}\left(1-\frac{1}{2}\mathrm{e}^{\left(-\left(u'(y_{\mathrm{FB}})/S_{\mathrm{l},0}\right)^{1/3}\right)}\right)s - 0.11\right)$,

Eq. (2.55) $s = \log_{10}\left(\frac{\Lambda}{\delta_{\mathrm{F}}}\right)$,

7) Eq. (2.26) Channel burner: $\frac{\overline{U}_{\mathrm{FB}}}{u_\tau} = \frac{1}{K}\ln\left(\frac{h\,u_\tau}{\nu_{\mathrm{u}}}\right) + B - \frac{1}{K}$,

Eq. (2.27) Tube burner: $u_\tau^2 = 0.03955\,\overline{U}_{\mathrm{FB}}^{7/4}\nu_{\mathrm{u}}^{1/4}h^{-1/4}$,

8) Eq. (2.23) $u'(y_{\mathrm{FB}}) = 2.6\,u_\tau$.

This system of non-linear equations can be solved for the flashback limit $\overline{U}_{\mathrm{FB}}$ at a certain equivalence ratio using Newton's method. The unburned mixture properties are extracted form *Cantera 2.2* [67]. The expansion ratio σ is obtained from equilibrium calculations with the reaction mechanism of Ó Conaire et al. [68] for hydrogen-air mixtures. The coefficient of the turbulent burning velocity correlation is set to $C_{\mathrm{S}} = 2.6$ for hydrogen-air mixtures as for this value good agreement of the predicted flashback limits with experimental data was achieved. If a different fuel is investigated, the correlation for the turbulent burning velocity has to be adapted accordingly. The turbulent macroscale is set to $\Lambda = 7\,\%$ of the hydraulic diameter as introduced in Eq. (2.24) for fully developed duct flow. The Markstein length L_{M} is computed from the method of Bechtold and Matalon [105] in Eq. (2.60). Resulting Markstein lengths of hydrogen-air mixtures are presented in Sec. 2.3.2.2 for different preheating temperatures and pressures. The unstretched laminar burning velocity $S_{\mathrm{l},0}$ is computed from the polynomial approach in Eq. (2.41) with the coefficients from C.1. The laminar flame thickness δ_{F} is obtained from the expression in Eq. (2.44) proposed by Turns [93] although it was developed for $\mathrm{Le} = 1$. A detailed discussion of unstretched laminar burning velocity and laminar flame thickness can be found in Sec. 2.3.1.2 and 2.3.1.3.

The described prediction model for flashback limits of confined flames was originally published in [58]. Compared to the original publication the following changes were made in this work: The expansion ratio is not replaced by the temperature ratio as this was an unnecessary simplification. The temperature dependence of the unstretched laminar burning velocity is defined in a different way as described in Sec. 2.3.1.2. This leads to changes in other parameters such as Markstein length, flame stretch rate and turbulent burning velocity. Consequently, the coefficient C_S of the turbulent burning velocity correlation is adapted. Furthermore, different equations are used to describe the dependence of shear stress velocity on bulk flow velocity for channel and tube burners to enhance accuracy.

5.3 Model Validation

The derived prediction model for flashback limits of confined flames is validated for atmospheric pressure using experimental tube burner and channel burner data of Eichler et al. [9, 24] ($1 \times 10^4 < \mathrm{Re} < 3.5 \times 10^4$). As experimental data is only available for lean hydrogen-air mixtures, the model can only be validated for these cases.

For Baumgartner's $d_\mathrm{h} = 40\,\mathrm{mm}$ tube burner, experimental data are available at $T_\mathrm{u} = 293\,\mathrm{K}$ [24]. A comparison of the predicted flashback limits and the experimental data is presented in Fig. 5.2 indicating a good prediction accuracy at ambient conditions.

Figure 5.3 depicts predicted and experimental flashback limits [9] for Eichler's $d_\mathrm{h} = 31.5\,\mathrm{mm}$ channel burner at different preheating temperatures. It can be seen that at ambient temperature, the prediction well reproduces the experimental data over the whole investigated range of equivalence ratios. For higher preheating temperatures, the prediction accuracy is good for $\phi > 0.6$. At very lean conditions, however, the flashback limits are underestimated. This can have several reasons: Firstly, there is a high uncertainty in the unstretched laminar burning velocity $S_{\mathrm{l},0}$ at preheated conditions because there is no experimental data available. The values used in the prediction model are based on one-dimensional free flame simulations in *Cantera 2.2* [67]. The discussion in Sec. 2.3.1.2 showed that the unstretched laminar burning velocity for

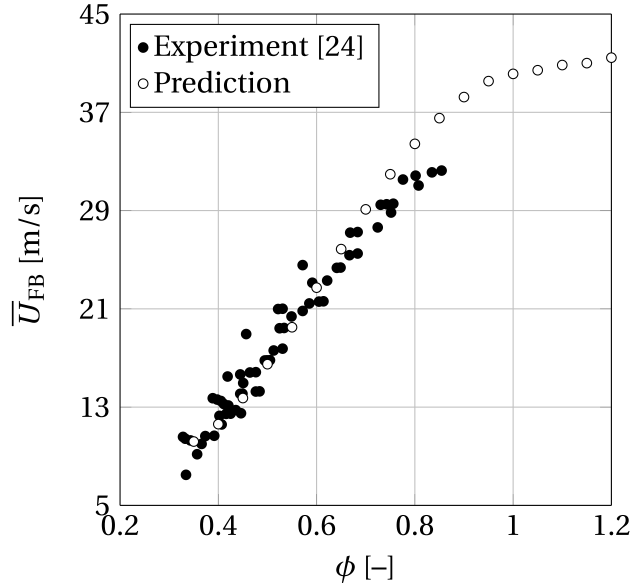

Figure 5.2: Predicted confined flashback limits of a $d_{\mathrm{h}} = 40\,\mathrm{mm}$ tube burner compared to experimental data [24].

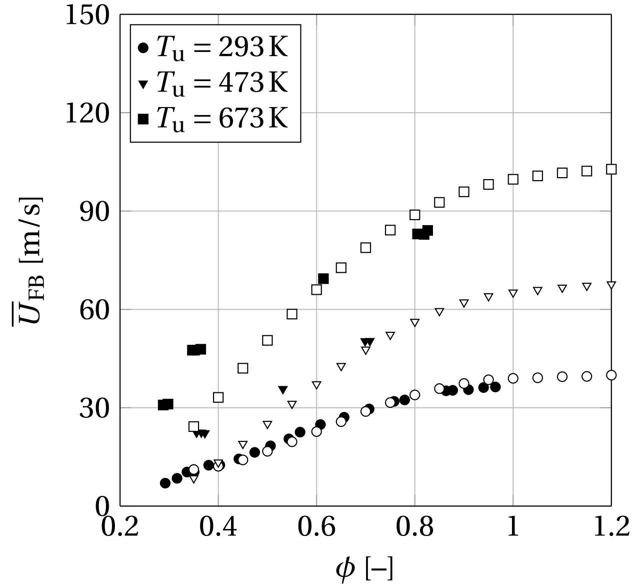

Figure 5.3: Predicted confined flashback limits (empty symbols) of a $d_{\mathrm{h}} = 31.5\,\mathrm{mm}$ channel burner at different preheating temperatures compared to experimental data [9] (filled symbols).

lean mixtures obtained from these simulations at ambient temperature is too low compared to the experimental data. Therefore, it is possible that $S_{l,0}$ is underestimated at preheated conditions as well. In the original publication of the confined flashback prediction model [58] a better prediction accuracy was achieved at lean preheated conditions because higher unstretched laminar burning velocities were assumed based on a power law approach which contained high uncertainty.

The second possible explanation for the deviations of prediction and experiment could be the uncertainty in the determination of the Markstein length. Similar to $S_{l,0}$, there are no experimental data available for L_M of hydrogen-air mixtures at preheated conditions. Hence, the calculated Markstein length cannot be validated in this region. It might be possible that the absolute value of L_M is underestimated for lean conditions where the influence of flame stretch should be significant. In the sensitivity analysis in the following section the influence of these parameters will be discussed in detail. It will be investigated how they have to be changed in order to improve the prediction accuracy at lean conditions.

Apart from the flashback limit, the predicted wall distance of flashback initiation can be validated although literature data is limited. Figure 5.4 shows the predicted wall distances y_{FB} for the channel burner at three different preheating temperatures as well as for the tube burner at ambient temperature. At ambient temperature, the wall distances of tube and channel burner decrease from $y_{FB} \approx 0.5\,\mathrm{mm}$ at $\phi = 0.35$ to $y_{FB} \approx 0.2\,\mathrm{mm}$ at stoichiometry. With increasing temperature, the flashback limits are shifted to higher velocities. Still, the Reynolds numbers at flashback decrease due to the increasing kinematic viscosity. For that reason, the wall distance y_{FB} corresponding to $y^+_{FB} = 16.4$ increases with temperature.

The only experimental data for wall distances in the context of confined boundary layer flashback are given by Eichler [9]: $y = 0.53\,\mathrm{mm}$ at $\phi = 0.543$ ($y^+ = 36$) and $y = 0.96\,\mathrm{mm}$ at $\phi = 0.345$ ($y^+ = 35$). However, these values do not describe the wall distance of flashback initiation shown in Fig. 5.4 but the height of the backflow region Eichler observed in his experiments. His values well agree with the numerically determined backflow region heights of Gruber

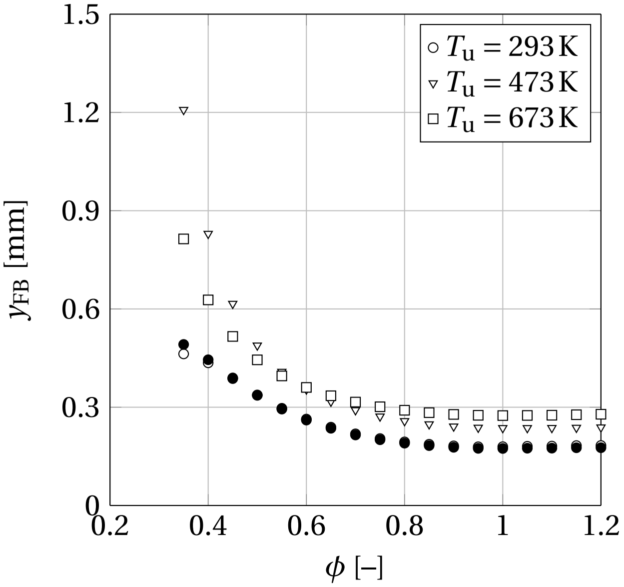

Figure 5.4: Predicted wall distances of flashback initiation for confined flashback. Empty symbols: $d_{\mathrm{h}} = 31.5\,\mathrm{mm}$ channel burner, filled symbols: $d_{\mathrm{h}} = 40\,\mathrm{mm}$ tube burner.

et al. [31]. It can be seen in their results that the most upstream position of the flame tip is located closer to the wall compared to the height of the backflow region. Hence, the here obtained ambient temperature values for y_{FB} seem reasonable as they are smaller than Eichler's backflow region heights. Furthermore, the normalized wall distance $y^{+}_{\mathrm{FB}} = 16.4$ used in the prediction model is in good agreement with the numerically determined flame tip position of Gruber et al. [31].

5.4 Sensitivity Analysis

The prediction model for flashback limits of confined flames includes assumptions and expressions for several parameters. The influence of a ±20% change in different parameters will be analyzed at $T_{\mathrm{u}} = 293\,\mathrm{K}$ and $T_{\mathrm{u}} = 673\,\mathrm{K}$ in the following sections based on Eichler's $d_{\mathrm{h}} = 31.5\,\mathrm{mm}$ channel burner [9] which was used for model validation.

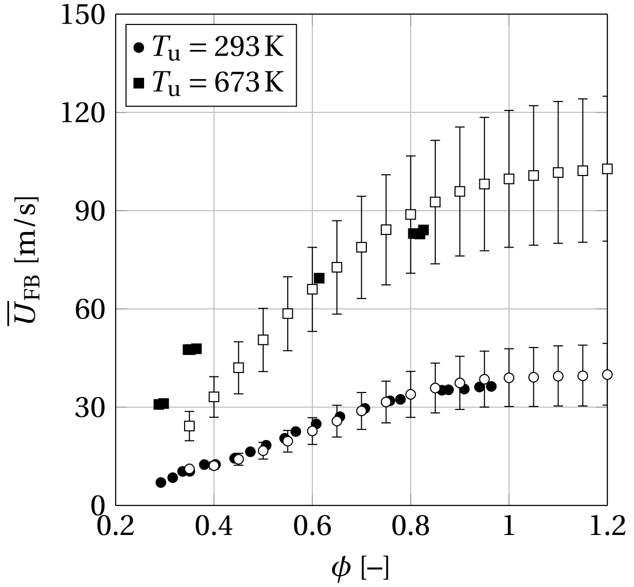

Figure 5.5: Influence of a ±20 % change in $S_{l,0}$ on the confined flashback limits of a $d_h = 31.5\,mm$ channel burner. Empty symbols: prediction, filled symbols: experiment [9].

5.4.1 Unstretched Laminar Burning Velocity

Figure 5.5 shows the effect of unstretched laminar burning velocity $S_{l,0}$ on the predicted flashback limits. The errorbars mark a $S_{l,0}$ change of ±20 %. At ambient temperature, the influence of $S_{l,0}$ is small at lean conditions and increases with equivalence ratio due to the decreasing effect of Markstein length on burning velocity. At $T_u = 673\,K$ and lean conditions, the relative change of flashback limit is higher compared to ambient temperature and only a small increase with equivalence ratio is observed. This is caused by the reduced absolute values of Markstein length at preheated conditions. Table 5.1 summarizes the relative changes of $\overline{U}_{FB}$ for three equivalence ratios. It can be noted that an increase in unstretched laminar burning velocity leads in all cases to higher flashback limits because the stretched laminar and the turbulent burning velocities are increased. This leads to higher pressure rises upstream of the flame tip and, consequently, to higher velocities at boundary layer separation.

In order to match the experimental flashback limits at $\phi = 0.35$ and $T_u = 673\,K$, $S_{l,0}$ has to be increased by about 60 %. This means that the unstretched lam-

Table 5.1: Relative changes of the predicted $\overline{U}_{\mathrm{FB}}$ of confined flames due to a ±20 % variation of $S_{\mathrm{l},0}$.

ϕ	T_{u} [K]	$\frac{\Delta\overline{U}_{\mathrm{FB}}(1.2\,S_{\mathrm{l},0})}{\overline{U}_{\mathrm{FB}}}$ [%]	$\frac{\Delta\overline{U}_{\mathrm{FB}}(0.8\,S_{\mathrm{l},0})}{\overline{U}_{\mathrm{FB}}}$ [%]
0.4	293	+9.58	−8.79
0.7	293	+19.45	−19.60
1.0	293	+22.76	−22.47
0.4	673	+18.60	−18.78
0.7	673	+19.73	−19.84
1.0	673	+20.96	−20.95

inar burning velocity obtained from the one-dimensional free flame simulation with the reaction mechanism of Ó Conaire et al. [68] would be 60 % too low. Compared to the underestimation of $S_{\mathrm{l},0}$ at $\phi = 0.35$ and ambient temperature, which amounts up to 63 % (cf. Fig. 2.9), it seems probable that too low values for $S_{\mathrm{l},0}$ are the reason for the bad prediction accuracy of the developed model at lean conditions.

5.4.2 Markstein Length

The influence of Markstein length L_{M} on the predicted flashback limits is illustrated in Fig. 5.6 and summarized for three equivalence ratios in Tab. 5.2. The errorbars in Fig. 5.6 mark a variation in the absolute value of L_{M} of ±20 %. At lean conditions, an increase of $|L_{\mathrm{M}}|$ leads to higher burning velocities due to flame stretch and, hence, higher flashback limits. The effect is reduced by preheating due to a reduction in absolute Markstein length. At $T_{\mathrm{u}} = 673\,\mathrm{K}$, the change in flashback limit is below 1 %. This shows that an uncertainty in Markstein length is not likely to be the reason for the unsatisfying prediction accuracy of the developed model at lean preheated conditions.

For equivalence ratios beyond the cross-over of L_{M} to positive values, an increase in Markstein length leads to lower velocities at flashback due to reduced burning velocities. Again, the relative changes in flashback limit are smaller at preheated conditions. Overall, the influence of a ±20 % variation in Markstein

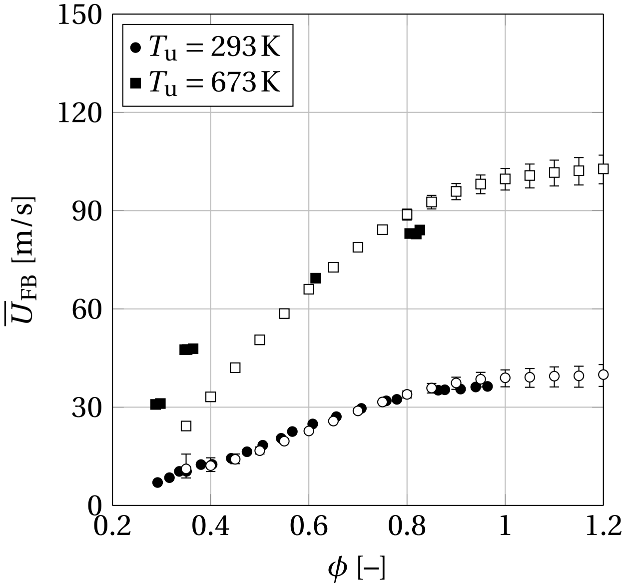

Figure 5.6: Influence of a ±20 % change in $|L_\mathrm{M}|$ on the confined flashback limits of a $d_\mathrm{h} = 31.5\,\mathrm{mm}$ channel burner. Empty symbols: prediction, filled symbols: experiment [9].

Table 5.2: Relative changes of the predicted $\overline{U}_{\mathrm{FB}}$ of confined flames due to a ±20 % variation of $|L_\mathrm{M}|$.

ϕ	T_u [K]	$\frac{\Delta\overline{U}_{\mathrm{FB}}(1.2\lvert L_\mathrm{M}\rvert)}{\overline{U}_{\mathrm{FB}}}$ [%]	$\frac{\Delta\overline{U}_{\mathrm{FB}}(0.8\lvert L_\mathrm{M}\rvert)}{\overline{U}_{\mathrm{FB}}}$ [%]
0.4	293	+19.70	−14.78
0.7	293	−1.04	+1.06
1.0	293	−6.20	+7.05
0.4	673	+0.61	−0.61
0.7	673	−1.24	+1.27
1.0	673	−3.18	+3.39

length is smaller than the effect of unstretched laminar burning velocity except from lean conditions where the absolute values of L_M are high.

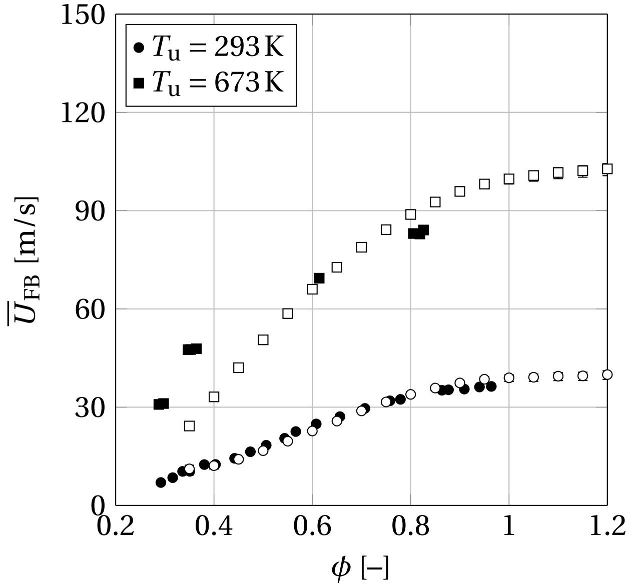

Figure 5.7: Influence of a ±20 % change in Λ on the confined flashback limits of a $d_{\mathrm{h}} = 31.5\,\mathrm{mm}$ channel burner. Empty symbols: prediction, filled symbols: experiment [9].

5.4.3 Turbulent Macroscale

Figure 5.7 shows the effect of a ±20 % variation of the turbulent macroscale Λ on the predicted flashback limits $\overline{U}_{\mathrm{FB}}$. As an increase in turbulent macroscale leads to lower flame stretch rates, it has a reversed effect on flashback limits compared to the Markstein length. This means that a higher Λ leads to lower $\overline{U}_{\mathrm{FB}}$ for $L_{\mathrm{M}} < 0$ and to higher $\overline{U}_{\mathrm{FB}}$ for $L_{\mathrm{M}} > 0$. The relative changes in flashback limit are small compared to a ±20 % variation of $|L_{\mathrm{M}}|$ as shown in Tab. 5.3.

5.4.4 Turbulent Velocity Fluctuations

The turbulent velocity fluctuations at the location of flashback are determined from the distribution of normalized turbulent velocity fluctuations close to the burner wall in fully developed duct flow. As this distribution is well known from experiments and direct numerical simulations, the uncertainty in $u'(y_{\mathrm{FB}})/u_\tau$ is low. However, if the flow in the burner duct was not fully developed, there would be a change in the maximum of $u'(y_{\mathrm{FB}})/u_\tau$. Figure 5.8

Table 5.3: Relative changes of the predicted $\overline{U}_{\mathrm{FB}}$ of confined flames due to a ±20 % variation of Λ.

ϕ	T_{u} [K]	$\frac{\Delta \overline{U}_{\mathrm{FB}}(1.2\,\Lambda)}{\overline{U}_{\mathrm{FB}}}$ [%]	$\frac{\Delta \overline{U}_{\mathrm{FB}}(0.8\,\Lambda)}{\overline{U}_{\mathrm{FB}}}$ [%]
0.4	293	−5.60	+8.45
0.7	293	+0.36	−0.47
1.0	293	+2.30	−2.93
0.4	673	−0.22	+0.30
0.7	673	+0.45	−0.60
1.0	673	+1.19	−1.56

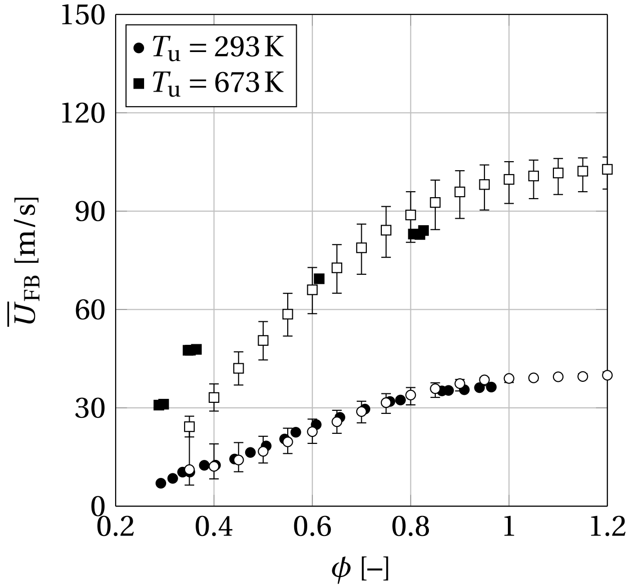

Figure 5.8: Influence of a ±20 % change in $u'(y_{\mathrm{FB}})/u_{\tau}$ on the confined flashback limits of a $d_{\mathrm{h}} = 31.5\,\mathrm{mm}$ channel burner. Empty symbols: prediction, filled symbols: experiment [9].

depicts the effect of such a change in normalized turbulent velocity fluctuations at the location of flashback. The errorbars mark a variation of ±20 % in $u'(y_{\mathrm{FB}})/u_{\tau}$. The resulting relative changes in $\overline{U}_{\mathrm{FB}}$ are summarized in Tab. 5.4.

As the normalized turbulent velocity fluctuations mainly influence the turbulent burning velocity, a change in $u'(y_{\mathrm{FB}})/u_{\tau}$ is directly proportional to the calculated flashback limits. At lean conditions, the relative changes in $\overline{U}_{\mathrm{FB}}$

Table 5.4: Relative changes of the predicted $\overline{U}_{\mathrm{FB}}$ of confined flames due to a ±20 % variation of $u'(y_{\mathrm{FB}})/u_\tau$.

ϕ	T_{u} [K]	$\frac{\Delta\overline{U}_{\mathrm{FB}}(1.2\,u'(y_{\mathrm{FB}})/u_\tau)}{\overline{U}_{\mathrm{FB}}}$ [%]	$\frac{\Delta\overline{U}_{\mathrm{FB}}(0.8\,u'(y_{\mathrm{FB}})/u_\tau)}{\overline{U}_{\mathrm{FB}}}$ [%]
0.4	293	+56.42	−31.41
0.7	293	+10.91	−11.93
1.0	293	+0.41	−3.15
0.4	673	+12.53	−12.47
0.7	673	+9.17	−10.24
1.0	673	+5.42	−7.37

are high compared to the other parameters investigated so far because the stretched laminar burning velocity is increased by higher flame stretch rates leading to an even higher increase in turbulent burning velocity. With increasing equivalence ratio, the influence is reduced as the effect of flame stretch decreases. Above the cross-over of L_{M} to positive values, high flame stretch rates reduce the stretched laminar burning velocity. At high preheating temperature, the effect of $u'(y_{\mathrm{FB}})/u_\tau$ is smaller compared to ambient temperature for lean mixtures but higher around stoichiometry. The strong influence of $u'(y_{\mathrm{FB}})/u_\tau$ shows that it is very important to correctly describe the turbulence field inside a burner geometry in order to estimate flashback limits.

5.4.5 Turbulent Burning Velocity Correlation

The turbulent burning velocity correlation applied in this study is based on Damköhler's theory for small scale turbulence. The only coefficient which was chosen to represent the experimental flashback limits as good as possible is the pre-exponential factor C_{S}. The influence of a variation in this factor is illustrated in Fig. 5.9 and Tab. 5.5. The errorbars in Fig. 5.9 mark a ±20 % variation of C_{S}. Overall, increasing C_{S} leads to higher turbulent burning velocities and a shift of flashback limits to higher flow velocities. As in the previous section, there is a high relative change of flashback limits at lean conditions and a reduced influence with increasing equivalence ratio. However, the influence around stoichiometry is still significantly higher than for the $u'(y_{\mathrm{FB}})/u_\tau$ vari-

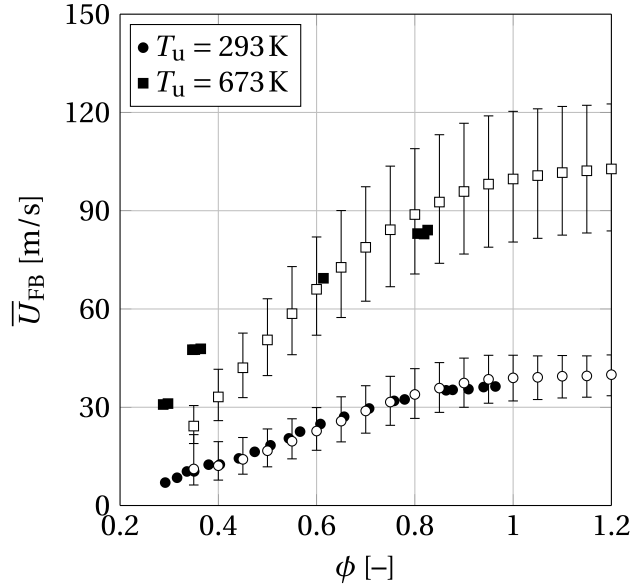

Figure 5.9: Influence of a ±20 % change in C_S on the confined flashback limits of a $d_h = 31.5$ mm channel burner. Empty symbols: prediction, filled symbols: experiment [9].

Table 5.5: Relative changes of the predicted $\overline{U}_{FB}$ of confined flames due to a ±20 % variation of C_S.

ϕ	T_u [K]	$\frac{\Delta\overline{U}_{FB}(1.2\,C_S)}{\overline{U}_{FB}}$ [%]	$\frac{\overline{U}_{FB}(0.8\,C_S)}{\overline{U}_{FB}}$ [%]
0.4	293	+60.49	−36.17
0.7	293	+26.71	−23.47
1.0	293	+17.74	−18.07
0.4	673	+25.48	−21.81
0.7	673	+23.47	−20.87
1.0	673	+20.71	−19.31

ation because flame stretch rates are not affected by C_S and, therefore, the stretched laminar burning velocity remains unchanged. This leads to the highest influence on flashback limits compared to the other analyzed parameters. At $T_\mathrm{u} = 673\,\mathrm{K}$, the relative changes in $\overline{U}_\mathrm{FB}$ are comparable to a variation of the unstretched laminar burning velocity. This shows that the correlation for S_t is also a candidate that might cause the unsatisfying prediction accuracy at lean preheated conditions.

In general, the sensitivity analysis shows that for the analysis of flame flashback it is very important to correctly reproduce the fuel properties and their responses to turbulence. For that purpose, basic studies should be conducted to improve the data base for unstretched laminar burning velocities, Markstein lengths and the effect of turbulence on burning velocity especially at conditions relevant for gas turbines.

6 Prediction of Unconfined Flashback Limits

The mechanism of boundary layer flashback of unconfined flames is significantly different than for confined flames as introduced in Sec. 1.1.2.1. At the beginning of this chapter, an analytic model to predict flashback limits of unconfined laminar flames is introduced. Afterwards, an analytic model for turbulent flames is developed.

6.1 Prediction Model for Laminar Flames

Boundary layer flashback in laminar tube burner flames was already investigated in 1943 by Lewis and von Elbe [14] and in 1945 by von Elbe and Mentser [15]. Figure 6.1 summarizes their observations. At sufficiently high velocity, a stable laminar flame forms at the burner exit (1). Close to the burner exit the reaction is quenched due to heat losses to the wall and the flame root is bent outwards. If the velocity is reduced, this outward bending is increased until in some parts the flame front becomes perpendicular to the incoming flow.

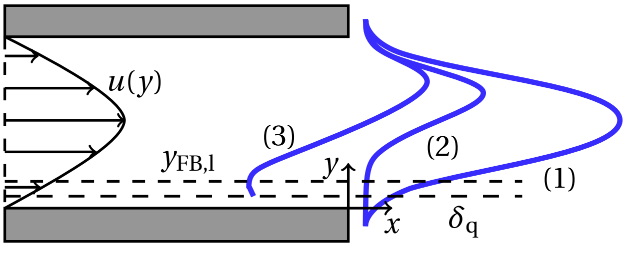

Figure 6.1: Boundary layer flashback of a laminar tube burner flame. (1): Stable flame, (2): flame at flashback conditions, (3): upstream propagating flame.

If this situation extends beyond the wall distance of laminar flashback $y_{\mathrm{FB,l}}$, the flashback limit is reached (2). Further reduction of the flow velocity leads to upstream flame propagation close to the burner wall at $y_{\mathrm{FB,l}}$ (3). According to these observations, the flashback limit can be estimated by comparing the flow velocity and the stretched laminar burning velocity at $y_{\mathrm{FB,l}}$:

$$u(y_{\mathrm{FB,l}}) = S_{\mathrm{l,s}}\,. \tag{6.1}$$

The wall distance of laminar flashback is determined by flame quenching close to the burner wall. As introduced in Sec. 2.3.4, $y_{\mathrm{FB,l}}$ can be set to three times the quenching distance δ_{q}:

$$y_{\mathrm{FB,l}} = 3\,\delta_{\mathrm{q}} = 3\,\mathrm{Pe}_{\mathrm{q}}\delta_{\mathrm{F}}\,. \tag{6.2}$$

The quenching distance is obtained from the quenching Péclet number Pe_{q}. The stretched laminar burning velocity required in Eq. (6.1) can be calculated from Eq. (2.48). L_{M} is derived as described in Sec. 2.3.2.2. The flame stretch rate in the laminar case significantly differs from the turbulent case where it is predominantly caused by velocity fluctuations (cf. Sec. 2.3.2.1). In laminar flames, flame stretch can be described by the dimensionless Karlovitz number

$$\mathrm{Ka} = \frac{\delta_F}{u}\frac{\mathrm{d}u}{\mathrm{d}y} \tag{6.3}$$

depending on the velocity gradient parallel to the flame front as introduced by Lewis and von Elbe [129]. At the location of flashback initiation, where the flame front is perpendicular to the flow of unburned mixture, the velocity gradient parallel to the flame front is described by $\mathrm{d}u/\mathrm{d}y$. As the flame stretch rate κ is directly proportional to Ka, it is also proportional to the velocity gradient:

$$\kappa = C_\kappa \frac{\mathrm{d}u}{\mathrm{d}y}\,. \tag{6.4}$$

Since the model constant C_κ depends on the ratio of local burning velocity to flow velocity it is set to unity. Using the derivative of the laminar velocity profile in Eq. (2.4), the flame stretch rate

$$\kappa = -\frac{8\overline{U}}{h}\left(2\frac{y}{h} - 1\right) \tag{6.5}$$

is obtained based on bulk flow velocity $\overline{U}$ and wall distance y. The final set of equations to predict boundary layer flashback limits of laminar unconfined flames is summarized in the following section.

6.1.1 Summary of Equations

The model to predict laminar flashback limits consists of the following five equations:

1) Eq. (2.4) $u(y_{\mathrm{FB,l}}) = 2\,\overline{U}_{\mathrm{FB,l}}\left(1-\left(\frac{2\,y_{\mathrm{FB,l}}}{h}-1\right)^2\right)$,
2) Eq. (6.2) $y_{\mathrm{FB,l}} = 3\,\mathrm{Pe_q}\delta_{\mathrm{F}}$,
3) Eq. (6.1) $u(y_{\mathrm{FB,l}}) = S_{\mathrm{l,s}}(y_{\mathrm{FB,l}})$,
4) Eq. (2.48) $S_{\mathrm{l,s}}(y_{\mathrm{FB,l}}) = S_{\mathrm{l,0}} - L_{\mathrm{M}}\kappa(y_{\mathrm{FB,l}})$,
5) Eq. (6.5) $\kappa(y_{\mathrm{FB,l}}) = -\frac{8\,\overline{U}_{\mathrm{FB,l}}}{h}\left(2\frac{y_{\mathrm{FB,l}}}{h}-1\right)$.

The wall distance at flashback is defined by quenching phenomena at the burner wall. The corresponding quenching Péclet numbers are set to $\mathrm{Pe_q} = 1.4$ for hydrogen-air mixtures and to $\mathrm{Pe_q} = 2.5$ for methane-air mixtures (cf. Sec. 2.3.4). Unstretched laminar burning velocity $S_{\mathrm{l,0}}$, laminar flame thickness δ_F and Markstein length L_{M} are defined as introduced in Sec. 2.3.1.2, 2.3.1.3 and 2.3.2.2. The system of equations can be solved analytically to one expression for the laminar flashback limit:

$$\overline{U}_{\mathrm{FB,l}} = \frac{S_{\mathrm{l,0}}}{2\left(1-\left(\frac{6\,\mathrm{Pe_q}\delta_{\mathrm{F}}}{h}-1\right)^2\right)-\frac{8\,L_{\mathrm{M}}}{h}\left(\frac{6\,\mathrm{Pe_q}\delta_{\mathrm{F}}}{h}-1\right)}\,. \tag{6.6}$$

This expression will be validated in the following section using literature data for experimentally determined flashback limits of laminar tube burner flames. It can be noted, that for laminar flames, the flashback limit is defined by flame stretch and wall quenching. In Sec. 6.2, it will be shown that this is different for turbulent flames, where turbulent velocity fluctuations have the main influence on $\overline{U}_{\mathrm{FB}}$.

6.1.2 Model Validation

Using the mixture properties introduced in Sec. 2.3, Eq. (6.6) can be validated for hydrogen-air and methane-air mixtures as shown in the following.

6.1.2.1 Hydrogen-Air Mixtures

Flashback studies of laminar hydrogen-air flames have been conducted by von Elbe and Mentser in 1945 [15]. In Fig. 6.2 their experimental flashback limits are compared to the results from Eq. (6.6) for different burner diameters h. The experimental data are well reproduced by the prediction model.

The corresponding wall distances of flashback are shown in Fig. 6.3(a). As the location of flashback only depends on quenching Péclet number and flame thickness, $y_{\mathrm{FB,l}}$ is not a function of tube diameter but decreases with equivalence ratio. Maximum wall distances of flashback around $y_{\mathrm{FB,l}} = 1\,\mathrm{mm}$ are found at $\phi = 0.35$. For fuel-rich mixtures $y_{\mathrm{FB,l}}$ drops down to 0.16 mm.

The associated flame stretch rates are depicted in Fig. 6.3(b). They increase with equivalence ratio up to $\kappa(y_{\mathrm{FB,l}}) = 9300\,/\mathrm{s}$ at $\phi = 1.3$. There is only a small variation with tube diameter. In all cases, the Karlovitz number is smaller than 0.3 so that Eq. (2.48) holds.

The importance of flame stretch can be easily seen if the Markstein length in Eq. (6.6) is set to $L_{\mathrm{M}} = 0$ which leads to high deviations of the predicted flashback limits from the experimental data (cf. Fig. 6.4). Especially around stoichiometry and at rich conditions, the velocity at flashback is significantly overestimated because the reduction of burning velocity due to flame stretch and positive Markstein length is not accounted for.

6.1.2.2 Methane-Air Mixtures

In 1949, Harris et al. [17] investigated flashback of laminar methane-air flames. In Fig. 6.5, their experimental results are compared to the flashback limits calculated with Eq. (6.6) for different burner diameters. The obtained

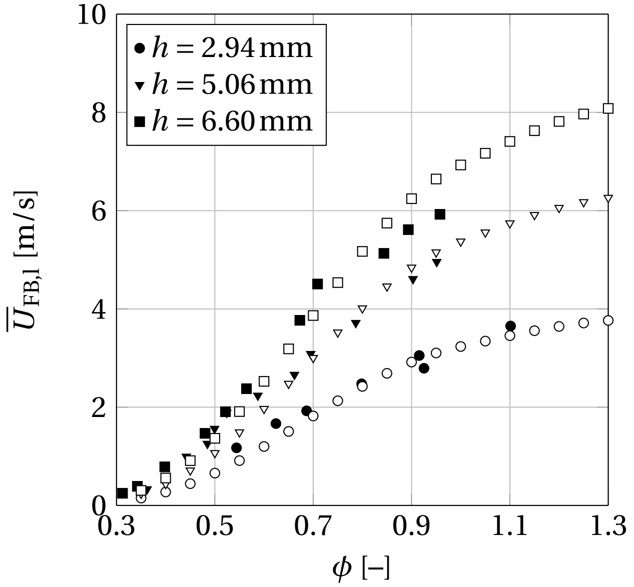

Figure 6.2: Comparison of calculated flashback limits of laminar hydrogen-air flames (empty symbols) with experimental data for different burner tube diameters [15] (filled symbols).

flow velocities at flashback are about ten times lower than the flashback limits for hydrogen-air mixtures presented in Fig. 6.2. Moreover, $\overline{U}_{\mathrm{FB,l}}$ decreases for fuel-rich mixtures after a maximum is reached around stoichiometry. This reflects the behavior of the unstretched laminar burning velocity of methane-air mixtures discussed in Sec. 2.3.1.2 and is well reproduced by the prediction model.

The calculated wall distances of flashback $y_{\mathrm{FB,l}}$ and the corresponding flame stretch rates at flashback conditions are presented in Fig. 6.6. Due to the higher Péclet number and the lower flame thicknesses, the wall distances of flashback are higher compared to hydrogen-air mixtures. The maximum wall distance of $y_{\mathrm{FB,l}} \approx 4\,\mathrm{mm}$ is found at lean conditions. With increasing equivalence ratio, $y_{\mathrm{FB,l}}$ drops to a minimum of $y_{\mathrm{FB,l}} \approx 1\,\mathrm{mm}$ around stoichiometry and increases again for fuel-rich mixtures. The flame stretch rate is directly proportional to the velocity at flashback and increases with equivalence ratio up to a maximum of $\kappa(y_{\mathrm{FB,l}}) = 350\,/\mathrm{s}$ at stoichiometry. The associated Karlovitz numbers are smaller than 0.12.

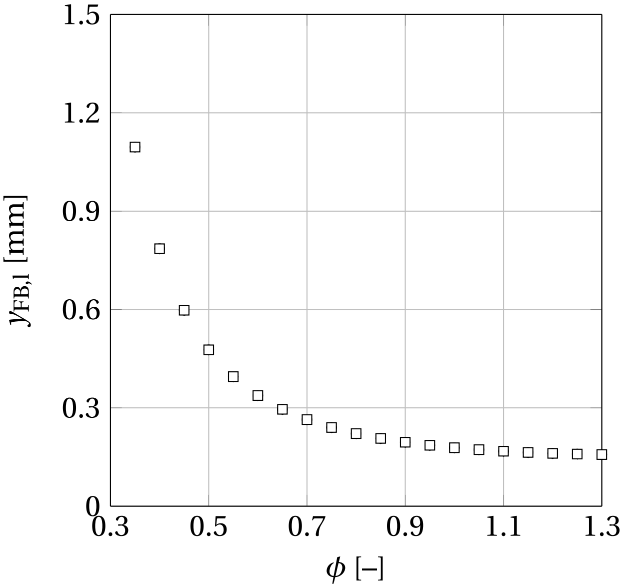

(a) Wall distance of flashback

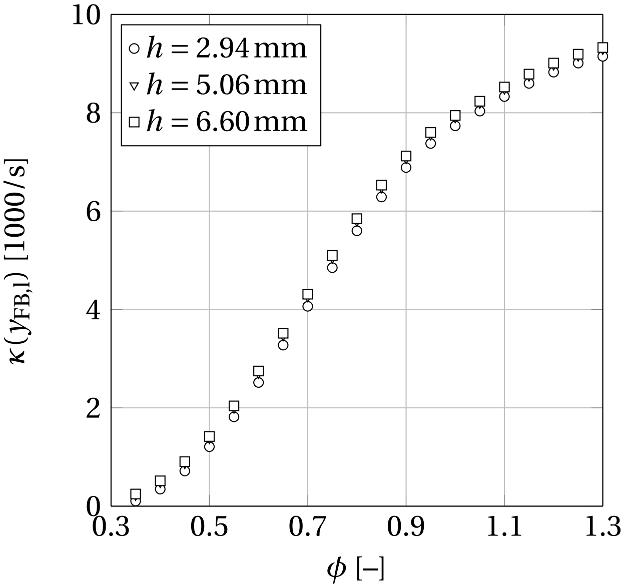

(b) Flame stretch rate at flashback conditions

Figure 6.3: Calculated parameters of boundary layer flashback of laminar hydrogen-air flames.

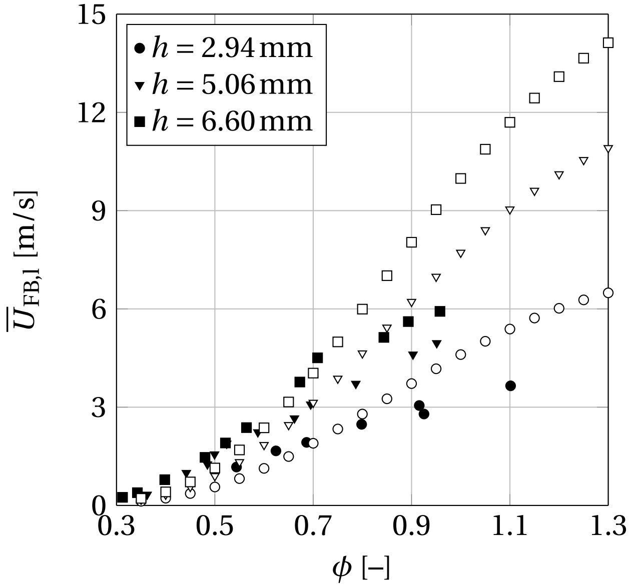

Figure 6.4: Calculated flashback limits of laminar hydrogen-air flames (empty symbols) neglecting the influence of flame stretch ($L_{\mathrm{M}} = 0$). Filled symbols: experimental data [15].

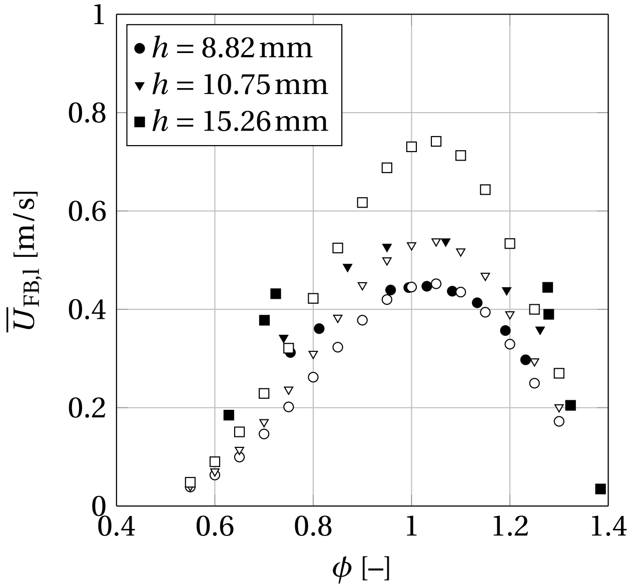

Figure 6.5: Comparison of calculated flashback limits of laminar methane-air flames (empty symbols) with experimental data for different burner tube diameters [17] (filled symbols).

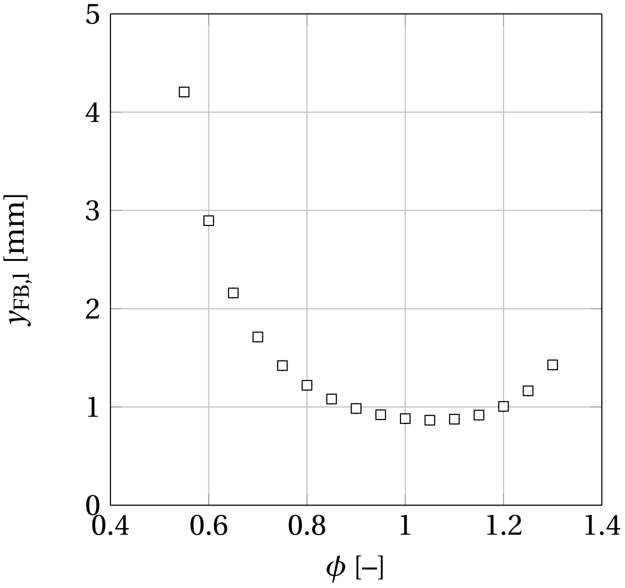

(a) Wall distance of flashback

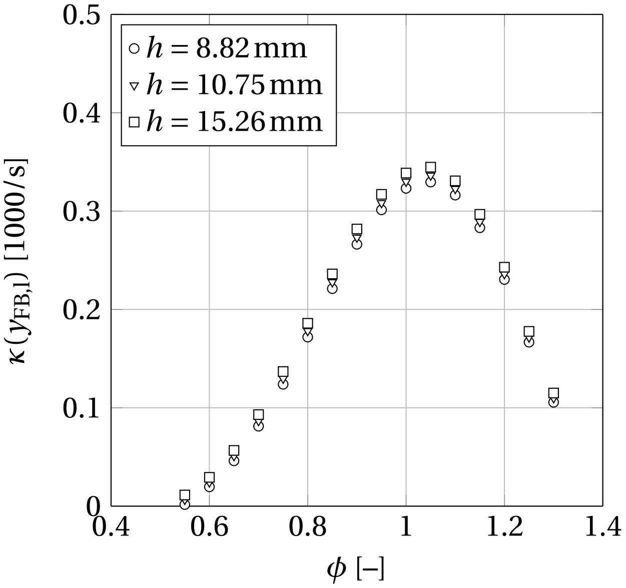

(b) Flame stretch rate at flashback conditions

Figure 6.6: Calculated parameters of boundary layer flashback of laminar methane-air flames.

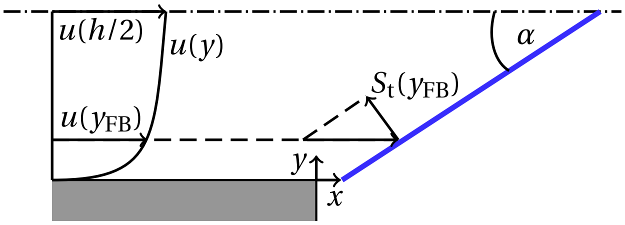

Figure 6.7: Local analysis of unconfined boundary layer flashback [35].

6.2 Prediction Model for Turbulent Flames

From their experimental results Baumgartner et al. [34] concluded that the boundary layer flashback limit in turbulent flames is reached if the local flow velocity falls below the turbulent burning velocity. A similar approach is presented in this work. In a local analysis, the flow velocity component perpendicular to the flame front is compared to the local turbulent burning velocity at the location of flashback initiation. The required flame angle is estimated from global mass conservation. However, other methods to define the flame angle can be easily combined with the local analysis which fully contains the physics of the flashback process. The prediction model described in the following sections estimates the flow conditions where the probability for the formation of an initial distortion in the flame front, which is then able to propagate upstream, is high. The transient phenomenon of upstream flame propagation is not described. It is assumed that the formation of the initial distortion is triggered by flame front instabilities.

6.2.1 Local Analysis of Flashback Initiation

The local conditions at the onset of boundary layer flashback are illustrated in Fig. 6.7. The flame front represented as a blue line is simplified to a triangular shape in channel burners and to a cone shape in tube burners. Based on the experimental observations of Baumgartner et al. [34], it is assumed that at the wall distance of flashback initiation y_{FB} the component of the local flow velocity $u(y_{FB})$ perpendicular to the flame front is equal to the local turbulent burning velocity $S_\mathrm{t}(y_\mathrm{FB})$:

$$S_\mathrm{t}(y_\mathrm{FB}) = u(y_\mathrm{FB})\,\sin(\alpha_\mathrm{FB})\,. \tag{6.7}$$

Assuming that the local velocity along the streamline of flashback initiation (dashed line) does not significantly change from the fully developed flow inside the burner to the point where it passes the flame front, $u(y_\mathrm{FB})$ can be connected to u_τ using Eq. (2.20) if the normalized wall distance of flashback y^+_FB is known. The shear stress velocity u_τ can then be related to the flashback limit $\overline{U}_\mathrm{FB}$ via Eq. (2.26) for channel and via Eq. (2.27) for tube burners. It is assumed that flashback is initiated along the streamline of maximum turbulent burning velocity which is, similar to the prediction model for confined flames, the streamline of maximum turbulent velocity fluctuations at $y^+_\mathrm{FB} = 16.4$. The turbulence field downstream of the burner exit was discussed in Sec. 2.2.4. From microscopic PIV data of Baumgartner [10] (cf. Fig. 2.4) the normalized turbulent velocity fluctuations are estimated to

$$\frac{u'(y_\mathrm{FB})}{u_\tau} = 1.5\,. \tag{6.8}$$

The normalized turbulent velocity fluctuations are used in combination with the stretched laminar burning velocity $S_\mathrm{l,s}$ (Eq. (2.48)) to compute the turbulent burning velocity. For S_t, the same correlation as in the confined flashback model is applied (Eq. (2.85),(5.10)). Finally, only the flame angle α_FB at flashback is required to solve the model for the flashback limit $\overline{U}_\mathrm{FB}$. One possible method to model the averaged flame angle is presented in the following section.

6.2.2 Global Analysis to Estimate Flame Angle at Flashback

The main purpose of the global analysis indicated in Fig. 6.8 is the estimation of the flame angle at flashback α_FB. If the simplification of a triangular or cone shaped flame is assumed, α_FB can be obtained from mass conservation:

$$\dot{m}_\mathrm{B} = \dot{m}_\mathrm{F}\,. \tag{6.9}$$

The mass flow rate $\dot{m}_\mathrm{B} = \rho_\mathrm{u} A_\mathrm{B} \overline{U}_\mathrm{FB}$ inside the burner duct has to be equal to the mass flow rate $\dot{m}_\mathrm{F} = \rho_\mathrm{u} A_\mathrm{F} \overline{S}_\mathrm{t}$ consumed by the turbulent flame brush leading

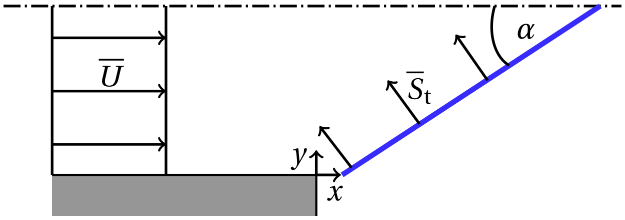

Figure 6.8: Local analysis of unconfined boundary layer flashback to estimate the flame angle at flashback [35].

to:

$$\frac{A_\mathrm{B}}{A_\mathrm{F}} = \frac{\overline{S}_\mathrm{t}}{\overline{U}_\mathrm{FB}}. \tag{6.10}$$

For triangular and cone shaped flames the area ratio $A_\mathrm{B}/A_\mathrm{F}$ can be replaced by $\sin(\alpha_\mathrm{FB})$. Finally, a relation very similar to the local analysis in Eq. (6.7) is obtained only based on average flow properties:

$$\sin(\alpha_\mathrm{FB}) = \frac{\overline{S}_\mathrm{t}}{\overline{U}_\mathrm{FB}}. \tag{6.11}$$

Since Eq. (6.11) also depends on the flashback limit $\overline{U}_\mathrm{FB}$, it is coupled to the local analysis and cannot be solved independently. Therefore, local and global analysis have to be combined to one system of equations which is solved numerically for $\overline{U}_\mathrm{FB}$.

The average turbulent burning velocity $\overline{S}_\mathrm{t}$ is computed from Eq. (5.10) based on average stretched laminar burning velocity $\overline{S}_\mathrm{l,s}$ and average turbulent velocity fluctuations $\overline{u'}_\mathrm{FB}$. $\overline{S}_\mathrm{l,s}$ is obtained from Eq. (2.48) and an average flame stretch rate $\overline{\kappa}$. The turbulent velocity fluctuations averaged over the flame front $\overline{u'}_\mathrm{FB}$ are discussed in the following section.

6.2.3 Flame Generated Turbulence

The average turbulent velocity fluctuations in the burner duct $\overline{u'}_\mathrm{B}$ can be estimated from the correlation for fully developed duct flow given in Eq. (2.25). However, experimental data show that the turbulence intensity increases if a flame is stabilized at the burner exit. Figure 6.9 depicts two examples for the

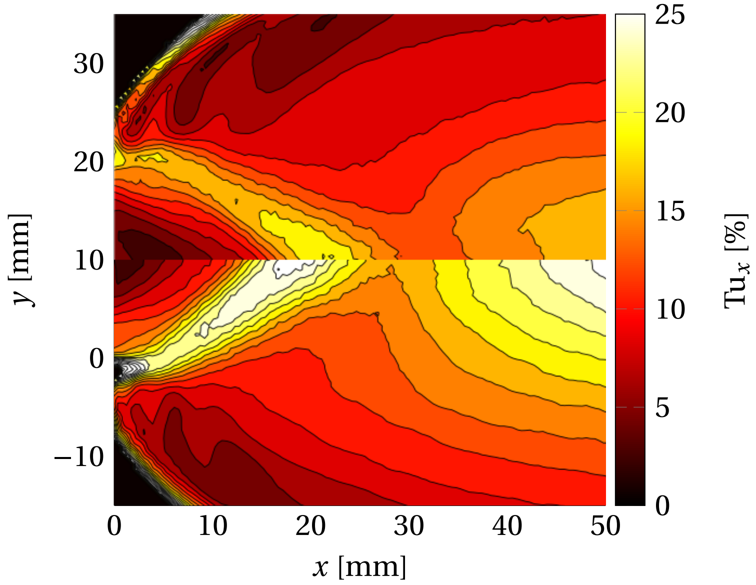

Figure 6.9: Turbulence field of a hydrogen-air flame downstream of a d_h = 31.5 mm channel burner. Lower half: $\phi = 0.77$, upper half: $\phi = 0.59$.

turbulence field of hydrogen-air flames at $\phi = 0.77$ (lower half) and $\phi = 0.59$ (upper half) obtained in PIV measurements downstream of the $d_\mathrm{h} = 31.5$ mm channel burner described in Chap. 3. At the burner exit, a typical duct flow turbulence intensity of around 5 % is observed. Further downstream the turbulence intensity increases up to a maximum at the flame front. This effect is caused by upstream parts of the flame which generate high turbulence intensities in more downstream flame regions. The maximum turbulence intensity increases with equivalence ratio.

A similar behavior was observed by Yansong Liu for premixed methane-air and hydrogen-methane-air flames at ambient temperature [130]. His results are summarized in Fig. 6.10. Liu derived the correlation

$$\frac{u'_\mathrm{F}}{u'_\mathrm{B}} = 1 + 0.181 \left(\frac{S_{\mathrm{l},0}}{u'_\mathrm{B}} \right)^{2.1} \tag{6.12}$$

to describe flame generated turbulence u'_F based on the turbulent velocity fluctuations upstream of the flame u'_B and the unstretched laminar burning

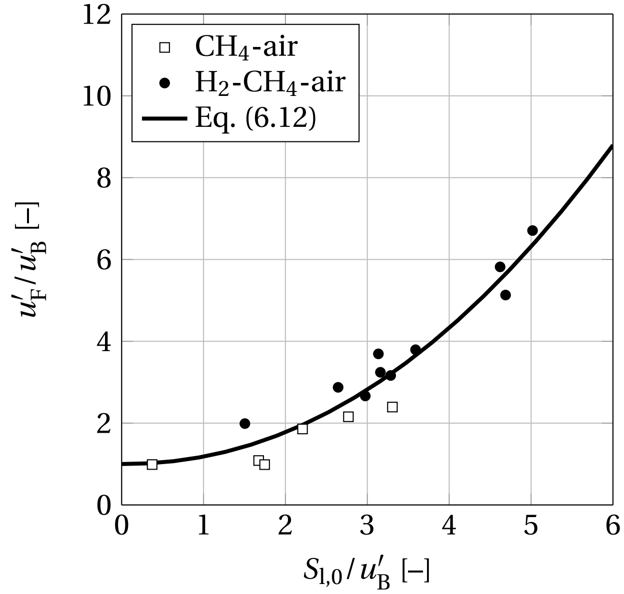

Figure 6.10: Turbulence generated in methane-air and hydrogen-methane-air flames [130].

velocity $S_{l,0}$. A similar correlation

$$\frac{\overline{u'}_{FB}}{\overline{u'}_B} = 1 + G_1 \left(\frac{S_{l,0}}{\overline{u'}_B}\right)^{G_2} \left(\frac{T_u}{T_{u,ref}}\right)^{G_3} \left(\frac{p}{p_{ref}}\right)^{G_4} \tag{6.13}$$

will be used here for the averaged turbulent velocity fluctuations $\overline{u'}_{FB}$ of hydrogen-air mixtures. As preheated conditions will be used for model validation in Sec. 6.2.5 as well, but Liu [130] only analyzed ambient temperatures, an additional temperature dependence is included ($T_{u,ref} = 293\,K$). In the same way a power law term can be used to estimate the effect of pressure ($p_{ref} = 1\,bar$). The pre-exponential factor G_1, the exponent G_2 and the temperature exponent G_3 are adapted to experimental data and are presented in Sec. 6.2.4. A discussion of the pressure effect is included in App. A.

6.2.4 Summary of Equations

The model to predict boundary layer flashback limits of unconfined, burner stabilized flames consisting of local and global analysis can be summarized in the following thirteen equations:

A) Local analysis:

1) Eq. (6.7) $S_{\mathrm{t}}(y_{\mathrm{FB}}) = u(y_{\mathrm{FB}})\sin(\alpha_{\mathrm{FB}})\,,$

2) Eq. (5.10) $S_{\mathrm{t}}(y_{\mathrm{FB}}) = S_{\mathrm{l,s}}(y_{\mathrm{FB}})\left(1 + C_{\mathrm{S}}\left(\frac{u'(y_{\mathrm{FB}})}{S_{\mathrm{l,s}}(y_{\mathrm{FB}})}\right)^{0.5}\right)\,,$

3) Eq. (2.48), (2.59) $S_{\mathrm{l,s}}(y_{\mathrm{FB}}) = S_{\mathrm{l,0}} - L_{\mathrm{M}}\left(\frac{2}{3}\Gamma_{\mathrm{K}}(y_{\mathrm{FB}})\frac{u'(y_{\mathrm{FB}})}{\Lambda} + \frac{1}{2}\frac{u'(y_{\mathrm{FB}})}{\Lambda}\right)\,,$

4) Eq. (2.54)

$$\log_{10}\left(\Gamma_{\mathrm{K}}(y_{\mathrm{FB}})\right) = -\frac{1}{s+0.4}\mathrm{e}^{-(s+0.4)} + \left(1-\mathrm{e}^{-(s+0.4)}\right)$$
$$\left(\frac{2}{3}\left(1-\frac{1}{2}\mathrm{e}^{\left(-\left(u'(y_{\mathrm{FB}})/S_{\mathrm{l,0}}\right)^{1/3}\right)}\right)s - 0.11\right)\,,$$

Eq. (2.55) $s = \log_{10}\left(\frac{\Lambda}{\delta_{\mathrm{F}}}\right)\,,$

5) Eq. (6.8) $u'(y_{\mathrm{FB}}) = 1.5\,u_\tau\,,$

6) Eq. (2.20)

$$y^+_{\mathrm{FB}} = u^+(y_{\mathrm{FB}}) + 0.1108\left(\mathrm{e}^{0.4\,u^+(y_{\mathrm{FB}})} - 1 - 0.4\,u^+(y_{\mathrm{FB}})\right.$$
$$\left. - \frac{\left(0.4\,u^+(y_{\mathrm{FB}})\right)^2}{2} - \frac{\left(0.4\,u^+(y_{\mathrm{FB}})\right)^3}{6} - \frac{\left(0.4\,u^+(y_{\mathrm{FB}})\right)^4}{24}\right) = 16.4\,,$$

7) Eq. (2.26) Channel burner: $\frac{\overline{U}_{\mathrm{FB}}}{u_\tau} = \frac{1}{K}\ln\left(\frac{h\,u_\tau}{\nu_{\mathrm{u}}}\right) + B - \frac{1}{K}\,,$

Eq. (2.27) Tube burner: $u_\tau^2 = 0.03955\,\overline{U}_{\mathrm{FB}}^{7/4}\,\nu_{\mathrm{u}}^{1/4}\,h^{-1/4}\,.$

B) Global analysis:

8) Eq. (6.11) $\sin(\alpha_{\mathrm{FB}}) = \frac{\overline{S}_{\mathrm{t}}}{\overline{U}_{\mathrm{FB}}}\,,$

9) Eq. (5.10) $\overline{S}_{\mathrm{t}} = \overline{S}_{\mathrm{l,s}}\left(1 + C_{\mathrm{S}}\left(\frac{\overline{u'}_{\mathrm{FB}}}{\overline{S}_{\mathrm{l,s}}}\right)^{0.5}\right)\,,$

10) Eq. (2.48), (2.59) $\overline{S}_{\mathrm{l,s}} = S_{\mathrm{l,0}} - L_{\mathrm{M}}\left(\frac{2}{3}\overline{\Gamma}_{\mathrm{K}}\frac{\overline{u'}_{\mathrm{FB}}}{\Lambda} + \frac{1}{2}\frac{\overline{u'}_{\mathrm{FB}}}{\Lambda}\right)\,,$

11) Eq. (2.54) $\log_{10}\left(\overline{\Gamma}_{\mathrm{K}}\right) = -\frac{1}{s+0.4}\mathrm{e}^{-(s+0.4)} + \left(1-\mathrm{e}^{-(s+0.4)}\right)$

$$\left(\frac{2}{3}\left(1-\frac{1}{2}\mathrm{e}^{\left(-\left(\overline{u'}_{\mathrm{FB}}/S_{\mathrm{l},0}\right)^{1/3}\right)}\right)s-0.11\right),$$

12) Eq. (2.25) $$\overline{u'}_{\mathrm{B}}=0.16\left(\frac{d_{\mathrm{h}}\overline{U}_{\mathrm{FB}}}{\nu_{\mathrm{u}}}\right)^{-1/8}\overline{U}_{\mathrm{FB}},$$

13) Eq. (6.13) $$\frac{\overline{u'}_{\mathrm{FB}}}{\overline{u'}_{\mathrm{B}}}=1+G_1\left(\frac{S_{\mathrm{l},0}}{\overline{u'}_{\mathrm{B}}}\right)^{G_2}\left(\frac{T_{\mathrm{u}}}{T_{\mathrm{u,ref}}}\right)^{G_3}\left(\frac{p}{p_{\mathrm{ref}}}\right)^{G_4}.$$

The local analysis contains the physical background of the flashback process, whereas the global analysis is one possibility to calculate the flame angle at flashback. The combined system of non-linear equations can be solved for the flashback limit $\overline{U}_{\mathrm{FB}}$ at a certain equivalence ratio using Newton's method.

The unburned mixture properties are extracted form *Cantera 2.2* [67]. The unstretched laminar burning velocity is computed from the polynomial approach in Eq. (2.41) and the coefficients presented in App. C. The Markstein lengths are calculated as described in Sec. 2.3.2.2. The turbulent macroscale is set to $\Lambda = 0.5\,h$ according to Eq. (2.29). The laminar flame thickness is obtained from Eq. (2.44). For hydrogen-air flames, the model parameter $C_{\mathrm{S}} = 2.6$ is used in agreement with Chap. 5. The parameters for the flame generated turbulence correlation are set to $G_1 = 2.5$, $G_2 = 0.7$ and $G_3 = -0.4$ as good agreement with the experimentally obtained turbulence field was achieved for these values (cf. Sec. 6.2.5). The pressure dependence G_4 is discussed in App. A. The validation of the developed prediction model at atmospheric pressure is described in the following section.

The prediction model for flashback limits of turbulent uconfined flames was originally published in [35]. Compared to the original publication the following details were changed in this work: The temperature dependence of the unstretched laminar burning velocity and the turbulent macroscale are defined differently as described in Sec. 2.3.1.2 and 2.2.4. This leads to changes in other model parameters such as Markstein length, flame stretch rate and turbulent burning velocity. For that reason, the coefficient of the turbulent burning velocity correlation and the parameters of the flame generated turbulence correlation are adapted.

6.2.5 Model Validation

Two different burners are used for validation of the prediction model described in the previous sections. The first data set is presented in Fig. 6.11 and 6.12. Figure 6.11(a) compares the ambient temperature flashback limits, obtained from the channel burner described in Chap. 3 without acoustic forcing, to the predicted values. It can be seen that the prediction model well reproduces the experimental data in the range $0.40 < \phi < 0.85$. Around stoichiometry and in the fuel-rich region no experimental flashback limits can be obtained from the channel burner due to limitations in the effectiveness of the required corner injection. The Reynolds numbers at flashback conditions vary from $\mathrm{Re} = 5000$ to $\mathrm{Re} = 9200$.

Fig. 6.11(b) shows the calculated flame angles at flashback corresponding to the flashback limits in Fig. 6.11(a). They are compared to flame angles obtained from averaged Mie-scattering images at near flashback conditions. The method to determine these averaged flame angles is described in [35]. The predicted flame angles exceed the measured flame angles by about 5°. This is understandable because the measured flame angles were obtained at near flashback conditions. In order to reach flashback conditions, the flame angle has to increase further. Another reason for the deviation between experiment and prediction might be the highly simplified assumption of a triangular shaped flame front.

From the same Mie-scattering images used to obtain the averaged flame angle at flashback, the turbulent velocity fluctuations downstream of the burner exit are extracted with the PIV technique. Two examples are shown in Fig. 6.9. From these fields the averaged turbulent velocity fluctuations are determined by integrating the velocity fluctuations in the flame front over half of the channel height:

$$\overline{u'} = \frac{2}{h}\int_0^{h/2} u'_{\mathrm{F}}(x)\mathrm{d}y\,. \tag{6.14}$$

The result is depicted in Fig. 6.12(a) compared to the predicted velocity fluctuations. Regarding the simplicity of the modeling approach for $\overline{u'}_{\mathrm{FB}}$, the calculated fluctuations satisfactorily follow the experimental values. Below

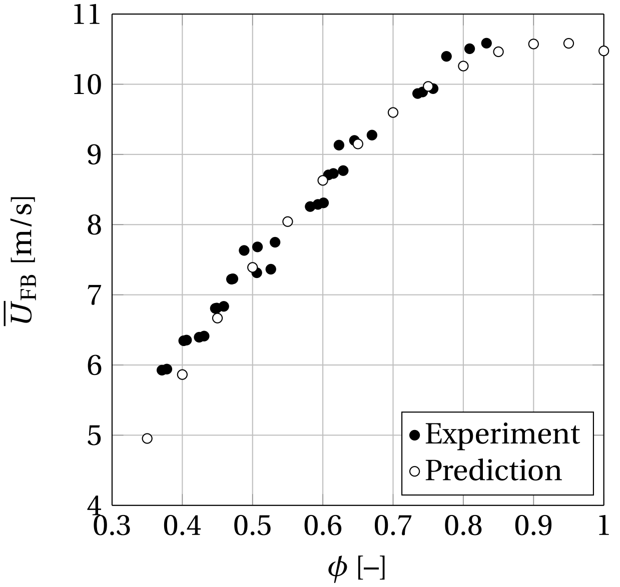

(a) Velocity at flashback

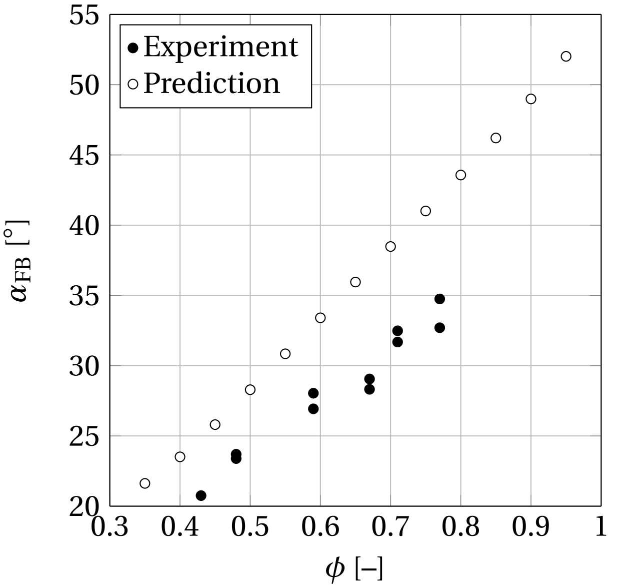

(b) Averaged flame angle at flashback

Figure 6.11: Comparison of predicted unconfined flashback parameters (empty symbols) with experimental results from a $d_{\mathrm{h}} = 31.5\,\mathrm{mm}$ channel burner (filled symbols).

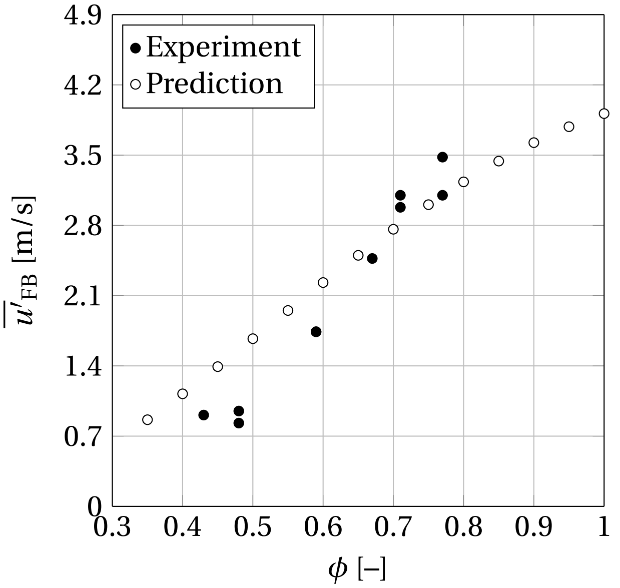

(a) Averaged turbulent velocity fluctuations at flashback

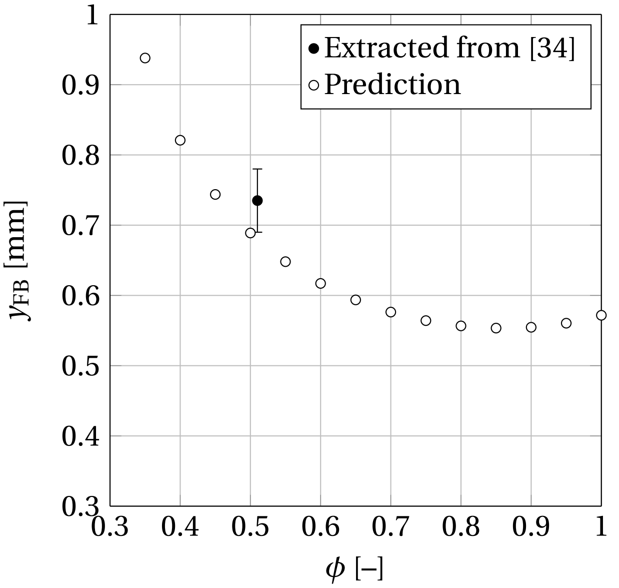

(b) Wall distance of flashback

Figure 6.12: Comparison of predicted unconfined flashback parameters (empty symbols) with experimental results from a $d_{\mathrm{h}} = 31.5\,\mathrm{mm}$ channel burner (filled symbols).

$\phi = 0.65$, the turbulent velocity fluctuations are overestimated whereas there is good agreement around $\phi = 0.7$. It has to be noted that, similar to the flame angles, the experimental data originate from measurements at near flashback conditions. This induces an uncertainty regarding the comparability of experimental and calculated data. Nevertheless, the comparison shows that both are in the same range and that Eq. (6.13) can be applied at ambient conditions to estimate $\overline{u'}_{\mathrm{FB}}$ at flashback.

The last flashback parameter, available from ambient temperature experiments, is the wall distance at flashback y_{FB} presented in Fig. 6.12(b). Baumgartner et al. [34] present an instantaneous microscopic Planar Laser Induced Fluorescence (PLIF) image of a flame at flashback in the $d_{\mathrm{h}} = 31.5\,\mathrm{mm}$ channel burner ($\phi = 0.52$). From their image, a wall distance of flashback of $y_{\mathrm{FB}} = 0.74 \pm 0.05\,\mathrm{mm}$ can be extracted. This value is included in Fig. 6.12(b). The errorbars indicate the uncertainty in the extraction from the PLIF image. The prediction underestimates the wall distance by about 0–10 %. The wall distance decreases for increasing equivalence ratio to a minimum of $y_{\mathrm{FB}} = 0.55\,\mathrm{mm}$ at $\phi = 0.85$.

In order to investigate the influence of preheating on the prediction accuracy of the developed model, flashback limits of a second burner are analyzed. The calculation results are compared to Baumgartner's $d_{\mathrm{h}} = 40\,\mathrm{mm}$ tube burner at three different preheating temperatures up to $T_{\mathrm{u}} = 673\,\mathrm{K}$ [10]. The results are presented in Fig. 6.13 and 6.14. The corresponding Reynolds numbers at flashback conditions are in the range of $6000 < \mathrm{Re} < 20000$. Figure 6.13(a) shows the flashback limits for fuel lean and slightly rich conditions. Filled symbols mark experimental and empty symbols calculated data. At ambient temperature, the flashback limits are satisfactorily reproduced in the whole equivalence ratio range. At $T_{\mathrm{u}} = 473\,\mathrm{K}$ and $\phi < 0.4$ the velocity at flashback is underestimated whereas good agreement is found between $\phi = 0.4$ and $\phi = 0.85$. Unfortunately, no validation data is available for higher equivalence ratios. For higher preheating up to $T_{\mathrm{u}} = 673\,\mathrm{K}$ the prediction model overestimates $\overline{U}_{\mathrm{FB}}$ for $\phi < 0.7$. The deviations at preheated conditions might be caused by the growing uncertainty in the unstretched laminar burning velocity $S_{\mathrm{l},0}$ which, in contrast to the ambient temperature case, is not based on experimental re-

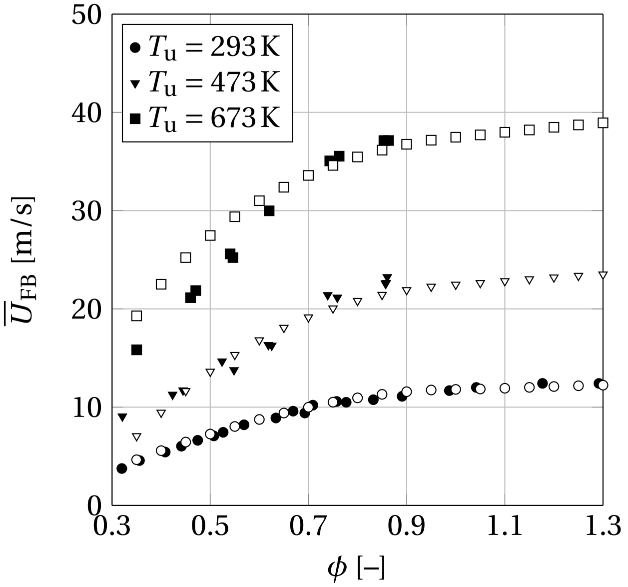

(a) Velocity at flashback

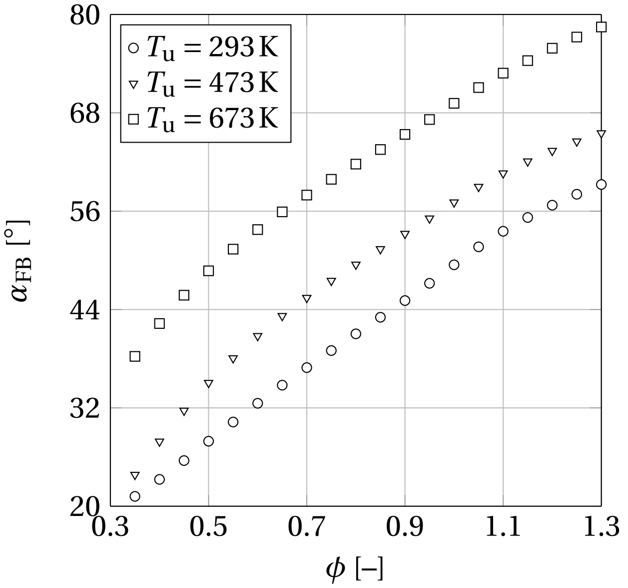

(b) Averaged flame angle at flashback

Figure 6.13: Comparison of predicted unconfined flashback parameters (empty symbols) with experimental results from a $d_h = 40\,\text{mm}$ tube burner (filled symbols) [10].

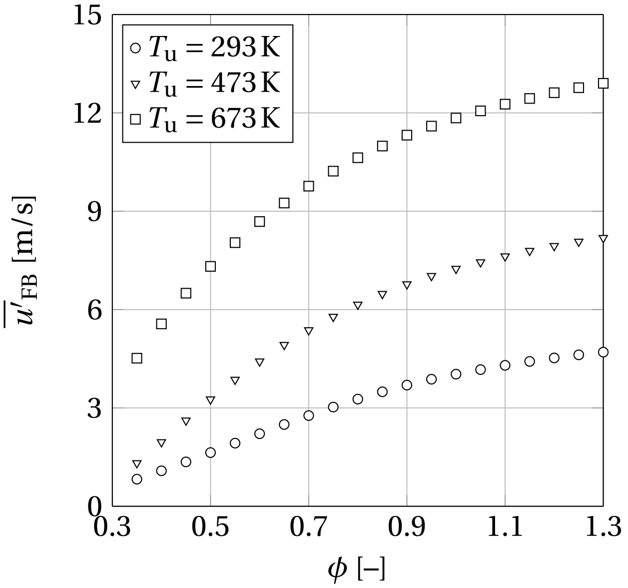

(a) Averaged turbulent velocity fluctuations at flashback

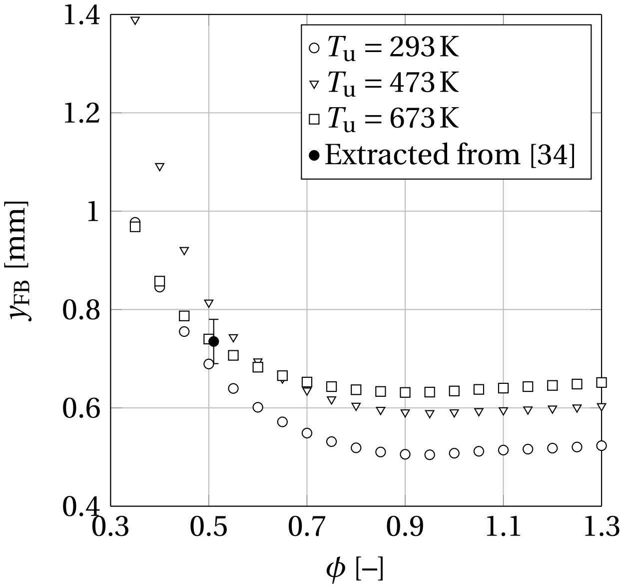

(b) Wall distance of flashback

Figure 6.14: Comparison of predicted unconfined flashback parameters (empty symbols) with experimental results from a $d_h = 40\,mm$ tube burner (filled symbols) [10].

sults but calculated in one-dimensional free flame simulations. Another reason might be the neglected influence of preheating temperature on the global activation energy E. The effect of uncertainties in these parameters will be investigated in a sensitivity analysis in the following sections.

For the sake of completeness, the calculated flame angles at flashback, the turbulent velocity fluctuations and the wall distances at flashback are shown in Fig. 6.13(b), 6.14(a) and 6.14(b) although no experimental validation data is available. The calculated flame angles increase with equivalence ratio and preheating and vary between $\alpha_{\mathrm{FB}} = 20°$ and $\alpha_{\mathrm{FB}} = 80°$. The averaged turbulent velocity fluctuations show a similar behavior and increase from $\overline{u'}_{\mathrm{FB}} = 0.8\,\mathrm{m/s}$ at $\phi = 0.35$ and ambient temperature up to $\overline{u'}_{\mathrm{FB}} = 13\,\mathrm{m/s}$ at $\phi = 1.3$ and $T_{\mathrm{u}} = 673\,\mathrm{K}$. In the plot for the wall distance at flashback the channel burner value extracted from the PLIF image of Baumgartner et al. [34] is included for reference. Similar to the channel burner, y_{FB} decreases with increasing equivalence ratio. Preheating reduces the Reynolds numbers at flashback due to lower kinematic viscosity. Consequently, the wall distance y_{FB} corresponding to $y^{+}_{\mathrm{FB}} = 16.4$ increases.

Overall, the developed prediction model satisfactorily reproduces experimentally determined flashback limits of tube as well as channel burners at atmospheric pressure and the preheating range of $293\,\mathrm{K} \leq T_{\mathrm{u}} \leq 673\,\mathrm{K}$. Furthermore, it delivers reasonable flame angles, turbulent velocity fluctuations and wall distances of flashback. To increase the generality of the applied correlation for $\overline{u'}_{\mathrm{FB}}$ more validation data at preheated conditions and different pressures would be beneficial. A discussion of the effect of elevated pressure on boundary layer flashback and the developed prediction model is included in App. A.

6.2.6 Sensitivity Analysis

Based on Baumgartner's $d_{\mathrm{h}} = 40\,\mathrm{mm}$ tube burner [10] discussed in the model validation, the influence of different parameters on $\overline{U}_{\mathrm{FB}}$ and α_{FB} will be discussed in the following sections. Changes of ±20 % will be analyzed at $T_{\mathrm{u}} = 293\,\mathrm{K}$ and $T_{\mathrm{u}} = 673\,\mathrm{K}$.

6.2.6.1 Unstretched Laminar Burning Velocity

The effect of a variation in $S_{\mathrm{l},0}$ of ±20 % is illustrated in Fig. 6.15 and Tab. 6.1. An increase of $S_{\mathrm{l},0}$ leads to increased velocities at flashback and larger flame angles. The relative change in $\overline{U}_{\mathrm{FB}}$ amounts 11–16 % and is smaller than for the confined prediction model presented in Chap. 5. With increasing preheating, the relative changes in velocity at flashback decrease for most investigated equivalence ratios. At both preheating temperatures, the effect of a $S_{\mathrm{l},0}$ reduction is higher than the influence of increasing $S_{\mathrm{l},0}$. Figure 6.15(a) shows that at $T_{\mathrm{u}} = 673\,\mathrm{K}$ and $\phi = 0.35$ the unstretched laminar burning velocity has to be reduced by more than 20 % to match Baumgartner's experimentally determined flashback limits [10]. This contradicts the observation in Sec. 5.4.1 where $S_{\mathrm{l},0}$ has to be increased by about 60 % to reproduce Eichler's experimental flashback limits for confined flames [9]. It indicates that the temperature dependence of other parameters is not correctly described causing the observed discrepancies between prediction and experiment at preheated conditions.

In general, the relative changes in flame angle at flashback are smaller than the relative changes in $\overline{U}_{\mathrm{FB}}$. They increase with equivalence ratio and vary between 5 and 12 %. It has to be noted that for the high preheating case around stoichiometry an increase in unstretched laminar burning velocity leads to flame angles close to or equal to 90°. As this causes numerical instabilities, the model equations are not solved properly at these conditions. Consequently, the errorbars in Fig. 6.15 beyond $\phi = 1.0$ for increases in $S_{\mathrm{l},0}$ do not represent correct solutions of the system of equations presented in Sec. 6.2.4 and should only be seen as trends and not quantitative results. For this reason, no value but only the sign is given for $\Delta\alpha_{\mathrm{FB}}(S^{+}_{\mathrm{l},0})/\alpha_{\mathrm{FB}}$ and $\Delta\overline{U}_{\mathrm{FB}}(S^{+}_{\mathrm{l},0})/\overline{U}_{\mathrm{FB}}$ at $\phi = 1.0$ and $T_{\mathrm{u}} = 673\,\mathrm{K}$.

6.2.6.2 Markstein Length

The influence of an uncertainty in L_{M} of ±20 % is shown in Fig. 6.16 and Tab. 6.2. Similar to the confined case discussed in Sec. 5.4.2, positive changes of the absolute value of L_{M} lead to increased velocities at flashback for $L_{\mathrm{M}} < 0$

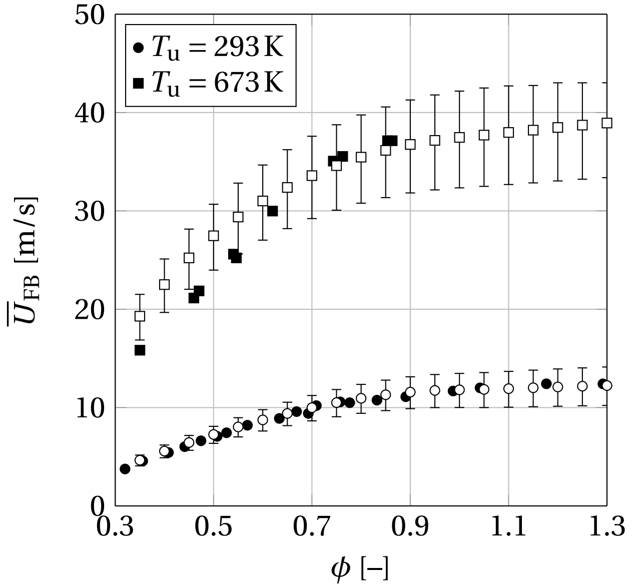

(a) Velocity at flashback

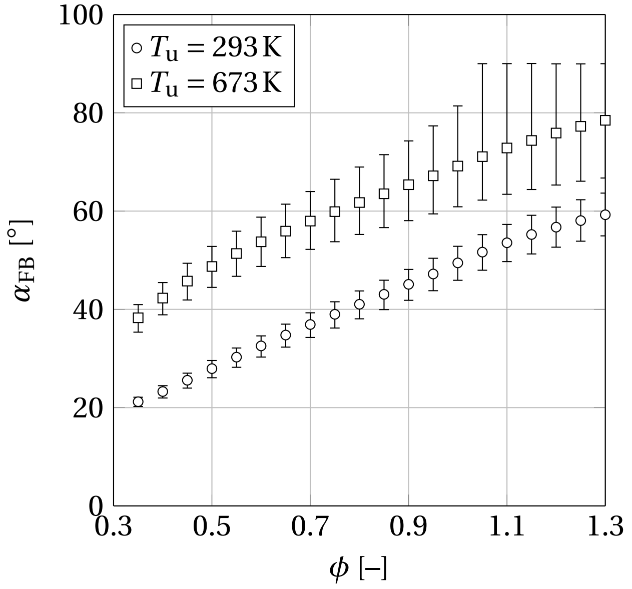

(b) Averaged flame angle at flashback

Figure 6.15: Influence of a ±20% change in $S_{l,0}$ on the unconfined flashback limits and the corresponding flame angles of a $d_h = 40\,mm$ tube burner. Empty symbols: prediction, filled symbols: experiment [10].

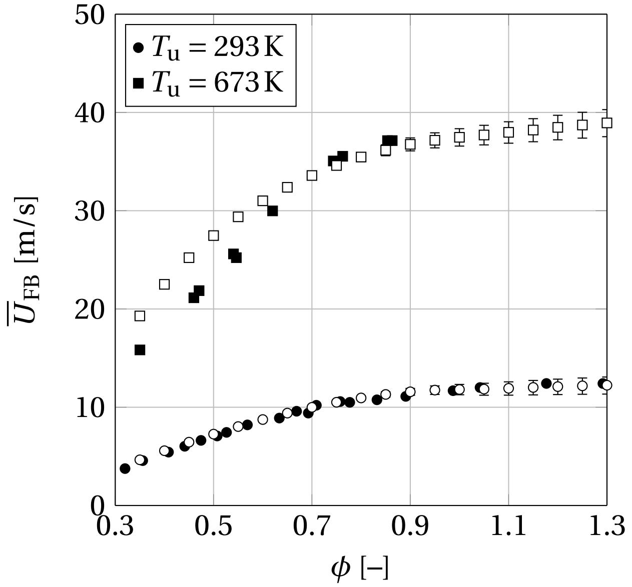

(a) Velocity at flashback

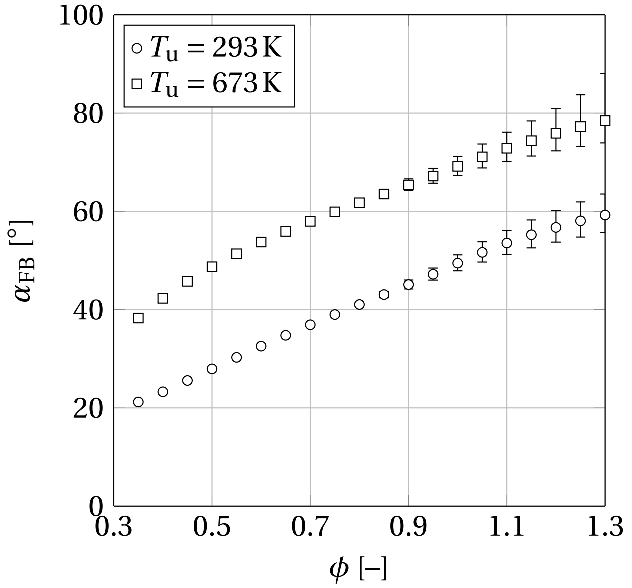

(b) Averaged flame angle at flashback

Figure 6.16: Influence of a ±20 % change in $|L_M|$ on the unconfined flashback limits and the corresponding flame angles of a $d_h = 40$ mm tube burner. Empty symbols: prediction, filled symbols: experiment [10].

Table 6.1: Relative changes of the predicted $\overline{U}_{\mathrm{FB}}$ and α_{FB} of unconfined flames due to a ±20 % variation of $S_{\mathrm{l},0}$.

ϕ	T_{u} [K]	$\frac{\Delta\overline{U}_{\mathrm{FB}}(1.2\,S_{\mathrm{l},0})}{\overline{U}_{\mathrm{FB}}}$ [%]	$\frac{\Delta\overline{U}_{\mathrm{FB}}(0.8\,S_{\mathrm{l},0})}{\overline{U}_{\mathrm{FB}}}$ [%]	$\frac{\Delta\alpha_{\mathrm{FB}}(1.2\,S_{\mathrm{l},0})}{\alpha_{\mathrm{FB}}}$ [%]	$\frac{\Delta\alpha_{\mathrm{FB}}(0.8\,S_{\mathrm{l},0})}{\alpha_{\mathrm{FB}}}$ [%]
0.4	293	+11.10	−12.17	+5.14	−5.62
0.7	293	+12.42	−13.42	+6.47	−7.13
1.0	293	+14.14	−15.21	+6.82	−7.17
0.4	673	+11.57	−12.58	+7.48	−8.04
0.7	673	+11.93	−13.00	+10.38	−9.93
1.0	673	+	−13.68	+	−11.98

Table 6.2: Relative changes of the predicted $\overline{U}_{\mathrm{FB}}$ and α_{FB} of unconfined flames due to a ±20 % variation of $|L_{\mathrm{M}}|$.

ϕ	T_{u} [K]	$\frac{\Delta\overline{U}_{\mathrm{FB}}(1.2\,\lvert L_{\mathrm{M}}\rvert)}{\overline{U}_{\mathrm{FB}}}$ [%]	$\frac{\Delta\overline{U}_{\mathrm{FB}}(0.8\,\lvert L_{\mathrm{M}}\rvert)}{\overline{U}_{\mathrm{FB}}}$ [%]	$\frac{\Delta\alpha_{\mathrm{FB}}(1.2\,\lvert L_{\mathrm{M}}\rvert)}{\alpha_{\mathrm{FB}}}$ [%]	$\frac{\Delta\alpha_{\mathrm{FB}}(0.8\,\lvert L_{\mathrm{M}}\rvert)}{\alpha_{\mathrm{FB}}}$ [%]
0.4	293	+3.97	−4.07	−0.78	+1.00
0.7	293	−0.54	+0.54	+0.30	−0.30
1.0	293	−4.37	+4.55	+3.41	−3.16
0.4	673	+0.46	−0.46	−0.25	+0.25
0.7	673	−0.87	+0.87	+0.72	−0.70
1.0	673	−2.34	+2.38	+2.96	−2.64

and to a reduction in $\overline{U}_{\mathrm{FB}}$ for $L_{\mathrm{M}} > 0$. The opposite trend is observed for α_{FB}. In general, the effect of L_{M} on $\overline{U}_{\mathrm{FB}}$ is smaller in the prediction model for unconfined flames compared to the confined case. The relative changes vary between 0 and 5 % and are small compared to the changes due to a variation in unstretched laminar burning velocity. The relative changes in α_{FB} are even smaller and lie between 0 and 4 %. Based on these observations, uncertainties in the Markstein length of hydrogen-air mixtures are unlikely to cause the prediction inaccuracies at lean conditions and high preheating temperatures.

6.2.6.3 Turbulent Macroscale

Figure 6.17 and Tab. 6.3 depict the effect of variations in the turbulent macroscale Λ of ±20 %. The result is similar to the confined case discussed in Sec. 5.4.3. An increase in turbulent macroscale leads to lower flame stretch rates and lower velocities at flashback for $L_{\mathrm{M}} < 0$. For positive Markstein length lower flame stretch rates result in higher burning velocities and a higher risk of flame flashback. The relative changes in $\overline{U}_{\mathrm{FB}}$ are smaller than in the confined case and are below 2 %. The relative changes in α_{FB} are even smaller (< 1.5 %). As for the confined case, it can be noted that uncertainties in the choice of Λ have negligible influence on the calculation results compared to other parameters such as unstretched laminar burning velocity or turbulence distribution.

6.2.6.4 Turbulent Velocity Fluctuations

The influence of the modeling approaches for the turbulent velocity fluctuations have to be divided into the local turbulent velocity fluctuations defined by Eq. (6.8) and the global values from the flame generated turbulence approach in Eq. (6.13). Both parameters are analyzed separately in the following two paragraphs.

Local Values at Position of Flashback Initiation: The local turbulent velocity fluctuations at the position of flashback initiation are estimated based on microscopic PIV results of Baumgartner [10]. The deduced assumption of

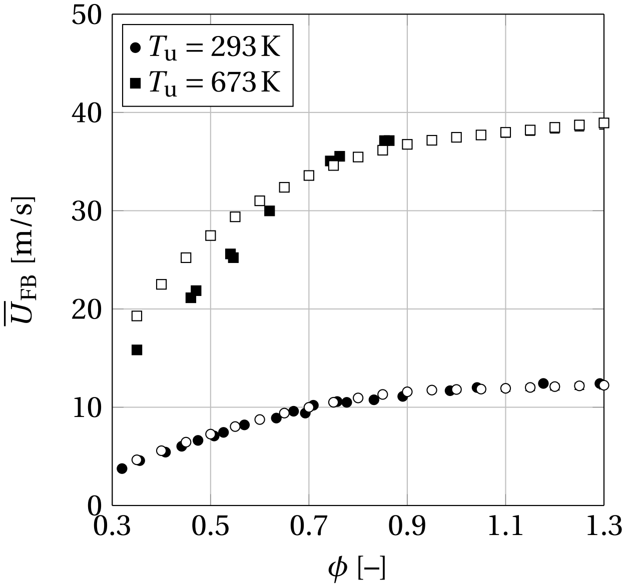

(a) Velocity at flashback

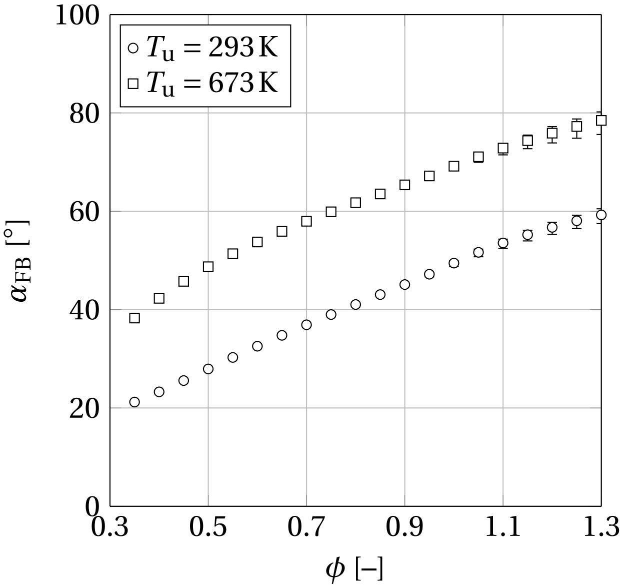

(b) Averaged flame angle at flashback

Figure 6.17: Influence of a ±20 % change in Λ on the unconfined flashback limits and the corresponding flame angles of a $d_{\mathrm{h}} = 40\,\mathrm{mm}$ tube burner. Empty symbols: prediction, filled symbols: experiment [10].

$u'(y_{\mathrm{FB}})\,/\,u_\tau = 1.5$ contains high uncertainty as the flashback initiation is located some distance downstream of the field of view in Baumgartner's experiments. Furthermore, the local turbulence field is only available for flashback at one specific equivalence ratio of $\phi = 0.5$.

Figure 6.18 and Tab. 6.4 summarize the effect of a ±20 % uncertainty in $u'(y_{\mathrm{FB}})\,/\,u_\tau$ on flashback limits and flame angles at flashback. Compared to the other investigated parameters the influence of $u'(y_{\mathrm{FB}})\,/\,u_\tau$ on the calculated flashback limits is high. The relative change in $\overline{U}_{\mathrm{FB}}$ due to a 20 % reduction of $u'(y_{\mathrm{FB}})\,/\,u_\tau$ amounts up to 45 % at very lean conditions and ambient temperature. In general, a reduction of the local turbulent velocity fluctuations leads to higher relative changes in flashback limit than an increase. The opposite trend is observed for the flame angle at flashback.

An increase in $u'(y_{\mathrm{FB}})\,/\,u_\tau$ results in higher local turbulent burning velocities $S_{\mathrm{t}}(y_{\mathrm{FB}})$. Assuming constant local velocity at flashback, the flame angle α_{FB} has to increase (cf. Eq. (6.7)). Equation (6.11) shows that consequently $\overline{U}_{\mathrm{FB}}$ has to decrease. However, this leads to a reduced $u(y_{\mathrm{FB}})$ and, therefore, to an additional increase in α_{FB}. Due to this feedback, a change in $u'(y_{\mathrm{FB}})\,/\,u_\tau$ has a disproportionately high effect on flashback limit and flame angle.

Table 6.4 reflects this behavior. As before, for numerically unstable solutions with $\alpha_{\mathrm{FB}} \geq 90^\circ$ only the sign of the relative changes in flame angle and flashback limit is given. Due to the observed high influence of $u'(y_{\mathrm{FB}})\,/\,u_\tau$ on the calculated flashback limits, more validation data at different equivalence ratios and preheating temperatures is eligible to minimize the model uncertainties regarding $u'(y_{\mathrm{FB}})$.

Global Values from Flame Generated Turbulence Correlation: The averaged turbulent velocity fluctuations $\overline{u'}_{\mathrm{FB}}$ are calculated from a correlation for flame generated turbulence (Eq. (6.13)) which was validated for ambient temperature using PIV data (cf. Sec. 6.2.5). The transfer to preheated conditions uses a power law approach which holds significant uncertainty as no validation data is available. The influence of a ±20 % uncertainty is shown in Fig. 6.19 and Tab. 6.5. In contrast to the local turbulent velocity fluctuations, an in-

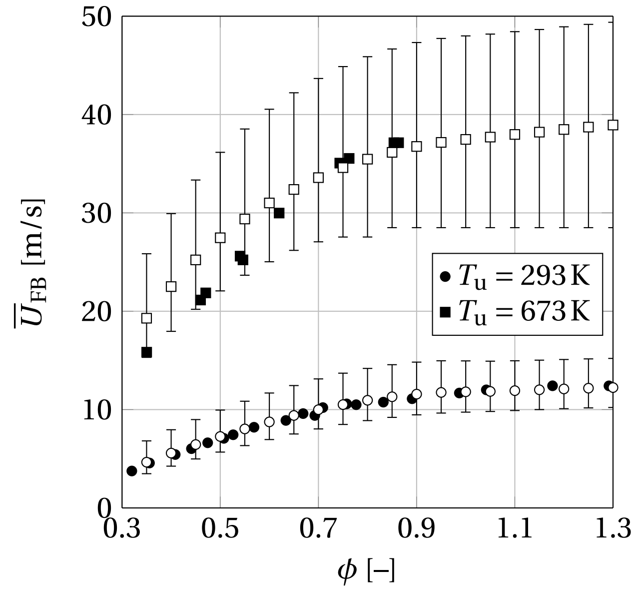

(a) Velocity at flashback

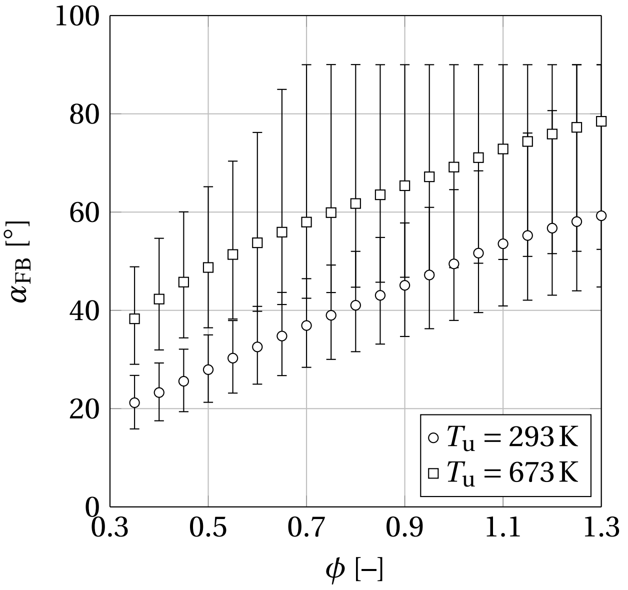

(b) Averaged flame angle at flashback

Figure 6.18: Influence of a ±20% change in $u'(y_{\mathrm{FB}})/u_\tau$ on the unconfined flashback limits and the corresponding flame angles of a $d_{\mathrm{h}} = 40\,\mathrm{mm}$ tube burner. Empty symbols: prediction, filled symbols: experiment [10].

Table 6.3: Relative changes of the predicted $\overline{U}_{\mathrm{FB}}$ and α_{FB} of unconfined flames due to a ±20 % variation of Λ.

ϕ	T_{u} [K]	$\frac{\Delta\overline{U}_{\mathrm{FB}}(1.2\,\Lambda)}{\overline{U}_{\mathrm{FB}}}$ [%]	$\frac{\Delta\overline{U}_{\mathrm{FB}}(0.8\,\Lambda)}{\overline{U}_{\mathrm{FB}}}$ [%]	$\frac{\Delta\alpha_{\mathrm{FB}}(1.2\,\Lambda)}{\alpha_{\mathrm{FB}}}$ [%]	$\frac{\Delta\alpha_{\mathrm{FB}}(0.8\,\Lambda)}{\alpha_{\mathrm{FB}}}$ [%]
0.4	293	−1.19	+1.54	+0.20	−0.22
0.7	293	+0.17	−0.23	−0.09	+0.12
1.0	293	+1.49	−1.94	−1.05	+1.42
0.4	673	−0.15	+0.20	+0.08	−0.10
0.7	673	+0.30	−0.39	−0.23	+0.31
1.0	673	+0.82	−1.08	−0.92	+1.28

Table 6.4: Relative changes of the predicted $\overline{U}_{\mathrm{FB}}$ and α_{FB} of unconfined flames due to a ±20 % variation of $u'(y_{\mathrm{FB}})/u_\tau$.

ϕ	T_{u} [K]	$\frac{\Delta\overline{U}_{\mathrm{FB}}(1.2\,u'(y_{\mathrm{FB}})/u_\tau)}{\overline{U}_{\mathrm{FB}}}$ [%]	$\frac{\Delta\overline{U}_{\mathrm{FB}}(0.8\,u'(y_{\mathrm{FB}})/u_\tau)}{\overline{U}_{\mathrm{FB}}}$ [%]	$\frac{\Delta\alpha_{\mathrm{FB}}(1.2\,u'(y_{\mathrm{FB}})/u_\tau)}{\alpha_{\mathrm{FB}}}$ [%]	$\frac{\Delta\alpha_{\mathrm{FB}}(0.8\,u'(y_{\mathrm{FB}})/u_\tau)}{\alpha_{\mathrm{FB}}}$ [%]
0.4	293	−23.82	+42.59	+25.85	−24.69
0.7	293	−19.59	+31.32	+25.84	−23.06
1.0	293	−17.50	+26.63	+30.56	−23.27
0.4	673	−20.21	+32.96	+29.24	−24.47
0.7	673	−	+30.02	+	−26.34
1.0	673	−	+28.09	+	−29.60

Table 6.5: Relative changes of the predicted $\overline{U}_{\mathrm{FB}}$ and α_{FB} of unconfined flames due to a ±20 % variation of $\overline{u'}_{\mathrm{FB}}$.

ϕ	T_{u} [K]	$\frac{\Delta\overline{U}_{\mathrm{FB}}(1.2\,\overline{u'}_{\mathrm{FB}})}{\overline{U}_{\mathrm{FB}}}$ [%]	$\frac{\Delta\overline{U}_{\mathrm{FB}}(0.8\,\overline{u'}_{\mathrm{FB}})}{\overline{U}_{\mathrm{FB}}}$ [%]	$\frac{\Delta\alpha_{\mathrm{FB}}(1.2\,\overline{u'}_{\mathrm{FB}})}{\alpha_{\mathrm{FB}}}$ [%]	$\frac{\Delta\alpha_{\mathrm{FB}}(0.8\,\overline{u'}_{\mathrm{FB}})}{\alpha_{\mathrm{FB}}}$ [%]
0.4	293	+42.98	−32.33	−16.30	+23.60
0.7	293	+28.65	−25.50	−15.16	+24.18
1.0	293	+19.60	−21.62	−13.08	+25.16
0.4	673	+31.44	−27.34	−16.99	+28.35
0.7	673	+28.01	−	−18.97	+
1.0	673	+24.45	−	−20.76	+

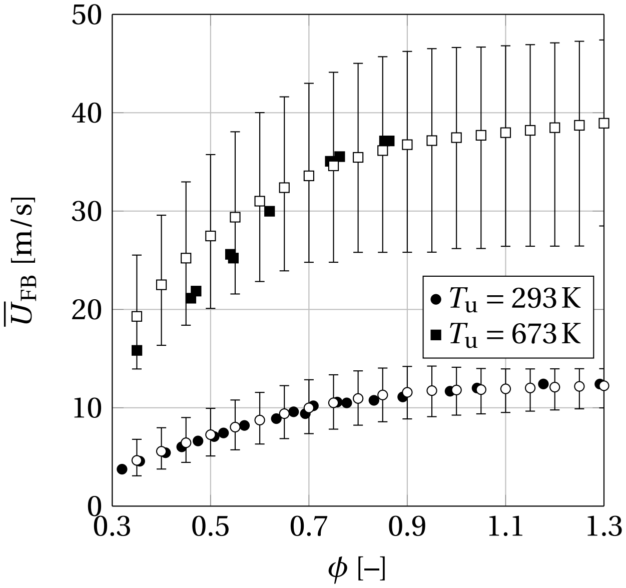

(a) Velocity at flashback

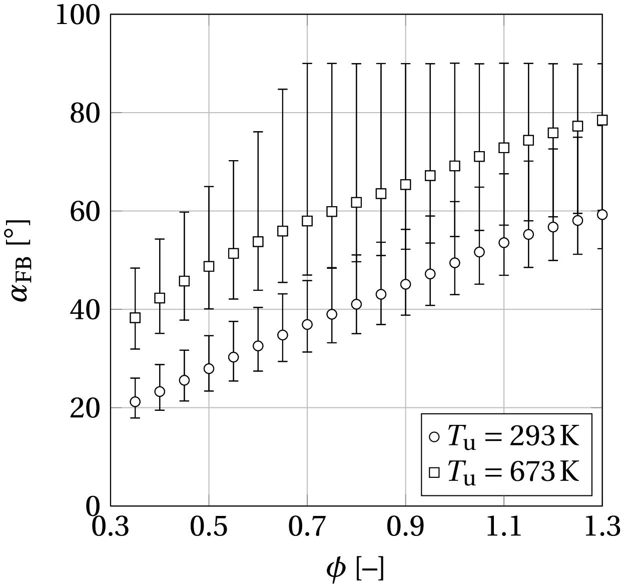

(b) Averaged flame angle at flashback

Figure 6.19: Influence of a ±20 % change in $\overline{u'}_{\mathrm{FB}}$ on the unconfined flashback limits and the corresponding flame angles of a d_h = 40 mm tube burner. Empty symbols: prediction, filled symbols: experiment [10].

crease in $\overline{u'}_{\mathrm{FB}}$ leads to higher average turbulent burning velocities $\overline{S}_{\mathrm{t}}$. Assuming a constant flame angle, $\overline{U}_{\mathrm{FB}}$ has to increase (cf. Eq. (6.11)). Due to the local balance in Eq. (6.7) and a constant local turbulent burning velocity S_{t}, the flame angle has to decrease. In the global balance of Eq. (6.11) this leads to an even further increase of $\overline{U}_{\mathrm{FB}}$ which is the reason for the high influence of $\overline{u'}_{\mathrm{FB}}$ on the calculated flashback limits.

The caused relative changes in flashback limit and flame angle at flashback are in the same range as for the local turbulent velocity fluctuations discussed in the previous paragraph. For conditions with unstable solutions due to flame angles $\alpha_{\mathrm{FB}} \geq 90°$, again only the sign of the resulting changes in $\overline{U}_{\mathrm{FB}}$ and α_{FB} is given. The high relative changes indicate that, together with the local turbulent velocity fluctuations, $\overline{u'}_{\mathrm{FB}}$ is one of the main sources for uncertainty in the developed prediction model. Especially for preheated conditions and elevated pressures more validation data is required to enhance the generality of the applied correlations.

6.2.6.5 Correlation for Turbulent Burning Velocity

Only the model constant C_{S} in the correlation for the turbulent burning velocity (Eq. (5.10)) was fitted to experimental flashback data. Section 5.4.5 showed that the influence of C_{S} on the calculated confined flashback limits is significant since turbulent burning velocity and pressure rise upstream of the flame front are directly affected. In the prediction model for unconfined flame flashback, the situation is different. Due to the fact that both local and global balance are affected by the choice of C_{S}, the resulting relative changes in $\overline{U}_{\mathrm{FB}}$ and α_{FB}, depicted in Fig. 6.20 and Tab. 6.6, are smaller than in the confined case. The influence of C_{S} on the unconfined flashback limit is comparable to the influence of the unstretched laminar burning velocity presented in Sec. 6.2.6.1. The relative changes in flashback limit and flame angle caused by a variation in C_{S} of ±20 % are smaller than 15 % and, hence, smaller than the influence of the turbulence distribution discussed in Sec. 6.2.6.4. This confirms the dominant influence of the turbulence distribution on the uncertainty of the developed prediction model for unconfined boundary layer flashback limits and

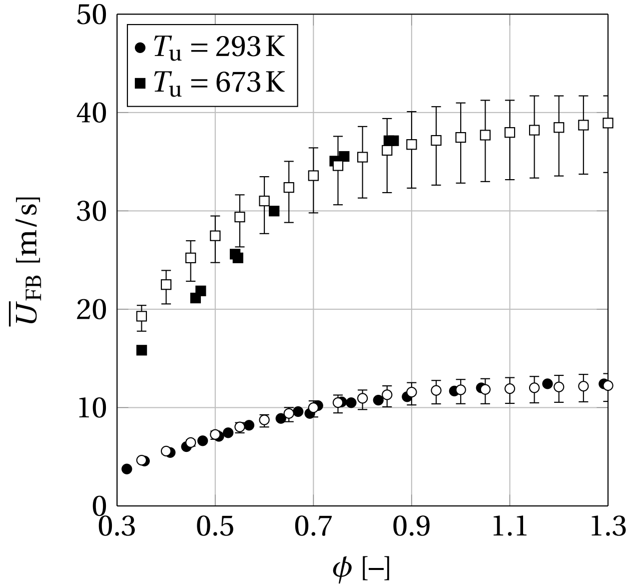

(a) Velocity at flashback

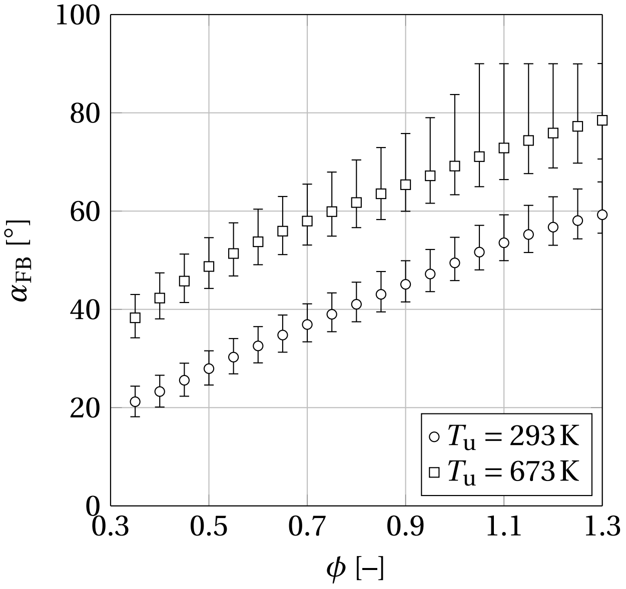

(b) Averaged flame angle at flashback

Figure 6.20: Influence of a ±20 % change in C_{S} on the unconfined flashback limits and the corresponding flame angles of a $d_{\mathrm{h}} = 40\,\mathrm{mm}$ tube burner. Empty symbols: prediction, filled symbols: experiment [10].

Table 6.6: Relative changes of the predicted $\overline{U}_{\mathrm{FB}}$ and α_{FB} of unconfined flames due to a ±20 % variation of C_{S}.

ϕ	T_{u} [K]	$\frac{\Delta\overline{U}_{\mathrm{FB}}(1.2\,C_{\mathrm{S}})}{\overline{U}_{\mathrm{FB}}}$ [%]	$\frac{\Delta\overline{U}_{\mathrm{FB}}(0.8\,C_{\mathrm{S}})}{\overline{U}_{\mathrm{FB}}}$ [%]	$\frac{\Delta\alpha_{\mathrm{FB}}(1.2\,C_{\mathrm{S}})}{\alpha_{\mathrm{FB}}}$ [%]	$\frac{\Delta\alpha_{\mathrm{FB}}(0.8\,C_{\mathrm{S}})}{\alpha_{\mathrm{FB}}}$ [%]
0.4	293	+3.24	−4.58	+14.24	−13.57
0.7	293	+6.90	−9.46	+11.41	−9.54
1.0	293	+8.94	−11.97	+10.57	−7.28
0.4	673	+6.40	−8.73	+12.13	−10.00
0.7	673	+8.42	−11.27	+12.98	−8.41
1.0	673	+	−12.39	+	−8.43

underlines the necessity of further validation data concerning local and averaged turbulent velocity fluctuations.

6.2.7 Influence of Different Degrees of Burner Exit Cooling on Flashback Limits

Depending on the degree of burner exit cooling, discrepancies in flashback data are observed in literature. This section will demonstrate that the developed prediction model is able to reproduce the effect of burner rim temperature on flashback limits.

The effect of burner exit temperature T_{B}, often called rim or tip temperature, has already been studied by Bollinger and Edse [20] and Duan et al. [23, 25]. Those studies agree that high burner rim temperatures increase the flashback limits $\overline{U}_{\mathrm{FB}}$ for a constant equivalence ratio. Duan et al. [23, 25] found improved correlation of flashback limits at different tip temperatures by using the unstretched laminar burning velocity $S_{\mathrm{l,0}}(T_{\mathrm{B}})$ instead of $S_{\mathrm{l,0}}(T_{\mathrm{u}})$. They assumed that the mixture close to the wall had been preheated to the burner rim temperature T_{B} in their experiments. A similar approach will be applied here as shown in the following.

The effect of high burner exit temperatures on local conditions at the onset of flashback is illustrated in Fig. 6.21. If the tip temperature T_{B} is higher than the temperature of the unburned mixture T_{u} a heat flux $\dot{q}$ is induced which

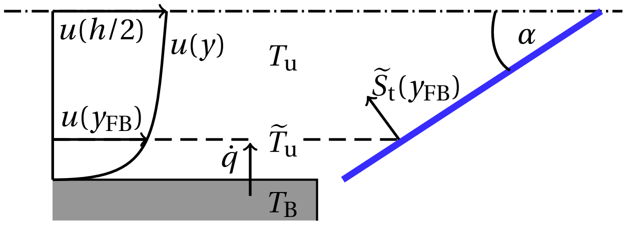

Figure 6.21: Influence of high burner exit temperatures on the local conditions at the onset of flashback [35].

locally increases preheating of the unburned mixture to the temperature $\widetilde{T}_u$. It is assumed that this local preheating increases the local turbulent burning velocities to $\widetilde{S}_t(y_{FB})$ by changing $S_{l,0}(y_{FB})$ but does not affect global flame parameters such as the flame angle. Hence, the local part of the developed prediction model can be used to study the effect of T_B on $\overline{U}_{FB}$ by changing $S_{l,0}$ and setting α_{FB} to the values presented in Sec. 6.2.5 at $T_u = 293\,\mathrm{K}$.

Results are presented in Fig. 6.22 for a $d_h = 40\,\mathrm{mm}$ tube burner. Filled symbols mark experimental data and empty symbols represent calculated data obtained from the presented model. For comparison the $T_u = 293\,\mathrm{K}$ flashback limits shown in Fig. 6.13(a) are also included. Baumgartner's experimental data [10] were measured with a water cooled brass tube burner. The experimental data of Duan et al. [25] for a water cooled stainless steel tube burner show slightly higher flashback limits. With the prediction model they can be well reproduced if a linear increase of local preheating from $\widetilde{T}_u = 310\,\mathrm{K}$ at $\phi = 0.35$ to $\widetilde{T}_u = 340\,\mathrm{K}$ at $\phi = 1$ is assumed. The resulting local preheating temperatures in the equivalence ratio range investigated by Duan et al. [25] lie between $\widetilde{T}_u = 315\,\mathrm{K}$ and $\widetilde{T}_u = 324\,\mathrm{K}$. This temperature range is very similar to the burner exit temperatures given by Duan et al. [25] ($T_B \approx 310$–$325\,\mathrm{K}$). The flashback limits of Baumgartner [10] and Duan et al. [25] show that the cooling of the stainless steel burner seemed to be less efficient than for the brass burner. This might be caused by the lower thermal conductivity of stainless steel compared to brass leading to higher surface temperatures and increased heat transfer to the hydrogen-air mixture.

In addition to the cooled burner data Duan et al. [25] present flashback limits of the same burner without cooling. They state that the burner exit temper-

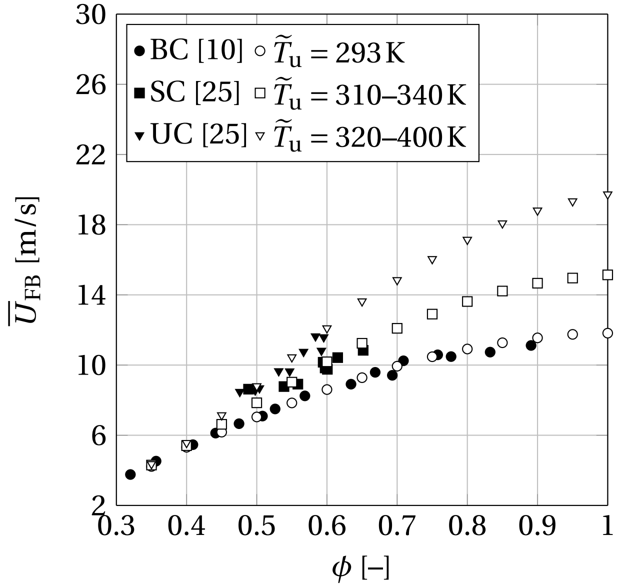

Figure 6.22: Effect of burner exit temperature on flashback limits of a $d_{\mathrm{h}} = 40\,\mathrm{mm}$ tube burner. Filled symbols: Experimental data for cooled brass burner (BC), cooled stainless steel burner (SC) and uncooled stainless steel burner (UC), empty symbols: predictions at different $\widetilde{T}_{\mathrm{u}}$. (adapted from [35])

ature increased to $T_{\mathrm{B}} \approx 340–370\,\mathrm{K}$. Their flashback limits can be well reproduced with the prediction model assuming a linear increase of local preheating from $\widetilde{T}_{\mathrm{u}} = 320\,\mathrm{K}$ at $\phi = 0.35$ to $\widetilde{T}_{\mathrm{u}} = 400\,\mathrm{K}$ at $\phi = 1$. This corresponds to local preheating temperatures of $\widetilde{T}_{\mathrm{u}} = 330–350\,\mathrm{K}$ in the investigated equivalence ratio range of Duan et al. [25]. These temperatures are again similar to T_{B}. This shows that the effect of increased burner tip temperatures can be captured by the presented approach of local preheating.

Another example for the effect of local preheating is shown in Fig. 6.23 based on the channel burner flashback limits obtained in this study (cf. Fig. 6.11(a)). They are compared to the data by Baumgartner et al. [34] measured at a similar burner geometry. The main difference between the two setups is the type of cooling system. Baumgartner et al. [34] used an air cooling system which was replaced by a water cooling system in the current study. The fact that the flow velocity at flashback was reduced especially at high flame temperatures shows that the water cooling system seems to achieve lower burner exit

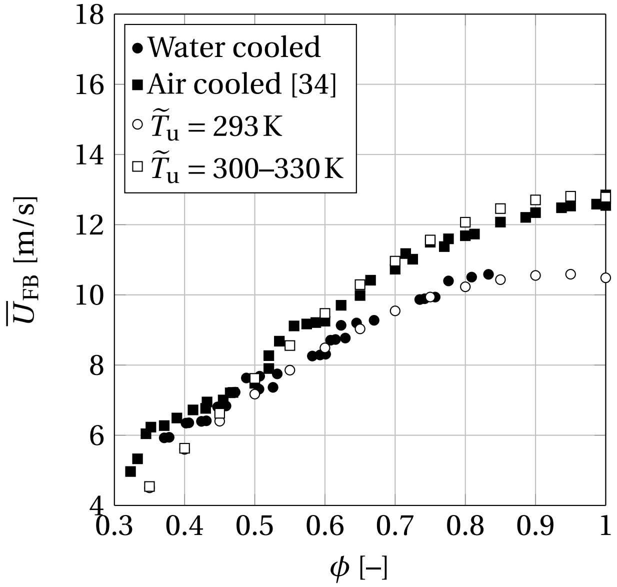

Figure 6.23: Effect of burner exit temperature on flashback limits of a $d_h = 31.5\,mm$ channel burner. Filled symbols: Experimental data for water cooled and air cooled burner, empty symbols: predictions at different $\widetilde{T}_u$. (adapted from [35])

temperatures. The experimental data of Baumgartner et al. [34] can be well reproduced with the presented prediction model if a linear increase of local preheating temperature from $\widetilde{T}_u = 300\,K$ at $\phi = 0.35$ to $\widetilde{T}_u = 330\,K$ at $\phi = 1$ is assumed. This shows that even low changes in local preheating temperature have a noticeable effect on flashback limits especially at high flame temperatures. In order to reliably predict the boundary layer flashback limits of a given burner configuration, precise knowledge on the material temperature and the heat transfer to the fuel-air mixture is crucial.

7 Summary and Conclusions

In the first part of this work, an experimental study was conducted at ambient conditions to identify the influence of acoustic velocity oscillations on the flashback characteristics of unconfined hydrogen-air flames. Frequencies were varied between 115 and 350 Hz representing typical intermediate frequency dynamics of gas turbine combustors. The following key findings were obtained:

- Acoustic velocity oscillations at the burner exit increase the burner's susceptibility to boundary layer flashback. This means that for a constant flow velocity flame flashback is observed at leaner mixtures than for unexcited unconfined flames.

- In the investigated frequency range the effect of velocity oscillations decreases with increasing frequency as, at constant equivalence ratio, the relative increase of the flow velocity at flashback decreases. A possible explanation is that there is less time for the flame to completely follow the acoustic velocity oscillations.

- For small normalized velocity oscillation amplitudes below a certain threshold, the obtained flashback limits represent the flashback limits of unconfined flames if the minimum flow velocity in the excitation cycle is used for comparison.

- At velocity oscillation amplitudes above the threshold, the flame periodically enters the burner duct and is washed out again. Flashback is initiated if the flame is able to penetrate a sufficient distance into the burner duct and if the maximum velocity in the oscillation cycle falls below the flashback limit of confined flames. At this point a transition from the unconfined to the confined flashback mechanism is observed.

Based on these results two different flashback regimes can be distinguished. The transition between both regimes is observed at a certain oscillation amplitude threshold. This threshold increases with frequency. For a detailed study on its dependency on frequency, flashback tests at high oscillation amplitudes and different frequencies need to be performed in the future.

As confined and unconfined boundary layer flashback were identified as limiting cases in the experimental study, prediction models for the flashback limits of both cases were developed in the second part of this work. The models are based on detailed descriptions of turbulence distribution and mixture properties.

The prediction model for confined boundary layer flashback utilizes the fact that at flashback conditions a backflow region forms upstream of the flame tip. Consequently, the flashback limit can be predicted by estimating the flow velocity at which a flame of a certain equivalence ratio induces a pressure rise high enough to cause boundary layer separation. For that purpose, a criterion developed in another context by Stratford in 1959 was applied. The developed model consists of eight non-linear equations which have to be solved numerically. It was validated for hydrogen-air flames of a tube burner at ambient temperature and a channel burner operated at preheating temperatures up to 673 K. The main results can be summarized as follows:

- Flashback is initiated along the streamline of maximum turbulence close to the burner wall. At this streamline, the maximum turbulent burning velocity is found leading to a maximum in combustion induced pressure rise.
- The model contains only one parameter which is adjusted to match the experimental data. This parameter is contained in the correlation for the turbulent burning velocity as pre-exponential factor.
- High prediction accuracy is achieved at ambient temperature for the validated equivalence ratio range of $0.35 \leq \phi \leq 1.0$. At preheated conditions, the flashback limits for equivalence ratios below $\phi = 0.6$ are underestimated.

- In a sensitivity analysis, the turbulent burning velocity correlation, the laminar burning velocity and the turbulent velocity fluctuations close to the burner wall were identified as the main parameters influencing flashback. It is therefore probable that uncertainties in the temperature dependence of these parameters cause the deviations between prediction and experiment at lean preheated conditions. The influence of Markstein length and turbulent macroscale on the predicted flashback limits is negligible.

For the unconfined case, two models were developed: One for laminar and one for turbulent flames. For laminar flames, boundary layer flashback is dominated by flame quenching at the wall and by flame stretch. Flashback conditions are reached if the flame front close to the burner wall becomes perpendicular to the flow direction and if the burning velocity exceeds the local flow velocity. The governing equations can be solved analytically to one expression for the flow velocity at flashback. The model was validated for hydrogen- and methane-air mixtures. The main findings from the laminar case are the following:

- Flashback is initiated at the wall distance where the flow velocity is as low as possible, but the laminar burning velocity is still significantly high. This distance is estimated to three times the quenching distance of the applied fuel-oxidizer mixture. Closer to the wall, the burning velocity is strongly reduced due to quenching effects.
- Flame stretch induced by the flow velocity gradient close to the wall has a significant influence on the flashback limit. If flame stretch is neglected high deviations between experiment and prediction are observed especially for hydrogen-air mixtures.
- The model shows high prediction accuracy for hydrogen- and methane-air mixtures in the analyzed equivalence ratio range of $0.35 \le \phi \le 1.3$. The effect of the tube diameter is correctly reproduced.

For turbulent unconfined flames, a different flashback process is observed. Flashback is initiated if the turbulent burning velocity exceeds the component of the flow velocity perpendicular to the flame front. In order to estimate the flashback conditions, the flame angle is calculated from mass conservation. The resulting prediction model consists of thirteen equations which are solved numerically. The model is validated for hydrogen-air flames of a channel burner at ambient conditions and a tube burner operated at preheating temperatures up to 673 K. The following conclusions can be drawn:

- Similar to the confined case, flashback is initiated along the streamline of maximum turbulence.
- At the flame front, turbulence is strongly increased by upstream parts of the flame. This significantly affects the flame angle.
- High prediction accuracy is achieved for hydrogen-air flames of $0.35 \le \phi \le 1.3$ at ambient temperature. With increasing temperature, the flashback limits at lean conditions are first underestimated for $\phi < 0.4$ (473 K). At 673 K they are overestimated for $\phi < 0.6$.
- A sensitivity analysis identified turbulence parameters to be the main influencing factors. It is therefore most likely that the observed deviations between experiment and prediction at preheated conditions are caused by uncertainties in the temperature dependence of these parameters. Compared to the confined case, the unstretched laminar burning velocity and the turbulent burning velocity correlation have a smaller effect on calculated flashback limits and flame angles. The influence of Markstein length and turbulent macroscale is negligible as in the confined case.

It can be concluded that for the prediction of the flashback limits of confined and unconfined turbulent flames a correct representation of the turbulence field and the response of the applied fuel-oxidizer mixture to flame stretch is essential. High velocity oscillations due to thermoacoustic instabilities can trigger the transition from an unconfined to a confined flame. For that reason, the flashback limits of confined flames should be considered as a worst case scenario in the design of gas turbine burners for highly reactive fuels.

A Pressure Effect on Boundary Layer Flashback Limits

Flashback experiments at elevated pressure are scarcely reported in literature. One study has been performed by Daniele et al. [26] up to $p = 15\,\mathrm{bar}$ for preheating temperatures between 577 and 674 K and hydrogen-carbon monoxide mixtures. They conclude that the flashback risk increases with pressure.

A similar trend was found in another experimental study by Kalantari et al. [27] who analyzed boundary layer flashback of hydrogen-air flames in a $h = 25.4\,\mathrm{mm}$ uncooled tube burner at $3\,\mathrm{bar} \leq p \leq 8\,\mathrm{bar}$ and $300\,\mathrm{K} \leq T_\mathrm{u} \leq 500\,\mathrm{K}$. The obtained flashback conditions correspond to Reynolds numbers in the range of $6 \times 10^4 < \mathrm{Re} < 3 \times 10^5$. For these conditions, Kalantari et al. [27] developed a correlation to predict boundary layer flashback limits which they validated for their experimental test rig data [27], for a commercial gas turbine combustor [28] and for the test rig data of Daniele et al. [26]. The correlation is based on dimensionless parameters to calculate the Damköhler number at flashback. For validation Kalantari et al. [27] compare the Damköhler number $\mathrm{Da_c}$ obtained from their correlation with the Damköhler number $\mathrm{Da_e}$ calculated from experimental results. This Damköhler approach is summarized in the following section.

A.1 Damköhler Approach

The Damköhler correlation developed by Kalantari et al. [27] for elevated pressures is based on dimensional analysis. This method was already applied by Duan et al. [131] for flashback limits at atmospheric pressure. The correlation includes the effect of mixture composition in terms of the fuel's Lewis number $\mathrm{Le_f} = \lambda_\mathrm{u}/(\rho_\mathrm{u} c_\mathrm{p,u} D_\mathrm{f})$ and the effect of flame stretch by means of a

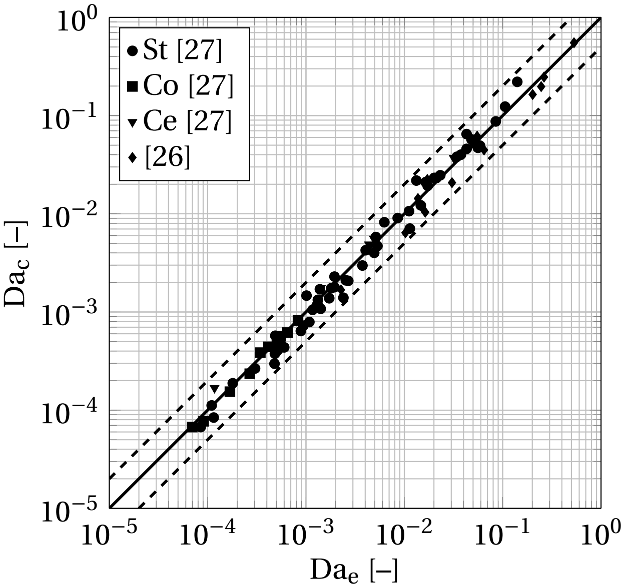

Figure A.1: Validation of Damköhler correlation to predict flashback limits (adapted from [27]). St: stainless steel burner, Co: copper burner, Ce: ceramic burner.

laminar flame speed based Péclet number $\mathrm{Pe_F} = h S_{\mathrm{l},0} \rho_\mathrm{u} c_{\mathrm{p,u}} / \lambda_\mathrm{u}$. Furthermore, the influences of preheating temperature, burner rim temperature and pressure are accounted for. The correlation optimized for $3\,\mathrm{bar} \leq p \leq 8\,\mathrm{bar}$ and $300\,\mathrm{K} \leq T_\mathrm{u} \leq 500\,\mathrm{K}$ ($6 \times 10^4 < \mathrm{Re} < 3 \times 10^5$) reads as:

$$\mathrm{Da_c} = 5.79 \times 10^{-6}\, \mathrm{Le_f^{1.68}}\, \mathrm{Pe_F^{1.91}} \left(\frac{T_\mathrm{u}}{T_{\mathrm{u,ref}}}\right)^{2.57} \left(\frac{T_\mathrm{B}}{T_{\mathrm{u,ref}}}\right)^{-0.49} \left(\frac{p}{p_\mathrm{ref}}\right)^{-2.1} . \tag{A.1}$$

Reference temperature and pressure are set to $T_{\mathrm{u,ref}} = 300\,\mathrm{K}$ and $p_\mathrm{ref} = 1.013\,\mathrm{bar}$. The validation of this correlation as given by Kalantari et al. [27] is shown in Fig. A.1 for different burner materials as well as the experimental results of Daniele et al. [26]. The experimental Damköhler numbers are obtained from the definition

$$\mathrm{Da_e} = \frac{S_{\mathrm{l},0}^2 \rho_\mathrm{u} c_{\mathrm{p,u}} \nu_\mathrm{u}}{\lambda_\mathrm{u} u_\tau^2} \tag{A.2}$$

evaluated at the experimentally determined flashback conditions. The solid line marks the ideal case where $\mathrm{Da_c} = \mathrm{Da_e}$. The dashed lines mark the observed scatter. Kalantari et al. [28] state that this scatter corresponds to 5–17 % uncertainty of their correlation in terms of bulk flow velocity at flashback.

Compared to their experiments, the uncertainty of the prediction decreases with bulk flow velocity at flashback from ≈ 17% at $\overline{U}_{\mathrm{FB}} = 20\,\mathrm{m/s}$ to ≈ 5% at $\overline{U}_{\mathrm{FB}} = 65\,\mathrm{m/s}$ [28]. The dashed lines in Fig. A.1 will be used in the following section to assess if the prediction model for unconfined flashback limits developed in the present work is able to reproduce the conditions at flashback with a similar accuracy as the Damköhler correlation of Kalantari et al. [27]. For that purpose, the flashback limits $\overline{U}_{\mathrm{FB}}$ obtained from the prediction model will be converted to Damköhler numbers $\mathrm{Da}_{\mathrm{PM}}$ using Eq. (A.2) and (2.27). $\mathrm{Da}_{\mathrm{PM}}$ is then compared to the values of Da_{c} after Eq. (A.1) has been evaluated at the same conditions.

A.2 Prediction of Unconfined Flashback Limits at High Pressure

The prediction model for flashback limits of turbulent unconfined flames presented in Sec. 6.2.4 can be easily adapted to elevated pressures as it is predominantly based on basic mixture and flow field properties. The model is evaluated for a $h = 25.4\,\mathrm{mm}$ tube burner at a preheating temperature of 673 K and four different pressures of 3, 5, 7 and 20 bar. The first three pressures represent the experimental conditions of Kalantari et al. [27] whereas the last one is included to cover gas turbine conditions, as well.

The parameters required in the prediction model are obtained as follows: The unburned mixture properties are extracted form *Cantera 2.2* [67]. The unstretched laminar burning velocity is computed from the polynomial approach in Eq. (2.41) and the coefficients presented in App. C. The Markstein lengths are calculated as described in Sec. 2.3.2.2. Unstretched laminar burning velocities and Markstein lengths are depicted in Fig. A.2.

According to Eq. (2.29), the turbulent macroscale is set to $\Lambda = 0.5\,h$. The laminar flame thickness is obtained from Eq. (2.44). The parameter of the turbulent burning velocity correlation is set to $C_{\mathrm{S}} = 2.6$ as in Chap. 5 and 6. The parameters for the flame generated turbulence correlation remain constant at $G_1 = 2.5$, $G_2 = 0.7$ and $G_3 = -0.4$ (cf. Sec. 6.2.4). The pressure dependence is

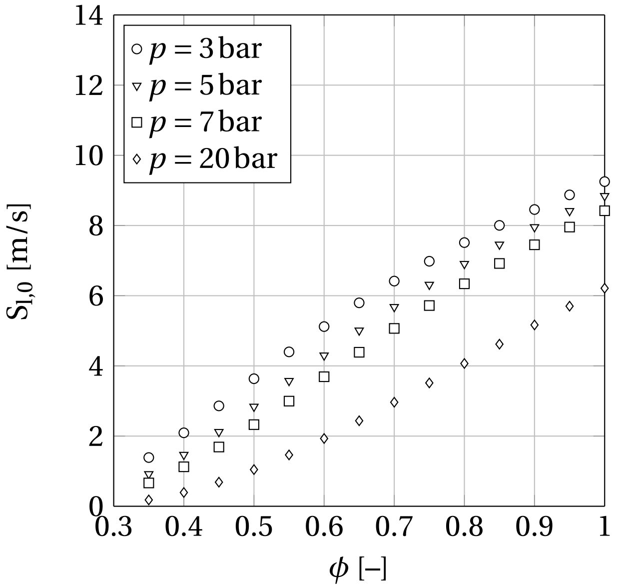

(a) Unstretched laminar burning velocity

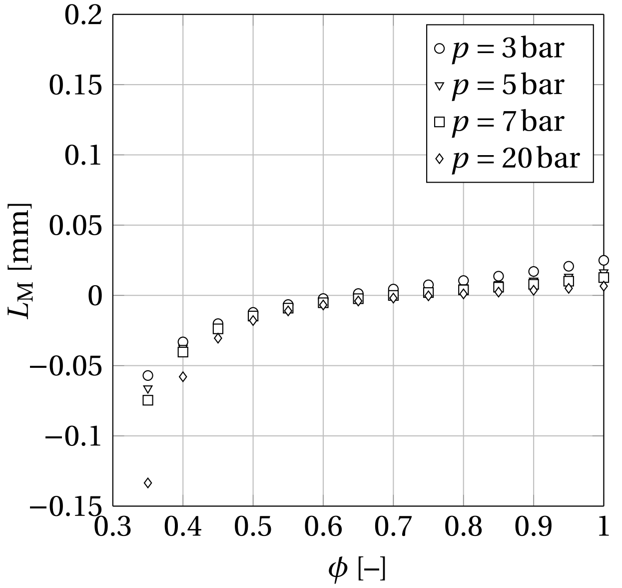

(b) Markstein length

Figure A.2: Unstretched laminar burning velocity and Markstein length of hydrogen-air mixtures at elevated pressure.

set to $G_4 = 0.5$ to obtain Damköhler numbers in the range of Eq. (A.1).

Figure A.3(a) shows the calculated flashback limits. The corresponding Reynolds numbers, flame angles and wall distances of flashback are depicted in Fig. A.3(b)–A.4(b). In agreement with the observations of Daniele et al. [26] and Kalantari et al. [27], the calculated velocity at flashback increases with pressure for $\phi > 0.45$. Below this equivalence ratio, no distinct effect is observed. The Reynolds numbers at flashback (Fig. A.3(b)) strongly increase with pressure because of higher flow velocities and lower kinematic viscosity. The flame angles at flashback (Fig. A.4(a)) decrease with increasing pressure. This agrees to the small flame angles and long flames observed by Daniele et al. [26]. The wall distances at flashback corresponding to $y^+_{\mathrm{FB}} = 16.4$ also decrease at elevated pressure due to lower kinematic viscosity and higher flow velocities. As no direct experimental validation data is available, it is unclear whether these observations are realistic and whether the pressure dependencies of the model parameters are correctly represented.

A comparison of the Damköhler numbers $\mathrm{Da}_{\mathrm{PM}}$ obtained from the prediction model and Eq. (A.2) and the corresponding Damköhler numbers Da_{c} computed with the correlation in Eq. (A.1) provides an initial indication of the answer to this question. The result is shown in Fig. A.5. The data are presented in the same way as in the validation of the Damköhler correlation in Fig. A.1. The experimental values are replaced by $\mathrm{Da}_{\mathrm{PM}}$. The dashed lines indicate the scatter observed in the experimental data in Fig. A.1. Since most of the obtained data points lie within this scatter and the Reynolds numbers are in the validity range of Eq. (A.1), it can be assumed that the prediction model delivers reasonable results which are in line with the experimental data of Kalantari et al. [27]. However, the slope of the Damköhler curves in Fig. A.5 significantly differ from the ideal slope of $\mathrm{Da}_{\mathrm{c}} = \mathrm{Da}_{\mathrm{PM}}$. It is observed that at low equivalence ratios Da_{c} is smaller than $\mathrm{Da}_{\mathrm{PM}}$ whereas at high equivalence ratio Da_{c} is higher than $\mathrm{Da}_{\mathrm{PM}}$. The fact that Eq. (A.1) underestimates the Damköhler number at low equivalence ratios but overestimates it around stoichiometry is an indication that flame stretch is not sufficiently accounted for. Increased burning velocities at low equivalence ratios and reduced burning velocities around stoichiometry would increase and reduce Da_{c}, respectively. In this way, the

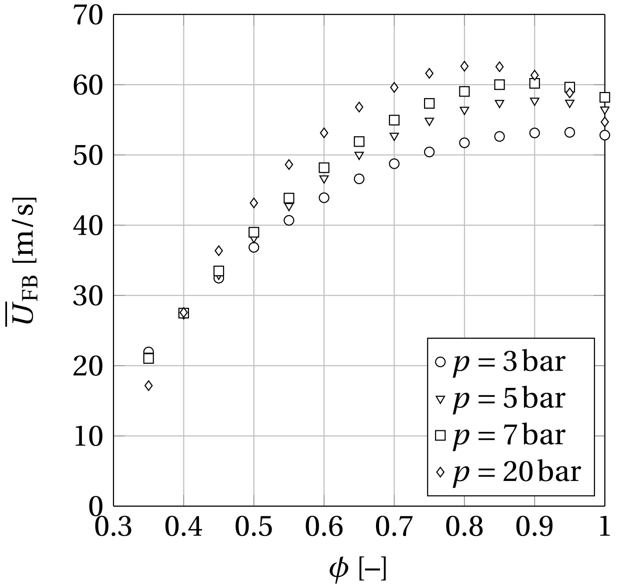

(a) Velocity at flashback

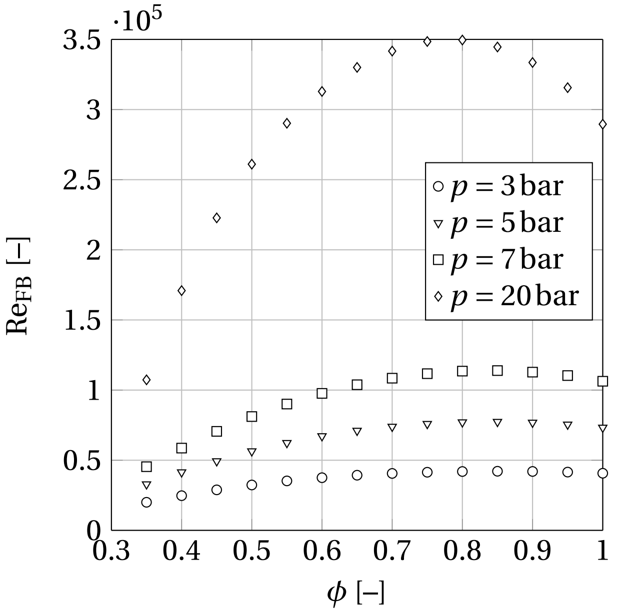

(b) Reynolds number at flashback

Figure A.3: Predicted unconfined flashback parameters for a $d_{\mathrm{h}} = 25.4\,\mathrm{mm}$ tube burner at elevated pressure.

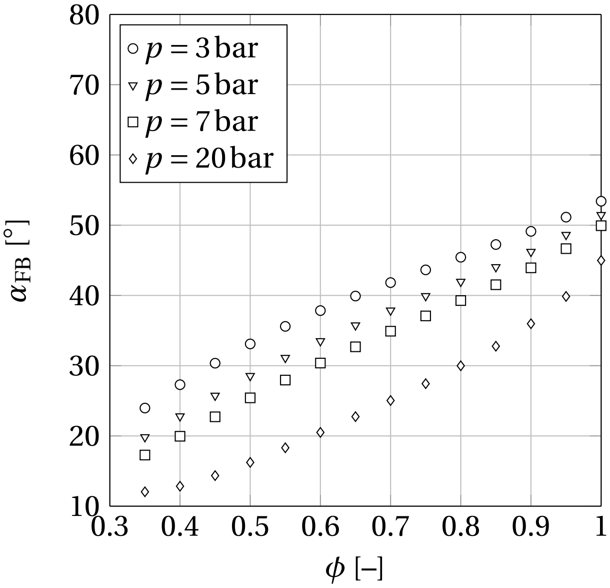

(a) Averaged flame angle at flashback

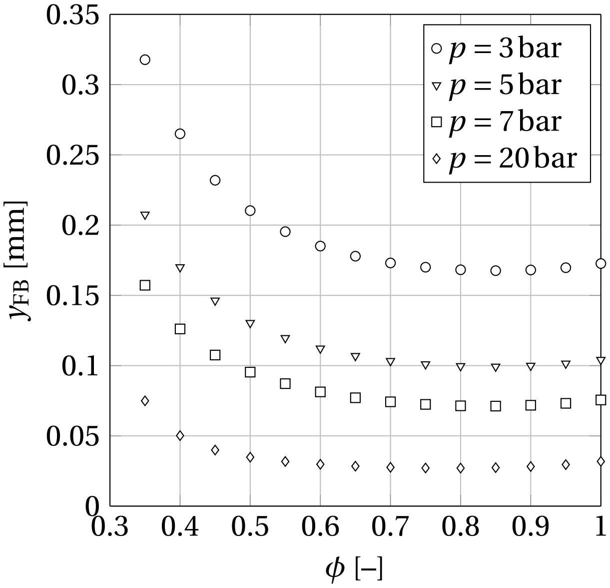

(b) Wall distance of flashback

Figure A.4: Predicted unconfined flashback parameters for a d_h = 25.4 mm tube burner at elevated pressure.

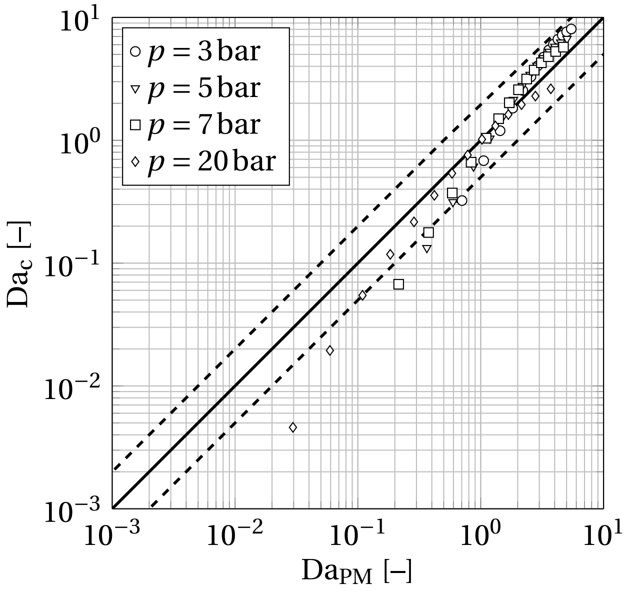

Figure A.5: Damköhler numbers obtained from prediction model compared to Damköhler correlation in Eq. (A.1). Dashed lines represent scatter of experimental data from Fig. A.1.

slope of the obtained Damköhler curves would be adjusted to the ideal slope of $\mathrm{Da}_\mathrm{c} = \mathrm{Da}_\mathrm{PM}$.

It can be further noted that the Damköhler numbers obtained from the prediction model are generally higher than those from the experiments of Kalantari et al. [27]. This is reasonable because the high burner rim temperatures in their uncooled burner lead to a higher flashback risk. The resulting higher flashback limits $\overline{U}_\mathrm{FB}$ reduce the Damköhler numbers due to higher shear stress velocities u_τ. As the rim temperature effect in the experiments of Kalantari et al. [27] cannot be separated from the pressure effect, the flashback limits obtained in the experiment cannot be used to validate the predicted values which do not take into account increased burner rim temperatures. For a proper validation of the prediction model at elevated pressure, experiments with a burner cooling system would be required to keep the material temperature close to the mixture's preheating temperature.

It can be concluded that the prediction model shows promising results since the calculated flow velocities and flame angles at flashback conditions are in a reasonable range. However, more validation experiments at elevated pressure and preheating temperature with well defined boundary conditions such as low burner rim temperature would be required for a proper validation of the developed model.

B Details of Experimental Setup

B.1 Test Rig Components

The test rig consists of three main components: the channel burner, the acoustic excitation section and the flow channel including a flame arrestor. These components will be described in the following sections. If not stated otherwise, the components are made of stainless steel.

B.1.1 Channel Burner

The channel burner is the main component influencing the flashback behavior of the test rig without acoustic excitation. A detailed drawing of the burner is shown in Fig. B.1. The flow channel is 158 mm wide and 17.5 mm high. The rectangular burner design was chosen in this work due to its advantages in the application of optical measurement techniques compared to tube burners. The burner is optically accessible through three quartz glass windows which are located close to the burner exit. In order to prevent high burner rim temperatures, the burner exit consists of a stainless steel frame including two separate water cooling circuits for the lower and upper burner wall. A type K thermocouple measures the temperature of the lower channel wall at the burner exit to ensure that the wall temperature does not strongly increase during the flashback experiment. Another type K thermocouple in the upper burner wall upstream of the quartz glass window detects the flame during flashback and triggers the shutoff of the fuel supply and the increase of the air mass flow rate to its maximum value.

A disadvantage of the rectangular geometry is the increased flashback risk in the thick boundary layers of the channel corners. To prevent corner flashback, additional air is injected into the corners increasing the momentum and di-

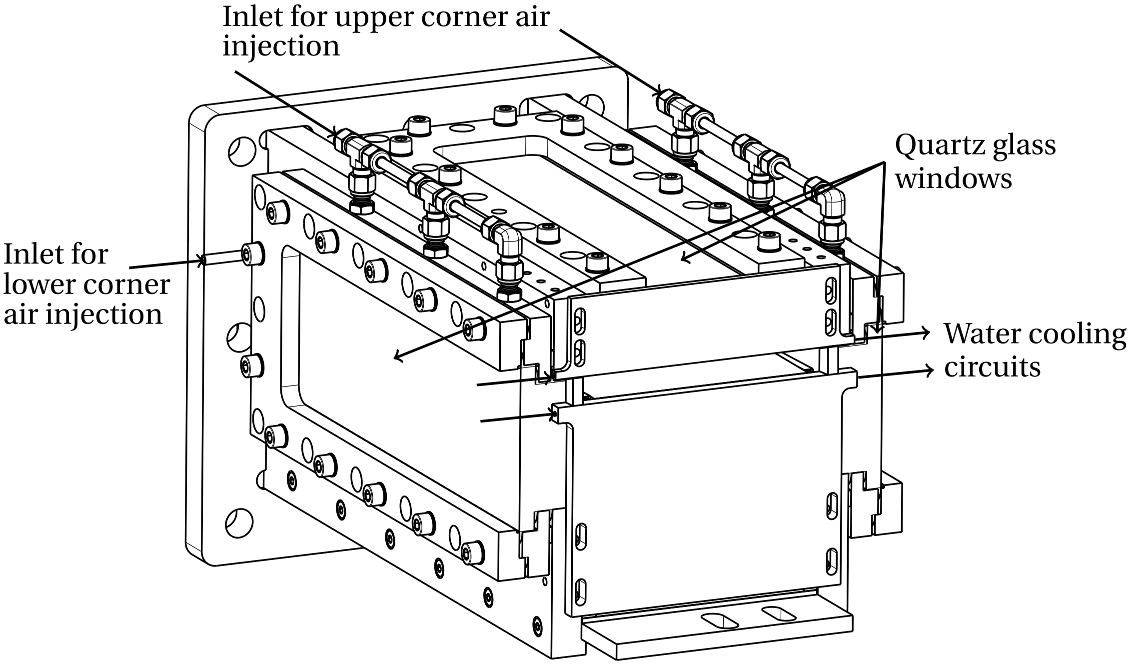

Figure B.1: Channel burner.

luting the mixture. However, at high main mass flow rates, i.e. at flashback tests close to stoichiometry or with high excitation amplitudes, the injection is not efficient enough to prevent flashback in the corners. In order to perform meaningful flashback tests at these conditions, the efficiency of the corner injection would have to be increased. Another possibility would be to use a tube burner instead of the channel burner. The constant boundary layer conditions over the whole circumference would be beneficial during the determination of the flashback limits.

B.1.2 Acoustic Excitation Section

In order to analyze the effect of velocity oscillations on the flashback behavior of the burner, the flow in the test rig is acoustically excited. For that purpose, an acoustic excitation section was designed with symmetrically arranged adapters for up to six speakers. The acoustic excitation section is shown in Fig. B.2. It consists of a flow channel segment which can be inserted into the test rig upstream of the flame arrestor. Two forcing tubes are con-

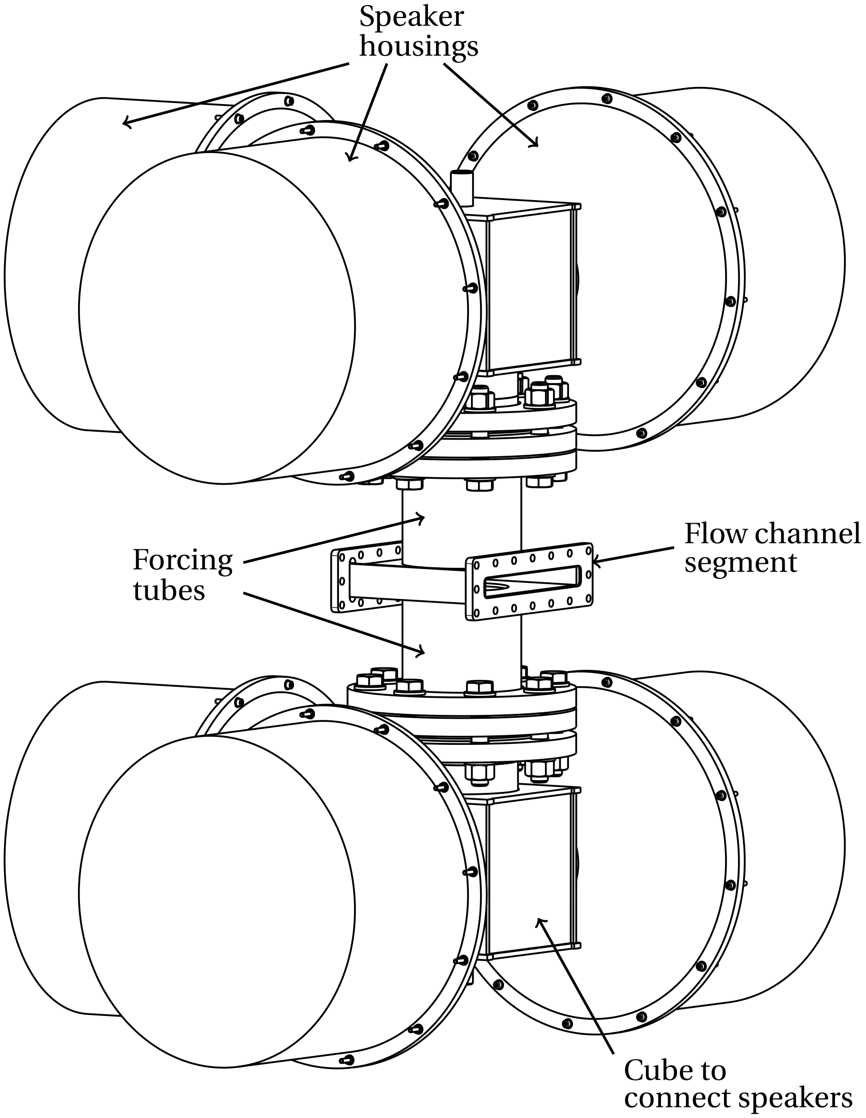

Figure B.2: Acoustic excitation section.

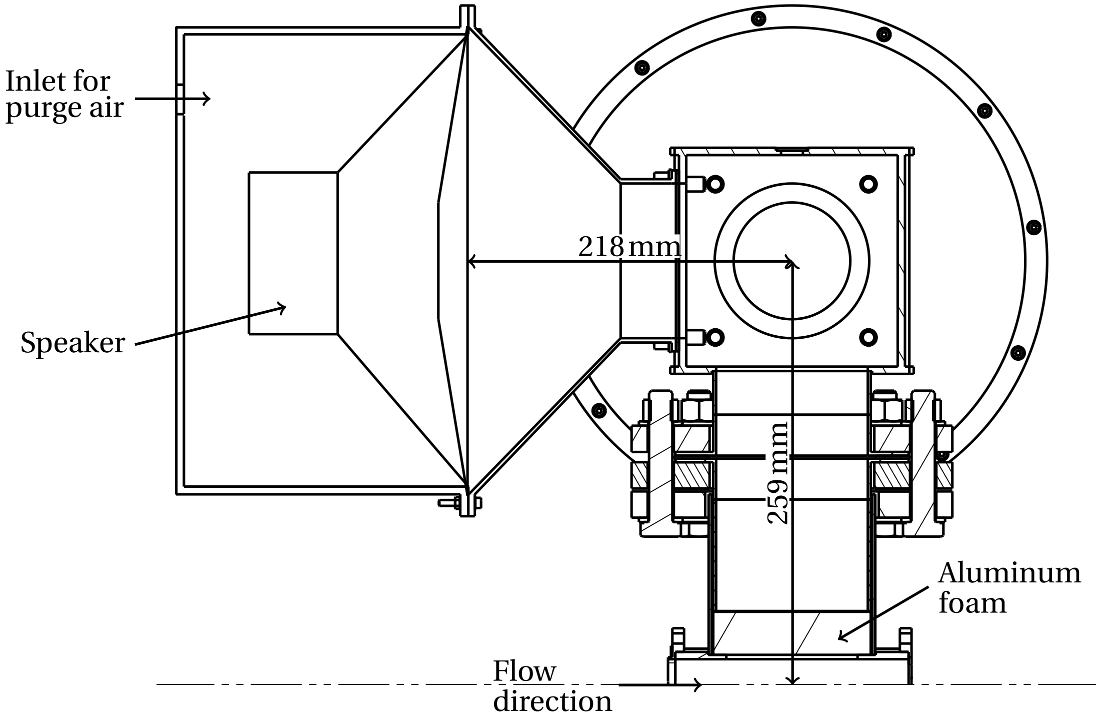

Figure B.3: Cut through acoustic excitation section.

nected to the upper and lower side of the flow channel segment. At the end of the forcing tubes, two adapter cubes are installed. Depending on the experiment, one or three speakers are connected to each cube.

Figure B.3 shows a cut through the acoustic excitation section. At the connection of the forcing tube to the flow channel segment, a 30 mm thick aluminum foam is inserted to prevent the formation of large scale vortices. In order to minimize acoustic losses, a high porosity foam is chosen. This material is not able to stop the upstream propagating hydrogen-air flame during flashback. A flame arrestor has to be installed downstream of the acoustic excitation section to prevent destruction of the speakers.

During a flashback experiment, where a hydrogen-air mixture flows through the main flow channel, some hydrogen diffuses into the forcing tubes. In order to avoid an accumulation of hydrogen, the excitation section is purged with air after the experiment. For that purpose, each speaker is equipped with an adapter for a purge air pipe.

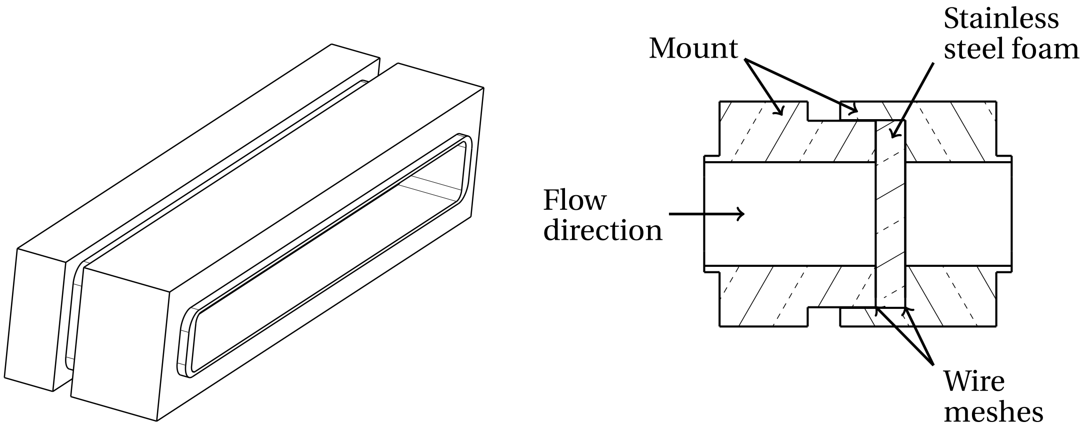

(a) Isometric view (b) Cut through center plane

Figure B.4: Flame arrestor.

B.1.3 Flow Channel and Flame Arrestor

Upstream of the acoustic excitation section, hydrogen and air are mixed in a static flow mixer. Downstream of a 90° bend, the flow is conditioned in a flow straightening section consisting of honeycomb structures and perforated plates. Details on mixture and flow conditioning can be found in [9]. From the flow straightening section, the hydrogen-air mixture enters the flow channel ($158 \times 17.5\,\mathrm{mm}^2$) and passes the acoustic excitation section.

Downstream of the acoustic excitation section, a flame arrestor is inserted into the test rig to prevent flame propagation further upstream. A type K thermocouple is positioned upstream of the flame arrestor to monitor whether the flame enters the excitation section. If the flame was able to propagate into the forcing tubes, the combustion of the accumulated hydrogen would lead to a significant pressure increase resulting in destruction of the speakers. The flame arrestor is sketched in Fig. B.4. It consists of a 5 mm stainless steel foam with a density of $0.6\,\mathrm{g/cm}^3$ and small pore sizes. Upstream and downstream of the metal foam two fine wire meshes with mesh sizes of 0.1 mm and wire diameters of 0.065 mm are located. The flame arrestor is connected to the main flow channel via a two-part mount. It has reliably stopped the flame propagation in all flashback experiments performed in this work as no temperature increase was detected by the thermocouple upstream of the flame arrestor. At the same time, the pressure loss of the flame arrestor is low enough to achieve reasonable high velocity oscillations at the burner exit.

The undisturbed burner duct extends from the flame arrestor to the burner exit. The length of this section of the flow channel can be changed from $l = 570\,\mathrm{mm}$ to $l = 1070\,\mathrm{mm}$ by inserting an additional channel segment. Since the hydrodynamic entrance length for turbulent duct flow is typically approximated by $l_\mathrm{h} = 10\,d_\mathrm{h} = 315\,\mathrm{mm}$ [132], the flow at the burner exit can in both cases be seen as fully developed. As the flashback process is sensitive to disturbances in the flow field, even small steps along the channel walls have to be avoided during the assembly of the flow channel segments. In order to facilitate the assembly, the segments are equipped with tongue and groove joints as shown in Fig. B.3 and B.4.

B.2 Acoustic Design of the Test Rig

During the design of the acoustic excitation section, the acoustic behavior and the natural frequencies of the test rig have been estimated. The open end configuration ensures that a pressure minimum and a velocity maximum are located at the burner exit. A first rough estimate of the natural frequencies can be obtained by analyzing only the channel segment downstream of the flame arrestor. For that purpose, the flame arrestor can be approximated as a closed end. The natural frequency can be estimated by

$$f = \frac{2\,n - 1}{4}\frac{C}{l} \tag{B.1}$$

depending on the order of the natural frequency n, the length of the channel l and the speed of sound $C \approx 346\,\mathrm{m/s}$. The resulting natural frequencies for the short and long channel configuration are summarized in Tab. B.1. This rough estimation indicated that the test rig should show natural frequencies in the frequency range of interest between 50 and 500 Hz. The additional channel segment seemed suitable to significantly modify the natural frequency.

In order to support the analytic estimation, a one-dimensional acoustic network model of the test rig was set up in taX [133]. The main components of

Table B.1: Natural frequencies of the test rig estimated with Eq. (B.1) for the short and long channel configuration.

n [–]	f [Hz]	f [Hz]
	$l = 570\,\mathrm{mm}$	$l = 1070\,\mathrm{mm}$
1	152	81
2	455	242
3	759	404

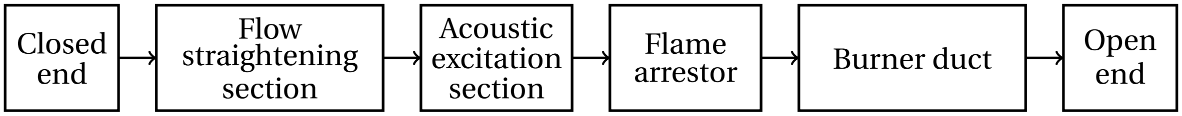

Figure B.5: Network model of flashback test rig.

the model are depicted in Fig. B.5. The upstream boundary is approximated as a closed end. The flow straightening section consists of a sequence of ducts and area change elements including pressure losses. The elements are listed in Tab. B.2. The network model for the acoustic excitation section is sketched in Fig. B.6. The forcing tubes are connected to the flow channel segment with two junctions. The metal foam inside the forcing tubes is included as an area change with pressure loss. Downstream of the acoustic excitation section, the

Table B.2: Elements of network model of flow straightening section.

	Element	Parameter	Function
1	Duct	$l = 243\,\mathrm{mm}$	Circular duct
2	Area change	$\zeta = 5$	Perforated plate
3	Duct	$l = 22\,\mathrm{mm}$	Rectangular duct
4	Area change	$\zeta = 1$	Honeycomb
5	Duct	$l = 38\,\mathrm{mm}$	Rectangular duct
6	Area change	$\zeta = 5$	Perforated plate
7	Duct	$l = 10\,\mathrm{mm}$	Rectangular duct
8	Area change	$\zeta = 5$	Perforated plate
9	Duct	$l = 12\,\mathrm{mm}$	Rectangular duct
10	Area change	$\zeta = 5$	Perforated plate

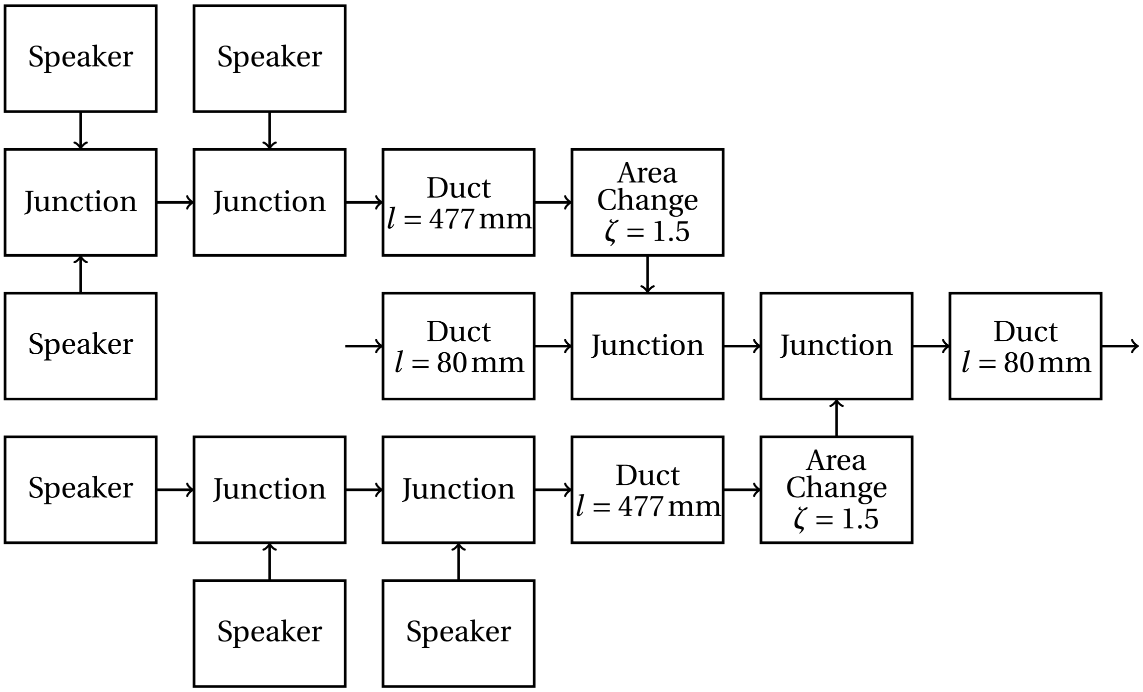

Figure B.6: Network model of acoustic excitation section.

flame arrestor is connected in the form of an area change with a pressure loss coefficient of $\zeta = 3$. It has to be noted that changing the pressure loss of the area changes does not significantly influence the obtained natural frequencies. The burner duct is represented with a duct element. Its length is set to $l = 570\,\text{mm}$ and $l = 1070\,\text{mm}$ for the short and long channel configuration.

The acoustic velocity oscillations at the burner exit obtained from the taX network model are shown in Fig. B.7 for frequencies between 50 and 750 Hz. The obtained peaks in velocity oscillation amplitudes can be attributed to the natural frequencies. The resulting acoustic velocity oscillations at the burner exit are normalized by the oscillation amplitude of the first natural frequency in the investigated frequency range. The obtained natural frequencies for the short and long channel are listed in Tab. B.3. Compared to the analytic approach in Eq. (B.1), the taX model predicts higher natural frequencies. The discrepancy between the estimations from Eq. (B.1) and the network model shows that the flow system upstream of the flame arrestor has a strong influence on the acoustic behavior. However, similar to Eq. (B.1), the taX model predicts two to three natural frequencies in the frequency range of interest and

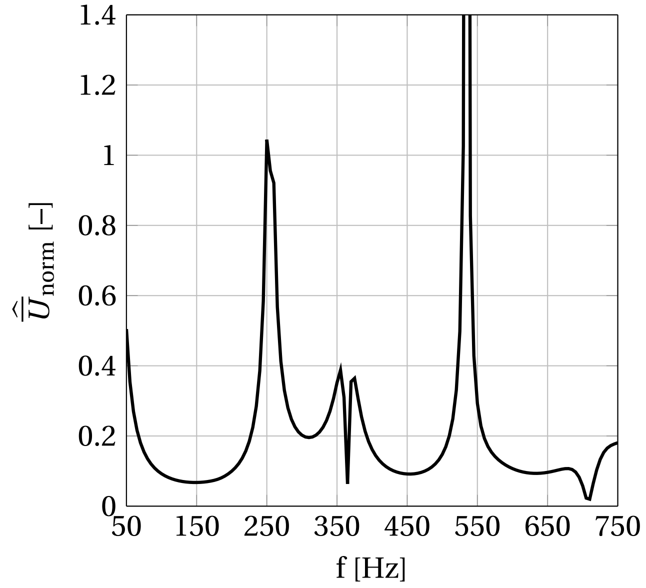

(a) Short channel ($l = 570\,\mathrm{mm}$)

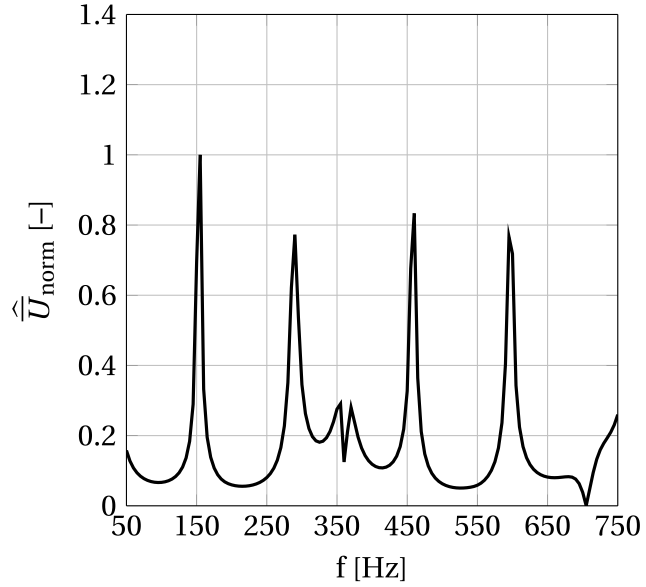

(b) Long channel ($l = 1070\,\mathrm{mm}$)

Figure B.7: Normalized acoustic velocity oscillation amplitudes at the burner exit obtained from taX network model.

Table B.3: Natural frequencies of the test rig calculated with the taX network model for the short and long channel configuration.

n [–]	f [Hz] $l = 570\,\mathrm{mm}$	f [Hz] $l = 1070\,\mathrm{mm}$
1	254	154
2	364	290
3	540	362

a significant difference between the short and long channel configuration.

From this starting point, the test rig was set up and its natural frequencies were determined using CTA as described in Sec. 3.3.1 and 4.1. First order natural frequencies of $f_1 = 135\,\mathrm{Hz}$ for the short channel and of $f_1 = 120\,\mathrm{Hz}$ for the long channel were obtained with speaker type 1 (cf. Tab. 4.1). These frequencies differ significantly from the described estimations. Especially the difference between the two configurations was overestimated with both the analytic and the network model approach. Due to the small difference in natural frequency induced by the additional channel segment, speaker type 2 was only investigated in the long channel configuration. The forcing tube length in the acoustic excitation section (cf. B.3) was shortened from 259 mm to 241 mm. With six speakers, natural frequencies of $f_1 = 135\,\mathrm{Hz}$ and $f_2 = 350\,\mathrm{Hz}$ were obtained. With only two installed speakers, the frequencies changed to $f_1 = 115\,\mathrm{Hz}$ and $f_2 = 330\,\mathrm{Hz}$. This shows again that geometric details of the acoustic excitation section influence the natural frequencies of the test rig. As neither the analytic approach in Eq. (B.1) nor the taX network model are able to represent the three-dimensional geometry of the flow system, it is understandable that the estimated natural frequencies strongly differ from the measured values. Regardless of this discrepancy between estimation and experiment, the test rig showed suitable natural frequencies to conduct flashback test at different frequency levels as promised by the estimations. The results of the flashback tests are discussed in Chap. 4.

C Polynomials for Unstretched Laminar Burning Velocity

C.1 Hydrogen-Air Mixtures

Table C.1: Coefficients for unstretched laminar burning velocity polynomials (Eq. (2.41)) for hydrogen-air mixtures at $p = 1\,\text{bar}$.

ϕ	b_7 [m/(s K^3)]	b_8 [m/(s K^2)]	b_9 [m/(s K)]	b_{10} [m/s]
0.35	4.4691×10^{-8}	-3.9805×10^{-5}	1.2105×10^{-2}	-1.0500
0.40	3.3006×10^{-8}	-2.0134×10^{-5}	3.5523×10^{-2}	0.1775
0.45	2.8495×10^{-8}	-1.2758×10^{-5}	1.4482×10^{-3}	0.3939
0.50	2.3415×10^{-8}	-5.6869×10^{-6}	-1.9500×10^{-4}	0.5378
0.55	2.0614×10^{-8}	-2.3736×10^{-6}	-7.5732×10^{-5}	0.4402
0.60	2.1572×10^{-8}	-4.6955×10^{-6}	2.5409×10^{-3}	0.0113
0.65	2.3868×10^{-8}	-9.0425×10^{-6}	5.9713×10^{-3}	-0.5159
0.70	2.0832×10^{-8}	-5.2343×10^{-6}	5.3254×10^{-3}	-0.4050
0.75	2.2390×10^{-8}	-8.1905×10^{-6}	7.7401×10^{-3}	-0.7350
0.80	2.5342×10^{-8}	-1.3190×10^{-5}	1.1025×10^{-2}	-1.1882
0.85	2.8243×10^{-8}	-1.8041×10^{-5}	1.4110×10^{-2}	-1.6099
0.90	2.8609×10^{-8}	-1.9000×10^{-5}	1.5271×10^{-2}	-1.7250
0.95	2.6543×10^{-8}	-1.6476×10^{-5}	1.4747×10^{-2}	-1.5977
1.00	2.6999×10^{-8}	-1.7489×10^{-5}	1.5774×10^{-2}	-1.6986
1.05	2.8439×10^{-8}	-2.0087×10^{-5}	1.7561×10^{-2}	-1.9232
1.10	2.8914×10^{-8}	-2.1081×10^{-5}	1.8475×10^{-2}	-2.0131
1.15	3.5393×10^{-8}	-3.1054×10^{-5}	2.3609×10^{-2}	-2.7413
1.20	3.0459×10^{-8}	-2.4021×10^{-5}	2.0689×10^{-2}	-2.2751
1.25	3.0091×10^{-8}	-2.3697×10^{-5}	2.0866×10^{-2}	-2.2711
1.30	3.0090×10^{-8}	-2.3868×10^{-5}	2.1222×10^{-2}	-2.2971

Table C.2: Coefficients for unstretched laminar burning velocity polynomials (Eq. (2.41)) for hydrogen-air mixtures at $p = 3\,\text{bar}$.

ϕ	b_7 [m/(s K^3)]	b_8 [m/(s K^2)]	b_9 [m/(s K)]	b_{10} [m/s]
0.35	4.1681×10^{-8}	-4.8119×10^{-5}	1.9466×10^{-2}	-2.6227
0.40	4.7248×10^{-8}	-5.2033×10^{-5}	2.0841×10^{-2}	-2.7678
0.45	4.4291×10^{-8}	-4.4041×10^{-5}	1.7055×10^{-2}	-2.1711
0.50	3.8885×10^{-8}	-3.3191×10^{-5}	1.2257×10^{-2}	-1.4350
0.55	3.1298×10^{-8}	-2.0294×10^{-5}	7.0328×10^{-3}	-0.6830
0.60	2.5922×10^{-8}	-1.1495×10^{-5}	3.9858×10^{-3}	-0.2576
0.65	2.1927×10^{-8}	-5.3562×10^{-6}	2.3464×10^{-3}	-0.0403
0.70	2.1129×10^{-8}	-4.2569×10^{-6}	3.0492×10^{-3}	-0.1482
0.75	2.1594×10^{-8}	-5.3503×10^{-6}	4.7936×10^{-3}	-0.4038
0.80	2.1304×10^{-8}	-5.2361×10^{-6}	5.8226×10^{-3}	-0.5277
0.85	2.0085×10^{-8}	-3.7392×10^{-6}	6.0795×10^{-3}	-0.5166
0.90	1.9491×10^{-8}	-3.2045×10^{-6}	6.7250×10^{-3}	-0.5602
0.95	1.8992×10^{-8}	-2.6903×10^{-6}	7.2440×10^{-3}	-0.5738
1.00	1.8953×10^{-8}	-2.8801×10^{-6}	8.0258×10^{-3}	-0.6234
1.05	1.8927×10^{-8}	-3.0118×10^{-6}	8.6754×10^{-3}	-0.6511
1.10	1.8762×10^{-8}	-2.9791×10^{-6}	9.2321×10^{-3}	-0.6783
1.15	1.8907×10^{-8}	-3.4250×10^{-6}	9.9664×10^{-3}	-0.7381
1.20	1.8502×10^{-8}	-2.8660×10^{-6}	1.0102×10^{-2}	-0.7054
1.25	1.8077×10^{-8}	-2.4019×10^{-6}	1.0302×10^{-2}	-0.7007
1.30	1.7817×10^{-8}	-2.1341×10^{-6}	1.0535×10^{-2}	-0.7057

Table C.3: Coefficients for unstretched laminar burning velocity polynomials (Eq. (2.41)) for hydrogen-air mixtures at $p = 5\,\text{bar}$.

ϕ	b_7 [m/(s K^3)]	b_8 [m/(s K^2)]	b_9 [m/(s K)]	b_{10} [m/s]
0.35	2.4161×10^{-8}	-2.6225×10^{-5}	9.9694×10^{-3}	-1.2786
0.40	3.4450×10^{-8}	-3.8231×10^{-5}	1.5382×10^{-2}	-2.0699
0.45	4.1255×10^{-8}	-4.4699×10^{-5}	1.8165×10^{-2}	-2.4356
0.50	4.0735×10^{-8}	-4.0458×10^{-5}	1.6081×10^{-2}	-2.0754
0.55	3.6811×10^{-8}	-3.1987×10^{-5}	1.2392×10^{-2}	-1.5001
0.60	3.1977×10^{-8}	-2.2975×10^{-5}	8.8054×10^{-3}	-0.9686

0.65	2.6014×10^{-8}	-1.2734×10^{-5}	4.7626×10^{-3}	-0.3582
0.70	2.3120×10^{-8}	-7.9255×10^{-6}	3.6122×10^{-3}	-0.2096
0.75	2.1038×10^{-8}	-4.6079×10^{-6}	3.1773×10^{-3}	-0.1506
0.80	1.8994×10^{-8}	-1.4912×10^{-6}	2.7818×10^{-3}	-0.0798
0.85	1.7343×10^{-8}	9.3317×10^{-7}	2.6464×10^{-3}	-0.0324
0.90	1.8220×10^{-8}	-5.0005×10^{-7}	4.2461×10^{-3}	-0.2300
0.95	1.8774×10^{-8}	-1.6246×10^{-6}	5.6910×10^{-3}	-0.4029
1.00	1.8767×10^{-8}	-1.8021×10^{-6}	6.5532×10^{-3}	-0.4731
1.05	1.5930×10^{-8}	2.1051×10^{-6}	5.4694×10^{-3}	-0.2599
1.10	1.4512×10^{-8}	4.0340×10^{-6}	5.2057×10^{-3}	-0.1655
1.15	1.4633×10^{-8}	3.6981×10^{-6}	5.9461×10^{-3}	-0.2261
1.20	1.3376×10^{-8}	5.3600×10^{-6}	5.6989×10^{-3}	-0.1478
1.25	1.3008×10^{-8}	5.8642×10^{-6}	5.8822×10^{-3}	-0.1339
1.30	1.4060×10^{-8}	4.2460×10^{-6}	7.0421×10^{-3}	-0.2799

Table C.4: Coefficients for unstretched laminar burning velocity polynomials (Eq. (2.41)) for hydrogen-air mixtures at $p = 7\,\text{bar}$.

ϕ	b_7 [m/(s K^3)]	b_8 [m/(s K^2)]	b_9 [m/(s K)]	b_{10} [m/s]
0.35	1.8622×10^{-8}	-2.0178×10^{-5}	7.5351×10^{-3}	-0.9441
0.40	2.4355×10^{-8}	-2.5894×10^{-5}	1.0020×10^{-2}	-1.3138
0.45	3.2326×10^{-8}	-3.4639×10^{-5}	1.3970×10^{-2}	-1.8780
0.50	3.7074×10^{-8}	-3.8399×10^{-5}	1.5576×10^{-2}	-2.0654
0.55	3.7275×10^{-8}	-3.5853×10^{-5}	1.4454×10^{-2}	-1.8551
0.60	3.5106×10^{-8}	-3.0187×10^{-5}	1.2082×10^{-2}	-1.4688
0.65	3.1495×10^{-8}	-2.2894×10^{-5}	9.1746×10^{-3}	-1.0171
0.70	2.7891×10^{-8}	-1.6322×10^{-5}	6.8919×10^{-3}	-0.6796
0.75	2.3992×10^{-8}	-9.8393×10^{-6}	4.8051×10^{-3}	-0.3709
0.80	2.0794×10^{-8}	-4.4389×10^{-6}	3.1547×10^{-3}	-0.1113
0.85	2.1045×10^{-8}	-4.6407×10^{-6}	4.2677×10^{-3}	-0.2667
0.90	1.9977×10^{-8}	-3.0853×10^{-6}	4.5133×10^{-3}	-0.2786
0.95	1.8450×10^{-8}	-8.0331×10^{-7}	4.3261×10^{-3}	-0.2159
1.00	1.7772×10^{-8}	8.0070×10^{-8}	4.7765×10^{-3}	-0.2472
1.05	1.7772×10^{-8}	-6.2774×10^{-8}	5.5978×10^{-3}	-0.3164

1.10	1.9314×10^{-8}	-2.4416×10^{-6}	7.3894×10^{-3}	-0.5315
1.15	1.9564×10^{-8}	-2.9253×10^{-6}	8.2150×10^{-3}	-0.6021
1.20	1.8887×10^{-8}	-1.9067×10^{-6}	8.2377×10^{-3}	-0.5593
1.25	1.8102×10^{-8}	-7.3028×10^{-7}	8.1299×10^{-3}	-0.5052
1.30	1.8244×10^{-8}	-9.7647×10^{-7}	8.6704×10^{-3}	-0.5630

Table C.5: Coefficients for unstretched laminar burning velocity polynomials (Eq. (2.41)) for hydrogen-air mixtures at $p = 20\,\text{bar}$.

ϕ	b_7 [m/(s K^3)]	b_8 [m/(s K^2)]	b_9 [m/(s K)]	b_{10} [m/s]
0.35	9.6381×10^{-9}	-1.2129×10^{-5}	1.2105×10^{-2}	-0.6913
0.40	1.1922×10^{-8}	-1.3460×10^{-5}	3.5523×10^{-2}	-0.6737
0.45	1.4794×10^{-8}	-1.5716×10^{-5}	1.4482×10^{-3}	-0.7770
0.50	1.7390×10^{-8}	-1.7798×10^{-5}	1.9500×10^{-4}	-0.9254
0.55	2.0158×10^{-8}	-1.9983×10^{-5}	7.5732×10^{-5}	-1.0673
0.60	2.3962×10^{-8}	-2.3635×10^{-5}	2.5409×10^{-3}	-1.3072
0.65	2.3357×10^{-8}	-2.0725×10^{-5}	5.9713×10^{-3}	-1.0878
0.70	2.7320×10^{-8}	-2.4578×10^{-5}	5.3254×10^{-3}	-1.3374
0.75	2.8397×10^{-8}	-2.4120×10^{-5}	7.7401×10^{-3}	-1.2867
0.80	3.0468×10^{-8}	-2.5500×10^{-5}	1.1025×10^{-2}	-1.3924
0.85	2.8633×10^{-8}	-2.1459×10^{-5}	1.4110×10^{-2}	-1.1681
0.90	2.7806×10^{-8}	-1.9154×10^{-5}	1.5271×10^{-2}	-1.0849
0.95	2.5655×10^{-8}	-1.5062×10^{-5}	1.4747×10^{-2}	-1.8807
1.00	2.3942×10^{-8}	-1.1823×10^{-5}	1.5774×10^{-2}	-0.7379
1.05	2.1577×10^{-8}	-7.8029×10^{-6}	1.7561×10^{-2}	-0.5196
1.10	2.0352×10^{-8}	-5.6889×10^{-6}	1.8475×10^{-2}	-0.4391
1.15	1.9243×10^{-8}	-3.6985×10^{-6}	2.3609×10^{-2}	-0.3473
1.20	1.9027×10^{-8}	-3.1748×10^{-6}	2.0689×10^{-2}	-0.3676
1.25	1.8432×10^{-8}	-2.0454×10^{-6}	2.0866×10^{-2}	-0.3352
1.30	1.7883×10^{-8}	-9.9567×10^{-7}	2.1222×10^{-2}	-0.3104

C.2 Methane-Air Mixtures

Table C.6: Coefficients for unstretched laminar burning velocity polynomials (Eq. (2.41)) for methane-air mixtures at $p = 1\,\text{bar}$.

ϕ	b_7 [m/(s K^3)]	b_8 [m/(s K^2)]	b_9 [m/(s K)]	b_{10} [m/s]
0.40	4.4462×10^{-9}	-4.0587×10^{-6}	1.4362×10^{-3}	−0.1737
0.45	4.4388×10^{-9}	-3.5156×10^{-6}	1.2383×10^{-3}	−0.1483
0.50	4.5577×10^{-9}	-3.2565×10^{-6}	1.2303×10^{-3}	−0.1490
0.55	4.3029×10^{-9}	-2.5341×10^{-6}	1.0406×10^{-3}	−0.1189
0.60	3.9855×10^{-9}	-1.8117×10^{-6}	8.8191×10^{-4}	−0.0912
0.65	3.6835×10^{-9}	-1.1788×10^{-6}	7.7379×10^{-4}	−0.0679
0.70	3.5466×10^{-9}	-8.7960×10^{-7}	8.3711×10^{-4}	−0.0695
0.75	3.2344×10^{-9}	-4.0313×10^{-7}	8.2385×10^{-4}	−0.0597
0.80	3.1466×10^{-9}	-2.7750×10^{-7}	9.4818×10^{-4}	−0.0669
0.85	2.7924×10^{-9}	2.0205×10^{-7}	8.8821×10^{-4}	−0.0466
0.90	2.8039×10^{-9}	1.2468×10^{-7}	1.0587×10^{-3}	−0.0609
0.95	2.5763×10^{-9}	3.8775×10^{-7}	1.0432×10^{-3}	−0.0500
1.00	2.6724×10^{-9}	1.6248×10^{-7}	1.2222×10^{-3}	−0.0699
1.05	2.6337×10^{-9}	1.6752×10^{-7}	1.2426×10^{-3}	−0.0683
1.10	2.7259×10^{-9}	-2.1875×10^{-8}	1.3195×10^{-3}	−0.0811
1.15	2.8180×10^{-9}	-2.2304×10^{-7}	1.3742×10^{-3}	−0.0992
1.20	2.8599×10^{-9}	-3.1911×10^{-7}	1.3323×10^{-3}	−0.1109
1.25	2.4780×10^{-9}	2.6208×10^{-7}	9.0936×10^{-4}	−0.0716
1.30	2.1016×10^{-9}	9.0589×10^{-7}	3.6914×10^{-4}	−0.0100

Table C.7: Coefficients for unstretched laminar burning velocity polynomials (Eq. (2.41)) for methane-air mixtures at $p = 20\,\text{bar}$.

ϕ	b_7 [m/(s K^3)]	b_8 [m/(s K^2)]	b_9 [m/(s K)]	b_{10} [m/s]
0.40	8.4904×10^{-10}	-8.4157×10^{-7}	3.1926×10^{-4}	−0.0402
0.45	1.0406×10^{-9}	-9.8351×10^{-7}	3.7574×10^{-4}	−0.0472
0.50	1.2193×10^{-9}	-1.0852×10^{-6}	4.1838×10^{-4}	−0.0519
0.55	1.3957×10^{-9}	-1.1720×10^{-6}	4.6267×10^{-4}	−0.0569

0.60	1.5181×10^{-9}	-1.1730×10^{-6}	4.7627×10^{-4}	-0.0569
0.65	1.6054×10^{-9}	-1.1291×10^{-6}	4.8037×10^{-4}	-0.0553
0.70	1.6394×10^{-9}	-1.0315×10^{-6}	4.7409×10^{-4}	-0.0524
0.75	1.6300×10^{-9}	-8.9146×10^{-7}	4.5480×10^{-4}	-0.0469
0.80	1.6927×10^{-9}	-8.8250×10^{-7}	5.0122×10^{-4}	-0.0509
0.85	1.7352×10^{-9}	-8.6042×10^{-7}	5.3771×10^{-4}	-0.0530
0.90	1.8016×10^{-9}	-8.8542×10^{-7}	5.8829×10^{-4}	-0.0572
0.95	1.8770×10^{-9}	-9.4024×10^{-7}	6.4604×10^{-4}	-0.0634
1.00	1.9364×10^{-9}	-9.8157×10^{-7}	6.8443×10^{-4}	-0.0675
1.05	1.9402×10^{-9}	-9.5627×10^{-7}	6.7698×10^{-4}	-0.0658
1.10	1.8546×10^{-9}	-8.0402×10^{-7}	5.8832×10^{-4}	-0.0547
1.15	1.8237×10^{-9}	-7.2707×10^{-7}	4.9635×10^{-4}	-0.0424
1.20	2.0455×10^{-9}	-1.0819×10^{-6}	5.9395×10^{-4}	-0.0552
1.25	2.1851×10^{-9}	-1.4225×10^{-6}	7.1323×10^{-4}	-0.0707
1.30	2.2361×10^{-9}	-1.7135×10^{-6}	8.6194×10^{-4}	-0.0958

Previous Publications

Teile dieser Dissertation wurden von der Autorin bereits vorab als Konferenz- und Zeitschriftenbeiträge veröffentlicht. Alle Vorveröffentlichungen sind entsprechend der gültigen Promotionsordnung ordnungsgemäß gemeldet und anschließend aufgeführt. Sie sind deshalb nicht zwangsläufig im Detail einzeln referenziert. Vielmehr wurde bei der Referenzierung eigener Vorveröffentlichungen Wert auf Verständlichkeit und inhaltlichen Bezug gelegt.

Parts of this Ph.D. thesis have been published by the author beforehand in conference proceedings and journal papers. All of these prior printed publications are registered according to the valid doctoral regulations and listed below. Therefore, they are not necessarily quoted explicitly in the text. Whether they were referenced, depended on maintaining comprehensibility and providing all necessary context.

Hoferichter, V., Boeck, L.R., Baumgartner, G., Sattelmayer, T., *Flame Flashback in Hydrogen Combustion with Acoustic Excitation: Simultaneous PIV and OH PLIF Measurements at High Repetition Rate.* Fachtagung "Lasermethoden in der Strömungsmesstechnik", 2014

Hoferichter, V., Keleshtery, P.M., Hirsch, C., Sattelmayer, T., Matsumura, Y., *Influence of Boundary Layer Air Injection on Flashback of Premixed Hydrogen-Air Flames.* ASME Turbo Expo, 2016, GT2016-56156

Hoferichter, V., Hirsch, C., Sattelmayer, T., *Prediction of Confined Flame Flashback Limits Using Boundary Layer Separation Theory*. Journal of Engineering for Gas Turbines and Power, 2017, 137, pp. 021505-1–10

Hoferichter, V., Hirsch, C., Sattelmayer, T., *Analytic Prediction of Unconfined Boundary Layer Flashback Limits in Premixed Hydrogen-Air Flames.* Combustion Theory and Modelling, 2016, pp. 1–37

Hoferichter, V., Sattelmayer, T., *Draft: Boundary Layer Flashback in Premixed Hydrogen-Air Flames with Acoustic Excitation.* Submitted to ASME Turbo Expo, 2017, GT2017-63080

Supervised Student Theses

Im Rahmen dieser Dissertation entstanden am Lehrstuhl für Thermodynamik, Technische Universität München in den Jahren 2013 bis 2016 unter wesentlicher wissenschaftlicher, fachlicher und inhaltlicher Anleitung der Autorin die im Folgenden aufgeführten studentischen Arbeiten. Ergebnisse aus diesen Arbeiten sind in Teilen in das vorliegende Dokument eingeflossen. Die Autorin dankt hiermit explizit allen ehemals betreuten Studenten für ihr Engagement bei der Unterstützung des hier behandelten Forschungsprojekts sowie der damit verknüpften Dissertation.

Associated with this Ph.D. thesis are a number of student theses (Bachelorarbeiten, Semesterarbeiten, Diplomarbeiten) that were supervised by the author of the present work. These theses were prepared at the Lehrstuhl für Thermodynamik, Technische Universität München in the years 2013 through 2016 under the close supervision of the present author. Parts of these supervised theses have been incorporated into the present thesis. The author would like to express her sincere gratitude to all formerly supervised students for their commitment and support of this research project and of the Ph.D. thesis at hand.

Student	**Thesis type, title, submission date**
Joel Bachmann	Bachelorarbeit, Bestimmung der Eigenfrequenzen eines Flammenrückschlag-prüfstands mit Hilfe von Constant Temperature Anemometry, 31.07.2014
Alexander Schein	Bachelorarbeit, Bestimmung der Eigenfrequenzen eines Flammenrückschlagsprüfstands mit Hilfe eines eindimensionalen akustischen Netzwerks, 10.09.2014
Christoph Haslinger	Bachelorarbeit, PIV Messungen des Geschwindigkeitsfeldes am Brenneraustritt eines Modellbrenners bei akustischer Anregung, 01.10.2014
Katrin Finke	Diplomarbeit, Entwicklung und Validierung eines MATLAB-Algorithmus zur Darstellung der Flammenfront aus OH-PLIF- und PIV-Aufnahmen einer turbulenten, vorgemischten Wasserstoffflamme, 23.04.2015
Ke Qu	IAESTE Internship, Boundary Layer Flashback with Acoustic Excitation in Turbulent Premixed Combustion Flow, 22.02.2016
Katharina Siegert	Semesterarbeit, Experimentelle Untersuchung des Einflusses von akustischen Geschwindigkeitsschwankungen auf das Wandrückschlagsverhalten vorgemischter Wasserstoff-Luft Flammen, 30.04.2016

Bibliography

[1] C. Lechner and J. Seume, *Stationäre Gasturbinen*, Springer, 2010.

[2] The European Parliament and the Council of the European Union, *Directive 2010/75/EU of the European Parliament and of the Council*, Official Journal of the European Union L 334 (2010), pp. 17–119.

[3] The European Parliament and the Council of the European Union, *Directive 2001/80/EC of the European Parliament and of the Council*, Official Journal of the European Union L 309 (2001), pp. 1–21.

[4] US Environmental Protection Agency, *Subpart KKKK–Standards of Performance for Stationary Combustion Turbines*, Code of Federal Regulations (2009), pp. 1097–1111.

[5] J. Gibbins and H. Chalmers, *Carbon Capture and Storage*, Energy Policy 36 (2008), pp. 4317–4322.

[6] R. Haszeldine, *Carbon Capture and Storage: How Green Can Black Be?*, Science 325 (2009), pp. 1647–1652.

[7] T. Lieuwen, V. McDonell, D. Santavicca, and T. Sattelmayer, *Burner Development and Operability Issues Associated with Steady Flowing Syngas Fired Combustors*, Combustion Science and Technology 180 (2008), pp. 1167–1190.

[8] F.E.C. Culick, *Unsteady Motions in Combustion Chambers for Propulsion Systems*, RTO / NATO, 2006.

[9] C. Eichler, *Flame Flashback in Wall Boundary Layers of Premixed Combustion Systems*, Ph.D. thesis, Technische Universität München, 2011.

[10] G. Baumgartner, *Flame Flashback in Premixed Hydrogen-Air Combustion Systems*, Ph.D. thesis, Technische Universität München, 2014.

[11] J. Fritz, M. Kröner, and T. Sattelmayer, *Flashback in a Swirl Burner With Cylindrical Premixing Zone*, Journal of Engineering for Gas Turbines and Power 126 (2004), pp. 276–283.

[12] F. Kiesewetter, M. Konle, and T. Sattelmayer, *Analysis of Combustion Induced Vortex Breakdown Driven Flame Flashback in a Premix Burner With Cylindrical Mixing Zone*, Journal of Engineering for Gas Turbines and Power 129 (2007), pp. 929–936.

[13] S. Burmberger and T. Sattelmayer, *Optimization of the Aerodynamic Flame Stabilization for Fuel Flexible Gas Turbine Premix Burners*, Journal of Engineering for Gas Turbines and Power 133 (2011), pp. 101501–1–10.

[14] B. Lewis and G. von Elbe, *Stability and Structure of Burner Flames*, The Journal of Chemical Physics 11 (1943), pp. 75–97.

[15] G. von Elbe and M. Mentser, *Further Studies of the Structure and Stability of Burner Flames*, The Journal of Chemical Physics 13 (1945), pp. 89–100.

[16] G. von Elbe and B. Lewis, *Theory of Ignition, Quenching and Stabilization of Flames of Nonturbulent Gas Mixtures*, Symposium on Combustion and Flame and Explosion Phenomena 3 (1949), pp. 68–79.

[17] M.E. Harris, J. Grumer, G. von Elbe, and B. Lewis, *Burning Velocities, Quenching, and Stability Data on Nonturbulent Flames of Methane and Propane with Oxygen and Nitrogen*, Symposium on Combustion and Flame and Explosion Phenomena 3 (1949), pp. 80–89.

[18] A.A. Putnam and R.A. Jensen, *Application of Dimensionless Numbers to Flash-Back and Other Combustion Phenomena*, Symposium on Combustion and Flame and Explosion Phenomena 3 (1949), pp. 89–98.

[19] K. Wohl, *Quenching, Flash-Back, Blow-Off – Theory and Experiment*, Symposium (International) on Combustion 4 (1953), pp. 68–89.

[20] L.E. Bollinger and R. Edse, *Effect of Burner-Tip Temperature on Flash Back of Turbulent Hydrogen-Oxygen Flames,* Industrial and Engineering Chemistry 48 (1956), pp. 802–807.

[21] L. Khitrin, P. Moin, D. Smirnov, and V. Shevchuk, *Peculiarities of Laminar- and Turbulent-Flame Flashbacks,* Symposium (International) on Combustion 10 (1965), pp. 1285–1291.

[22] B. Fine, *The Flashback of Laminar and Turbulent Burner Flames at Reduced Pressure,* Combustion and Flame 2 (1958), pp. 253–266.

[23] Z. Duan, B. Shaffer, and V. McDonell, *Study of Fuel Composition, Burner Material and Tip Temperature Effect on Flashback of Enclosed Jet Flame,* Journal of Engineering for Gas Turbines and Power 135 (2013), pp. 121504–1–10.

[24] C. Eichler, G. Baumgartner, and T. Sattelmayer, *Experimental Investigation of Turbulent Boundary Layer Flashback Limits for Premixed Hydrogen-Air Flames Confined in Ducts,* Journal of Engineering for Gas Turbines and Power 134 (2012), pp. 011502–1–8.

[25] Z. Duan, B. Shaffer, V. McDonell, G. Baumgartner, and T. Sattelmayer, *Influence of Burner Material, Tip Temperature and Geometrical Flame Configuration on Flashback Propensity of* H_2*-Air Jet Flames,* Journal of Engineering for Gas Turbines and Power 136 (2014), pp. 021502–1–10.

[26] S. Daniele, P. Jansohn, and K. Boulouchos, *Flashback Propensity of Syngas Flames at High Pressures: Diagnostic and Control,* in *Proceedings of ASME Turbo Expo,* 2010.

[27] A. Kalantari, E. Sullivan-Lewis, and V. McDonell, *Flashback Propensity of Turbulent Hydrogen-Air Jet Flames at Gas Turbine Premixer Conditions,* Journal of Engineering for Gas Turbines and Power 138 (2016).

[28] A. Kalantari, E. Sullivan-Lewis, and V. McDonell, *Application of a Turbulent Jet Flame Flashback Propensity Model to a Commercial Gas Turbine Combustor,* Journal of Engineering for Gas Turbines and Power 139 (2017), pp. 041506–1–8.

[29] S. Lee and J. T'ien, *A Numerical Analysis of Flame Flashback in a Premixed Laminar System*, Combustion and Flame 48 (1982), pp. 273–285.

[30] A. Gruber, R. Sankaran, E.R. Hawkes, and J.H. Chen, *Turbulent Flame-Wall Interaction: A Direct Numerical Simulation Study*, Journal of Fluid Mechanics 658 (2010), pp. 5–32.

[31] A. Gruber, J.H. Chen, D. Valiev, and C.K. Law, *Direct Numerical Simulation of Premixed Flame Boundary Layer Flashback in Turbulent Channel Flow*, Journal of Fluid Mechanics 709 (2012), pp. 516–542.

[32] C. Lietz, M. Hassanaly, and V. Raman, *Large Eddy Simulation of Premixed Flame Flashback in a Turbulent Channel*, in *AIAA SciTech*, 2014.

[33] A. Gruber, A.R. Kerstein, D. Valiev, C.K. Law, H. Kolla, and J.H. Chen, *Modeling of Mean Flame Shape During Premixed Flame Flashback in Turbulent Boundary Layers*, Proceedings of the Combustion Institute 35 (2015), pp. 1485–1492.

[34] G. Baumgartner, L.R. Boeck, and T. Sattelmayer, *Experimental Investigation of the Transition Mechanism from Stable Flame to Flashback in a Generic Premixed Combustion System With High-Speed Micro-PIV and Micro-PLIF Combined With Chemiluminescence Imaging*, Journal of Engineering for Gas Turbines and Power 138 (2015), pp. 021501–1–10.

[35] V. Hoferichter, C. Hirsch, and T. Sattelmayer, *Analytic Prediction of Unconfined Boundary Layer Flashback Limits in Premixed Hydrogen-Air Flames*, Combustion Theory and Modelling (2016), pp. 1–37.

[36] C. Eichler and T. Sattelmayer, *Premixed Flame Flashback in Wall Boundary Layer Studied by Long-Distance Micro-PIV*, Experiments in Fluids 52 (2012), pp. 347–360.

[37] D. Thibaut and S. Candel, *Numerical Study of Unsteady Turbulent Premixed Combustion: Application to Flashback Simulation*, Combustion and Flame 113 (1998), pp. 53–65.

[38] J. Keller, L. Vaneveld, D. Korschelt, G. Hubbard, A. Ghoniem, J. Daily, and A. Oppenheim, *Mechanism of Instabilities in Turbulent Combustion Leading to Flashback*, AIAA Journal 20 (1982), pp. 254–262.

[39] D. Davu, R. Franco, and A. Choudhuri, *Investigation on Flashback Propensity of Syngas Premixed Flames*, in *41st AIAA/ASME/SAE/ASEE Joint Propulsion Conference & Exhibit*, 2005.

[40] M. Subramanya and A. Choudhuri, *Investigation of Combustion Instability Effects on the Flame Characteristics of Fuel Blends*, in *5th International Energy Conversion Engineering Conference and Exhibit*, 2007.

[41] B. Dam, N. Love, and A. Choudhuri, *Flashback Propensity of Syngas Fuels*, Fuel 90 (2011), pp. 618–625.

[42] V. Sabel'nikov, C. Brossard, M. Orain, F. Grisch, M. Barat, A. Ristori, and P. Gicquel, *Thermo-Acoustic Instabilities in a Backward-Facing Step Stabilized Lean-Premixed Flame in High Turbulence Flow*, in *14th International Symposium on Applications of Laser Techniques to Fluid Mechanics*, 2008.

[43] T. Lieuwen and V. Yang, *Combustion Instabilities in Gas Turbine Engines*, AIAA, 2005.

[44] T. Sattelmayer, *Influence of the Combustor Aerodynamics on Combustion Instabilities From Equivalence Ratio Fluctuations*, Journal of Engineering for Gas Turbines and Power 125 (2003), pp. 11–19.

[45] J.E. Pieringer, *Simulation selbsterregter Verbrennungsschwingungen in Raketenschubkammern im Zeitbereich*, Ph.D. thesis, Technische Universität München, 2008.

[46] J.W.S. Rayleigh, *The Explanation of Certain Acoustic Phenomena*, Nature 18 (1878), pp. 319–321.

[47] F.M. White, *Viscous Fluid Flow*, McGraw-Hill, 2006.

[48] S.B. Pope, *Turbulent Flows*, Cambridge University Press, 2000.

[49] H. Schlichting and K. Gersten, *Boundary Layer Theory*, Springer-Verlag, 2000.

[50] L.F. Richardson, *Weather Prediction by Numerical Process*, Cambridge University Press, 1922.

[51] A.N. Kolmogorov, *The Local Structure of Turbulence in Incompressible Viscous Fluid for Very Large Reynolds Numbers*, Proceedings of the Royal Society of London A 434 (1991), pp. 9–13.

[52] D.B. Spalding, *A Single Formula for the "Law of the Wall"*, Journal of Applied Mechanics 28 (1961), pp. 455–458.

[53] B.S. Stratford, *The Prediction of Separation of the Turbulent Boundary Layer*, Journal of Fluid Mechanics 5 (1959), pp. 1–16.

[54] T. Cebeci, G.J. Mosinskis, and A.M.O. Smith, *Calculation of Separation Points in Incompressible Turbulent Flows*, Journal of Aircraft 9 (1972), pp. 618–624.

[55] J.P. Monty, N. Hutchins, H.C.H. NG, I. Marusic, and M.S. Chong, *A Comparison of Turbulent Pipe, Channel and Boundary Layer Flows*, Journal of Fluid Mechanics 632 (2009), pp. 431–442.

[56] J. Laufer, *Investigation of Turbulent Flow in A Two-Dimensional Channel*, Tech. Rep. 1053, National Advisory Committee for Aeronautics, 1951.

[57] T. Wei and W.W. Willmarth, *Reynolds-Number Effects on the Structure of a Turbulent Channel Flow*, Journal of Fluid Mechanics 204 (1989), pp. 57–95.

[58] V. Hoferichter, C. Hirsch, and T. Sattelmayer, *Prediction of Confined Flame Flashback Limits Using Boundary Layer Separation Theory*, Journal of Engineering for Gas Turbines and Power 139 (2017), pp. 021505–1–10.

[59] ANSYS, *ANSYS Fluent User's Guide*, 2014.

[60] H.W. Liepmann and J. Laufer, *Investigation of Free Turbulent Mixing*, Tech. Rep. 1257, National Advisory Committee for Aeronautics, 1947.

[61] I. Wygnanski and H.E. Fiedler, *The Two-Dimensional Mixing Region*, Journal of Fluid Mechanics 41 (1970), pp. 327–361.

[62] F.H. Champagne, Y.H. Pao, and I.J. Wygnanski, *On the Two-Dimensional Mixing Region*, Journal of Fluid Mechanics 74 (1976), pp. 209–250.

[63] C.W. Foley, I. Chterev, J. Seitzman, and T. Lieuwen, *High Resolution Particle Image Velocimetry and CH-PLIF Measurements and Analysis of a Shear Layer Stabilized Flame*, Journal of Engineering for Gas Turbines and Power 138 (2016).

[64] N. Peters, *The Turbulent Burning Velocity for Large-Scale and Small-Scale Turbulence*, Journal of Fluid Mechanics 384 (1999), pp. 107–132.

[65] G. Ciccarelli and S. Dorofeev, *Flame Acceleration and Transition to Detonation in Ducts*, Progress in Energy and Combustion Science 34 (2008), pp. 499–550.

[66] N. Peters, *Turbulente Brenngeschwindigkeit – Abschlussbericht zum Forschungsvorhaben Pe 241/9-2*, Tech. Rep., 1994.

[67] D.G. Goodwin, H.K. Moffat, and R.L. Speth, *Cantera: An Object-oriented Software Toolkit for Chemical Kinetics, Thermodynamics, and Transport Processes*, http://www.cantera.org (2015), version 2.2.

[68] M. Ó Conaire, H.J. Curran, J.M. Simmie, W.J. Pitz, and C.K. Westbrook, *A Comprehensive Modeling Study of Hydrogen Oxidation*, International Journal of Chemical Kinetics 36 (2004), pp. 603–622.

[69] G.P. Smith, D.M. Golden, M. Frenklach, N.W. Moriarty, B. Eiteneer, M. Goldenberg, C.T. Bowman, R.K. Hanson, S. Song, J. William C. Gardiner, V.V. Lissianski, and Z. Qin, *GRI-Mech 3.0*, http://www.me.berkeley.edu/gri_mech (2016).

[70] J. Göttgens, F. Mauss, and N. Peters, *Analytic Approximations of Burning Velocities and Flame Thicknesses of Lean Hydrogen, Methane, Ethylene,*

Ethane, Acetylene and Propane Flames, Symposium (International) on Combustion 24 (1992), pp. 129–135.

[71] M. Metghalchi and J.C. Keck, *Laminar Burning Velocities of Propane-Air Mixtures at High Temperature and Pressure*, Combustion and Flame 38 (1980), pp. 143–154.

[72] M. Metghalchi and J.C. Keck, *Burning Velocities of Mixtures of Air with Methanol, Isooctane, and Indolene at High Pressure and Temperature*, Combustion and Flame 48 (1982), pp. 191–210.

[73] A.E. Dahoe, *Laminar Burning Velocities of Hydrogen-Air Mixtures from Closed Vessel Gas Explosions*, Journal of Loss Prevention in the Process Industries 18 (2005), pp. 152–166.

[74] A.A. Konnov, *Remaining Uncertainties in the Kinetic Mechanism of Hydrogen Combustion*, Combustion and Flame 152 (2008), pp. 507–528.

[75] K.T. Aung, M.I. Hassan, and G.M. Faeth, *Flame Stretch Interactions of Laminar Premixed Hydrogen/Air Flames at Normal Temperature and Pressure*, Combustion and Flame 109 (1997), pp. 1–24.

[76] K.T. Aung, M.I. Hassan, and G.M. Faeth, *Effects of Pressure and Nitrogen Dilution on Flame/Stretch Interactions of Laminar Premixed* $H_2/O_2/N_2$ *Flames*, Combustion and Flame 112 (1998), pp. 1–15.

[77] D.R. Dowdy, D.B. Smith, and S.C. Taylor, *The Use of Expanding Spherical Flames to Determine Burning Velocity and Stretch Effects in Hydrogen/Air Mixtures*, Symposium (International) on Combustion 23 (1991).

[78] O.C. Kwon and G.M. Faeth, *Flame/Stretch Interactions of Premixed Hydrogen-Fueled Flames: Measurements and Predictions*, Combustion and Flame 124 (2001), pp. 590–610.

[79] S.D. Tse, D.L. Zhu, and C.K. Law, *Morphology and Burning Rates of Expanding Spherical Flames in* H_2/O_2*/Inert Mixtures up to 60 Atmospheres*, Proceedings of the Combustion Institute 28 (2000), pp. 1793–1800.

[80] C.M. Vagelopoulos, F.N. Egolfopoulos, and C.K. Law, *Further Considerations on the Determination of Laminar Flame Speeds with the Counterflow Twin-Flame Technique*, Symposium (International) on Combustion 25 (1994), pp. 1341–1347.

[81] C.K. Wu and C.K. Law, *On the Determination of Laminar Flame Speeds from Stretched Flames*, Symposium (International) on Combustion 20 (1985), pp. 1941–1949.

[82] B.E. Gelfand, *Flame Acceleration and Deflagration to Detonation Transition in Nuclear Safety - Appendix A: Laminar and Turbulent Flame Propagation in Hydrogen-Air-Steam Mixtures*, Tech. Rep., OECD Nuclear Energy Agency, 2000.

[83] S. Heimel, *Effect of Initial Mixture-Temperature on Burning Velocity of Hydrogen-Air Mixtures with Preheating and Simulated Preburning*, Tech. Rep., National Advisory Committee for Aeronautics, 1957.

[84] T. Iijima and T. Takeno, *Effects of Temperature and Pressure on Burning Velocity*, Combustion and Flame 65 (1986), pp. 35–43.

[85] Z. Chen, *On the Extraction of Laminar Flame Speed and Markstein Length from Outwardly Propagating Spherical Flames*, Combustion and Flame 158 (2011), pp. 291–300.

[86] S.C. Taylor, *Burning Velocity and the Influence of Flame Stretch*, Ph.D. thesis, University of Leeds, 1991.

[87] M.I. Hassan, K.T. Aung, and G. Faeth, *Measured and Predicted Properties of Laminar Premixed Methane/Air Flames at Various Pressures*, Combustion and Flame 115 (1998), pp. 539–550.

[88] X.J. Gu, M.Z. Haq, M. Lawes, and R. Woolley, *Laminar Burning Velocity and Markstein Lengths of Methane-Air Mixtures*, Combustion and Flame 121 (2000), pp. 41–58.

[89] G. Rozenchan, D.L. Zhu, C.K. Law, and S.D. Tse, *Outward Propagating, Burning Velocities, and Chemical Effects of Methane Flames up to 60 ATM*, Proceedings of the Combustion Institute 29 (2002), pp. 1461–1469.

[90] F. Halter, C. Chauveau, N. Djebaili-Chaumeix, and I. Gökalp, *Characterization of the Effects of Pressure and Hydrogen Concentration on Laminar Burning Velocities of Methane-Hydrogen-Air Mixtures*, Proceedings of the Combustion Institute 30 (2005), pp. 201–208.

[91] T. Tahtouh, F. Halter, and C. Mounaim-Rousselle, *Measurement of Laminar Burning Speeds and Markstein Lengths Using a Novel Methodology*, Combustion and Flame 156 (2009), pp. 1735–1743.

[92] E. Hu, Z. Huang, J. He, C. Jin, and J. Zheng, *Experimental and Numerical Study on Laminar Burning Characteristic of Premixed Methane-Hydrogen-Air Flames*, International Journal of Hydrogen Energy 34 (2009), pp. 4876–4888.

[93] S.R. Turns, *An Introduction to Combustion*, McGraw-Hill, 2000.

[94] N. Peters, *Turbulent Combustion*, Cambridge University Press, 2004.

[95] G. Markstein, *Nonsteady Flame Propagation*, McMillan Publication, 1964.

[96] T. Poinsot and D. Veynante, *Theoretical and Numerical Combustion*, Edwards, 2005.

[97] C.K. Law and C.J. Sung, *Structure, Aerodynamics, and Geometry of Premixed Flamelets*, Progress in Energy and Combustion Science 26 (2000), pp. 459–505.

[98] L.T.W. Chong, T. Komarek, M. Zellhuber, J. Lenz, C. Hirsch, and W. Polifke, *Inlfuence of Strain and Heat Loss on Flame Stabilization in a Non-Adiabatic Combustor*, in *Proceedings of the European Combustion Meeting*, 2009.

[99] C. Meneveau and T. Poinsot, *Stretching and Quenching of Flamlets in Premixed Turbulent Combustion*, Combustion and Flame 86 (1991), pp. 311–332.

[100] D. Veynante, J. Piana, J.M. Duclos, and C. Martel, *Experimental Analysis of Flame Surface Density Models for Premixed Turbulent Combustion*, Symposium (International) on Combustion 26 (1996), pp. 413–420.

[101] K.N.C. Bray, *Studies of the Turbulent Burning Velocity,* Proceedings of the Royal Society of London A: Mathematical, Physical and Engineering Sciences 431 (1990), pp. 315–335.

[102] C.J. Sun, C.J. Sung, L. He, and C.K. Law, *Dynamics of Weakly Stretched Flames: Quantitative Description and Extraction of Global Flame Parameters,* Combustion and Flame 118 (1999), pp. 108–128.

[103] M. Matalon and B.J. Matkowsky, *Flames as Gasdynamic Discontinuities,* Journal of Fluid Mechanics 124 (1982), pp. 239–259.

[104] Z. Chen and Y. Ju, *Theoretical Analysis of the Evolution from Ignition Kernel to Flame Ball and Planar Flame,* Combustion Theory and Modelling 11 (2007), pp. 427–453.

[105] J.K. Bechtold and M. Matalon, *The Dependence of the Markstein Length on Stoichiometry,* Combustion and Flame 127 (2001), pp. 1906–1913.

[106] T. Mitani and F.A. Williams, *Studies of Cellular Flames in Hydrogen-Oxygen-Nitrogen Mixtures,* Combustion and Flame 39 (1980), pp. 169–190.

[107] M.J. Brown, I.C. McLean, D.B. Smith, and S.C. Taylor, *Markstein Length of $CO/H_2/Air$ Flames, Using Expanding Spherical Flames,* Symposium (International) on Combustion 26 (1996), pp. 875–881.

[108] G. Dixon-Lewis, *Kinetic Mechanism, Structure and Properties of Premixed Flames in Hydrogen-Oxygen-Nitrogen Mixtures,* Philosophical Transactions of the Royal Society of London A292 (1979), pp. 45–99.

[109] F.N. Egolfopoulos and C.K. Law, *Chain Mechanisms in the Overall Reaction Orders in Laminar Flame Propagation,* Combustion and Flame 80 (1990), pp. 7–16.

[110] R. Borghi, *On the Structure and Morphology of Turbulent Premixed Flames,* in *Recent Advances in the Aerospace Sciences: In Honor of Luigi Crocco on His Seventy-fifth Birthday,* C. Casci and C. Bruno, eds., Springer US (1985), pp. 117–138.

[111] N. Peters, *Laminar Flamelet Concept in Turbulent Combustion*, Symposium (International) on Combustion 21 (1986), pp. 1231–1250.

[112] J.F. Driscoll, *Turbulent Premixed Combustion: Flamelet Structure and its Effect on Turbulent Burning Velocities*, Progess in Energy and Combustion Science 34 (2008), pp. 91–134.

[113] G. Damköhler, *The Effect of Turbulence on the Flame Velocity in Gas Mixtures*, Zeitschrift für Elektrochemie und angewandte Physikalische Chemie 46 (1940), pp. 601–652.

[114] B. Boust, J. Sotton, S.A. Labuda, and M. Bellenoue, *A Thermal Formulation for Single-Wall Quenching of Transient Laminar Flames*, Combustion and Flame 149 (2007), pp. 286–294.

[115] J. Sotton, B. Boust, S.A. Labuda, and M. Bellenoue, *Head-on Quenching of Transient Laminar Flame: Heat Flux and Quenching Distance Measurements*, Combustion Science and Technology 177 (2005), pp. 1305–1322.

[116] M. Bellenoue, T. Kageyama, S.A. Labuda, and J. Sotton, *Direct Measurement of Laminar Flame Quenching Distance in a Closed Vessel*, Experimental Thermal and Fluid Sciences 27 (2003), pp. 323–331.

[117] M. Enomoto, *Sidewall Quenching of Laminar Premixed Flames Propagating Along the Single Wall Surface*, Proceedings of the Combustion Institute 29 (2002), pp. 781–787.

[118] F. Dabireau, B. Cuenot, O. Vermorel, and T. Poinsot, *Interaction of Flames of* $H_2 + O_2$ *with Inert Walls*, Combustion and Flame 135 (2003), pp. 123–133.

[119] V. Hoferichter and T. Sattelmayer, *Draft: Boundary Layer Flashback in Premixed Hydrogen-Air Flames with Acoustic Excitation*, in *Submitted to ASME Turbo Expo*, GT2017-63080, 2017.

[120] V. Hoferichter, P.M. Keleshtery, C. Hirsch, T. Sattelmayer, and Y. Matsumura, *Influence of Boundary Layer Air Injection on Flashback of Pre-*

mixed Hydrogen-Air Flames, in *Proceedings of ASME Turbo Expo 2016*, GT2016-56156, 2016.

[121] H. Bruun, *Hot-Wire Anemometry: Principles and Signal Analysis*, Oxford University Press, 1995.

[122] G. Lomas, *Fundamentals of Hot Wire Anemometry*, Cambridge University Press, 1986.

[123] A. Perry, *Hot-Wire Anemometry*, Clarendon Press, 1982.

[124] T. Fiala, *Radiation from High Pressure Hydrogen-Oxygen Flames and its Use in Assessing Rocket Combustion Instability*, Ph.D. thesis, Technische Universität München, 2015.

[125] A.G. Gaydon, *The Spectroscopy of Flames*, 2nd ed., Chapman and Hall, 1974.

[126] F. Mayinger and O. Feldmann, *Optical Measurements*, Springer, 2001.

[127] W. Thielicke and E.J. Stamhuis, *PIVlab – Towards User-friendly, Affordable and Accurate Digital Particle Image Velocimetry in MATLAB*, Journal of Open Research Software 2 (2014).

[128] W. Thielicke and E.J. Stamhuis, *PIVlab - Time-Resolved Digital Particle Image Velocimetry Tool for MATLAB (version: 1.4)* (2014).

[129] B. Lewis and G. von Elbe, *The Concept of Flame Stretch*, International Journal of Research in Physical Chemistry and Chemical Physics 37 (1963), pp. 287–298.

[130] Y. Liu, *Untersuchung zur stationären Ausbreitung turbulenter Vormischflammen*, Ph.D. thesis, Universtität Fridericiana Karlsruhe, 1991.

[131] Z. Duan, A. Kalantari, and V. McDonell, *Parametric Analysis of Flashback Propensity with Various Fuel Compositions and Burner Materials*, in *Proceedings of the ASME Turbo Expo*, GT2015-43629, 2015.

[132] M. Thirumaleswar, *Fundamentals of Heat and Mass Transfer*, Pearson Education, 2009.

[133] T. Emmert, R. Leandro, A. Huber, and W. Polifke, *taX Manual*, Vol. v1.0, Lehrstuhl für Thermodynamik, Technische Universität München, 2013.